

Metal–Insulator Transitions in Heterostructures of Quantum Materials

Mattoni, Giordano

DOI

[10.4233/uuid:695c7410-ac2d-4fee-879b-2501a0d72421](https://doi.org/10.4233/uuid:695c7410-ac2d-4fee-879b-2501a0d72421)

Publication date

2017

Document Version

Final published version

Citation (APA)

Mattoni, G. (2017). *Metal–Insulator Transitions in Heterostructures of Quantum Materials*. [Dissertation (TU Delft), Delft University of Technology]. <https://doi.org/10.4233/uuid:695c7410-ac2d-4fee-879b-2501a0d72421>

Important note

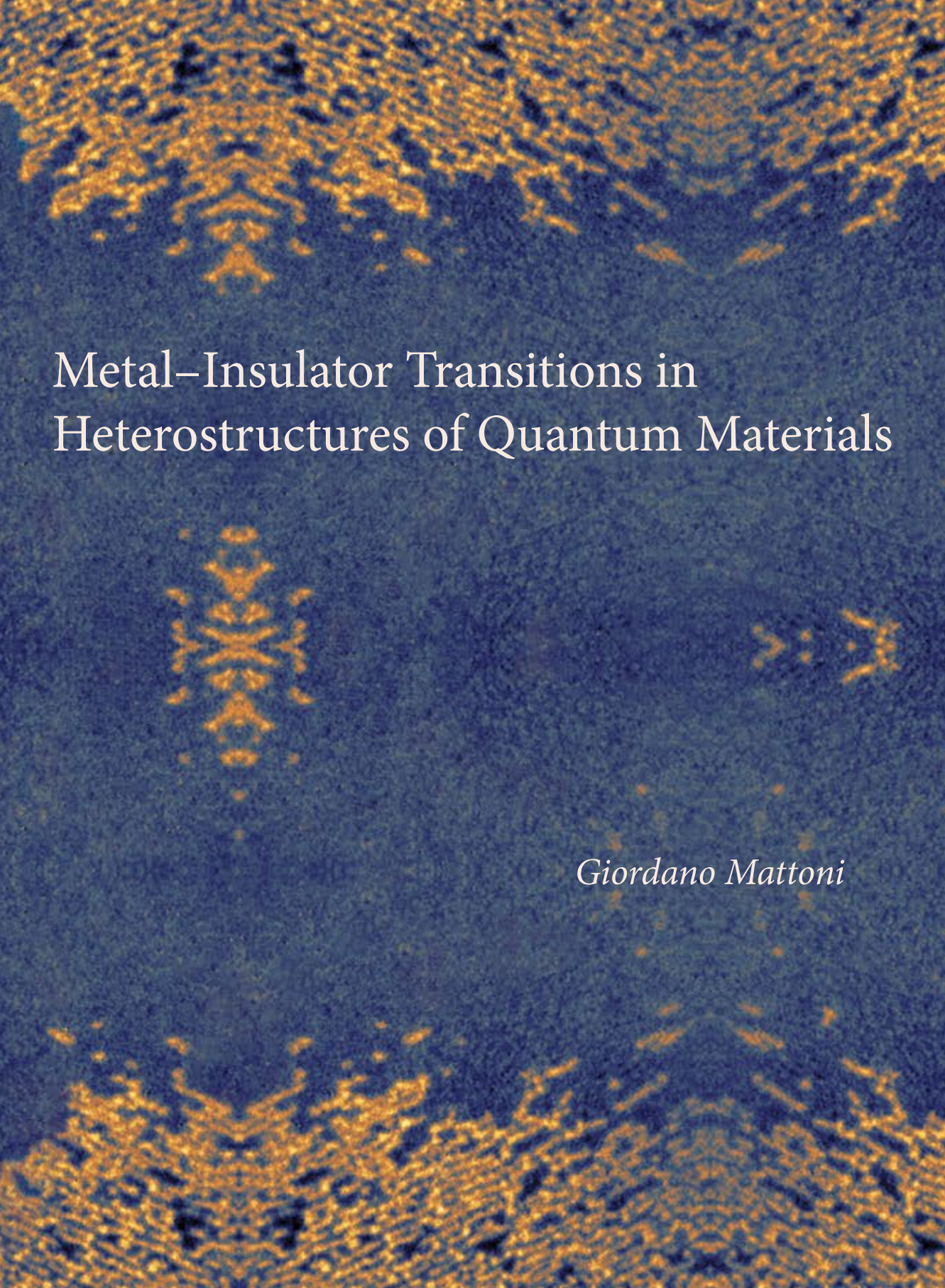
To cite this publication, please use the final published version (if applicable). Please check the document version above.

Copyright

Other than for strictly personal use, it is not permitted to download, forward or distribute the text or part of it, without the consent of the author(s) and/or copyright holder(s), unless the work is under an open content license such as Creative Commons.

Takedown policy

Please contact us and provide details if you believe this document breaches copyrights. We will remove access to the work immediately and investigate your claim.



Metal–Insulator Transitions in
Heterostructures of Quantum Materials

Giordano Mattoni

METAL–INSULATOR TRANSITIONS IN HETEROSTRUCTURES OF QUANTUM MATERIALS

Proefschrift

ter verkrijging van de graad van doctor
aan de Technische Universiteit Delft,
op gezag van de Rector Magnificus Prof. Ir. K.C.A.M. Luyben,
voorzitter van het College voor Promoties,
in het openbaar te verdedigen op maandag 18 december 2017 om 10:00 uur

door

Giordano MATTONI

Master of Science in Materials Science and Technology,
Tor Vergata University, Rome, Italy,
geboren te Rome, Italië.

This dissertation has been approved by

Promotor: Prof. Dr. Ir. H. S. J. van der Zant

Copromotor: Dr. A. D. Caviglia

Composition of the doctoral committee:

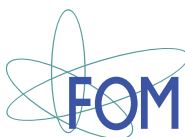
Rector Magnificus,
Prof. Dr. Ir. H. S. J. van der Zant,
Dr. A. D. Caviglia,

Voorzitter
Technische Universiteit Delft
Technische Universiteit Delft

Independent Members:

Prof. Dr. M. Bibes,
Prof. Dr. Y. Blanter,
Prof. Dr. A. Filippetti,
Prof. Dr. N. Pryds,
Prof. Dr. Ir. G. Rijnders,
Prof. Dr. Ir. P. G. Steeneken,

Unité Mixte de Physique CNRS/Thales
Technische Universiteit Delft
University of Cagliari
Technical University of Denmark
University of Twente
Technische Universiteit Delft (*reserve*)



European Research Council
Established by the European Commission

Keywords: Quantum materials, metal–insulator transitions, X-ray photoemission electron microscopy, low-temperature electronic transport, complex oxide heterostructures

Printed by: Gildeprint, Enschede

Front & Back: Photoelectron emission microscopy of metallic (blue) and insulating (orange) nanodomains in heteroepitaxial nickelates. Multiple "grain boundaries" are artificially created in image post processing.

Copyright © 2017 by G. Mattoni

Casimir PhD series 2017-46

ISBN 978-90-8593-330-4

An electronic version of this dissertation is available at
<http://repository.tudelft.nl/>.

*To those who explore—
cos they make innovation possible*

CONTENTS

List of abbreviations	ix
Summary	xi
Samenvatting	xiii
1 Introduction	1
1.1 The many WHYS	2
1.1.1 Why materials?	3
1.1.2 Why quantum materials?	3
1.1.3 Why heterostructures?	4
1.1.4 Why metal–insulator transitions?	5
1.2 The materials making up this thesis.	7
1.2.1 Nickelates	7
1.2.2 Tungsten trioxide	9
1.2.3 The LAO/STO conductive interface	10
1.3 Thesis outline.	12
2 Striped nanoscale phase separation in nickelates	15
2.1 Sample characterisation	16
2.2 Imaging contrast mechanism	17
2.3 Nanoscale evolution of the MIT.	19
2.4 MIT through bulk and surface techniques	22
2.5 Conclusions.	23
2.6 Methods	24
2.7 Supplementary information	25
2.7.1 PEEM contrast change with temperature	26
3 Light control of nickelates phase separation	29
3.1 Light effects on the MIT.	30
3.2 MIT cycles with photoexcitation	32
3.3 Transient heating by transport	33
3.4 Laser heating simulation	34
3.5 Conclusions.	36
3.6 Supplementary information	37
3.6.1 Laser heating model	40
4 Charge doping and large lattice expansion in WO₃	45
4.1 Film growth	46
4.2 Experimental characterisation	47
4.2.1 X-ray diffraction	47

4.2.2	Electrical transport.	49
4.3	Ab initio calculations	50
4.4	Conclusions.	54
4.5	Supplementary information	55
4.5.1	Additional ab initio calculations	61
5	Insulator-to-metal transition induced by WO₃ overlayers	65
5.1	Structural characterisation	66
5.2	Insulator-to-metal transition	67
5.3	Magnetotransport.	70
5.4	Temperature-dependent magnetotransport	72
5.5	Quantum oscillations of conductance	73
5.6	Conclusions.	75
5.7	Methods	75
5.8	Supplementary information	77
5.8.1	SdH oscillations with two-channel magnetoresistance.	85
6	Hydrogen sensing with heteroepitaxial WO₃	89
6.1	Material preparation	90
6.2	WO ₃ response to hydrogen	91
6.3	Hydrogen sensing.	93
6.4	Kinetic model.	94
6.5	Temperature-dependent electrical transport	97
6.6	Conclusions.	98
6.7	Methods	98
6.8	Supplementary information	99
6.8.1	Model for hydrogen reaction kinetics	104
6.8.2	Model for activated electrical transport	105
7	Conclusions and perspectives	107
7.1	Nickelates for neural networks and ultra-fast switches	108
7.2	Towards ballistic transport at oxide interfaces.	109
7.3	WO ₃ for hydrogen sensing, nano-ionics and beyond	112
A	Classical magnetotransport formulas	115
A.1	Charge transport for a single conduction channel.	115
A.2	Multichannel transport	117
A.3	Calculated Hall effect and magnetoresistance.	119
	References	123
	Curriculum vitae	135
	List of publications	137
	Acknowledgements	139

LIST OF ABBREVIATIONS

2DES	two-dimensional electron system
a.u.	arbitrary units
AFM	atomic force microscopy
C_H	atomic hydrogen concentration in the material lattice
C_{H_2}	molecular hydrogen concentration in gas phase
cps	counts per second
DFT	density functional theory
EELS	electron energy loss spectroscopy
FT	Fourier transform
FY	fluorescence yield
LAO	$LaAlO_3$
MIT	metal-insulator transition
MR	magnetoresistance
NNO	$NdNiO_3$
PEEM	photoemission electron microscopy
PLD	pulsed laser deposition
p_{O_2}	oxygen pressure during PLD growth
ppm	parts per million
r.l.u.	relative lattice units
RHEED	reflection high-energy electron diffraction
RRR	residual resistivity ratio
SdH	Shubnikov-de Haas
STO	$SrTiO_3$
TEM	transmission electron microscopy
TEY	total electron yield
uc	unit cell
XAS	X-ray absorption spectroscopy
XRD	X-ray diffraction
XRR	X-ray reflectivity

SUMMARY

This thesis is an experimental investigation of the physical properties of different transition metal oxide ultra-thin films. A common feature of these various materials and structures is that they exhibit a solid-state phase transition from a metallic to an insulating state, which is triggered upon changing sample composition, or by varying an external stimulus such as temperature, illumination or gas pressure. The results are achieved using several experimental techniques and theoretical support, ranging from thin film growth by pulsed laser deposition, material structural characterisation and nanodevice fabrication to low-temperature magnetotransport, density functional theory calculations, synchrotron microscopy and gas sensing.

Chapter 1 provides a general overview of the research covered in this thesis, followed by a brief introduction to the different materials of interest, namely rare-earth nickelates, tungsten trioxide WO_3 and the two-dimensional electron gas at the $\text{LaAlO}_3/\text{SrTiO}_3$ interface.

Chapter 2 makes use of X-ray photoemission electron microscopy to visualise the coexistence of metallic and insulating nanodomains across the metal–insulator transition of heteroepitaxial nickelates. A direct relationship between structural and electronic properties is found, which manifests itself in the preferential nucleation of insulating nanodomains along the surface terraces.

Chapter 3 explores the effect of illumination with short laser pulses on the phase-separated state in heteroepitaxial nickelates. By tuning the laser intensity, reversible control over the phase separation is achieved, which is described in terms of thermal effects on different timescales.

Chapter 4 deals with tungsten trioxide WO_3 , a perovskite material with important prospects for applications such as optoelectronic or electrochromic devices. High-quality ultra-thin films are grown by pulsed laser deposition and their structural and electronic properties are investigated. By regulating the formation of oxygen vacancies during material growth, a large lattice expansion along with charge doping are observed.

Chapter 5 discusses how amorphous WO_3 overlayers can be employed to induce a two-dimensional electron system with very high mobility at $\text{LaAlO}_3/\text{SrTiO}_3$ interfaces. A strong magnetoresistance, presence of multiple conduction channels and quantum oscillations of conductance are among the several interesting properties measured in this system.

Chapter 6 presents the use of WO_3 single-crystal thin films for H_2 gas sensing applications. By monitoring the change in resistivity induced by the platinum-catalysed intercalation of hydrogen in the WO_3 lattice, very low gas concentrations can be detected at room temperature and in a fully reversible process.

Chapter 7 concludes this work by summarising the most important findings of the previous chapters, and providing perspectives for future research work. Some challenges

and still open questions are discussed, along with some preliminary results concerning on-going experiments.

SAMENVATTING

Dit proefschrift beschrijft experimenteel onderzoek naar de fysische eigenschappen van verschillende ultradunne oxidelagen van overgangsmetalen. Een gemeenschappelijk kenmerk van deze materialen en structuren is dat ze een faseovergang in vaste toestand ondergaan, van een metaalachtige naar een isolerende toestand, die wordt geactiveerd door het veranderen van de samenstelling van het materiaal, of door het variëren van een externe stimulus, zoals temperatuur, belichting of gasdruk. De resultaten zijn verkregen met behulp van verschillende experimentele technieken en theoretische modellen: van dunne filmgroei met gepulseerde laserdepositie, karakterisering van de materiaalstructuur en nanodevice-fabricatie tot magnetotransport bij lage temperaturen, berekeningen met dichtheidsfunctionaaltheorie, synchrotronmicroscopie en gasdetectie.

Hoofdstuk 1 geeft een algemeen overzicht van het onderzoeksveld dat in dit proefschrift wordt behandeld, gevolgd door een korte inleiding van de verschillende onderzochte materialen, namelijk zeldzame aard-nikkelaten, wolframtrioxide WO_3 en het tweedimensionale elektronengas op het $\text{LaAlO}_3/\text{SrTiO}_3$ grensvlak.

Hoofdstuk 2 maakt gebruik van X-ray photoemission electron microscopy om de fase-coëxistentie van metaalachtige en isolerende nanodomeinen rond de metaal-isolator transitie van heteroepitaxiale nikkelaten zichtbaar te maken. Een directe relatie tussen materiaalstructuur en elektronische eigenschappen wordt gevonden, die zich uit in nucleatie van isolerende nanodomeinen, met name langs de oppervlakteterrassen.

Hoofdstuk 3 onderzoekt het effect van belichting met korte laserpulsen op de fasegescheiden toestand in heteroepitaxiale nikkelaten. Door het afstemmen van de laserintensiteit wordt omkeerbare controle over de fasescheiding bereikt, wat beschreven wordt in termen van thermische effecten op verschillende tijdschalen.

Hoofdstuk 4 behandelt wolframtrioxide WO_3 , een perovskietmateriaal met belangrijke eigenschappen voor toepassingen in bijvoorbeeld opto-elektronica of elektrochrome apparaten. Hoogwaardige, ultradunne films worden gegroeid met gepulseerde laserdepositie en de structurele en elektronische eigenschappen worden onderzocht. Door de vorming van zuurstofvacatures tijdens de materiaalgroei te reguleren, wordt een grote roosteruitzetting en ladingsdotering waargenomen.

Hoofdstuk 5 bespreekt hoe amorfe WO_3 bovenlagen kunnen worden gebruikt om een tweedimensionaal elektronensysteem met zeer hoge mobiliteit op $\text{LaAlO}_3/\text{SrTiO}_3$ grensvlakken te induceren. Een grote magnetoweerstand, aanwezigheid van meerdere geleidingskanalen en kwantumoscillaties van geleiding behoren tot de vele interessante eigenschappen die in dit systeem worden gemeten.

Hoofdstuk 6 presenteert het gebruik van WO_3 monokristallijne dunne films voor H_2 gasdetectietoepassingen. Door de veranderingen in de soortelijke weerstand te meten die veroorzaakt worden door de platina-gekatalyseerde intercalatie van waterstof in het WO_3 rooster, kunnen zeer lage gasconcentraties worden gedetecteerd bij kamertemperatuur in een volledig omkeerbaar proces.

Hoofdstuk 7 concludeert dit proefschrift door de belangrijkste bevindingen van de vorige hoofdstukken samen te vatten en in perspectief te plaatsen voor toekomstig onderzoek. Uitdagingen en openstaande vragen worden besproken, samen met enkele voorlopige resultaten met betrekking tot lopende experimenten.

1

INTRODUCTION

This chapter is meant to introduce the topic of this thesis. The fundamental concepts behind this work will be presented, providing directions on how to read and understand the following chapters.

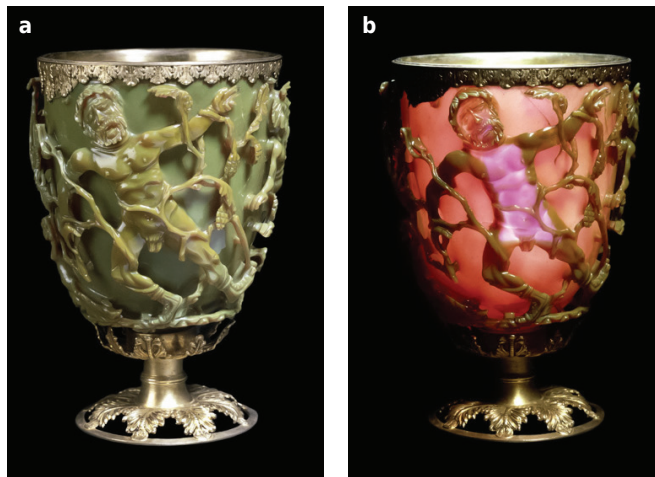


Figure 1.1: **Lycurgus cup.** (a) Glass cage cup from the late Roman period (4th century) covered with various scenes representing the death of King Lycurgus. The cup is made of a special dichroic glass, containing gold and silver nanoparticles, which shows a different colour when illuminated with reflected or (b) transmitted light; © Trustees of the British Museum.

MATERIALS are the constituents of every thing around us. Humans have always exploited different materials for their needs, often being faced with fascinating new effects which they were not able to control. A notable example dates back to the 4th century A.D., when the Romans built a celebrative cup with a special dichroic glass material (Fig. 1.1). The glass shows a green colouration when it is lit from the front, and a red one when light passes through it. Only recently, it was discovered that the glass contains a very small amount of silver and gold nanoparticles (about 70 nm in diameter) which, due to a surface plasmon resonance, determine different light scattering according to the method of illumination. The Romans certainly could not understand nor control this level of technology, and the special glass remained a unique piece of its kind.

With the development of materials science, fascinating new effects and novel technologies became available and controllable. The scope of this thesis is to investigate advanced electronic materials, whose properties can be controlled by external stimuli.

1.1. THE MANY WHYS

Scientists strongly believe that the motivation is one of the key aspects of effective science dissemination. Any result, as intriguing and spectacular as it may be, in fact, loses almost all its *verve* if it does not address a clear fundamental question, and it is considered out of its context. I would thus like to start opening this *matryoshka* of scientific research by motivating the title of this thesis, and showing how it is meant to gradually immerse the reader from the observable world, right into fundamental physics and materials science.

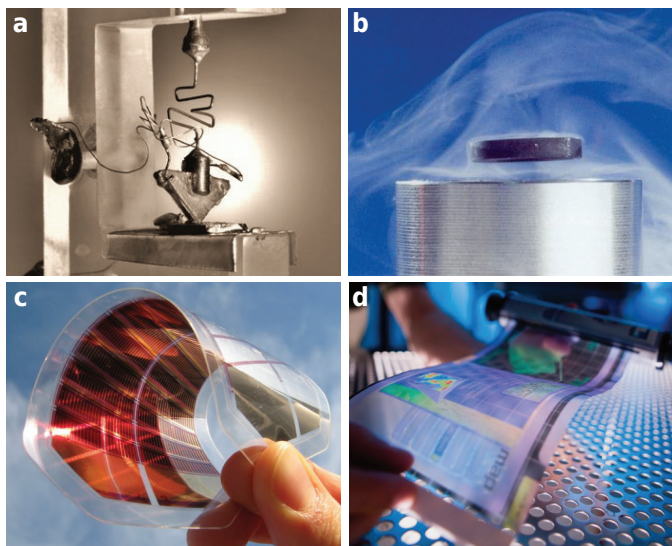


Figure 1.2: **Novel materials enable the progress of new technologies.** (a) Germanium point contact transistor from Bardeen, Shockley and Brattain, the first working transistor ever invented (1947); © *Bell Labs*. (b) A superconducting crystal of $\text{YBa}_2\text{Cu}_3\text{O}_7$ cooled down to 77 K floating over a magnet. (c) A flexible, semi-transparent solar panel; © *Fraunhofer ISE*. (d) A flexible O-LED display; © *U.S. Army RDECOM*.

1.1.1. WHY MATERIALS?

Many technologies that became part of everyday life are achieved thanks to advanced electronic materials. One can think of the most basic ones, such as a light bulb or a battery, or the most powerful ones, such as the transistor (Fig. 1.2a). Since its invention in 1947 [1], the transistor became the building block of modern electronics. Its importance lies in the possibility of tuning its properties by means of an external stimulus. This paved the way to an increasing number of materials that can be controlled by external parameters. Promising examples are the high-temperature superconductors (Fig. 1.2b), which allow the fabrication of fast electrical circuits and magnetic levitation trains, semi-transparent solar panels (Fig. 1.2c), which are being integrated directly in transparent windows, and flexible displays and electronics (Fig. 1.2d), which are enabling the industry of wearable technologies. While some of these materials are nowadays becoming industrial realities, many classes of materials still require a more fundamental physical understanding.

1.1.2. WHY QUANTUM MATERIALS?

A rapidly growing research field in condensed matter physics is the novel class of quantum materials, which is characterised by the dominant role of quantum mechanical effects in determining the material physical properties [2–4]. This can be attributed to the *strongly correlated* nature of the electrons (Fig. 1.3), usually belonging to d electron shells, where the strong interaction between their charge, spin, orbital and lattice degrees of freedom has an energy scale comparable to their kinetic energy. As a result, the

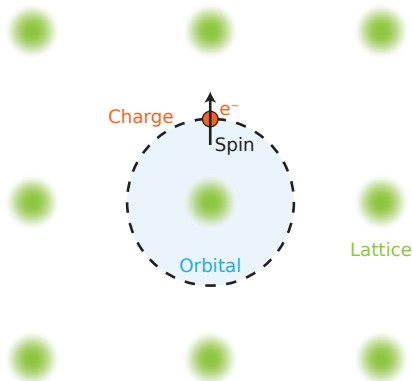


Figure 1.3: **Strongly correlated character of quantum materials.** Schematic illustration of the strong interactions between the charge, spin, orbital and lattice degrees of freedom of quantum materials constituent particles.

properties of these materials *emerge* as collective phenomena of their constituents, giving rise to novel phases of matter. Interesting examples include the formation of charge density waves [5], where electrons form standing wave patterns, skyrmions [6], a twisting spin texture important in the field of spintronics, and vortices in superconductors [7], that are boundaries between superconducting and normal regions which are an attractive candidate for information technology.

Due to the delicate balance of energy scales of the different interactions, multiple phases of matter can compete with each other. This often leads to the formation of phase-separated states, which are a hallmark of quantum materials. Mesoscopic states can be stabilised in different spatial regions thanks to elements that locally modify the potential landscape, such as point defects, compositional variations, strain and controlled patterning. Memory effects are also often observed as a direct consequence of phase separations, holding great potential for technological purposes [8].

Quantum materials are extremely sensitive to external stimuli, which can be used to tune their properties *on demand*. Notable examples include static external perturbations, such as hydrostatic pressure [9], which has a direct influence on the orbital overlap of the atoms in a lattice, and high magnetic fields [10], which orient magnetic textures or change the dispersion of electronic bands. Ultra-fast perturbations are another interesting knob, which can be used to drive quantum phases on the time scale of their fundamental electronic and atomic motion [11, 12], thus probing materials strongly out of equilibrium and potentially revealing *hidden phases of matter*.

1.1.3. WHY HETEROSTRUCTURES?

An important means for controlling quantum materials is heterostructuring, that is the combination of multiple materials stacked on top of each other. This offers the possibility of engineering novel electronic phases at the interface of dissimilar oxides [13], inducing interlayer couplings by superlattice modulation [14], and stabilising crystal phases of ultra-thin film materials [15]. Growth of these structures has been greatly boosted

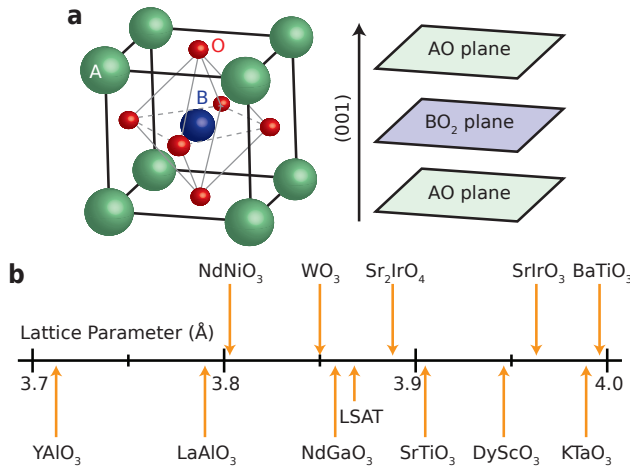


Figure 1.4: **Complex oxide heterostructures.** (a) Schematic of the ABO_3 perovskite unit cell, typical crystal structure for many complex oxide materials. The B-site cation is in octahedral coordination with six oxygen atoms. Along the (001) crystallographic direction, the structure can be visualised as alternating AO and BO_2 planes. (b) Simple cubic lattice parameter of several complex oxides, which lies in a small range of values between 3.7 Å and 4.0 Å. The similarity in lattice structure and size enables the fabrication of heterostructures of complex oxide materials.

in the last decade by technological advancements in thin film growth techniques, such as off-axis magnetron sputtering, molecular beam epitaxy (MBE) [16], and pulsed laser deposition (PLD) [17].

A subclass of quantum materials are the perovskite complex oxides, which are ideal candidates to build heterostructures. These materials of chemical formula ABO_3 crystallise in the structure illustrated in Fig. 1.4a, where A and B are two cations and the B-atom is surrounded by an oxygen octahedron. Along the (001) crystal direction, this structure can be visualised as a stacking of AO and BO_2 planes, which play a crucial role in the formation of oxide interfaces, as further described in Section 1.2.3. Several complex oxides have a simple cubic lattice parameter ranging from 3.7 Å to 4 Å (Fig. 1.4b). This enables the growth of heterostructures with a coherent crystal lattice. Stacking materials with different lattice parameters determines the insurgence of heteroepitaxial strain, which can be used to tune material properties. Furthermore, heterostructuring allows us to combine and couple materials presenting different functionalities, with the potential of creating *novel states of matter*.

1.1.4. WHY METAL–INSULATOR TRANSITIONS?

Electrical transport, a tool to measure the resistivity of a material, is usually the first step to study novel functionalities. The resistivity is, in fact, a key property that characterises a material, which can be generally classified as a metal or as an insulator, according to its temperature dependence (Fig. 1.5a). For insulators, the electrical resistivity decreases with temperature ($dR/dT < 0$), while the opposite is valid for metals ($dR/dT > 0$). In weakly- or non-interacting electron systems this is a direct consequence of the material's

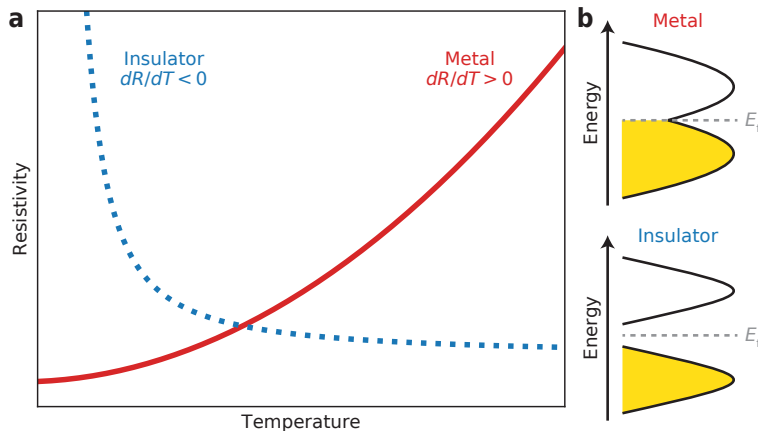


Figure 1.5: **Insulators and metals.** (a) Insulators are usually defined as materials where the resistivity decreases as a function of temperature ($dR/dT < 0$), while the opposite holds for metals. (b) Schematic band diagram for metals and insulators. Metals show a continuous density of states at the Fermi level (E_F), while insulators present an energy gap between the filled valence band (bottom) and the empty conduction band (top); figure adapted from ref. [18].

band structure, which is schematically depicted in Fig. 1.5b. Metals have a continuous density of states at the Fermi level (E_F), while insulators present an energy gap between the filled valence band and the empty conduction band.

Simple band theory usually breaks down when strong correlations come into play. Many materials with partially filled d orbitals should be metals according to band theory, but are actually insulators [18]. Different scenarios can be responsible for this anomalous behaviour according to the nature of the electron–electron interactions. In the case of Mott insulators, a large Coulomb repulsion U comes into play when two electrons occupy the same lattice site [19]. If this term is larger than the energy required for an electron to hop from one lattice site to another (usually indicated as $-t$), the charge carriers become localised and the material is an insulator. In the case of Slater insulators, usually materials with an antiferromagnetic ground state, the formation of long-range magnetic order is responsible for the insulating state [20]. Another case is the one of Anderson insulators, materials where strong crystal disorder, such as defects and impurities, determines the localisation of the charge carriers [21].

In a scenario of competing energy scales for strong correlations, metal–insulator transitions (MITs) often occur, constituting a hallmark of many families of quantum materials. These transitions can be triggered by tuning several external parameters, such as pressure, lattice distortions and doping [22]. Because MITs occur in solid-state phases, inducing drastic changes in the properties of a material without altering its physical state of matter, they hold great scientific interest both from the technological and from the fundamental point of view.

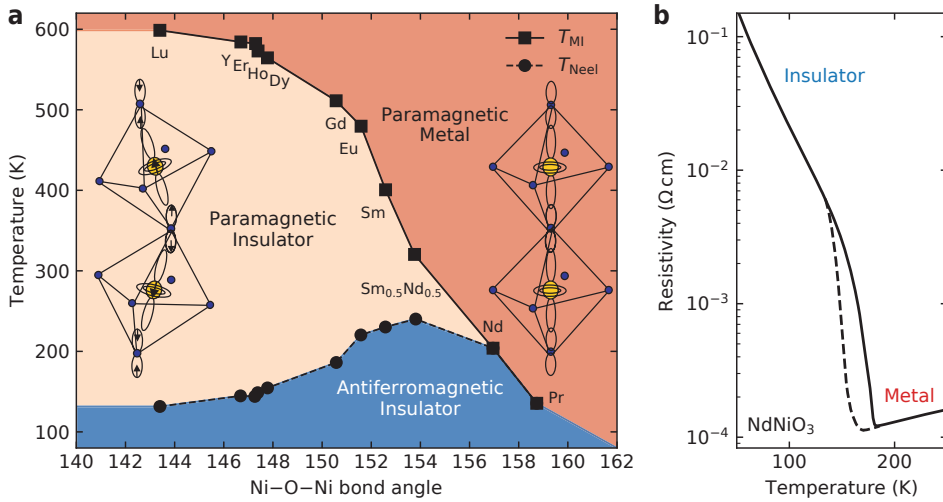


Figure 1.6: **MIT in nickelates.** (a) Phase diagram of perovskite nickelates, showing the dependence of the electronic (T_{MI}) and magnetic (T_{Neel}) phase transitions from the Ni-O-Ni bond angle. The insets show a schematic representation of the change in bond angle; panel adapted from ref. [15]. (b) Resistivity versus temperature of a NdNiO₃ thin film on NdGaO₃ substrate during a cooling (dashed) and warming ramp (solid line). The curves show the hysteretic nature of the phase transition from high-temperature metallic to low-temperature insulating state; sample characterisation in Chapter 2.

1.2. THE MATERIALS MAKING UP THIS THESIS

In this section we introduce the material classes that are investigated in the following chapters. Our work focuses on heteroepitaxial thin film materials showing an MIT, which we control by tuning external parameters. Epitaxial strain and temperature will be used in the case of the nickelates, while chemical and electrostatic doping will be employed for WO₃ and LaAlO₃/SrTiO₃ oxide interfaces. In the following brief overviews, we present the key aspects of the MIT occurring in these three classes of materials.

1.2.1. NICKELATES

Perovskite nickelates are a class of materials with chemical formula RNiO₃, where R is a rare-earth element and Ni is in its 3+ oxidation state. While these compounds are difficult to synthesise in bulk form, the template provided by a perovskite substrate favours the stabilisation of the same crystal lattice in heterostructures, such that high-quality nickelate thin films can nowadays be synthesised [15, 25]. Electrical conduction in these materials is regulated by the hybridisation of Ni 3d and oxygen 2p orbitals, such that the Ni-O-Ni bond angle plays a crucial role in determining the electronic properties. As shown in the nickelates phase diagram of Fig. 1.6a, the bond angle is influenced by the atomic size of the rare-earth atom, where larger species determine higher overlap of the atomic orbitals, increasing the electronic bandwidth. Metallic or insulating phases are thus promoted in different temperature ranges according to the choice of the rare-earth, with an MIT occurring at a temperature T_{MI} that gradually shifts from about 600 K, in

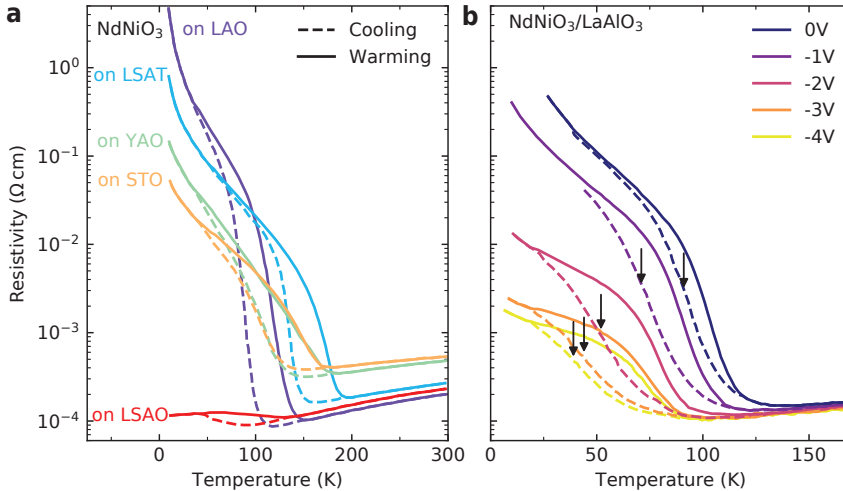


Figure 1.7: **Tunability of the MIT in NdNiO₃ thin films.** (a) Resistivity versus temperature curves of NdNiO₃ thin films deposited on different substrates; panel adapted from ref. [23]. (b) Resistivity versus temperature of a thin film grown on LaAlO₃ with different applied gate voltages. An ionic liquid is used as gate dielectric, determining a change of the MIT temperature (indicated by the black arrows upon a cooling ramp); panel adapted from ref. [24].

the case of LuNiO₃, to about 100 K for PrNiO₃. Some compounds present an additional transition at T_{Neel} from a high-temperature paramagnetic insulator to a low-temperature antiferromagnetic insulating state. Individual magnetic transitions are, however, out of the scope of this thesis because we will focus on NdNiO₃, where both the electronic and the magnetic phase transition occur at the same temperature (i.e., $T_{\text{MI}} = T_{\text{Neel}}$).

The nature of the MIT in nickelates is still matter of intense research [26–30]. Many experimental reports show that an orthorhombic-to-monoclinic structural transition occurs below T_{MI} , determining the formation of two inequivalent Ni lattice sites, with different distribution of their charge. In this regime, both charge and spin ordering can emerge, determining the formation of an insulating state.

A sharp temperature-driven MIT can be detected by electrical transport in several nickelate compounds. In the case of NdNiO₃, where the electronic and magnetic phase transitions are coupled, the phase transition is of the first order and a broad hysteresis occurs (Fig. 1.6). In heteroepitaxial thin films, several reports show that the MIT can be tuned by external parameters such as hydrostatic pressure [31, 32], epitaxial strain (Fig. 1.7a) and static electric field (Fig. 1.7b). Due to the first-order nature of the phase transition, a coexistence of metallic and insulating regions in the vicinity of the MIT is expected to occur. We investigate this aspect in Chapter 2 by performing the first real-space nanoscale imaging in nickelates. By using photoemission electron microscopy, we find that the MIT has nanoscale inhomogeneous character, with the insurgence of a phase-separated state of metallic and insulating domains. In Chapter 3 we further develop these findings, demonstrating that reversible control over the phase transition can be achieved by using laser light.

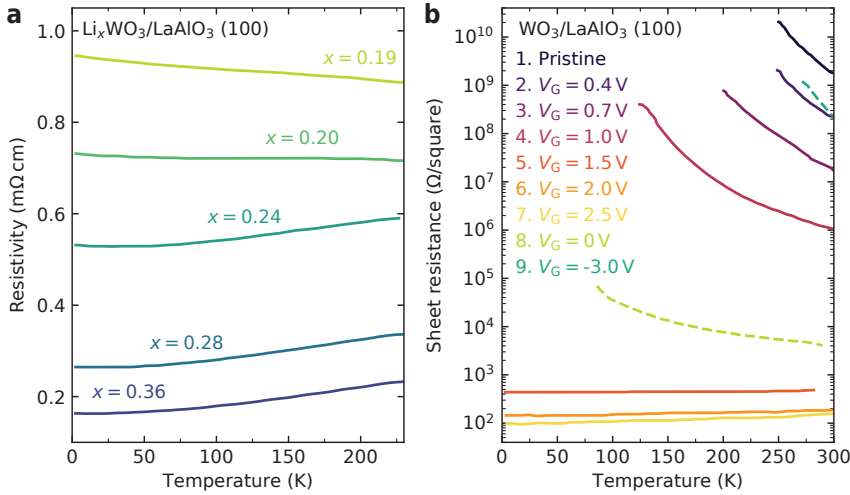


Figure 1.8: **Resistivity versus temperature of WO₃ thin films undergoing an MIT.** (a) Li atoms are introduced into the WO₃ lattice using an electrochemical method. The intercalated atoms induce electron doping of W 5d orbitals, determining a semiconductor-to-insulator transition for $x \geq 0.24$; panel adapted from ref. [33]. (b) An ionic liquid gate is used to modulate the resistivity of WO₃ thin films. The mechanism involves the electric-field-induced motion of oxygen atoms, which leads to major structural changes in WO₃ that stabilise higher symmetry phases. These changes determine variations of the electronic structure, accounting for metallisation of the oxide material; panel adapted from ref. [34].

1.2.2. TUNGSTEN TRIOXIDE

Tungsten oxide WO₃ is a semiconductor material that has a particular perovskite structure, where the A lattice sites are left vacant. In its stoichiometric form, the W⁶⁺ ions have empty 5d states, entailing a band gap of about 3 eV [35]. Due to its open crystal structure, WO₃ is very sensitive to the intercalation of atomic species, which induce electron doping, changing both the material electronic and optical properties. For this reason, WO₃ is widely used for electrochromic, smart windows, photocatalysis, and gas sensing applications [36–38].

The material has a complex phase diagram, where the ideal cubic phase is distorted into several, lower-symmetry crystalline phases which are stable in different pressure and temperature conditions [39, 40]. Only recently, heterostructuring of crystalline WO₃ thin films on perovskite substrates has enabled the stabilisation of the cubic structure at room temperature, leading to materials with enhanced surface-to-volume ratio and high crystal quality [41–44]. Thanks to the long-range crystal order, WO₃ thin films have enhanced sensitivity to doping, which can be used to trigger MITs. We show in Fig. 1.8a, as an example, how intercalation of Li atoms can be used to gradually tune the material from a semiconducting to a metallic state. Another possibility for doping WO₃ is illustrated in Fig. 1.8b, and it involves the formation of oxygen vacancies acting as electron donors.

In this thesis we grow heteroepitaxial WO₃ by pulsed laser deposition on (001) SrTiO₃ substrates. As shown in Fig. 1.9, we can obtain thin films of high crystal quality, where

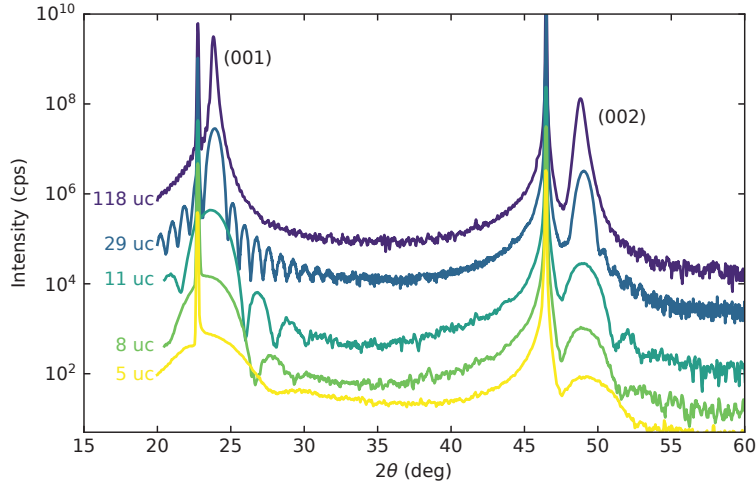


Figure 1.9: **WO₃ thin films of different thickness.** X-ray diffraction characterisation of heteroepitaxial WO₃ thin films grown by pulsed laser deposition on (001) SrTiO₃ substrates. The (001) and (002) film diffraction peaks appear on the right of the sharp substrate peaks, and show neat finite size oscillations which indicate high crystalline quality.

precise control over film thickness is enabled by *in-situ* monitoring of the deposition process with reflection high-energy electron diffraction (RHEED). In [Chapter 4](#) we show how tuning the oxygen pressure during pulsed laser deposition allows us to modify the material structure and electronic properties. WO₃ overlayers, in amorphous form, are exploited in [Chapter 5](#), where they are used to induce charge transfer at LaAlO₃/SrTiO₃ interfaces in a modulation doping configuration.

Another interesting approach for controlling MITs in WO₃ involves doping with H₂ gas. This process is catalysed by Pt particles, which facilitate the intercalation of H species into WO₃ lattice [45, 46]. These aspects are investigated in more detail in [Chapter 6](#), where we develop a highly sensitive hydrogen sensor based on WO₃ heteroepitaxial thin films.

1.2.3. THE LAO/STO CONDUCTIVE INTERFACE

The LaAlO₃/SrTiO₃ interface (in short LAO/STO) constitutes a paradigmatic example of how novel states of matter can be artificially created in quantum materials. Both LAO and STO are, in fact, insulating perovskites with a large band gap of 3.2 eV and 5.6 eV, respectively. When a sharp heterostructure of the two materials is created, an abrupt polar discontinuity forms at the interface, and it is responsible for the formation of a conductive, two-dimensional electron system (2DES). This system shows a series of fascinating effects, among which two-dimensional superconductivity [49], gate tunability [50], strong spin-orbit coupling [51, 52] and signatures of magnetism [53, 54].

The origin of the 2DES can be traced back to the crystal lattice of LAO and STO. Along the (001) lattice direction ([Fig. 1.10a](#)), LAO is a stacking of La³⁺O²⁻ and Al³⁺O₂⁴⁻ planes with alternating net charge +1 and -1, while STO is made of neutral planes of Sr²⁺O²⁻

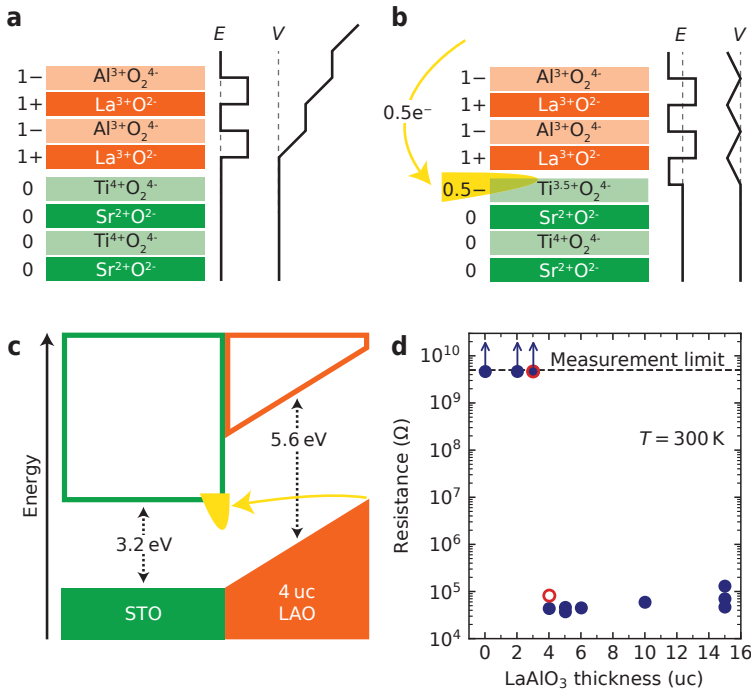


Figure 1.10: **Polar discontinuity at the LAO/STO interface.** (a) Pristine and (b) reconstructed interface where STO has TiO_2 termination. The electric field E and the electrostatic potential V are indicated layer-by-layer in the side sketches, while the yellow arrow indicates the electron charge transfer towards the interface; panels adapted from ref. [47]. (c) Schematic band structure showing the filled valence (bottom) and empty conduction (top) states in the LAO/STO heterostructure. (d) Sheet resistance as a function of LAO unit cells showing the critical thickness for conductivity; panel adapted from ref. [48].

and $\text{Ti}^{4+}\text{O}_2^{4-}$. Starting from the STO side, the LAO/STO heterostructure can thus be viewed as a series of charged parallel plate capacitors, which generate an electrostatic potential V that increases by about 1 eV per LAO unit cell. With increasing thickness of the LAO layer, the electrostatic potential diverges, determining what is usually described as a *polar catastrophe* [48, 55]. When the accumulated electrostatic energy becomes larger than the energetic cost associated with the rearrangement of electronic charges, a charge transfer from the LAO valence band to the STO conduction band occurs (Figs. 1.10b and 1.10c), determining the formation of a 2DES.

This electronic reconstruction is responsible for an insulator-to-metal transition at the LAO/STO interface. As presented in Fig. 1.10d, experimental reports show that the reconstruction occurs at the critical LAO thickness of 4 uc. Furthermore, a metallic 2DES is observed only if a TiO_2 -terminated STO substrate is used, whereas SrO termination leads to insulating systems [47, 56]. Many experiments indicate that the polar catastrophe scenario is a simplified description of the LAO/STO system, and a consistent picture should include the presence of point defects, among which oxygen vacancies and cation off-stoichiometry [57–60]. We study these aspects in Chapter 5, where we demonstrate

that oxygen-deficient WO_3 overlayers can be employed to induce an MIT at LAO/STO interfaces below the critical thickness of 4 uc of LAO. Moreover, our overlayers enhance the properties of the LAO/STO system, determining the formation of high-mobility electron channels and a large magnetoresistance.

1.3. THESIS OUTLINE

The present work investigates MITs in different material systems. Thin films are the target of all our studies, most of which are grown directly in our group by pulsed laser deposition, with the exception of the nickelates which are grown by sputtering in Geneva University, Switzerland. A certain extent of low-temperature electrical transport measurements, atomic force microscopy and X-ray diffraction characterisations are presented in each chapter, and are performed in the TU Delft laboratories, The Netherlands. Fabrication of the devices used for transport measurements is performed in the cleanroom facilities of the Kavli Nanolab Delft, The Netherlands. Synchrotron measurements at the Diamond Light Source (Didcot, UK) allowed us to perform microscopy with nanoscale resolution on the nickelates system. Transmission electron microscopy, carried out by our collaborators in Cornell University, USA, allowed us to image with atomic resolution our sharp WO_3 /LAO/STO heterostructures. Finally, constant theoretical support was provided by our collaborators in Cagliari University and University of Rome Tor Vergata, both in Italy. The different topics are organised in several chapters which are outlined in the following.

Chapter 2 explores the MIT in nickelates, showing the first real-space images of how this phase transition occurs at the nanoscale. Employing photoelectron emission microscopy, we unravel the formation of a phase-separated state of insulating and metallic nanodomains. The domains present a striped pattern, which is directly linked to the surface morphology of our heteroepitaxial thin film.

Chapter 3 builds up from the results of the previous chapter, showing that nickelates phase separation can be controlled by means of laser light. An ultra-fast laser at 800 nm is used for this purpose, demonstrating reversible control over the distribution of insulating and metallic phases.

Chapter 4 deals with WO_3 heteroepitaxial thin films, grown by pulsed laser deposition. We show how the material properties are strongly modified by oxygen pressure during deposition, which is responsible for a lattice volume increase up to 10% and an electron doping towards a metallic state. Density functional theory is employed to unravel the properties of oxygen defect states, responsible for the doping, providing a thorough understanding of WO_3 material properties.

Chapter 5 exploits the high reactivity of amorphous WO_3 overlayers to induce an insulator-to-metal transition at $\text{LaAlO}_3/\text{SrTiO}_3$ interfaces. The overlayers lead to the formation of a two dimensional electron gas, where we measure high electron mobilities up to $80\,000\text{ cm}^2\text{ V}^{-1}\text{ s}^{-1}$. Low-temperature measurements reveal the presence of two conduction channels dominating the electronic transport, which give rise to a strong magnetoresistance and quantum oscillations of conductance.

Chapter 6 shows how crystalline WO_3 thin films can be exploited for H_2 gas sensing. Hydrogen gas acts as a dopant for the WO_3 material, determining a very large change in resistivity which is directly related to the gas concentration. This effect is used in a proof

of principle detection scheme to reveal H_2 over a large range of concentrations, down to 1 ppm. We develop a simple model based on chemical rate equations to explain the intercalation and deintercalation of H species into the WO_3 lattice.

Chapter 7 contains a final discussion on the achievements of this thesis. Preliminary results regarding on-going developments and suggestions for future experiments are also provided.

2

STRIPED NANOSCALE PHASE SEPARATION AT THE METAL–INSULATOR TRANSITION OF HETEROEPITAXIAL NICKELATES

Nucleation processes of mixed-phase states are an intrinsic characteristic of first-order phase transitions, typically related to local symmetry breaking. Direct observation of emerging mixed-phase regions in materials showing a first-order metal–insulator transition (MIT) offers unique opportunities to uncover their driving mechanism. Using photoemission electron microscopy, we image the nanoscale formation and growth of insulating domains across the temperature-driven MIT in NdNiO₃ epitaxial thin films. Heteroepitaxy is found to strongly determine the nanoscale nature of the phase transition, inducing preferential formation of striped domains along the terraces of atomically flat stepped surfaces. We show that the distribution of transition temperatures is a local property, set by surface morphology and stable across multiple temperature cycles. Our data provides new insights into the MIT of heteroepitaxial nickelates and points to a rich, nanoscale phenomenology in this strongly correlated material.

Parts of this chapter have been published in Nature Communications 7, 13141 (2016), by G. Mattoni, P. Zubko, F. Maccherozzi, A. J. H. van der Torren, D. B. Boltje, M. Hadjimichael, N. Manca, S. Catalano, M. Gibert, Y. Liu, J. Aarts, J.-M. Triscone, S. S. Dhési, and A. D. Caviglia [61].

RARE-EARTH nickelates are strongly correlated electron systems in which structural and electronic properties are interconnected [15, 25]. A well-studied member of this family is NdNiO_3 , which shows a first-order temperature-driven metal-insulator transition (MIT) accompanied by a structural phase change and the appearance of unconventional magnetic order [62–65]. Several models have been proposed to describe its electronic structure, however the microscopic mechanism of the phase transition is still debated [26–29, 66–68]. A number of experiments underscores the key role of the lattice, as demonstrated by the influence of hydrostatic pressure, epitaxial strain and resonant phonon excitation on the MIT [12, 23, 24, 31, 32, 69–73]. The coexistence of metallic and insulating regions in the vicinity of the MIT, typical of first-order phase transitions, has been discussed with an expected domain size of a few tens of nanometre [69, 74]. However, the formation of insulating domains has been inferred, so far, mainly from macroscopic transport measurements [75–78]. In this thermodynamic limit the influence of nanoscale control parameters, such as local strain fields, lattice distortions and inhomogeneity, is buried in the statistical average of multiple domains. To achieve fundamental understanding and control of phase separation, access to the nanoscale regime is required [79, 80].

Several methodologies have been used for nanoscale imaging of mixed metallic and insulating phases in correlated oxides, including scanning tunnelling microscopy [81], near-field infrared microscopy [82] and scanning electron microscopy [83]. Nanoscale phase separation across a phase transition has also been studied using photoemission electron microscopy (PEEM) [84, 85].

Here we use PEEM to image nano-domain formation and disappearance in NdNiO_3 . This technique combines a spatial resolution of a few tens of nanometres with real-time imaging, allowing us to track the MIT in nickelates at different stages of its evolution. Our findings show that heteroepitaxy of NdNiO_3 on atomically flat stepped surfaces leads to the formation of striped insulating domains, which nucleate and grow along surface terraces across the MIT. We discuss how morphological characteristics act as a template for phase separation, determining the local transition temperature, as well as domain nucleation and growth pathways. Our data provides evidence, for the first time in the nanometre range, for the strong coupling between structural and electronic degrees of freedom in the rare-earth nickelates.

2.1. SAMPLE CHARACTERISATION

For this experiment a 30-unit-cell-thick NdNiO_3 $(001)_{\text{pc}}$ epitaxial film was grown on a NdGaO_3 substrate. The epitaxial strain imposed by the substrate sets the transition temperature for the MIT and the width of the hysteresis loop [24]. As shown in the atomic force microscopy image and related line profile in Figs. 2.1a and 2.1b, the film presents an atomically flat surface with steps and terraces that mimic the underlying substrate. Figure 2.1c shows a θ - 2θ X-ray diffraction scan around the $(001)_{\text{pc}}$ peak of the NdNiO_3 film. Finite size oscillations are observed and fitted with a kinematic scattering model, indicating high crystalline quality and confirming the expected film thickness of about 11 nm.

The MIT hysteresis, associated with the formation of insulating domains, is mea-

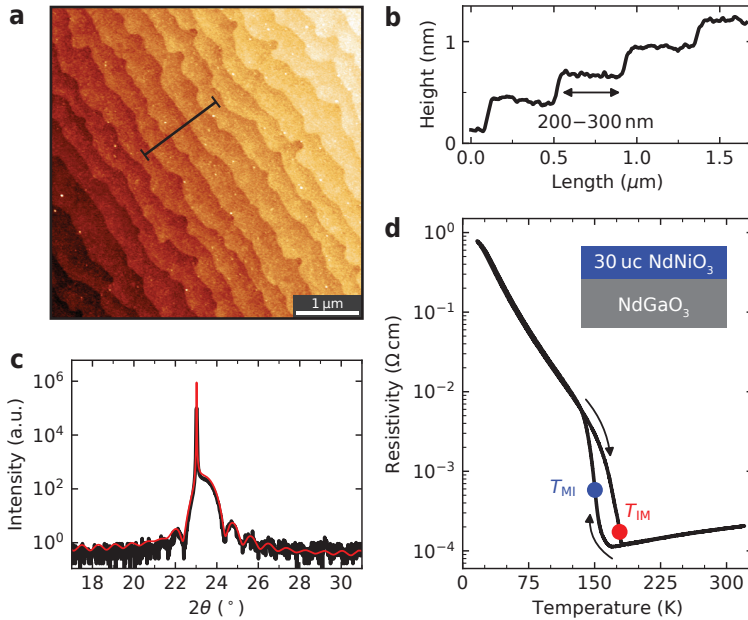


Figure 2.1: **Characterisation of the 30-unit-cell-thick NdNiO₃ film.** (a) Surface morphology with single unit cell steps (~ 0.4 nm) and terraces (200–300 nm in width) as measured by atomic force microscopy. (b) Cross-section profile showing the film step height and average terrace width. (c) X-ray diffraction data (black) around NdNiO₃ (001)_{pc} peak, fitted with a kinematic scattering model (red). (d) Resistance versus temperature from the transport measurement, where T_{MI} (blue dot) and T_{IM} (red dot) are indicated as extracted from the peaks of $-\partial \log R / \partial T$. (uc, unit cell).

sured by four probe DC transport (Fig. 2.1d). We define the transition temperatures $T_{MI} = 150$ K and $T_{IM} = 178$ K as the peaks of $-\partial \log R / \partial T$ on cooling and heating, respectively (Fig. 2.6). From the peaks separation we calculate the hysteresis width $\Delta T_{MIT} = 28$ K. In agreement with previous reports [69], the MIT width in thin films appears much broader than in bulk NdNiO₃, signalling the influence of heteroepitaxy on the phase transition evolution.

2.2. IMAGING CONTRAST MECHANISM

To image the different electronic phases, we perform X-ray absorption spectroscopy (XAS) at Ni L₃ absorption edge. We use σ -polarised X-rays and acquire the signal in total electron yield, thus probing the material surface down to a few nanometres. In Fig. 2.2a the temperature dependence of the Ni L₃ XAS is presented (see Fig. 2.7 for XAS on a broader photon energy range and with different polarisation). The most intense absorption peak shifts towards lower photon energies upon cooling the sample from the metallic state at $T = 185$ K to the insulating one at $T = 140$ K. This is consistent with an increased energy splitting of the Ni L₃ multiplet in the insulating phase due to a partial change of Ni valence state [68, 86]. The observed energy shift provides a contrast mech-

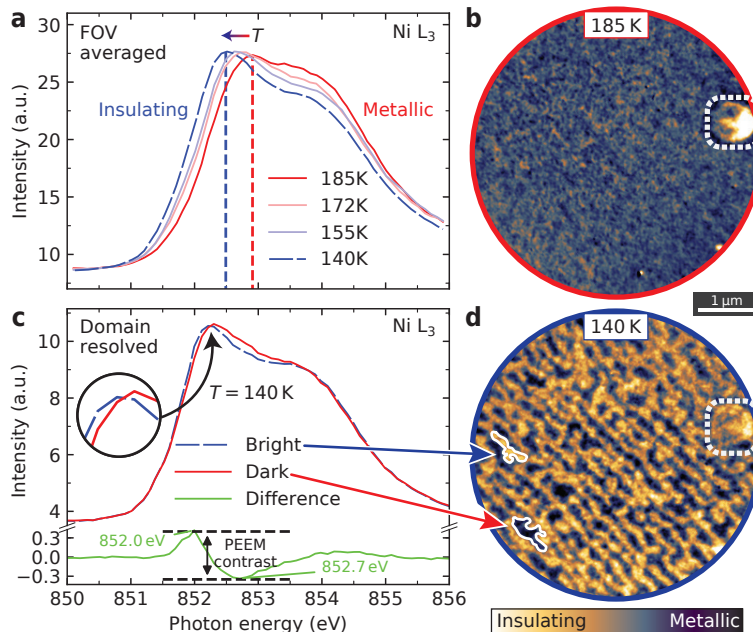


Figure 2.2: **The PEEM imaging contrast from photon-energy-shifted XAS spectra of metallic and insulating phases.** (a) Temperature dependence of Ni L₃ XAS spectra measured over the full field of view (FOV). PEEM images showing (b) the metallic phase at 185 K and (d) the insulating phase at 140 K. A surface defect used as a reference feature for drift-correction is indicated by the dashed square. (c) Domains resolved XAS spectra of bright and dark features in panel (d).

anism suitable for our study.

Above the MIT, the XAS spectra measured over the full field of view do not display significant variations compared with the noise level of the experiment. Below the MIT, instead, the sample shows different spatially-dependent XAS spectra, divided in two subsets with a relative shift in absorption edge (Fig. 2.2c). The maximum difference between the two subsets spectra is observed at 852.0 eV and 852.7 eV. We thus construct electronic phase maps by acquiring PEEM images at these two photon energies, and calculating their difference pixel by pixel. The use of fixed energy values slightly reduces the PEEM contrast in the high temperature region, but allowed us to perform faster acquisitions, thus increasing the number of data points taken during the temperature ramps (for further details see Fig. 2.8 and Section 2.7.1). In all images a round-shaped surface defect (dashed square) provides a well-contrasted reference feature used to compensate for the time-dependent spatial drift and keep the same area of interest in focus during the experiment.

At $T = 185$ K the resulting map (Fig. 2.2b) is spatially homogeneous, while at $T = 140$ K alternating bright and dark features (Fig. 2.2d) appear. We identify the bright features as insulating domains nucleating in a metallic matrix during the MIT. Indeed, as shown in Fig. 2.2c, the bright features display local spectra that are shifted to lower energies when

compared with the dark ones. Such shift is in qualitative agreement with the spatially averaged XAS spectra of Fig. 2.2a measured above and below the transition temperature. We note that, even if the detection of this energy shift is at the resolution limit of the PEEM technique, we obtained a sufficiently high signal-to-noise ratio by considering relative intensity differences at two distinct energies.

If we compare the PEEM and atomic force microscopy measurements acquired with the same sample orientation (Figs. 2.1a and 2.2d), we find a direct relationship between the insulating domains and surface morphology. Our *ex-situ* comparison is allowed by the single-crystal nature of our samples (see additional X-ray diffraction characterisation in Fig. 2.9), where the surface terraces orientation is preserved over millimetres. The surface terraces act as nucleation centres for the insulating phase, so that insulating domains form and grow preferentially along them, resulting in a striped shape. This is consistent with reports of sensitivity to strain for the nickelates [24], suggesting that the local periodic strain field at the step edges can confine the insulating phase on the terraces, limiting its expansion. These observations have been reproduced on three different samples, confirming that the domain orientation and size are dictated by surface morphology (Fig. 2.10). Our finding establishes an important link between sample local morphology and electronic phase separations.

2.3. NANOSCALE EVOLUTION OF THE MIT

To investigate the evolution of the insulating domains across the MIT, the sample temperature is cycled below and above the transition, following the hysteresis loop. A representative set of images is reported in Fig. 2.3a. The percentage of area covered by the insulating domains in each PEEM image of the series is presented in the inner panel of Fig. 2.3a. From room temperature down to 152 K the sample shows a homogeneous metallic phase. Below 152 K insulating domains nucleate and grow along the preferential direction given by surface terraces, gradually forming striped regions. Between 146 K and 140 K the domain evolution saturates at about 60% coverage and no additional insulating regions are formed. This domain configuration is stable for the whole duration of the measurements (several hours).

The reverse transition, back to the metallic state, is rather different. Upon heating, no change is initially observed up to 161 K, in agreement with the hysteretic, first-order nature of NdNiO₃ MIT. Above 161 K the insulating stripes become narrower and are pinched off by the expanding metallic matrix into many, small and closely spaced nano-domains. These appear to be evenly distributed across the field of view, in stark contrast to the striped domains observed on cooling (i.e. compare the Fig. 2.3a heating and cooling images at 164 K and 150 K, respectively, with approximately the same insulating domain coverage). At $T = 165$ K all the insulating domains disappear and the homogeneous metallic phase is recovered. Interestingly, we note that the insulating domains do not fully populate the surface as the area coverage reaches the saturation value of about 60%. We observe no significant variation of the coverage down to 130 K, the lowest temperature attainable in our experiment. The domains are often spaced by metallic regions, which persist at the surface step edges. This effect might be related either to local strain fields in proximity of the step edges or to inhomogeneous surface termination.

A clear asymmetry between the metal-to-insulator and insulator-to-metal transition

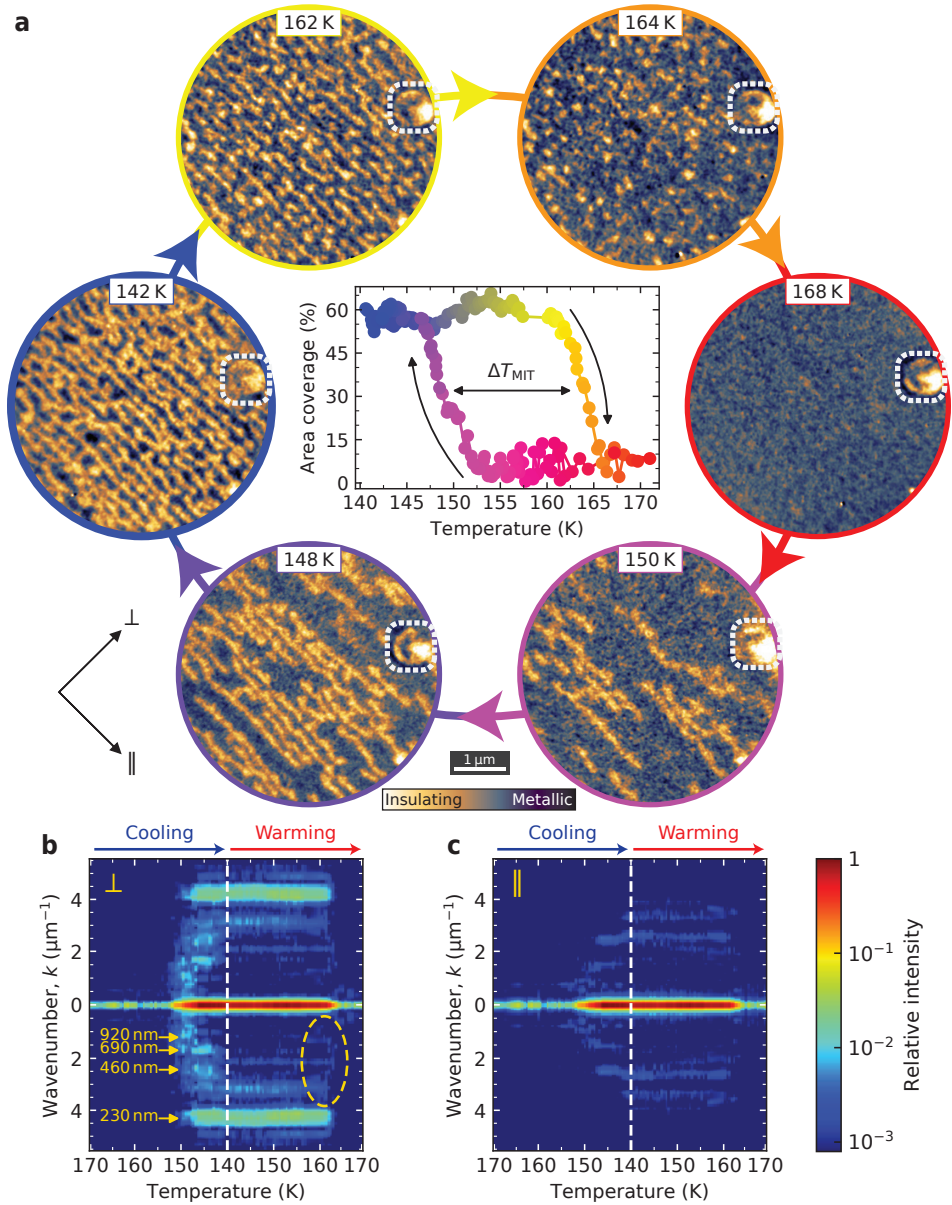


Figure 2.3: **Temperature evolution of insulating domains across the MIT.** (a) During each thermal cycle the insulating domains nucleate and grow on cooling, while they gradually disappear on warming. The inner panel shows the percentage of image area covered by the insulating domains as a function of temperature, highlighting the hysteretic behaviour of the MIT with a finite width down to the single domain. (b) Perpendicular and (c) parallel linecuts of the two-dimensional Fourier transform with respect to the insulating domains orientation (indicated by the black arrows) as a function of temperature. The colour scale represents the power spectrum normalised with respect to the maximum value at $T = 140$ K and $k = 0$. The dashed ellipse evidences the asymmetry between the cooling and warming directions.

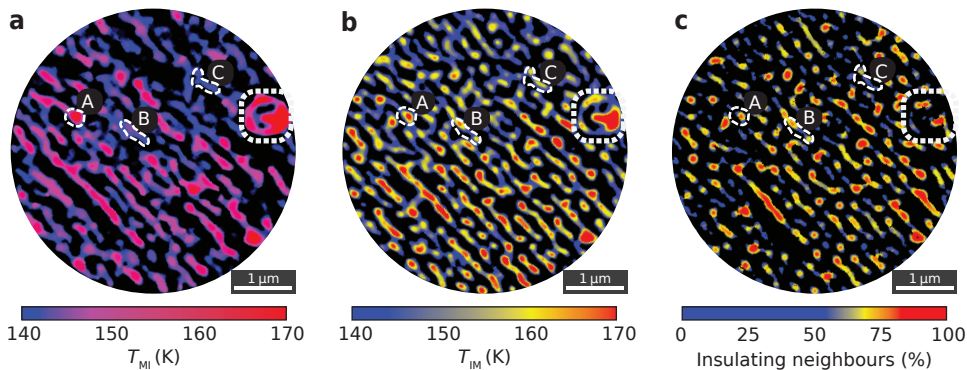


Figure 2.4: **Spatial distribution of MIT temperature.** Maps of (a) T_{MI} and (b) T_{IM} showing the transition temperature is a local property of the material. Three areas are encircled to indicate the order with which they become insulating (A, B and C) and revert to the metallic state (C, B and A). The map in (c) shows point-by-point the amount of insulating region at 140 K in a neighbouring area of radius 100 nm.

is underscored by the two-dimensional Fourier transform (FT) of the PEEM images acquired during the temperature cycle. The temperature dependence of the FT power spectrum line-cuts along the direction perpendicular and parallel to the striped domains is reported in Figs. 2.3b and 2.3c. The intensity at $k = 0$ corresponds to the domains area coverage in the inner panel of Fig. 2.3a, and its maximum value at 140 K is used to normalise the spectrum. In the perpendicular direction (Fig. 2.3b) we see the appearance of an intense peak, corresponding to a periodicity of about 230 nm, at the nucleation of the insulating phase. This value matches with the average terrace width of Fig. 2.1b, highlighting the direct relationship between insulating domains and surface morphology. On cooling, the domain formation pattern is characterised by the appearance of peaks corresponding to multiple integers of the terrace width. These features disappear when the domain area coverage reaches saturation. Remarkably, these additional peaks are absent during warming (dashed ellipse in Fig. 2.3b), indicating that a different pattern underlies the disappearance of the insulating phase. The formation of the insulating domains is thus a nucleation and growth process, while their disappearance is a homogeneous melting that originates from the domain edges. This is consistent with previous reports [75], where a supercooling mechanism was associated with the metal-to-insulator transition only. In the parallel direction (Fig. 2.3c), instead, negligible domain ordering is observed, where dim peaks one order of magnitude weaker than in the perpendicular case appear. We relate this signal with the average on-terrace distance of the residual metallic matrix in the insulating phase.

The presented MIT evolution is consistent across multiple temperature cycles. This allows us to assign local transition temperatures to the material. In Figs. 2.4a and 2.4b we present spatially resolved maps of local T_{MI} and T_{IM} , showing the temperature at which the phase transition occurs on a certain region of the sample. Repeating the temperature cycle several times, the insulating domains are observed nucleating and growing always in the same position and in the same order. As an example we considered the areas labelled as A, B and C in Figs. 2.4a and 2.4b. If on a cool-down cycle they turn insulating

in an (A, B and C) order, during a warm-up they will revert to the metallic state in the reversed (C, B and A) order.

We find in Fig. 2.4b that the spatial distribution of insulator-to-metal transition temperature seems to be related to the size and shape of the domains themselves. In particular, the cores of bigger domains show higher values of T_{IM} . This indicates that the melting process of the insulating phase starts from the domain edges. To support this observation, in Fig. 2.4c we determine the amount of insulating region neighbouring each insulating point in a radius of 100 nm at 140 K. We note how the data in Fig. 2.4c is evaluated from a single PEEM image at 140 K, in contrast to Figs. 2.4a and 2.4b which are extracted by using all the images in the temperature cycle. The striking similarity between Figs. 2.4b and 2.4c is a clear indication of how the insulator-to-metal transition progresses continuously from the edges to the core of each domain, so that the bigger ones are the last to disappear. This is in agreement with previous reports of an intrinsic asymmetry in the phase transition of NdNiO_3 [75].

A relevant result of our analysis is the preservation of the MIT hysteresis down to the single domain. From the inner panel of Fig. 2.3a we can extract the hysteresis width $\Delta T_{\text{MIT}} = (14 \pm 2) \text{ K}$, defined as the temperature difference between appearance and complete melting of the insulating phase. This value is in sharp contrast with our macroscopic transport measurements, where we found $\Delta T_{\text{MIT}} = 28 \text{ K}$. We also note that the observed nanoscale inhomogeneities appear on a smaller length scale than the field of view used in the experiment, thus providing a representative evaluation of the properties of the material. The existence of a finite hysteresis width down to the single domain scale, and the spatial distribution of T_{MI} and T_{IM} provide a further insight on the nature of the phase transition. Such results can hardly be inferred by macroscopic measurements which are subject to statistical averaging.

2.4. MIT THROUGH BULK AND SURFACE TECHNIQUES

At this point it is worth comparing the temperature dependence of the domain area coverage measured by PEEM with the resistivity data, both shown in the relevant temperature range in Fig. 2.5. We see a striking difference in the extremal temperatures of the two hysteresis loops. In the PEEM data the hysteresis loop closes at 165 K on the high temperature end, about 15 K lower than in the transport case. This means that while the insulating domains coverage goes to zero at 165 K during a warming ramp, the resistivity is still almost an order of magnitude higher than in the metallic state. Assuming the domains propagate completely through the film thickness (that is, that 0% area coverage also corresponds to 0% volume fraction), it is not possible to explain the difference between area coverage and transport.

To get a further insight into this difference, we additionally measure the evolution of macroscopic XAS intensity at 853 eV in the fluorescence yield configuration as a function of temperature (green diamonds in Fig. 2.5). The MIT hysteresis measured this way is in qualitative agreement with the transport data. In contrast to the measurements in total electron yield performed in the PEEM set-up, the XAS in fluorescence yield probes the whole thickness of our NdNiO_3 thin film, also providing a more extended spatial averaging as the X-ray spot size is about two orders of magnitude larger.

We consider two different explanations for the measured discrepancy between PEEM

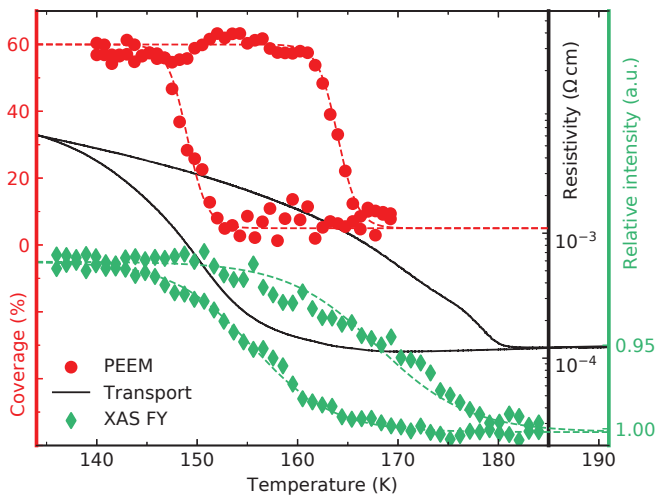


Figure 2.5: **MIT hysteresis measured with different techniques.** Insulating domains area coverage from the inset of Fig. 2.3a (red dots), low-temperature transport from Fig. 2.1d (black line), and X-ray absorption intensity at 853 eV photon energy relative to the intensity at 180 K measured in fluorescence yield (FY, green diamonds).

and transport/XAS data. A possibility is that the observed domains do not fully penetrate through the whole film but are, instead, confined to the surface. In this case, our measurements indicate that the MIT at the surface occurs at a lower temperature than in the bulk, eventually related to local lattice distortions at the free boundary. Another explanation involves the possibility of local material metallisation due to X-ray illumination. This is a well-known open issue when irradiating oxide materials with intense X-rays, and changes in metal-insulator characteristics have been previously reported [87]. Since the use of X-rays is an intrinsic requirement of the PEEM technique, further insight into this question will be provided by additional experiments, such as transport measurements at the nanoscale and scanning probe techniques.

2.5. CONCLUSIONS

Through direct imaging by PEEM, we reported on nanoscale phase separation during the MIT of NdNiO₃ thin films. Striped domains nucleate and grow along the terraces of the atomically flat surface, highlighting the influence of heteroepitaxy on the phase transition. Performing systematic imaging as a function of temperature, we showed that the transition temperature is a local property of the material, stable across multiple temperature cycles. The measurements point towards a strong interconnection between structural and electronic degrees of freedom in rare-earth nickelates, suggesting a new approach for controlling phase separation at the nanoscale.

2.6. METHODS

SAMPLE FABRICATION.

The commercially available NdGaO_3 substrate was annealed at 1000°C in 1 atm of oxygen before sample growth to achieve a flat surface with a regular step and terrace structure. The NdNiO_3 (001)_{pc} film was grown by off-axis radio-frequency magnetron sputtering in 1.80×10^{-1} mbar of an oxygen/argon mixture of ratio 1:3 at a substrate temperature of 490°C .

TEMPERATURE-DEPENDENT MEASUREMENTS.

Transport, PEEM and XAS fluorescence yield measurements have been performed cycling sample temperature at a constant rate of 0.5 K min^{-1} for both ramp directions, guaranteeing that the sample is kept in a quasi-static condition. As each PEEM acquisition required about 20 s, we estimate an error of 0.2 K on each data-point. Such temperature variation is negligible compared with the phase transition evolution.

SYNCHROTRON X-RAY MEASUREMENTS.

PEEM and XAS fluorescence yield data have been acquired at the beamline I06 of Diamond Light Source. An X-ray beam $10 \mu\text{m} \times 10 \mu\text{m}$ in spot size with a fluency of 1 mJ cm^{-2} was used in the PEEM setup, while a $100 \mu\text{m} \times 100 \mu\text{m}$ beam with 0.01 mJ cm^{-2} of fluency was employed for the XAS fluorescence yield measurements. In both cases the X-rays were σ -polarised. The absolute peak photon energies measured by PEEM are subjected to an uncertainty of about 0.2 eV due to the small integration time of 1 s compared with the noise level of the system. However, this does not affect the reported data as all PEEM images are based on relative spatial shifts of X-ray absorption intensity.

2.7. SUPPLEMENTARY INFORMATION

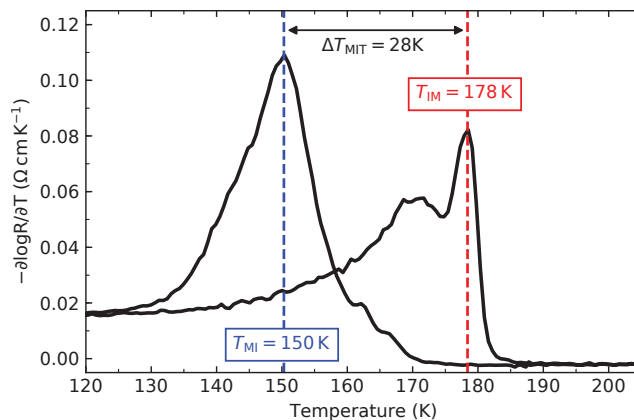


Figure 2.6: **Logarithmic derivative of the resistivity from the transport measurement.** The transition temperatures $T_{MI} = 150\text{ K}$ and $T_{IM} = 178\text{ K}$ are defined as the peaks of $-\partial \log R / \partial T$ during a cooling and warming cycle, respectively. From the peaks separation the hysteresis width $\Delta T_{MIT} = 28\text{ K}$ is extracted.

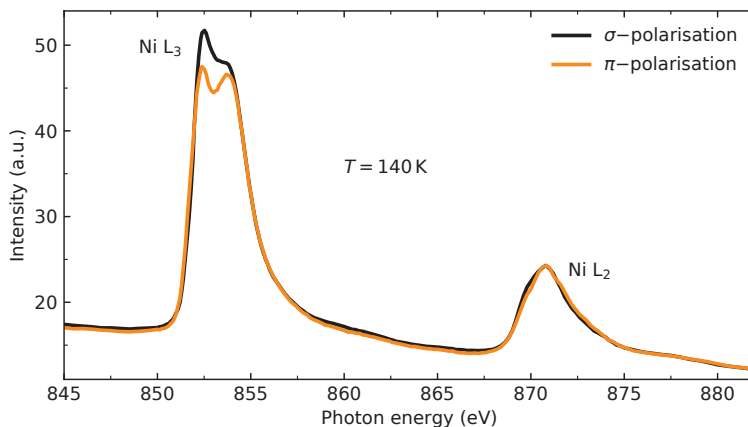


Figure 2.7: **Full-range Nickel XAS taken with different X-ray linear polarisations.** A small dichroism in the XAS is observed, stemming from a combined effect of orbital symmetry and charge ordering, consistent with previous reports [88]. When considering the spatial distribution of dichroic signal measured by PEEM, however, we do not observe any spatial variation compared to our noise level, for any photon energy and sample temperature. As described in the main text for the case of σ -polarisation, it is also possible to acquire PEEM measurements at 852.0 eV and 852.7 eV with π -polarised X-rays. Calculating their difference pixel-by-pixel, it is possible to construct equivalent PEEM images to the one presented in the main text. We overall used σ -polarisation as it provides the most intense absorption peak, thus determining a better signal-to-noise ratio.

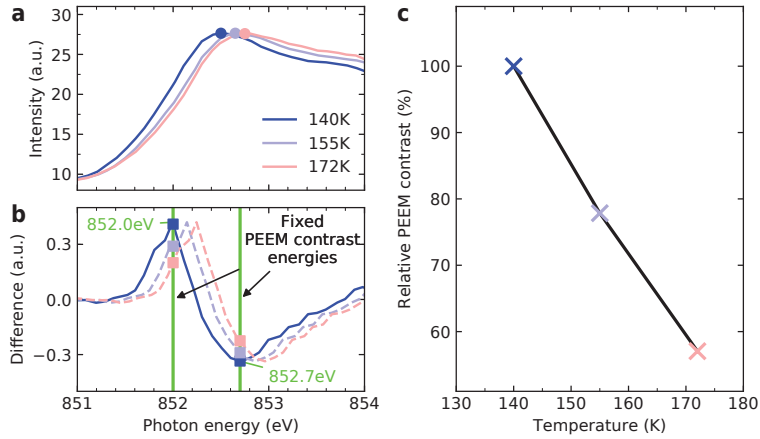


Figure 2.8: **Temperature dependence of PEEM imaging contrast.** (a) close-up of the shift in photon energy of Ni L₃ XAS peak as a function of temperature, measured over the full field of view, from Fig. 2.2a. Panel (b) indicates how the XAS difference of Fig. 2.2c changes in temperature and (c) shows the relative change in PEEM contrast.

2.7.1. PEEM CONTRAST CHANGE WITH TEMPERATURE

In the main text we used two fixed photon energies (852.0 eV and 852.7 eV) to construct PEEM images at all temperatures. Because the Ni L₃ XAS peaks change in temperature, the specific pair of energies that maximises the PEEM contrast is slightly different for each different temperature. This would have involved repeating the analysis presented in Fig. 2.2c for all the temperature points, which is a very long measurement. Therefore we decided to slightly sacrifice the contrast at higher temperatures in order to perform faster acquisitions, thus improving the number of data points taken during the temperature ramps. In Fig. 2.8 we estimate the amount of contrast-loss as a function of temperature, demonstrating it has a negligible impact on our analysis. In particular, in Fig. 2.8a we present a close-up of the shift in photon energy of Ni L₃ XAS peak as a function of temperature, measured over the full field of view, from Fig. 2.2a. The most intense peak of the multiplet (solid circles) shifts about 0.2 eV. At a given temperature, the domain resolved XAS spectra of the metallic and insulating areas are slightly displaced as shown in Fig. 2.2c. The difference between these spectra at 140 K is maximum at 852.0 eV and 852.7 eV, therefore the PEEM contrast at 140 K is optimal at such energies. Figure 2.8b indicates how the XAS difference of fig. 2c changes in temperature under the assumption that both the metallic and insulating spectra evolve similarly. The dashed lines in Fig. 2.8b are rigid shifts of the 140 K curve (solid line) by amounts extracted from the peak positions in Fig. 2.8a. In Fig. 2.8c we estimate the relative change in PEEM contrast by calculating the vertical difference between the squares in Fig. 2.8b normalised with respect to 140 K. We see that, in the studied temperature range (140–170 K), the PEEM contrast loss is smaller than 50%. This allowed to track the evolution of the insulating phase at all temperatures, supporting the validity of our assumptions.

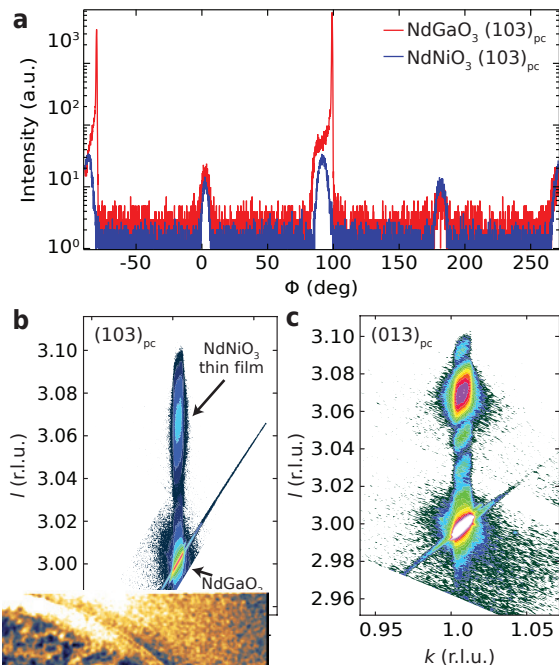


Figure 2.9: **Additional X-ray diffraction measurements of the NdNiO_3 film.** (a) ϕ -scan recorded along the $(103)_{pc}$ direction. The aligned scans of the NdGaO_3 substrate and NdNiO_3 thin film confirm a crystallographically oriented heteroepitaxy. In (b) and (c) reciprocal space maps of the NdNiO_3 film around the $(103)_{pc}$ and $(013)_{pc}$ reflections. The in-plane intensity distribution of the NdNiO_3 film and NdGaO_3 substrate are confined to the same value of reciprocal lattice vector $h = 1$ in (b) and $k = 1$ in (c). The film is thus coherently oriented to the substrate lattice. From the position of the peaks we extract $c_{\text{NdGaO}_3} = 3.86$ nm and $c_{\text{NdNiO}_3} = 3.77$ nm, consistent with previous reports [69].

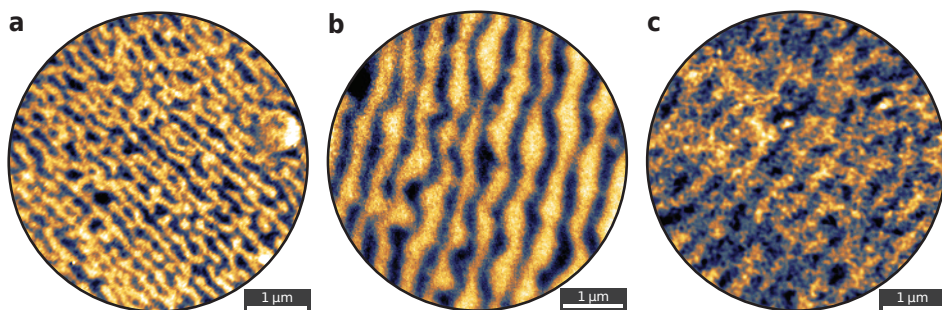


Figure 2.10: **PEEM images taken on 3 different samples.** (a) sample discussed in the main text, (b) sample with larger surface terraces, and (c) another sample. The insulating domains orientation and size changes from sample to sample according to direction and size of the surface terraces. This remarks the determining contribution of heteroepitaxy in driving the formation of the insulating phase at the metal-insulator transition.

3

LIGHT CONTROL OF THE NANOSCALE PHASE SEPARATION IN HETEROEPITAXIAL NICKELATES

Strongly correlated materials show unique solid state phase transitions with rich nanoscale phenomenology that can be controlled by external stimuli. Particularly interesting is the case of light–matter interaction in the proximity of the metal–insulator transition of heteroepitaxial nickelates. Here we use near-infrared laser light in the high-intensity excitation regime to manipulate the nanoscale phase separation in NdNiO₃. By tuning the laser intensity, we can reproducibly set the coverage of insulating nano-domains, which we image by photoemission electron microscopy, thus semi-permanently configuring the material state. With the aid of transport measurements and finite element simulations, we identify energy redistribution to the crystal lattice as the mechanism dominating the light control. These results open interesting perspectives for manipulating electronic order at the nanoscale.

Parts of this chapter have been submitted for peer review (2017), by G. Mattoni, N. Manca, P. Zubko, M. Hadjimichael, A. J. H. van der Torren, C. Yin, S. Catalano, M. Gibert, F. Maccherozzi, Y. Liu, S. S. Dhesi, and A. D. Caviglia

RARE-EARTH nickelates have received significant research attention, motivated by their unique properties, including a sharp metal–insulator transition (MIT) and unusual magnetic order [15, 25]. The microscopic origin of these phenomena is still intensely studied and various models of charge localisation are being considered in light of a bond disproportionated insulating state observed in experiments [26–30, 64, 68, 86]. Independently of the exact microscopic picture, it is clear that these materials are characterised by a delicate balance between lattice distortions, covalency and electronic correlations [14, 73, 89–91]. This leads to a remarkable tunability of the MIT with chemical and static pressure, epitaxial strain, heterointerfaces, and even near- or mid-infrared light excitation [12, 24, 31, 32, 70, 92–94]. The case of light–matter interaction is particularly interesting. For near-infrared charge excitations it was demonstrated that the system shows an ultrafast demagnetisation process driven by a photoexcited electronic mechanism [65, 95, 96]. Only at high excitation intensities an energy redistribution to the lattice becomes apparent. Since heteroepitaxial nickelates show rich nanoscale physics, including phase separation at the MIT, it would be interesting to explore the effects of light excitation on the domain structure [61, 69, 74].

In this work we focus on the high-intensity excitation regime, in the vicinity of the MIT, where we image the nanoscale phase separation using photoemission electron microscopy (PEEM). We show that, by tuning the intensity of a near-infrared laser, the equilibrium properties of heteroepitaxial nickelates can be controlled in two ways. Firstly, the insulating nano-domains can be rewritten to obtain a desired surface coverage. Secondly, the MIT hysteresis sharpness and width can be manipulated. We discuss the interplay between light–matter interaction, heat transfer and localised temperature increments with the support of both resistive measurements and finite element simulations.

3.1. LIGHT EFFECTS ON THE MIT

The experiment is performed on a 25 unit cell-thick (9.5 nm) NdNiO₃ (NNO) film grown on a NdGaO₃ substrate. X-ray diffraction measurements indicate that the NNO is a single crystal, coherently strained to the substrate lattice (Fig. 3.5). Electrical transport characterisation shows the presence of a sharp resistive transition from a high temperature metallic state to a low temperature insulating state (Fig. 3.6), in agreement with what expected from high-quality NNO thin films [24, 72, 97]. The sample is irradiated by a pulsed laser source (140 fs, 800 nm, 25 kHz) focused on a 80 μm × 100 μm spot. We track the changes induced by optical excitation by imaging the spatial distribution of metallic and insulating areas with PEEM, as sketched in Fig. 3.1a. Our imaging contrast is based on the different Ni L₃ X-ray absorption in the metallic and insulating phases, which in this case peak at 852.7 eV and 853.4 eV, respectively, as detailed in [61]. The sample is mounted on a cold finger, capable of controlling its temperature between 130 K and 300 K. At 200 K, above the MIT, we find a homogeneous metallic phase (Fig. 3.1b), while at 130 K, right below the MIT, the material is in a mixed-phase state (Fig. 3.1c), with coexistence of insulating and metallic regions. Their striped shape is determined by the step and terrace surface morphology imposed by the substrate, as confirmed by topographic images acquired by atomic force microscopy (Fig. 3.6).

Figure 3.1d shows the temperature evolution of the insulating domains during a ramp

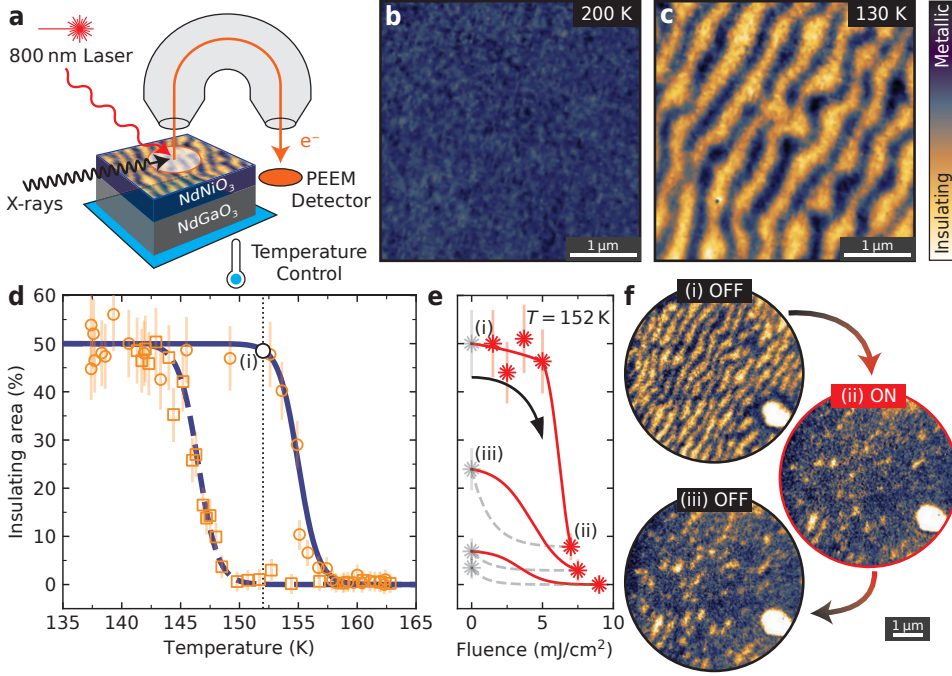


Figure 3.1: MIT imaged by PEEM and controlled by light. (a) Experimental setup, showing the X-ray probe, the photoelectrons measured by PEEM and the 800 nm laser light. (b) Homogeneous metallic state at 200 K and (c) striped insulating state at 130 K imaged by PEEM. (d) MIT hysteresis measured by PEEM upon cooling (squares) and warming (circles). The data is fitted with Eq. (3.1). (e) Effect of the laser light on the domain configuration at 152 K as indicated by the white dot in (d) and some example PEEM images in (f).

of cooling (squares) and warming (circles) while the laser is off. Each data point is calculated from a single PEEM image as discussed in Fig. 3.7. The data shows the typical hysteresis of NNO phase transition, where the insulating area increases upon cooling from 0% to a saturation coverage of 50%. This temperature dependence is well described by two sigmoid functions, representing the cooling (dashed) and warming (solid) ramps:

$$A_{\text{ins}}(T) = \frac{A_{\text{ins}}^{\text{max}}}{1 + e^{-w_i(T-T_i)}}, \quad (3.1)$$

where $A_{\text{ins}}^{\text{max}} = 50\%$ is the maximum area covered by the insulating phase and w_i , T_i are fitting parameters. In this case we find $T_{\text{MI}} = 146\text{ K}$ and $T_{\text{IM}} = 155\text{ K}$, determining a hysteresis width $\Delta T_{\text{MIT}} = 9\text{ K}$.

To study the optical excitation effects, we start with the laser off and set the thermal bath at 152 K by heating the sample from base temperature. This initial state (i) lies on the upper branch of the hysteresis loop and corresponds to a saturated insulating phase, as indicated in Figs. 3.1d to 3.1f. The size of the region measured by PEEM ($5\ \mu\text{m} \times 5\ \mu\text{m}$) is much smaller than the laser light focus, ensuring the probing of a homogeneously excited region. We acquire a series of PEEM images for different values of laser fluence Φ . The images represent a steady-state condition of the system because the acquisition

of a single PEEM measurement requires about 30 s of integration time, a time scale much longer than the 40 μs laser repetition period. An example of the laser excitation effect on the domain structure is shown in Fig. 3.1f, where a laser fluence $\Phi = 7 \text{ mJ cm}^{-2}$, reduces the insulating domain coverage A_{ins} from 50 % to about 10 %, leaving on the surface a few disconnected insulating regions (state (ii)). When turning off the laser, A_{ins} does not recover to its initial value, but it settles to an intermediate coverage of 25 % (state (iii)). This partial recovery is a consequence of the hysteretic nature of NNO phase transition, which keeps memory of the laser excitation (discussed below).

3

The described process is fully reproducible and the final coverage is set by the laser fluence. In Fig. 3.1e we show that, by increasing the laser fluence, it is possible to gradually reduce A_{ins} down to a complete suppression of the insulating domain coverage with $\Phi = 9 \text{ mJ cm}^{-2}$ at 152 K. Upon switching the laser off, a few insulating patches reappear also in this case. This insulating domain configuration is stable over time and the initial condition can be restored by cooling the sample below T_{MI} . Below we discuss the mechanism leading to laser control of the domain configuration and we argue that it is dominated by thermal effects as opposed to non-thermal photoexcitation processes. One first indication comes from the threshold observed in the fluence dependence of Fig. 3.1e. In order to observe a reduction of A_{ins} , a fluence $\Phi > 5 \text{ mJ cm}^{-2}$ is required. Previous reports indicated that below this threshold ultrafast photoexcitation determines an ultrafast dynamics of nickelates materials, even leading to a complete demagnetisation of the low temperature insulating phase [65, 95]. Thermal effects were shown to take place in the range considered in this work, involving energy redistribution to the crystal lattice.

3.2. MIT CYCLES WITH PHOTOEXCITATION

Additional insight into the light control mechanism of NNO insulating domains comes from considering the temperature dependence of A_{ins} for different fixed laser fluences. To this end we acquired a series of PEEM spectroscopic maps under laser irradiation in a steady-state condition and at different bath temperatures. A steady-state condition is achieved by maintaining constant laser fluence Φ for several minutes before cycling the temperature. For each cycle, a hysteretic trend of A_{ins} is observed as shown in Fig. 3.2a for the cooling (dashed) and warming (solid) curves (raw data in Fig. 3.7). Upon increasing Φ , the hysteresis loop changes in two ways: it shifts to lower temperatures and it shrinks in width. These effects are summarised in Fig. 3.2b, where the values of T_{MI} (squares) and T_{IM} (circles) are shown as a function of Φ . Both temperatures have a decreasing trend, but the slope of T_{MI} is smaller, resulting in a shrinkage of the hysteresis width ΔT_{MIT} (Fig. 3.2c). Furthermore, its linear fit suggests that $\Delta T_{\text{MIT}} \sim 0$ at about $\Phi = 20 \text{ mJ cm}^{-2}$, corresponding to a full suppression of the MIT hysteresis. This effect cannot be caused by a steady-state laser heating, which would systematically increase the sample temperature compared to the thermal bath and identically offset both T_{MI} and T_{IM} . Instead, changes in ΔT_{MIT} can be explained by considering both a steady-state and a transient temperature increase, which are revealed by the MIT memory effect.

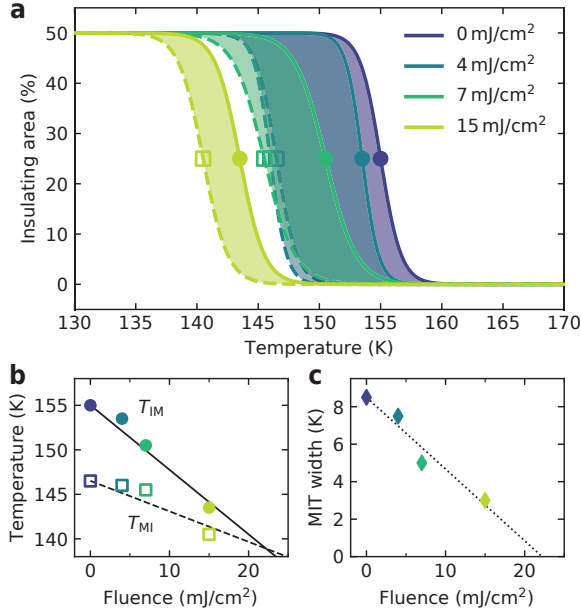


Figure 3.2: **MIT hysteresis with different laser fluence.** (a) Change of the PEEM hysteresis loop with different laser fluence. (b) T_{IM} (circles), T_{MI} (squares), and (c) ΔT_{MIT} extracted from the sigmoid fit. The lines are linear regressions of the data.

3.3. TRANSIENT HEATING BY TRANSPORT

We consider the effects of a transient heating on the NNO phase transition by studying the resistive transition during selected warming and cooling cycles. Inside the MIT hysteresis window it is possible to perform nested loops by sweeping the temperature in a span narrower than the full hysteresis width. We carry out transport measurements monitoring sample resistivity while slowly varying the temperature at a rate of 0.5 K min^{-1} , thus preserving a quasi-static condition. The resistance vs temperature relationship is presented in Fig. 3.3, where the black lines represent the full hysteresis loop, with the lower branch relative to cooling (dashed line) and the upper branch relative to warming (solid line). Initially, similarly to what done in Fig. 3.2, the thermal bath is fixed to the middle of the hysteresis at $T_0 = 155 \text{ K}$. This value is reached starting from base temperature, in order to set the sample in a state on the upper branch, with maximum amount of insulating domains. Nested loops are then performed increasing the temperature by an amount ΔT and bringing it back to T_0 . The sample resistance at T_0 , marked by circles in Fig. 3.3a, stays rather constant for $\Delta T \leq 8 \text{ K}$ while for higher ΔT it decreases monotonously, reaching the lower hysteresis branch for $\Delta T \sim 20 \text{ K}$. At this point the insulating domains have turned metallic and no further change is observed. The lower branch, in fact, is the minimum resistivity curve that can be reached in the hysteresis region. To show this, in Fig. 3.3b we set the sample at $T_0 = 150 \text{ K}$, this time starting from room temperature, thus obtaining a state on the lower branch. Performing nested loops

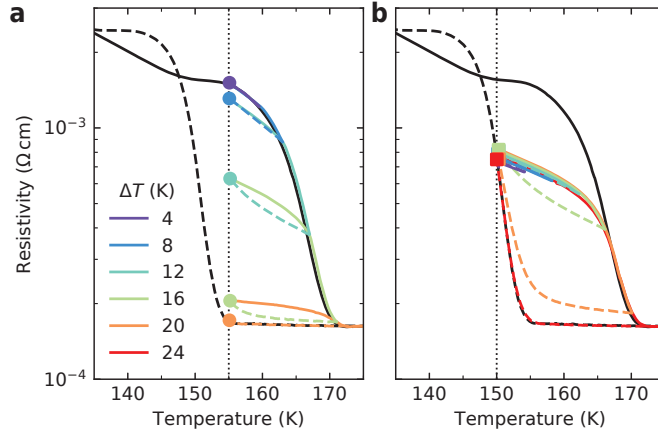


Figure 3.3: **Nested MIT cycles measured by electrical transport.** (a) Heating loops starting from the MIT hysteresis upper branch at 155 K and (b) from the lower branch at 150 K. The end point of each nested cycle is indicated by a dot or a square.

we find that all the end points, marked as squares, lie on top of each other. Such analysis indicates that if the system is probed at a certain T_0 after a transient temperature increase ΔT , the domain population is not affected if the initial state is already lying on the lower hysteresis branch. Similar behaviour has been reported in other oxides showing mixed phase states [98, 99]. This explains how a transient heating induced by the laser pump can shrink the hysteresis width, as observed in Fig. 3.2. Since most of the heat transferred by a laser pulse is dissipated in a time scale much faster than the laser repetition period ($40 \mu\text{s}$), the material stays in a steady-state condition most of the time. Because PEEM measurements average the surface state over 30 s, the hysteresis upper branch shifts to lower temperatures, while the lower branch is not affected, resulting in a reduced ΔT_{MIT} . The experimentally observed shift of the lower branch should then be related to a steady-state NNO temperature rise, determined by the average incident light power. Because it is not possible to access the transient heating dynamics in our experimental configuration, we qualitatively study the sample thermal response using classical heat transfer theory.

3.4. LASER HEATING SIMULATION

We model the laser interaction with the sample by considering its heating implications through a finite element simulation (Fig. 3.4a). A linear response function with a characteristic time $\tau = 100 \text{ ps}$ is used to represent the system heat response (details in Section 3.6.1) and is shown together with the periodic laser excitation in Fig. 3.4b. In the initial conditions, the system is in equilibrium with a thermal bath at 150 K (state (i) of Figs. 3.4c and 3.4d). Since the light absorption coefficient is much larger in the film rather than in the substrate ($\alpha_{\text{NNO}} \gg \alpha_{\text{NdGaO}_3}$), the film absorbs the laser light with higher energy density, determining a sharp temperature rise which peaks at $t = 100 \text{ ps}$ (state (ii)). After 1 ns (state (iii)), most of this heat has diffused into the colder substrate. The same

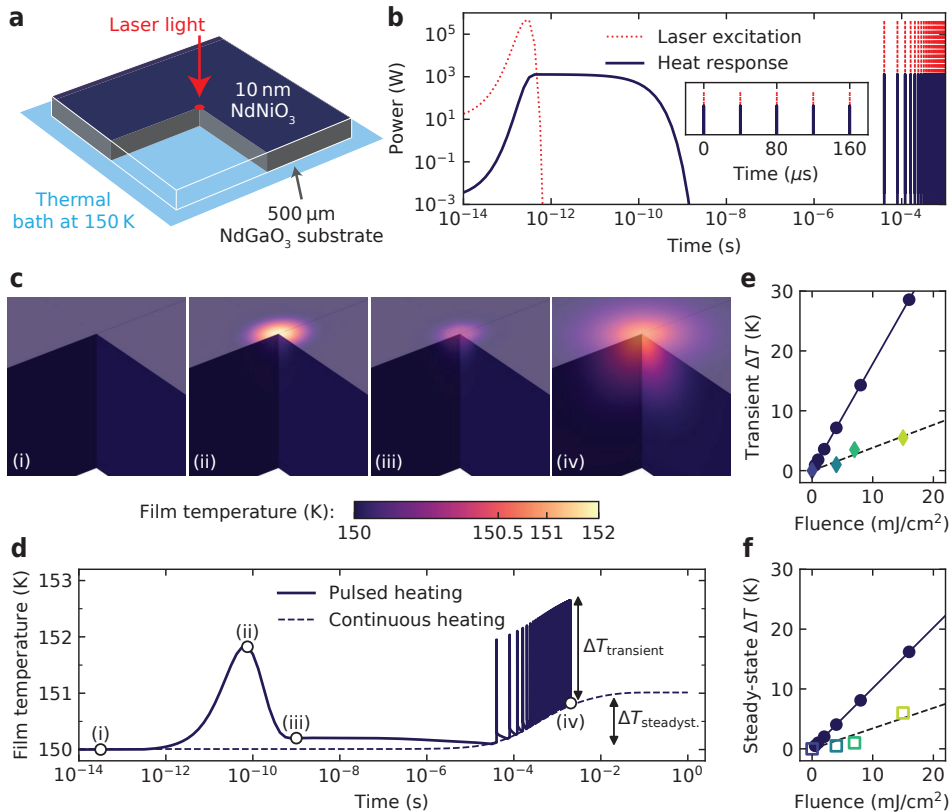


Figure 3.4: **Laser heating by finite element simulation.** (a) Model used in the simulation: the substrate bottom is anchored to a thermal bath at 150 K and a laser pulse is directed on the sample top surface. (b) Power of the laser excitation (red dotted line) and the corresponding system heat response (blue solid line) with $\tau = 100$ ps and $\Phi = 1 \text{ mJ cm}^{-2}$. The inset shows in linear scale the 25 kHz repetition period. (c) Film temperature map due to laser heating at different time instants and (d) temperature of the innermost area that is probed by PEEM. The temperature raise just after the laser pulse ($\Delta T_{\text{transient}}$) and the constant one at thermal equilibrium ($\Delta T_{\text{steadystate}}$) are indicated by arrows. (e) Transient and (f) steady-state heating as a function of laser fluence taken from the simulation (blue circles) and compared to the experimental data (diamonds and squares) of Figs. 3.2b and 3.2c.

sharp peak in temperature ($\Delta T_{\text{transient}}$) is observed for each laser pulse. Because of the slow heat dissipation towards the thermal bath, some residual heat is retained at the arrival of the next laser pulse ($t = 40 \mu\text{s}$). After multiple pulses, this residual heat determines a steady-state temperature rise ($\Delta T_{\text{steadystate}}$). These two temperature variations are indicated by arrows in Fig. 3.4d, where a laser fluence $\Phi = 1 \text{ mJ cm}^{-2}$ was employed. We show in Figs. 3.4e and 3.4f that both $\Delta T_{\text{transient}}$ and $\Delta T_{\text{steadystate}}$ increase with a linear trend as a function of Φ .

In accordance with the results of Fig. 3.3, we identify the transient heating as responsible for the shrinking of the MIT hysteresis ($\Delta T_{\text{transient}}(\Phi) \sim [\Delta T_{\text{MIT}}(\Phi) - \Delta T_{\text{MIT}}(0)]$), while the steady-state heating is responsible for the hysteresis shift to lower tempera-

tures ($\Delta T_{\text{steadystate}}(\Phi) \sim [T_{\text{MI}}(\Phi) - T_{\text{MI}}(0)]$). In Figs. 3.4e and 3.4f we compare our experimental data with the simulation results. The trends are compatible with each other, signalling that our interpretation of a dual heating mechanism is consistent with the experiment. However, the experimental and simulated slopes differ by a factor 3 to 4, suggesting that our finite element model does not achieve a quantitative description of the NNO response. It is possible that we underestimated the material reflectivity (Fig. 3.8), which might reduce the absorbed power in the low-angle geometry used in our experiment. Furthermore, our model is based on a linear optical response, while in the considered high laser fluence regime the absorption might be saturated, reducing the effective value of α_{NNO} (Fig. 3.9). Another source of uncertainty is the relaxation time (electron-phonon $\tau = 100$ ps) that we used in the simulation (Fig. 3.10). Finally, additional heat dissipation effects that we did not include in our model might be responsible for the experimental heat response. In any case, the main result of this analysis, which is the presence of a dual transient and steady-state heating mechanism, is intrinsic to the system as it is found for all combinations of the simulation parameters. This scenario qualitatively accounts for the observed dynamics.

3.5. CONCLUSIONS

To conclude, we have shown how ultra-fast laser radiation in the high-intensity excitation regime can be used to control the phase transition in nickelates. By tuning the laser fluency we were able to manipulate the equilibrium properties of the material and semi-permanently configure the coverage of insulating nano-domains. With the aid of electrical transport measurements and finite element simulations we identified thermal effects to be the driving mechanism for the light control in this regime. Our results show how laser light can be used to reversibly trigger phase transitions, opening new possibilities for controlling nanoscale order in strongly correlated materials.

3.6. SUPPLEMENTARY INFORMATION

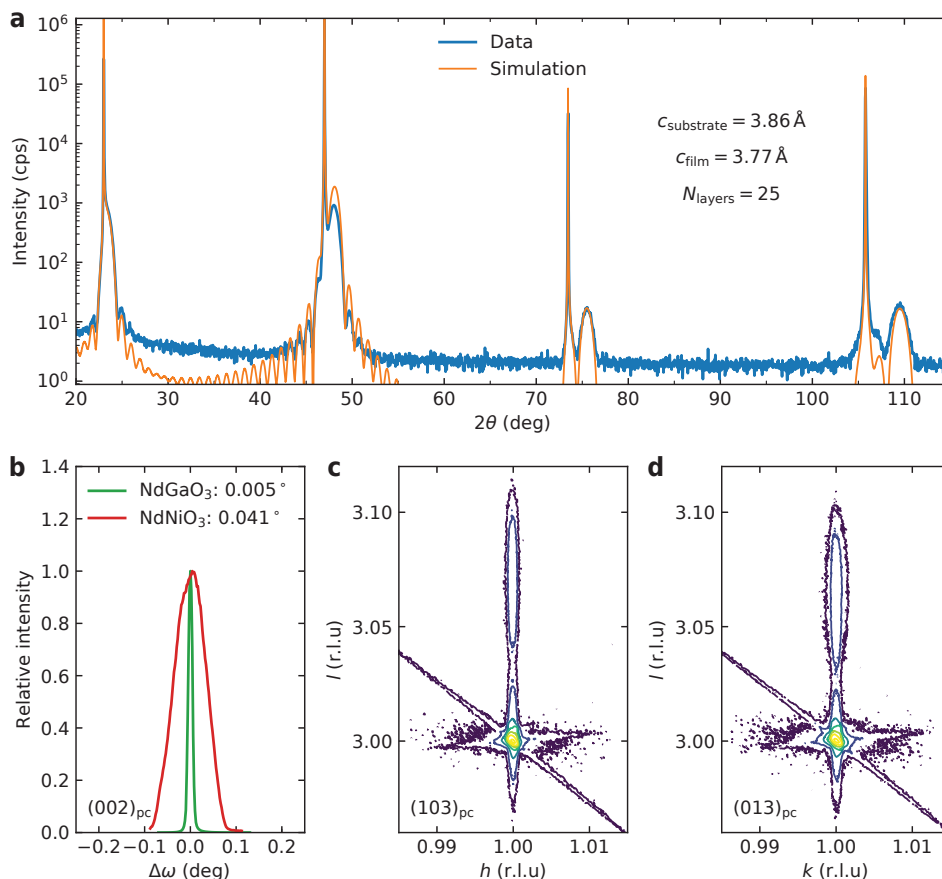


Figure 3.5: **X-ray diffraction characterisation of the NNO film.** (a) θ - 2θ diffraction data around the (001), (002), (003), and (004) peaks of the substrate and film, in pseudocubic notation. The experimental data (blue) is simulated with a conventional kinematic scattering model (orange) in order to extract the c -axis parameters of the substrate ($c_{\text{NdGaO}_3} = 3.86 \text{ \AA}$) and film ($c_{\text{NNO}} = 3.77 \text{ \AA}$). A film thickness $N_{\text{NNO}} = 25$ unit cells is found, corresponding to 9.4 nm. (b) Rocking curve of the film and the substrate around the (002) direction show good heteroepitaxial growth, with low mosaicity. (c) Reciprocal space map around the (103) and (d) the (013) substrate reflections showing the NNO film is coherently strained to the substrate lattice.

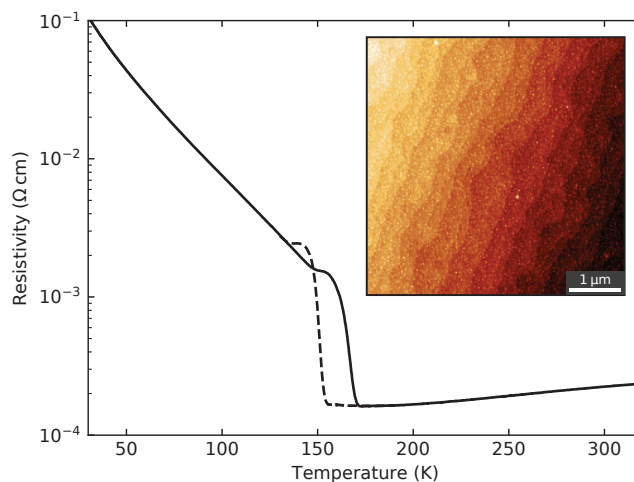


Figure 3.6: **Transport and surface morphology.** Resistivity vs temperature curve during a cooling (dashed) and warming (solid) temperature ramp showing the typical hysteretic behaviour of the MIT in NNO. The measurements are performed in a van der Pauw geometry, contacting the NNO film by direct ultrasonically bonded Al wires. In the inset, the surface morphology measured by means of atomic force microscopy. The film mimics the step and terrace surface of the underlying substrate, indicating good heteroepitaxial growth. The size and orientation of the surface terraces matches the insulating stripes measured by PEEM in the main text, underlying the role of surface morphology in driving the electronic phase transition.

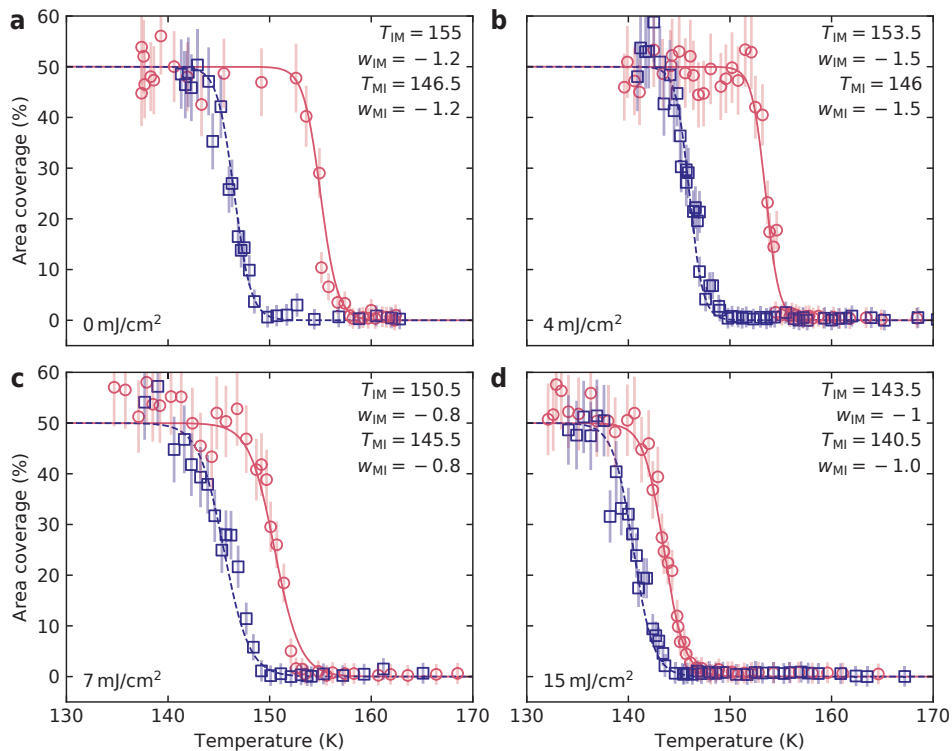


Figure 3.7: **PEEM hysteresis with different laser power.** (a) Insulating area extracted from PEEM images along a cooling (blue squares) and warming (red circles) temperature cycle performed with the laser switched off. (b) Temperature cycle with the laser on at 4 mJ cm^{-2} , (c) 7 mJ cm^{-2} and (d) 15 mJ cm^{-2} . The experimental data is fit with Eq. (3.1) of the main text along the cooling (red dashed line) and warming (black solid curve) branches. The fitting parameters T_i and w_i are reported in each graph. Due to the increased difficulty in evaluating the insulating area at higher coverages, the error on a measurement A_{ins} is estimated as $(0.1 \cdot A_{\text{ins}} + 2)\%$.

3.6.1. LASER HEATING MODEL

We model the laser interaction with the sample considering a $5 \text{ mm} \times 5 \text{ mm} \times 0.5 \text{ mm}$ NdGaO_3 substrate with a 10 nm NNO film on top. The system is initially in thermal equilibrium at 150 K and the laser light impinges on the centre of the top surface, determining a positive heat flow into the system. Heat diffusion occurs only through the sample volume and its bottom surface, which works as a heat sink anchored to a thermal bath at a constant temperature of 150 K . The laser excitation as a function of space and time coordinates is represented by

$$f(x, y, z, t) = (1 - R)Q_0 G_{\bar{x}}(x) G_{\bar{y}}(y) L_{\alpha}(z) G_{\bar{t}}(t - t_0), \quad (3.2)$$

where R is the sample reflectivity, Q_0 is the energy per pulse, $G_{\bar{x}}(x)$ are normalised Gaussian functions with full width at half maximum \bar{x} . The laser penetration in the materials is regulated by the Lamber-Beer law $L_{\alpha}(z) = \frac{1}{\alpha} e^{-\alpha z}$, where α is the absorption coefficient. For the Gaussians we use $\bar{x} = 100 \mu\text{m}$, $\bar{y} = 80 \mu\text{m}$, $\bar{t} = 140 \text{ fs}$, while the material properties relative to NdNiO_3 and NdGaO_3 are indicated in Table 3.1. For computational purposes, we take $t_0 = 280 \text{ fs}$ as time of the first laser pulse. The laser excitation (Eq. (3.2)) is periodically repeated every $40 \mu\text{s}$, corresponding to the experimental 25 kHz laser repetition rate.

We model the heat response of the system Q through a linear response function

$$Q(x, y, z, t) = \int_{-\infty}^t dt' \chi(t - t') f(x, y, z, t'), \quad (3.3)$$

where the response function is taken as $\chi(t) = e^{-t/\tau}$, with response time τ . In this picture, $\chi(t)$ represents the whole series of processes that transform the laser excitation in local heating of the material. For our analysis, we consider a total response time $\tau = 100 \text{ ps}$.

Table 3.1: **Material parameters used in the finite element simulation.** Data from refs. [100–102].

Property		NdGaO_3 (substrate)	NdNiO_3 (film)
Thermal Conductivity	k ($\text{W m}^{-1} \text{K}^{-1}$)	10	2
Density	ρ (kg m^{-3})	7550	7600
Heat capacity	c_p ($\text{J kg}^{-1} \text{K}^{-1}$)	305	265
Reflectivity	R	0.1	0.2
Absorption coefficient	α (cm^{-1})	300	1×10^4

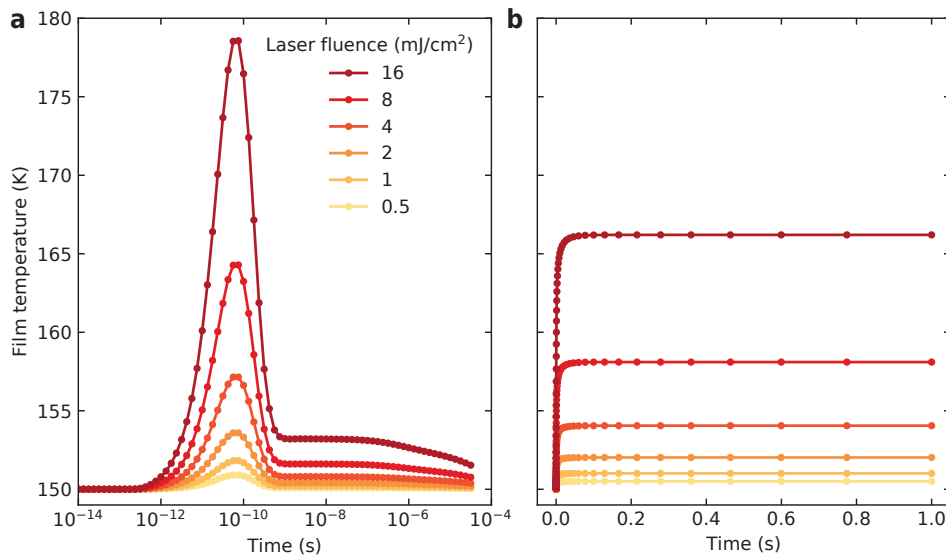


Figure 3.8: **Simulated laser heating for different incident power.** Using $\tau = 100$ ps and $\alpha_{\text{NNO}} = 1 \times 10^4 \text{ cm}^{-1}$, we calculate the effect of changing the incident laser fluence. Higher power determines a linear increase of the heating effects, both in the cases of (a) pulsed (short time scale) and (b) continuous (long time scale) heating. The corresponding values of $\Delta T_{\text{transient}}$ and $\Delta T_{\text{steadystate}}$ are in Fig. 3.4 of the main text.

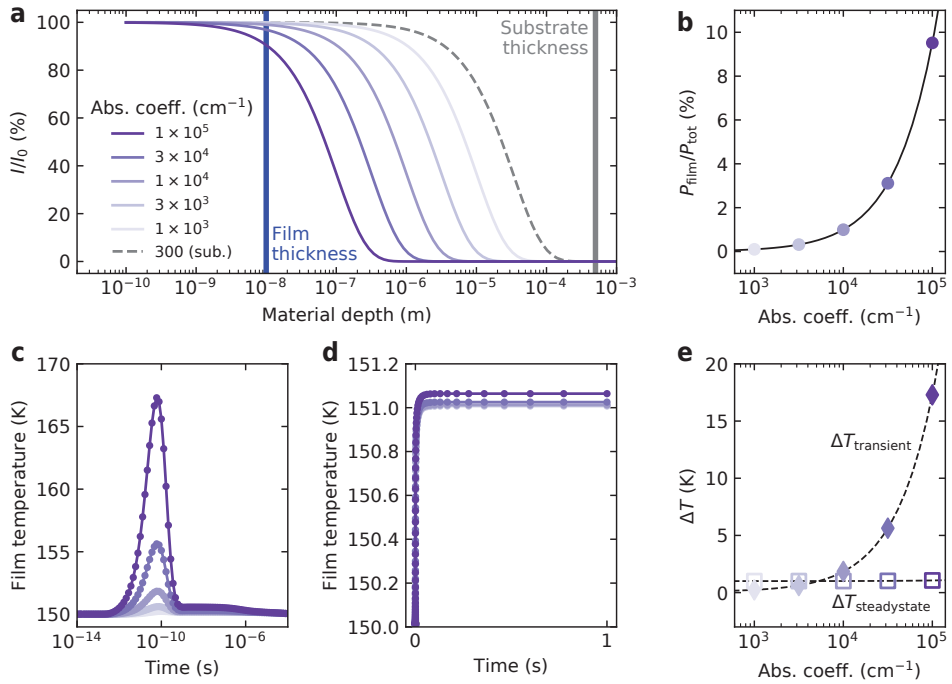


Figure 3.9: **Effect of different film absorption coefficient on the system response.** (a) The Lambert-Beer law $I(z) = I_0 e^{-\alpha z}$ is calculated for different values of α_{NNO} (solid curves) and for the substrate α_{NdGaO_3} (dashed curve). The film and substrate thickness (10 nm and 500 μm , respectively) are indicated by the vertical solid lines. Here we use $\tau = 100$ ps and a laser fluence of 1 mJ cm^{-2} . Independently of the values of α_{NNO} , the whole laser power is absorbed by the film and substrate combination. (b) The percentage of laser power absorbed by the film and (c) the peak of the transient temperature rise both strongly depend on α_{NNO} . (d) Conversely, the steady state temperature is weakly affected by α_{NNO} . (e) Values for $\Delta T_{\text{transient}}$ and $\Delta T_{\text{steadystate}}$ extracted from panels (c) and (d).

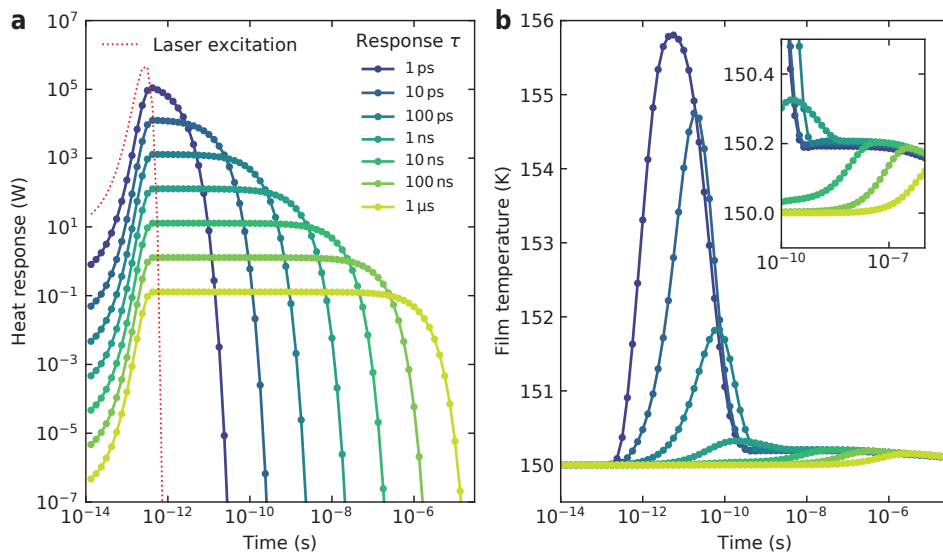


Figure 3.10: **Effect of different response time.** (a) The system heat response time τ is varied in the range 1 ps to 1 μ s and the heat response function is calculated as a function of time. Here $\alpha_{\text{NNO}} = 1 \times 10^4 \text{ cm}^{-1}$ and the laser fluence is 1 mJ cm^{-2} . With smaller τ , the function approaches the Gaussian laser excitation (red dashed line). For larger τ , instead, the function has a broader temporal extent and a lower power at its peak. (b) The film reaches a higher peak in temperature for smaller τ values. This affects $\Delta T_{\text{transient}}$ while has no effect on $\Delta T_{\text{steadystate}}$, considering the total energy transferred to the system is unvaried. The inset of (b) shows the presence of a secondary plateau starting at 1 ns, which signals the onset of the substrate thermalisation.

4

CHARGE DOPING AND LARGE LATTICE EXPANSION IN OXYGEN-DEFICIENT HETEROEPITAXIAL WO_3

Tungsten trioxide is a versatile material with widespread applications ranging from electrochromic and optoelectronic devices to water splitting and catalysis of chemical reactions. For technological applications, thin films of WO_3 are particularly appealing, taking advantage from high surface-to-volume ratio and tunable physical properties. However, the growth of stoichiometric, crystalline thin films is challenging because the deposition conditions are very sensitive to the formation of oxygen vacancies. In this work, we show how background oxygen pressure during pulsed laser deposition can be used to tune the structural and electronic properties of WO_3 thin films. By performing X-ray diffraction and low-temperature transport measurements, we find changes in WO_3 lattice volume up to 10%, concomitantly with an insulator-to-metal transition as a function of increased level of electron doping. We use advanced ab initio calculations to describe in detail the properties of the oxygen vacancy defect states, and their evolution in terms of excess charge concentration. Our results depict an intriguing scenario where structural, electronic, optical, and transport properties of WO_3 single-crystal thin films can all be purposely tuned by a suited control of oxygen vacancies formation during growth.

Parts of this chapter appeared online in preprint arXiv:1711.05106, and are submitted for peer review (2017), by G. Mattoni, A. Filippetti, N. Manca, P. Zubko, and A. D. Caviglia [103].

THE tungsten oxide WO_3 holds a special place in the family of complex oxides, since its perovskite ABO_3 crystal structure has an empty A-site. This characteristic determines an open crystalline structure, which is prone to host interstitial species which act as dopants for the otherwise insulating material [40, 104–107]. For these reasons, WO_3 finds wide use in electrochromic, optoelectronic and gas sensing applications [36–38]. Most works so far focused on thick films, amorphous layers and nanorods [108, 109]. Only recently the growth of crystalline thin films has been demonstrated by means of several techniques such as sputtering, molecular beam epitaxy and pulsed laser deposition [41–44]. Because WO_3 structure and electronic properties are very sensitive to oxygen stoichiometry [34, 110–112], a precise control of oxygen partial pressure during the growth process is crucial to obtain high-quality thin films.

In this work, we study the effects of oxygen pressure during pulsed laser deposition (PLD) of WO_3 thin films, and show how it modifies the material structural and electronic properties. X-ray diffraction measurements reveal that heteroepitaxial WO_3 thin films are in a tetragonal phase, where the out-of-plane lattice parameter can be gradually tuned by 10 %, changing from 3.7 Å measured in the most stoichiometric compound to 4.1 Å in the most oxygen-deficient case. By performing electrical transport measurements, we find a semiconducting trend characterised by an activated regime, with an energy gap that vanishes for increased level of oxygen vacancies. These findings are corroborated by *ab initio* calculations, showing that oxygen vacancies form in-gap states, effectively donating electron carriers and increasing WO_3 lattice volume. Our results show how to obtain WO_3 thin films with high crystal quality and controlled electronic properties.

4

4.1. FILM GROWTH

To study the effect of background oxygen pressure (p_{O_2}) on WO_3 thin films growth by PLD, we prepare a series of samples deposited on top of TiO_2 -terminated SrTiO_3 (001) substrates. We use a laser fluence of 1 J cm^{-2} , a repetition rate of 1 Hz, a target-to-sample distance of 55 mm and a fixed deposition duration of 1000 laser pulses. The growth temperature is 500°C , while p_{O_2} is varied in the range 5–100 μbar . The plasma plume is more diffused at lower p_{O_2} and more intense at higher p_{O_2} (Fig. 4.5). This is because the oxygen pressure in the PLD chamber strongly influences the plume dynamics, enhancing scattering of the ablated species and thermalisation with the background gas. As a consequence, their oxidation state and kinetic energy can be modified, so that the stoichiometry of the deposited material strongly depends upon p_{O_2} [113, 114]. We monitor the growth *in situ* by reflection high-energy electron diffraction (RHEED) and observe clear intensity oscillations (Fig. 4.1a) when p_{O_2} is in the range 10–60 μbar . The RHEED pattern evolves from three well defined diffraction points, typical for SrTiO_3 single crystals [115], to a series of stripes that indicate bidimensional film growth. As shown in the photograph of Fig. 4.1b, the sample colour is also affected by the oxygen pressure, and it gradually changes from transparent to dark grey with lowering p_{O_2} . All the deposited WO_3 films have a step-and-terrace surface morphology with single unit cell steps (Figs. 4.1c and 4.1d). This structure mimics the underlying SrTiO_3 substrate, indicating uniform growth (Fig. 4.6). The samples have very low surface roughness (Fig. 4.1e) in the range

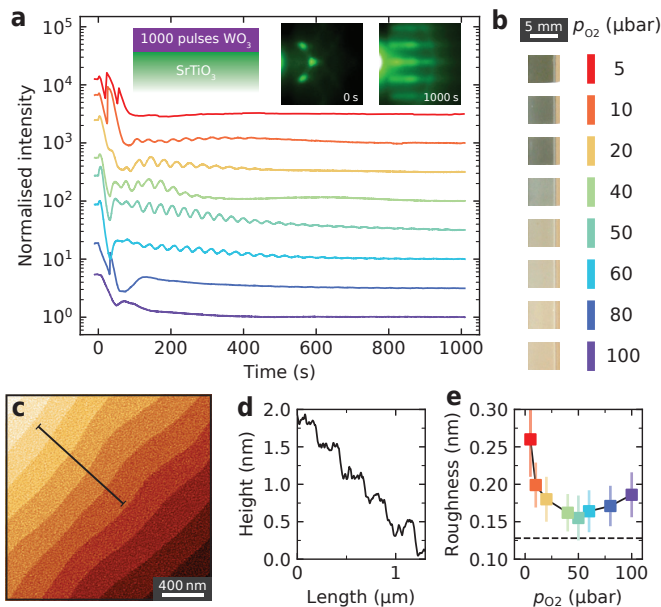


Figure 4.1: **Growth of WO₃ thin films.** (a) RHEED intensity oscillations during film growth at different p_{O_2} and (inset) heterostructure schematic with initial and final RHEED diffraction patterns at $p_{O_2} = 50 \mu\text{bar}$. (b) Photograph of the samples, (c) surface topography by atomic force microscopy, (d) line profile along the black line, and (e) surface roughness calculated as the root mean square of the topographic signal.

0.15–0.25 nm, which is comparable to what we measure in a pristine substrate (0.13 nm). Interestingly, the roughness is minimal at $p_{O_2} = 50 \mu\text{bar}$, pressure for which the RHEED oscillations during growth are more accentuated. This characterisation indicates that for all p_{O_2} in the explored range the films grow with a smooth surface morphology.

4.2. EXPERIMENTAL CHARACTERISATION

4.2.1. X-RAY DIFFRACTION

To evaluate the crystal quality of our WO₃ thin films, we perform X-ray diffraction measurements. Figure 4.2a shows θ - 2θ scans around the sharp (001) and (002) peaks of the SrTiO₃ substrate. The WO₃ film grown at $p_{O_2} = 100 \mu\text{bar}$ presents peaks at $2\theta = 24^\circ$ and 49° , surrounded by neat finite size oscillations that demonstrate a high crystalline quality. No additional diffraction peaks are observed, indicating that the thin films are in a single-crystal phase. For lower p_{O_2} , the peaks and finite size oscillations gradually shift to lower 2θ angles. At $p_{O_2} \leq 20 \mu\text{bar}$, the finite size oscillations become less defined, concurrently with a broadening of the diffraction peaks. Such signal degradation is usually determined by a decreased crystal quality, similarly to what has previously been observed for highly doped WO₃ [116, 117]. In Fig. 4.2b, we evaluate the presence of defects in WO₃ by measuring rocking curves around the film (001) peak. We find for all samples a sharp peak with full width at half maximum between 0.02° and 0.03° , very close to the value

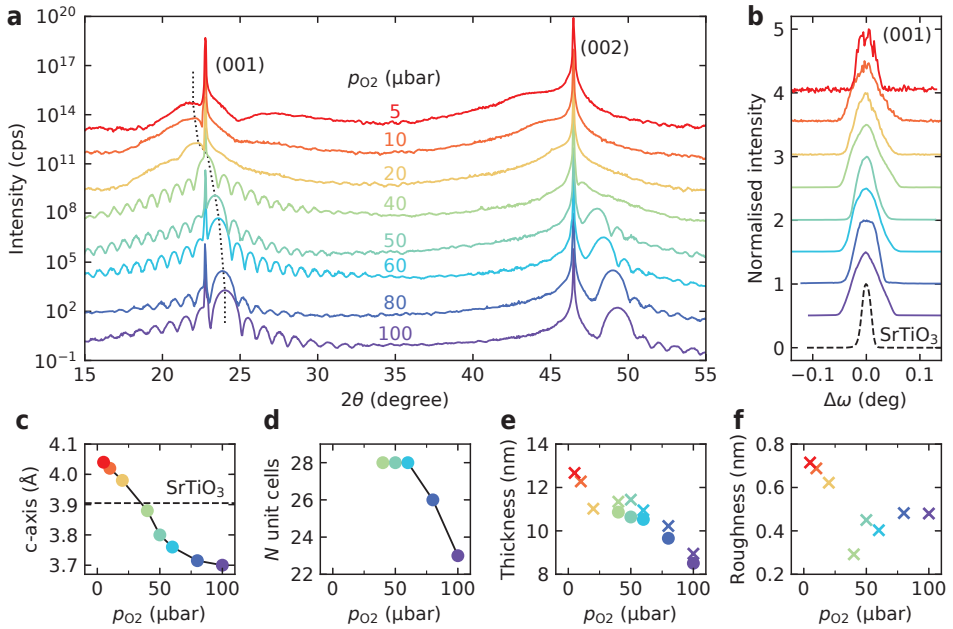


Figure 4.2: **X-ray diffraction characterisation.** (a) θ - 2θ scans around the (001) and (002) peaks of the SrTiO_3 substrate. The dotted line highlights the position of the WO_3 (001) peak. (b) Rocking curves around WO_3 (001) peak compared to the substrate (001) peak (black dashed line). (c) Film c -axis parameter and substrate lattice constant (dashed line), (d) number of WO_3 unit cells extracted by simulating the finite size oscillations with a kinematic scattering model. (e) Film thickness and (f) interface roughness obtained from reflectivity measurements (crosses) and the θ - 2θ data (circles).

found for the underlying SrTiO_3 substrate (0.01°). The sharp rocking curves indicate that the WO_3 films have low mosaicity and present single-crystal quality. By performing reciprocal space maps (Fig. 4.7), we find that the in-plane lattice of all films is coherently strained to the substrate one ($a_{\text{WO}_3} = a_{\text{SrTiO}_3} = 3.905 \text{ \AA}$). By using Bragg's law, we extract in Fig. 4.2c the out of plane c -axis parameter from the 2θ position of WO_3 diffraction peaks. At $p_{\text{O}_2} = 100 \mu\text{bar}$ we obtain $c = 3.70 \text{ \AA}$, while samples grown at lower p_{O_2} present a larger c -axis parameter (Fig. 4.2c). Because all films are epitaxially locked in-plane to the substrate lattice, this points to an increased WO_3 unit cell volume, a trend compatible with a higher concentration of oxygen vacancies as previously reported for oxygen deficient thin films grown by PLD [73, 118–121]. For $p_{\text{O}_2} < 40 \mu\text{bar}$, the c -axis becomes bigger than a_{SrTiO_3} , signalling a transition from tensile to compressive strain. We note that, concomitantly with this crossover, the finite size oscillations disappear, suggesting that films grown at $p_{\text{O}_2} < 40 \mu\text{bar}$ have a lower crystal quality.

By simulating the finite size fringes of the XRD data with a kinematic scattering model, we extract in Fig. 4.2d the number of unit cells N_{WO_3} forming the thin films. We find a constant $N_{\text{WO}_3} = 28 \text{ uc}$ for $p_{\text{O}_2} \leq 60 \mu\text{bar}$, and lower values at higher oxygen pressures. Considering that all films were deposited with the same total number of laser pulses, we associate the decreased N_{WO_3} with enhanced scattering of the plasma plume at higher

pressures, which reduces the amount of material deposited on the substrate. For $p_{\text{O}_2} \leq 20 \mu\text{bar}$, the absence of finite size oscillations makes impossible to determine the number of unit cells by θ - 2θ measurements. We thus perform X-ray reflectivity measurements (raw data in Fig. 4.8) from which we extract the thin film thickness and interface roughness indicated by the crosses in Figs. 4.2e and 4.2f. The total film thickness shows an increasing trend with lower pressure, which is a combined effect of the c -axis expansion and decreased plume scattering. In Fig. 4.2e we also evaluate the film thickness from the θ - 2θ measurements as $c \cdot N_{\text{WO}_3}$ (circles), finding good agreement with the reflectivity data. Concerning the interface roughness in Fig. 4.2f, we observe a minimum at $p_{\text{O}_2} = 40 \mu\text{bar}$, consistent with the minimum value obtained from the topography data of Fig. 4.1e. These measurements show that WO_3 c -axis parameter can be changed up to 10 % by tuning the oxygen pressure during growth, while preserving the in-plane match with the substrate lattice and a flat surface. It is then interesting to study how WO_3 electronic properties are affected by p_{O_2} , which we investigate by low-temperature electrical transport measurements.

4.2.2. ELECTRICAL TRANSPORT

To investigate the effect of oxygen vacancies on WO_3 electronic properties, we measure resistivity vs temperature curves on samples grown in different oxygen pressure conditions. The measurements are performed in a van der Pauw configuration, and electrical contact to WO_3 is obtained with ultrasonic bonded Al wires. All the samples show a semiconducting behaviour (Fig. 4.3a), with the resistivity monotonously increasing upon lowering temperature. The resistivity ρ is calculated using the film thickness measured by X-ray reflectivity. Lower p_{O_2} results in flatter curves with lower room-temperature resistivity, as highlighted in Fig. 4.3b where we report $\rho_{300\text{K}}$ for the different samples. The data shows a sigmoid trend, with a variation of more than 5 orders of magnitude in the studied range. Such trend is comparable to the one observed for the c -axis parameter in Fig. 4.2c, suggesting the existence of a direct correlation between the lattice expansion and the electronic doping. We describe the transport data using an Arrhenius-type behaviour

$$\sigma(T) = \frac{1}{\rho(T)} \propto \exp\left(-\frac{E_a}{k_B T}\right), \quad (4.1)$$

where E_a is the activation energy for charge transport. The experimental curves are fit from room temperature down to 150 K (dashed lines in Fig. 4.3a), showing good agreement (fits on a larger temperature range are discussed in Fig. 4.9). We extract $E_a \sim 220 \text{ meV}$ at the highest p_{O_2} , which is about one order of magnitude smaller than the optical band of 3 eV found in bulk WO_3 [35, 110]. This suggests that the observed activated transport arises from localized states lying inside WO_3 band gap, which formed in a certain amount even at the highest p_{O_2} value. At lower p_{O_2} , the concentration of oxygen vacancies in the film increases determining a vanishing E_a . Even though the WO_3 films are on the verge of an insulator-to-metal transition, we measure semiconducting behaviour even at the highest vacancies concentration. This is different from what observed with other doping mechanism, where a metallic state was achieved at high doping levels [33, 34, 106, 110]. Decreased crystal quality and disorder during low-pressure PLD

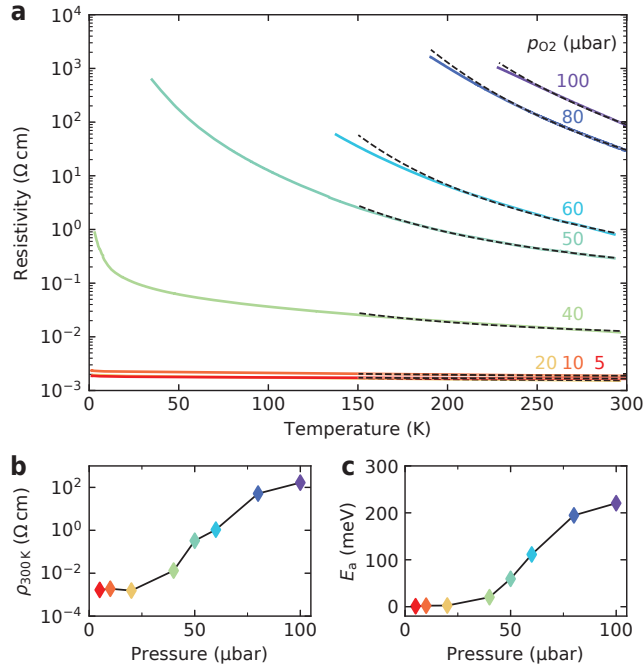


Figure 4.3: **Resistivity measurements.** (a) Four probe resistivity vs temperature curves. The dashed lines are best fits to the Arrhenius model for activated transport in Eq. (4.1). (b) Room temperature resistivity and (c) activation energy for transport extracted from the fits.

growth are the most probable causes for the persistent semiconducting state measured in our most doped WO_3 thin films.

To get indication on the density of the charge carriers, we perform low temperature magnetotransport measurements. Because most of the samples are highly resistive, reliable Hall measurements could be obtained only for samples grown at $p_{\text{O}_2} \leq 20 \mu\text{bar}$. In this high-doping condition, all the samples show similar magnetotransport data (Fig. 4.10), from which we extract a carrier density $n_{3\text{D}} = 4 \times 10^{21} \text{cm}^{-3}$ and a mobility $\mu = 0.6 \text{cmV}^{-1} \text{s}^{-1}$ at 1.5 K, in agreement with previous reports of oxygen-deficient WO_3 materials [34, 112]. The measured electron density corresponds to about 0.25 electrons per unit cell, which would be equivalent to an oxygen vacancy concentration of about 4%, if these are the only source of electron donors.

4.3. AB INITIO CALCULATIONS

To investigate the origin of the observed structural and transport behaviour of WO_3 films, we performed *ab initio* calculations by variational pseudo-self-interaction-corrected (VP-SIC) density functional theory (DFT) [122–125]. To validate our results, we first calculated several WO_3 bulk phases (further details in Fig. 4.11 and Section 4.5.1). The growth on SrTiO_3 substrates was simulated using pseudo-cubic supercells, with in-plane lattice

constant fixed at $a_{\text{SrTiO}_3} = 3.905 \text{ \AA}$ and the orthogonal axis left free to relax. The calculations show that the stress associated with the planar expansion is partially relieved with a shrinkage of the out-of-plane lattice parameter to $c = 3.685 \text{ \AA}$ (Table 4.1). This value is comparable with the experimental data of WO_3 films grown at the highest oxygen pressure reported in Fig. 4.2c, which are thus identified as stoichiometric.

Starting from the strained WO_3 structure, we introduce vacancies by removing oxygen atoms in the WO_2 crystal planes. We study oxygen vacancy concentrations of 2% ($\text{WO}_{2.94}$) and 4% ($\text{WO}_{2.88}$). After a further structural relaxation, our calculations find a lattice increase to $c = 3.72 \text{ \AA}$ and $c = 3.73 \text{ \AA}$ for the two vacancy concentrations (Table 4.1). This expansion is in qualitative agreement with our experimental results of Fig. 4.2, even though the calculated values are considerably lower than what measured for films grown at low pressure. Previous literature reports show that the lattice expansion due to oxygen vacancies is maximum when the charge is fully localised [126, 127]. As discussed in the following, the structures described by our DFT calculations are in the metallic regime, and this may partially explain the quantitative discrepancy with the experiments. Furthermore, temperature-related effects, which are not included in our calculations, could also affect the lattice expansion [128].

In Fig. 4.4a we show the calculated in-plane band structure for strained WO_3 films with different oxygen vacancy concentrations (extended plots in Fig. 4.12). A single oxygen vacancy generates an excess of two electrons. In the limit of an isolated point defect, this charge remains trapped by the W atoms surrounding the vacancy, which change their ionic charge from the stoichiometric W^{6+} to a lower value, also giving rise to colour centres responsible for the photochromic effect [36, 129]. Localisation may eventually be strengthened by the formation of small polarons [129]. According to our calculations, the excess charge reverses into the t_{2g} orbitals of the W atoms, forming a shallow band (orange curve in Fig. 4.4a) right below the bottom of the conduction band. Although this band is optically separated from the bulk-like t_{2g} conduction bands running above it, the system for both the examined doping levels is metallic, as indicated by the position of the Fermi energy (green dashed lines in Fig. 4.4a). The defect state can be visualised in real space through the isosurface plot of Fig. 4.4b: the defect charge is mostly localised on the two W atoms nearest neighbours of the vacancy, with clear t_{2g} symmetry. This is also seen by the broader bandwidth of the vacancy state along the diagonal direction X–M, characteristic of t_{2g} orbitals, instead of the cubic edge direction Γ –X.

In Table 4.1 we report the band gaps and effective masses along the planar Γ –M

Table 4.1: **Ab initio results.** Properties for bulk δ - WO_3 and for films strained in-plane to the SrTiO_3 substrate lattice. Different concentrations of oxygen vacancies in the WO_2 planes are considered, and the effective mass m^* is calculated along the planar Γ –M direction.

	Bulk δ - WO_3	WO_3	$\text{WO}_{2.94}$	$\text{WO}_{2.88}$
O vac.	0%	0%	2%	4%
c (\AA)	3.75	3.685	3.72	3.73
E_g (eV)	2.71	2.83	-	-
m^* (m_e)	0.56	0.85	2.41	1.16

direction. The vacancy-free structure shows an insulating state with a direct gap $E_g = 2.83$ eV at the Γ point, substantially larger than the indirect gap in bulk $\delta\text{-WO}_3$ of 2.71 eV. This is a consequence of the tensile strain present in the structure which stretches the planar bonds and reduces the t_{2g} bandwidth, as evidenced by the increased effective mass. Even though the $\text{WO}_{2.94}$ and $\text{WO}_{2.88}$ structures have a small optical gap at Γ of 75 meV and 150 meV, respectively, they show metallic character in transport due to the broader density of states in the orthogonal direction (Fig. 4.12). With more excess charge, the gaps and effective masses are progressively reduced. This is due to electronic correlation and band filling effects, which cause a spread in the bandwidth with respect to the empty conduction bands of the undoped system. For lower vacancy concentration, up to the limit of isolated point defect, instead, the carrier density is expected to be reduced, leading to the formation of an insulating state.

4

In order to theoretically estimate electron mobility and resistivity in a wider range of vacancy concentrations, we apply the Bloch-Boltzmann approach to mix the *ab initio* band energies of the $\text{WO}_{2.94}$ structure with a model description of the electron-phonon scattering [130, 131]. We tune the Fermi level in a rigid band approximation to simulate the variation in the excess carrier density produced by the vacancies. Results of three-dimensional averages of mobility vs carrier density at 1.5 K are reported in Fig. 4.4c. As a consequence of the increasing population of high-energy t_{2g} bands of WO_3 , the mobility increases with the carrier density and, for 2% vacancies, we find $n = 2.2 \times 10^{21} \text{ cm}^{-3}$ and $\mu = 30 \text{ cm}^2 \text{ V}^{-1} \text{ s}^{-1}$ (white circle in Fig. 4.4c). In our oxygen deficient films, we measure a Hall mobility $\mu = 0.5 \text{ cm}^2 \text{ V}^{-1} \text{ s}^{-1}$ (orange diamond in Fig. 4.4c and raw data in Fig. 4.10) which, in our calculations, would be achieved for a considerably lower carrier density $n = 1 \times 10^{18} \text{ cm}^{-3}$. By using the *ab initio* transport coefficients, we calculate the corresponding resistivity vs temperature in Fig. 4.4d. At densities below $n = 1 \times 10^{19} \text{ cm}^{-3}$, we observe an insulating transport regime for which only the energy-flat lowest portion of the defect state is populated, with vanishing band velocities. In this regime, the electrical transport is thermally activated, similarly to what we measure experimentally. Above $n = 1 \times 10^{19} \text{ cm}^{-3}$, a metallic state is observed in our calculations, but it is not achieved experimentally. This is a clear indication that disorder in our thin films plays a crucial role in preventing occurrence of an insulator-to-metal transition, consistently with the experimental observation of a low electron mobility.

Several aspects of our transport calculations are in good agreement with our measurements. In particular, the amplitude of resistivity vs temperature matches well the experimental data, and the shallow temperature dependence of the resistivity is experimentally verified for most of the doped samples. Furthermore, the calculations show that an insulator-to-metal transition occurs for $\rho_{300\text{K}} < 1 \times 10^{-2} \Omega \text{ cm}$, a value consistent with our experimental observations. On the other hand, there is an offset between calculated and Hall charge densities corresponding to the same mobility value, the former being two orders of magnitude lower. This discrepancy suggests that a large portion of excess charge in the samples may be scarcely mobile, possibly stuck in deep traps or in highly localized polarons. The hypothesis of additional charge in the samples coming from in-gap states is coherent with the experimentally measured Arrhenius trend of the resistivity.

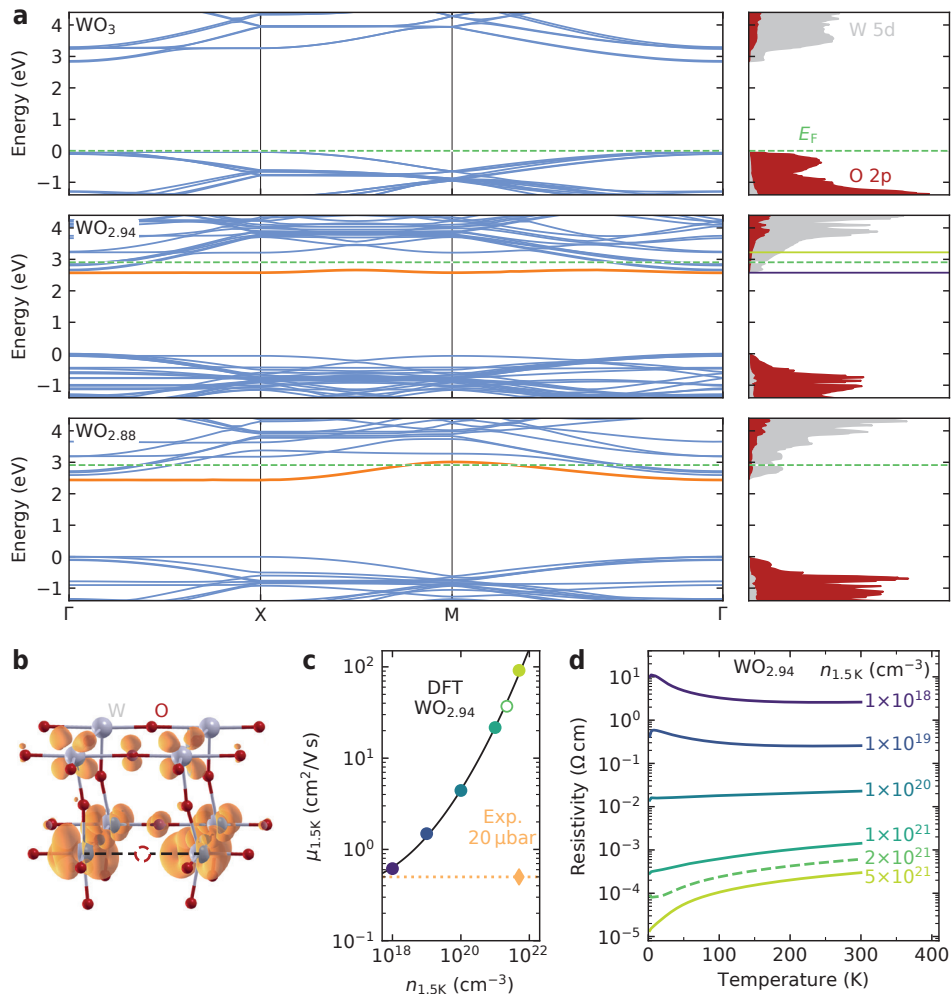


Figure 4.4: DFT calculations of heteroepitaxial WO_3 films with oxygen vacancies. (a) Left panels: in-plane band structure for WO_3 with 0%, 2%, and 4% oxygen vacancies. The calculations are performed using $2 \times 2 \times 4$ supercells, with an oxygen vacancy in the WO_2 planes. The band of the oxygen defect states is indicated in orange, and the Fermi level is represented by the green dashed line. Right panels: density of states projected on the oxygen 2p (red) and tungsten 5d (grey) orbitals. For $\text{WO}_{2.94}$ the horizontal solid lines show the Fermi level corresponding to carrier densities $n_{1.5\text{K}} = 5 \times 10^{21} \text{ cm}^{-3}$ (green) and $1 \times 10^{18} \text{ cm}^{-3}$ (violet). (b) Computed $2 \times 1 \times 1$ supercell of $\text{WO}_{2.94}$ showing the real space charge density isosurface of the defect band (orange). The oxygen vacant site at the bottom is indicated by the dashed red circle. (c) Mobility as a function of carrier density (circles) at 1.5 K from the DFT calculations. The density at the Fermi level is indicated by the white circle, and the diamond represents the experimental Hall data for the sample grown at $p_{\text{O}_2} = 20 \mu\text{bar}$. (d) Resistivity vs temperature curves for $\text{WO}_{2.94}$ from the DFT calculations.

4.4. CONCLUSIONS

In summary, we demonstrated that structural, electronic and transport properties of WO₃ thin films can be controlled by changing the oxygen pressure during PLD growth. The out-of-plane lattice constant of our thin films increases up to 10 % as a consequence of the introduction of oxygen defects, while a pseudocubic phase of single crystal quality is maintained. Oxygen vacancies act as electron donors and dope the material towards a metallic state. Our VPSIC-DFT calculations describe oxygen vacancies in strained WO₃ films as weakly localized, shallow donors of t_{2g} orbital character, lying only a few tenths of meV below the bulk-like t_{2g} mobility edge. According to our Bloch-Boltzmann rigid-band calculations, full localization is only reached for $n < 1 \times 10^{19} \text{ cm}^{-3}$, corresponding to an extremely small vacancy concentration of 0.01 %. While several aspects of the calculations are coherent with the measurements, it is very likely that additional effects, like disorder and defect clustering, can enhance charge localization, thus shifting to higher values the vacancy concentration threshold separating charge-localised and delocalised regimes. Our results represent a fundamental step towards the understanding and engineering of a material which is likely destined to become a rising star in the energy and nanoelectronic applications of the future.

4.5. SUPPLEMENTARY INFORMATION



Figure 4.5: **Plasma plume of WO_3 ablated at different oxygen pressures.** Photographs of the PLD vacuum chamber, showing the carousel of targets on the left (the WO_3 target is facing backwards) and the sample holder on the right. The sample (square) is heated from the back with an 800 nm continuous laser (saturating the camera). The pulsed laser radiation ($\lambda = 248\text{ nm}$) enters the vacuum chamber from the bottom right and impinges on the rotating WO_3 target, generating a plasma plume directed perpendicularly towards the sample. At the lowest p_{O_2} , the plume is barely visible due to minimal scattering of the ablated species with the background gas. With increasing p_{O_2} , the plume becomes more intense and confined. At $p_{\text{O}_2} \geq 80\mu\text{bar}$, the plume almost completely vanishes in intensity before reaching the sample, indicating the occurrence of many scattering events that ensure a high oxidation of the material depositing on the substrate. This is consistent with our experimental observations in Fig. 4.2 of the main text, and also explains the decreased WO_3 thickness which is deposited at the highest p_{O_2} values, since more scattering events reduce the amount of material reaching the sample.

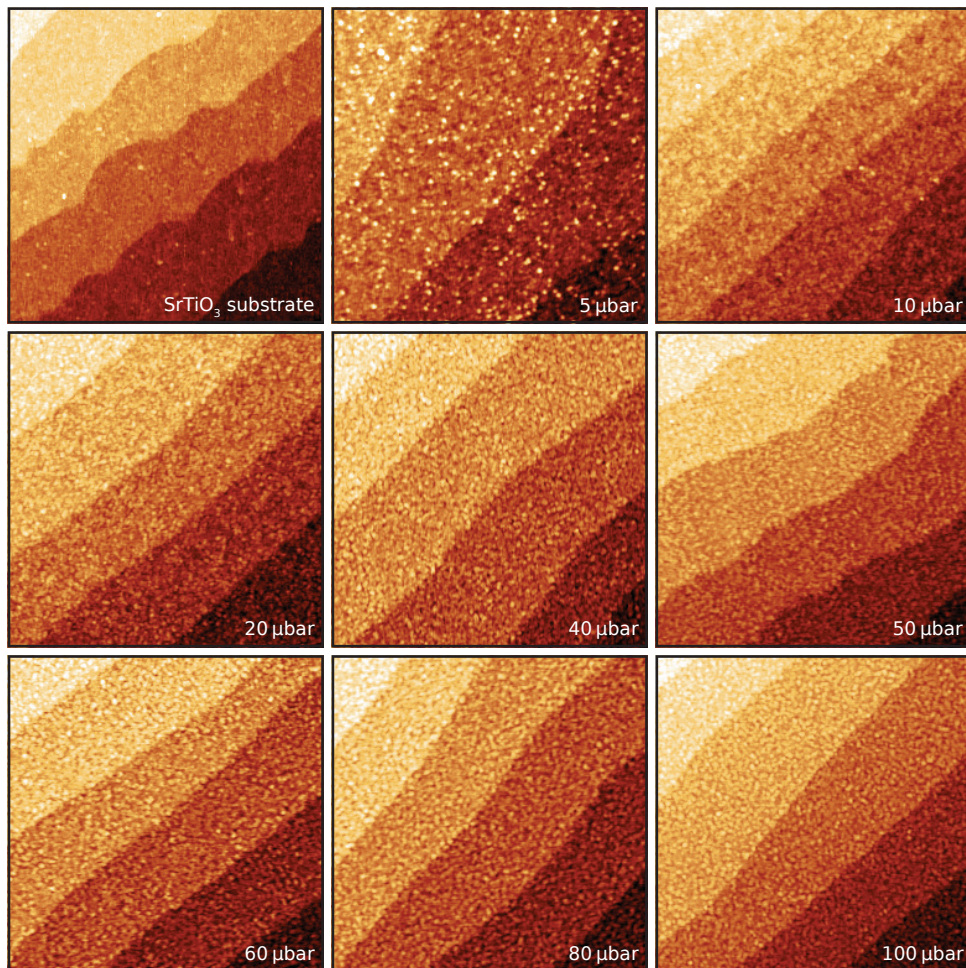


Figure 4.6: **Topography of the samples.** Atomic force microscopy images ($2\mu\text{m} \times 2\mu\text{m}$ in size) show the surface of the SrTiO_3 substrate and of WO_3 films grown in different oxygen pressures. A flat morphology with single unit cell steps and terraces is observed for all pressure conditions, with a minimum surface roughness at $p_{\text{O}_2} = 50\mu\text{bar}$ (data in Fig. 4.1e of the main text).

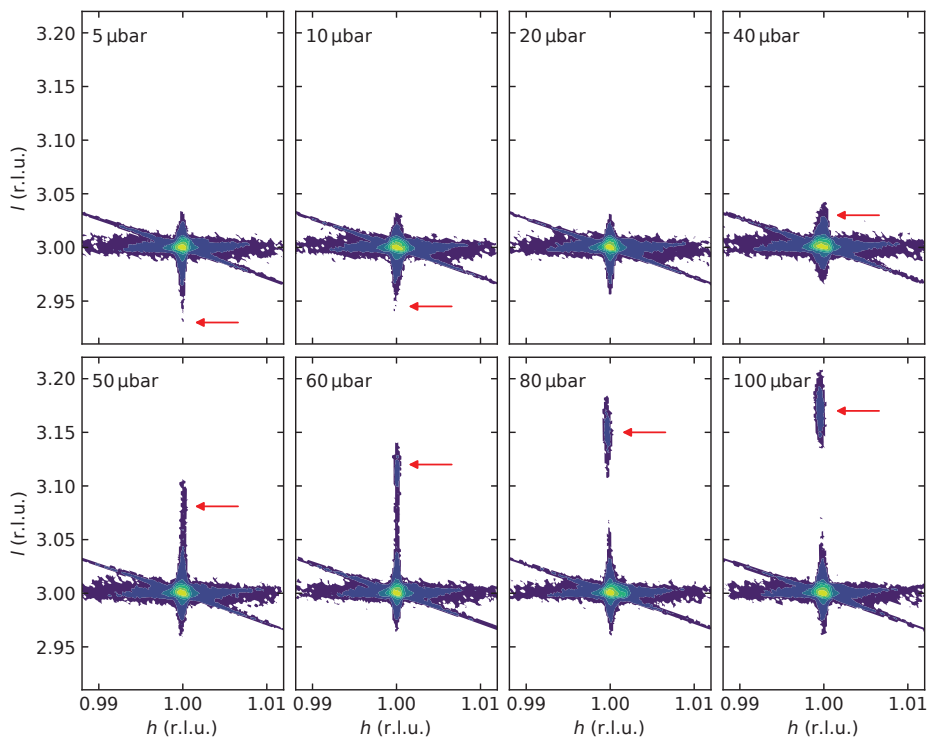


Figure 4.7: **Reciprocal space maps around SrTiO₃ (103) diffraction peak.** The WO₃ films determine a peak (indicated by the red arrows) which continuously changes from $l \sim 2.93$ to $l \sim 3.17$ upon increasing p_{O_2} . For all growth pressures, the WO₃ films are coherently strained in-plane to the substrate lattice, as indicated by the identical alignment along the in-plane direction h .

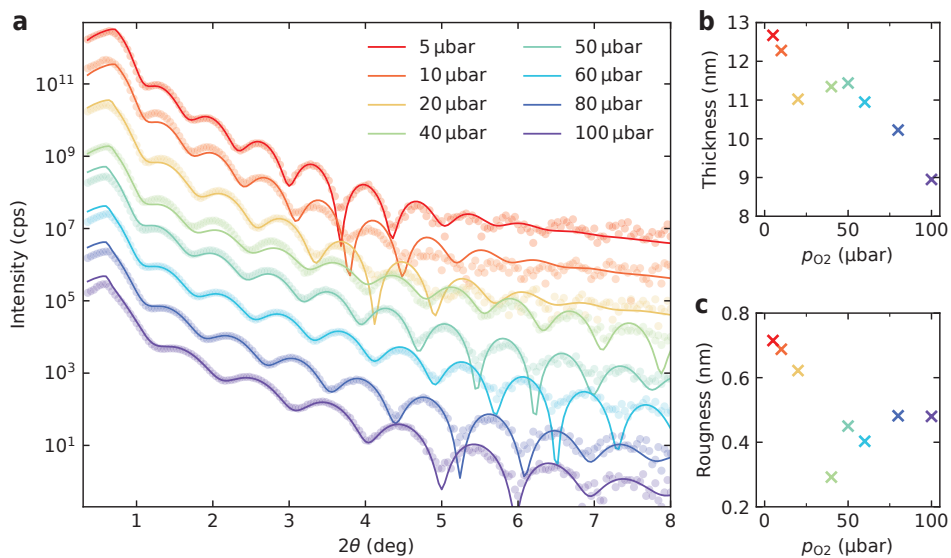


Figure 4.8: **X-ray reflectivity of WO_3 thin films.** (a) Low-angle θ - 2θ measurements (circles) fit with a conventional thin film reflectivity model (solid lines). (b) Film thickness and (c) interface roughness extracted from the fits.

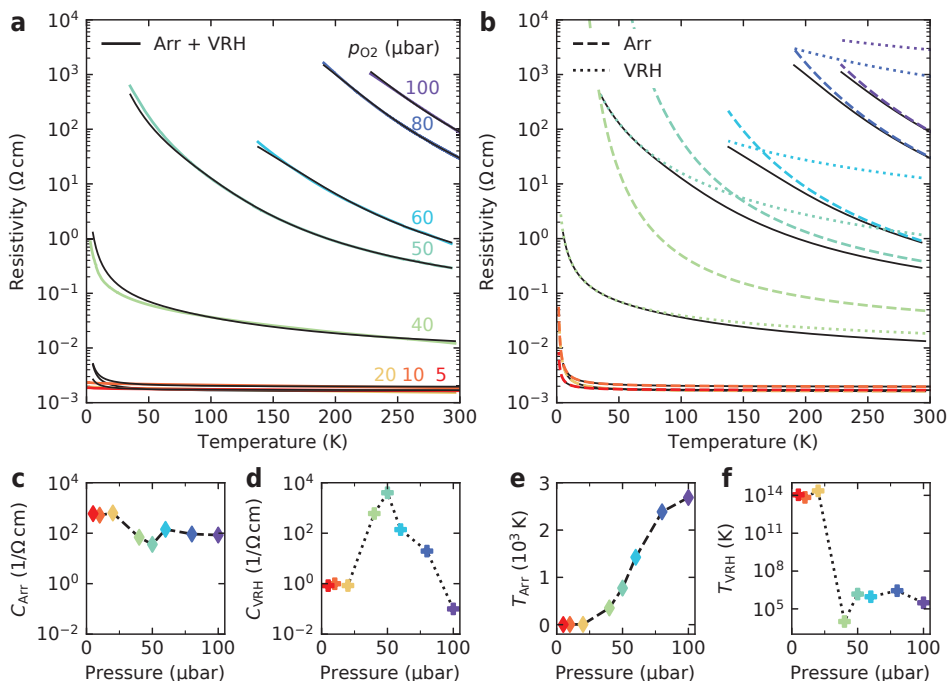


Figure 4.9: **Resistivity curves fit with Arrhenius and Mott variable range hopping.** (a) The experimental curves are fit with $\sigma(T) = 1/\rho(T) = C_{\text{Arr}} \exp(-T_{\text{Arr}}/T) + C_{\text{VRH}} \exp(-(T_{\text{VRH}}/T)^{1/4})$ (black lines) from room temperature down to $T = 10\text{K}$. This is a typical trend for electrical transport in complex oxide semiconductors [69]. Good agreement with the experimental data is observed at all temperatures. (b) Separated contribution to the fit of the Arrhenius term (dashed lines) and variable range hopping term (dotted lines). The main resistivity contribution at $T \geq 150\text{K}$ is provided by the Arrhenius term, justifying the analysis performed in Fig. 4.3 of the main text. (c) Arrhenius and (d) variable range hopping scaling constants and (e), (f) corresponding temperature constants extracted from the fits. Note that the activation energy discussed in the main text can be calculated as $E_a = T_{\text{Arr}} k_B$, where k_B is the Boltzmann constant.

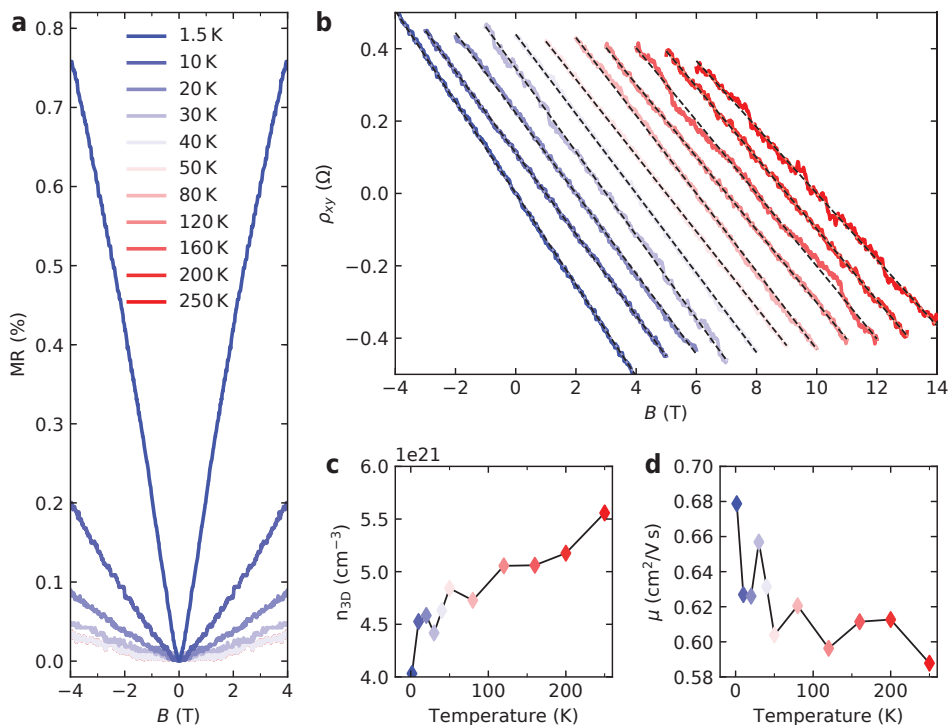


Figure 4.10: **Magnetotransport measurements of WO_3 grown at $20 \mu\text{bar}$.** (a) Magnetoresistance and (b) Hall effect curves measured at different temperatures (curves horizontally offset by 1 T for clarity). The magnetoresistance is defined as $\text{MR} = \frac{\rho_{xx}(B) - \rho_{xx}(0)}{\rho_{xx}(0)}$, where ρ_{xx} is the longitudinal resistivity. A small positive MR is observed and it becomes negligible above 30 K, reminiscent of low-temperature localisation effects. The Hall effect is negative and linear, indicating electron carriers, from which we extract (c) the three-dimensional carrier density and (d) the mobility. At the lowest temperature we find $n_{3D} = 4 \times 10^{21} \text{ cm}^{-3}$, corresponding to 0.25 electrons per WO_3 formula unit. Both n_{3D} and μ are almost constant in the studied temperature range.

4.5.1. ADDITIONAL AB INITIO CALCULATIONS

To validate our DFT results, we applied VPSIC to several WO_3 bulk structures, for which an amount of experiments and earlier calculations is available. As an example, for the triclinic $\delta\text{-WO}_3$ phase stable at room temperature we obtain an indirect band gap of 2.71 eV against a measured value of 2.75 eV [132], while for the low-temperature monoclinic $\epsilon\text{-WO}_3$ we have $E_g = 3.34$ eV, which compares well with $E_g = 3.27$ eV obtained with the accurate, but computationally demanding, GW approach [133]. A comprehensive review with results for WO_3 by a variety of advanced methods can be found in ref. [134].

We simulated growth on the SrTiO_3 substrate by using pseudocubic supercells with the in-plane lattice constant kept fixed at $a_{\text{SrTiO}_3} = 3.905 \text{ \AA}$, and the orthogonal axis free to relax. Concerning atomic positions, we started the structural simulations from a hypothetical triclinic array with no symmetry imposed, and left all the atoms free to relax towards the energy minimum. Several supercell symmetries were considered, corresponding to different oxygen vacancy concentrations and configurations. In Fig. 4.11 we show the atomic structure obtained for the pristine strained film. Since the average lattice parameter in the $\delta\text{-WO}_3$ phase is $a = 3.75 \text{ \AA}$ [135], we can estimate that the match with the substrate induces a linear tensile strain of about 4 % in the film plane. To partially relieve the stress associated with the planar expansion, the film shrunk longitudinally, with $c = 3.685 \text{ \AA}$. Overall, the strained film displays a 6 % volume expansion with respect to the $\delta\text{-WO}_3$ bulk phase. This value is compatible with the experimental lattice parameter of our most stoichiometric WO_3 films $c = 3.70 \text{ \AA}$, within the 1 % underestimation usually observed in DFT calculations [136, 137].

Another remarkable difference with respect to the bulk is in octahedral tiltings: in the planes (Fig. 4.11a), the W–O bonds are stretched out and the octahedral tiltings largely suppressed, with W–O–W angles of $\sim 175^\circ$, on average. In the orthogonal direction (Fig. 4.11b), the W–O bonds are more bulk-like, and the tiltings slightly larger (W–O–W angles $\sim 168^\circ$). The structure displays octahedral distortions and shifts of W atoms from the octahedral centres, which are also present in the triclinic phase. The overall tilting pattern is $a^- b^- c^-$, like in $\delta\text{-WO}_3$ bulk.

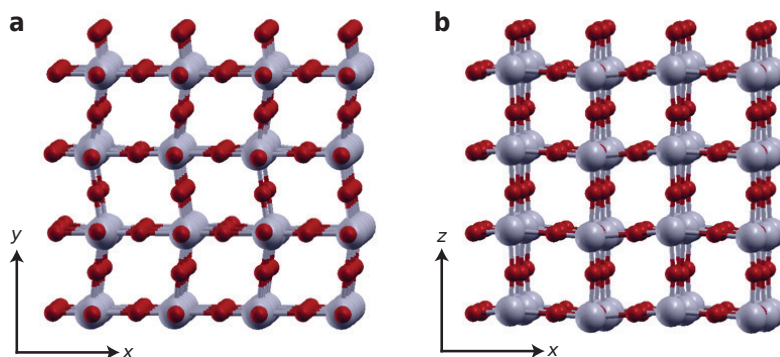


Figure 4.11: **Calculated structure for the WO_3 film strained in the (x,y) plane to match the SrTiO_3 substrate lattice.** (a) Film top view from the (x,y) plane and (b) side view in the growth direction from the (x,z) plane. Grey and red balls are W and O atoms, respectively.

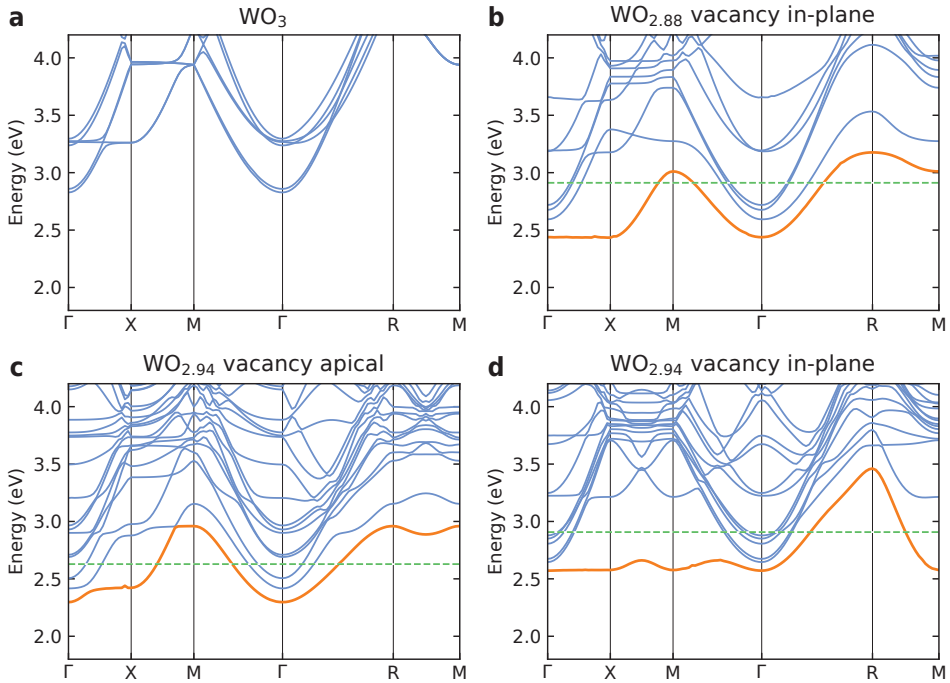


Figure 4.12: **Band structure calculated for strained WO_3 with and without oxygen vacancies.** (a) Pristine WO_3 and with (b) 4% vacancies with oxygens missing in the WO_2 planes, (c) 2% vacancies in apical position and (d) 2% vacancies in-plane. The donor state resulting from the oxygen vacancies is drawn in orange. Zero energy is fixed at the valence band top (not shown) and the Fermi level of the neutral state is indicated by the green dashed lines. The k -points coordinates are $\Gamma = [0, 0, 0]$, $X = [1/2, 0, 0]$, $M = [1/2, 1/2, 0]$, and $R = [1/2, 1/2, 1/2]$ expressed in units of $[\pi/a, \pi/a, \pi/c]$, where a and c refer to the single WO_3 unit cell.

In Fig. 4.12 we show the calculated bands for the strained WO_3 films. The bands of the vacancy-free structure are visibly similar to that of the bulk $\delta\text{-WO}_3$ phase, with two significant differences. Firstly, $E_g = 2.83$ eV is slightly larger than in bulk. Secondly, our calculations show that in bulk $\delta\text{-WO}_3$ the valence band at X is 3 meV higher than at Γ , resulting in an indirect X \rightarrow Γ band gap. For the strained film, instead, the valence band at Γ is 38 meV higher than at X, thus the gap is direct at the Γ point. We note that the band-gap nature for WO_3 at room temperature is debated [133, 134], although the indirect gap hypothesis seems the most credited by experimental reports [39, 138, 139]. However, the flatness of the topmost valence band segment between X and Γ suggests that minor structural differences in the sample could be sufficient to change the band gap nature.

Let us see more in detail these results: for 4% vacancies distributed in WO_2 planes (Fig. 4.12b), the defect state (orange) is separated, at its energy-lowest Γ point, by an optical gap of about 150 meV from the t_{2g} bottom. A large band dispersion of the defect state is visible both in plane (along X–M) and out of plane (along R–M), indicating that vacancies separated by two lattice units are still affected by a fair amount of mutual inter-

action. Overall the system is a semi-metal, that is optically insulating but metallic from the transport viewpoint. Notice a significant detail: the broader bandwidth direction of the vacancy state is not along the cubic edge (Γ -X) but along the diagonal (X-M). This is a consequence of the t_{2g} orbitals orientation, which do not point towards the nearest oxygen atoms, but diagonally. In the attempt to further reduce the metallic character of the system, we tested two arrays with 2% vacancy concentration, one with vacancy in apical positions (Fig. 4.12c), another with vacancy in WO_2 planes (Fig. 4.12d). In both cases the vacancy distance is doubled with respect to the 4% concentration, resulting in a substantial decrease of the bandwidth along the significant k -space direction (X-M for in-plane, and R-M for apical configuration). For both cases the band bottom is still at Γ , with optical gaps equal to 120 meV and 75 meV for apical and in-plane vacancies, respectively. Even at this lower vacancy concentration, however, the fully localized regime is not reached. The calculated effective masses give a measure of the localization degree of the defect state: for the in-plane vacancy state $m^* = 2.41 m_e$, while $m^* = 1.01 m_e$ in Γ -M and Γ -R directions, respectively. These values can be compared with $m^* = 0.85 m_e$ and $0.57 m_e$ along the analogous directions for the lowest bulk-like t_{2g} band. The defect state is thus about 2-3 times less mobile than the states of the t_{2g} conduction bottom. For the apical vacancy state, we obtain $m^* = 1.17 m_e$ and $1.25 m_e$ along Γ -M and Γ -R, which are not much larger than the bulk-like t_{2g} band values $m^* = 0.86 m_e$ and $0.74 m_e$ in the corresponding k -space directions.

5

INSULATOR-TO-METAL TRANSITION AT OXIDE INTERFACES INDUCED BY WO_3 OVERLAYERS

Interfaces between complex oxides constitute a unique playground for two-dimensional electron systems (2DESs), where superconductivity and magnetism can arise from combinations of bulk insulators. The 2DES at the $\text{LaAlO}_3/\text{SrTiO}_3$ interface is one of the most studied in this regard, and its origin is determined by the polar field in LaAlO_3 as well as by the presence of point defects, like oxygen vacancies and intermixed cations. These defects usually reside in the conduction channel and are responsible for a decrease of the electronic mobility. In this work, we use an amorphous WO_3 overlayer to obtain a high-mobility 2DES in $\text{WO}_3/\text{LaAlO}_3/\text{SrTiO}_3$ heterostructures. The studied system shows a sharp insulator-to-metal transition as a function of both LaAlO_3 and WO_3 layer thickness. Low-temperature magnetotransport reveals a strong magnetoresistance reaching 900% at 10 T and 1.5 K, the presence of multiple conduction channels with carrier mobility up to $80\,000\text{ cm}^2\text{ V}^{-1}\text{ s}^{-1}$ and quantum oscillations of conductance.

Parts of this chapter have been published in ACS Applied Materials & Interfaces (2017), by G. Mattoni, D. J. Baek, N. Manca, N. Verhagen, D. J. Groenendijk, L. F. Kourkoutis, A. Filippetti, and A. D. Caviglia [140].

THE formation of a two-dimensional electron system (2DES) at the interface between band insulators SrTiO₃ (STO) and LaAlO₃ (LAO) is among the most intriguing effects studied in oxide electronics [55]. Gate-tunable superconductivity [49, 50], strong spin-orbit coupling [51, 52] and magnetism [53, 54] are some of the many phenomena observed. The origin of this 2DES is a long-standing question and recent results indicate that a consistent picture should take into account both the built-in polar field and the presence of point defects [47, 58, 60]. Among these, oxygen vacancies and cation off-stoichiometry in STO are capable of inducing a 2DES [57, 59]. However, although defects can contribute to the conductivity, they also act as scattering centres within the potential well, lowering the electronic mobility [141]. To promote high electron mobility, it is desirable to spatially separate the donor sites from the conducting plane, while allowing 2DES formation in the STO top layers. There have been various approaches to control the defect concentration profile and enhance the mobility which involve the use of crystalline insulating overlayers [142, 143], adsorbates [144], amorphous materials [145] and even thin metallic layers [146, 147]. The potential of these overlayers for defect management is determined by their reactivity and capacity to host defects such as oxygen vacancies. A promising material in this respect is the transition metal oxide WO₃. Both crystalline and amorphous WO₃ can host vacancies and interstitial atoms, thus allowing cation accommodation and diffusion, with a tendency to form compounds such as tungsten bronzes [116, 148]. In addition, the several possible oxidation states of tungsten make WO₃ particularly active in undergoing redox reactions and, for this reason, this material is often utilized in electrochemical applications and electrochromic devices [36, 38, 112].

In this work, we combine the use of a crystalline LAO/STO interface with the high reactivity of amorphous WO₃ to realise a high-mobility 2DES in WO₃/LAO/STO heterostructures. The WO₃ overlayers reduce the critical LAO thickness required for the formation of a 2DES. We characterise the transport properties of this system as a function of WO₃ and LAO thickness and find multiple conduction channels with high electron mobility up to 80 000 cm² V⁻¹ s⁻¹. The multichannel conduction leads to a remarkably strong classical magnetoresistance (MR), which reaches 900% at 10 T and 1.5 K. In the low-temperature regime, Shubnikov–de Haas (SdH) oscillations indicate strong two-dimensional confinement of the charge carriers. Our results underscore WO₃ as an efficient extrinsic dopant for oxide interfaces that can be used to engineer novel conductive electron systems.

5.1. STRUCTURAL CHARACTERISATION

Heterostructures of amorphous WO₃ and crystalline LAO are grown on TiO₂-terminated STO (001) substrates by pulsed laser deposition (details on the growth and X-ray diffraction analysis are provided in Figs. 5.6 and 5.7). We use the notation (m, n) to denote the heterostructures consisting of m unit cells (uc) of WO₃ and n uc of LAO. Because WO₃ is amorphous, this corresponds to the crystalline equivalent number of unit cells. To investigate the atomic structure of the WO₃/LAO/STO system, we perform high-angle annular dark-field scanning transmission electron microscopy (HAADF-STEM). The HAADF-STEM images in Figs. 5.1a and 5.1b acquired on a (4, 2) heterostructure show a uniform

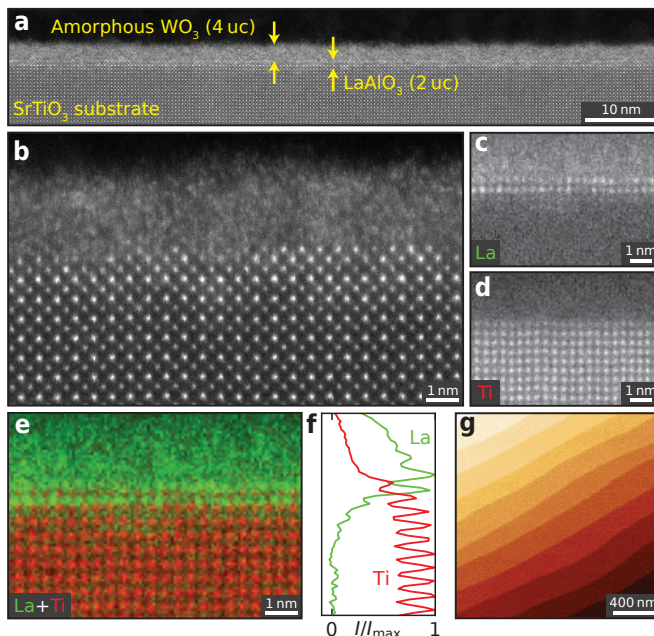


Figure 5.1: **Structural characterisation of $\text{WO}_3/\text{LAO}/\text{STO}$ heterostructures.** (a) Lower magnification and (b) close-up HAADF-STEM image from a (4,2) heterostructure along the (001) direction. (c) EELS elemental map showing normalized core-loss signals for La $M_{4,5}$, (d) Ti $L_{2,3}$ edges and (e) combined signal. (f) Normalised EELS intensity profile averaged in the direction parallel to the interface. (g) Surface topography by AFM.

layer of amorphous WO_3 corresponding to 4 uc thickness, on top of 2 uc crystalline LAO. Because of the difference in the atomic number of La and Sr, the HAADF signal from the LAO is more intense than that of the underlying STO. To further confirm the crystallinity and conformity of the LAO layers, electron energy loss spectroscopy (EELS) is performed. With an energy dispersion of 0.25 eV/channel, the Ti $L_{2,3}$ and La $M_{4,5}$ edges are recorded simultaneously, providing atomic-resolution Ti and La elemental maps as presented in Figs. 5.1c to 5.1e. By averaging the La map parallel to the interface in Fig. 5.1f, two clear peaks are found for La, consistent with the growth of two LAO layers in our heterostructure. The measurements indicate a crystalline LAO/STO interface, with small amount of La interdiffusion into the substrate. However, we observe significant diffusion of La into the WO_3 layer. The surface of all heterostructures is additionally measured by atomic force microscopy (Fig. 5.1g) which reveals the steps and terraces of the underlying STO substrate, indicating uniform film growth.

5.2. INSULATOR-TO-METAL TRANSITION

The series of resistance versus temperature curves of (m, n) heterostructures in Fig. 5.2a shows a sharp thickness-dependent insulator-to-metal transition. The transport measurements are performed in a van der Pauw configuration (see Methods for details). For different (m, n) combinations the samples show either insulating (orange curves)

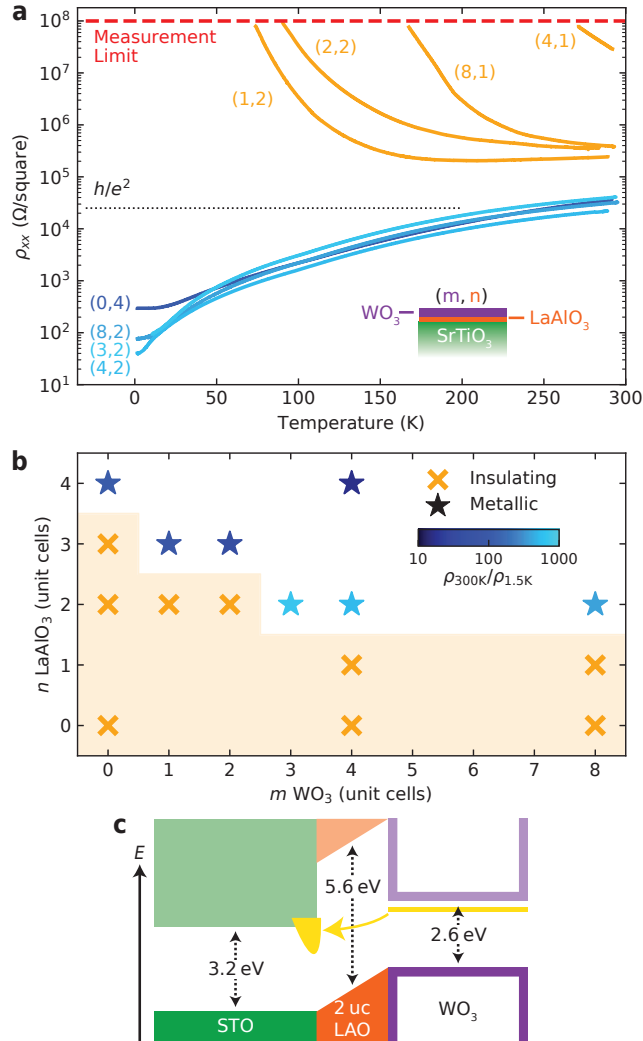


Figure 5.2: **Insulator-to-metal transition in $\text{WO}_3/\text{LAO}/\text{STO}$ heterostructures.** (a) Resistance vs temperature for different (m, n) thickness combinations and (b) transport phase diagram showing insulating (orange crosses) and metallic (stars with colour scale) heterostructures. The colour scale indicates the residual-resistance ratio for the metallic samples, and the orange shaded area marks the (m, n) combinations constituting insulating heterostructures. (c) Schematic of the energy levels alignment for a $(m \geq 3, 2)$ heterostructure. Valence band (solid colours), conduction band (shaded colours) and amorphous WO_3 energy levels. Charge transfer from the oxygen vacancy levels, residing just below WO_3 conduction states, to STO is indicated by the yellow arrow.

or metallic (blue curves) character, with a sharp transition between the two regimes as a function of the layer thickness. This is particularly evident when comparing the (4, 1) and (4, 2) curves, where a variation of a single uc of the LAO interlayer determines a 3 orders

of magnitude difference in room temperature resistivity, which diverges upon cooling. The onset of the metallic state corresponds to the sheet resistance value h/e^2 (dotted line in Fig. 5.2a) which is the quantum limit for metallicity in 2D [149–151], providing strong evidence for the two-dimensional nature of this electronic system.

The interplay between WO_3 and LAO thicknesses is summarised in the phase diagram of Fig. 5.2b, where we indicate the (m, n) combinations resulting in insulating samples with a shaded orange background. For LAO-only films $(0, n)$ we reproduce the critical thickness for metallicity of 4 uc in crystalline LAO/STO interfaces, whereas samples with only WO_3 $(m, 0)$ are always insulating. Heterostructures with 1 uc of LAO $(m, 1)$ are insulating independent of the WO_3 layer thickness. When $n = 2$ the insulating state persists for WO_3 thickness $m \leq 2$ only, above which a metallic state is induced. With three uc of LAO, a single layer of WO_3 is enough to trigger the metallic state.

The main difference between our metallic $\text{WO}_3/\text{LAO}/\text{STO}$ heterostructures compared to typical LAO/STO interfaces manifests itself below 30 K. Although the resistivity curves approximately overlap above 30 K, the resistivity of the WO_3 -doped samples decreases sharply at lower temperatures. To highlight this trend, we compare the metallicity of the conducting heterostructures by evaluating their residual resistivity ratio defined as $\text{RRR} = \rho_{xx}(300\text{K})/\rho_{xx}(1.5\text{K})$. Higher RRR values indicate more pronounced metallic behaviour and are represented by the colour map in Fig. 5.2b. Our reference LAO/STO heterostructure $(0, 4)$ has $\text{RRR} = 110$, which is similar to previous reports [59, 152]. In the $\text{WO}_3/\text{LAO}/\text{STO}$ system, we find higher values for decreasing thickness of the LAO interlayer. As an example, the $(4, 2)$ combination shows $\text{RRR} = 700$.

On the basis of our experimental observations, we propose the mechanism sketched in Fig. 5.2c for the 2DES formation. The nonpolar STO and the amorphous WO_3 have flat energy levels along the direction perpendicular to the interface, whereas the polar field in LAO determines a potential rise of about 1 eV per uc. According to our self-interaction-free density functional calculations [122] in Fig. 5.8 and the following paragraph, oxygen vacancies form donor levels in WO_3 that reside about 0.1 eV below its conduction states. Above a critical LAO thickness, a charge transfer to STO conduction band occurs. Our data shows that the minimum LAO thickness required to observe metallicity is 2 uc and, as a general trend above this value, thinner LAO determines higher RRR. This phenomenon is the balance of two competing effects. On the one hand, a sufficiently thick LAO interlayer is required to provide the electric field necessary for driving charge carriers at the LAO/STO interface [153]. On the other hand, the doping mechanism is enhanced if the WO_3 overlayer is closer to the STO. Within this picture, the optimal LAO thickness for the formation of a conductive state with high RRR is found to be 2 uc. This is in agreement with previous works on STO-based systems, where a polar interlayer was shown to effectively separate the conductive interface from its source of doping, enhancing its metallicity [143].

Insights into the doping mechanism involving oxygen vacancies can be obtained by varying the WO_3 growth conditions. Conductive $\text{WO}_3/\text{LAO}/\text{STO}$ heterostructures are obtained only if WO_3 is deposited at sufficiently low oxygen pressure ($p_{\text{O}_2} < 4 \times 10^{-2}$ mbar), determining oxygen-deficient films [43, 103]. Furthermore, a postannealing treatment in O_2 atmosphere performed on conductive samples turns them insulating (Fig. 5.9). This is a strong indication that oxygen vacancies in the top layers play an important

role in the insulator-to-metal transition in WO₃/LAO/STO heterostructures, where the dopants are in a thermodynamically quenched state [154]. We also note that, although the WO₃ overlayers are amorphous, if their growth is performed at room temperature the resulting heterostructures are insulating. This indicates that the doping mechanism is a thermally-activated process happening during the high-temperature growth of WO₃. In contrast to other STO-based 2DES where the dopant layer lies directly on top of the conductive interface [153, 155], here the crystalline LAO interlayer effectively separates it from the STO, determining a 2DES with high-mobility carriers, as discussed below. With this approach, we are thus able to combine the doping provided by the amorphous overlayer with the advantage of a crystalline conductive interface.

5.3. MAGNETOTRANSPORT

The characteristics of the metallic state in WO₃/LAO/STO are investigated by performing magnetotransport measurements on a (4,2) heterostructure, which has a high RRR value. In Fig. 5.3a we present its magnetoresistance (MR) defined as $MR = \frac{\rho_{xx}(B) - \rho_0}{\rho_0}$, where ρ_0 is the sheet resistance at $B = 0$ and the magnetic field is applied perpendicular to the interface plane. At 1.5 K, the MR is positive and reaches 900% at 10 T, corresponding to 1 order of magnitude increase in sheet resistance. This differs greatly from what is usually observed in LAO/STO heterostructures (0, n) as can be seen from the comparison with a (0,4) sample in Fig. 5.3a. The LAO/STO, in fact, shows a positive MR in the order of 10 % at 10 T, consistent with previous reports [51, 156, 157].

The Hall resistance of the (4,2) heterostructure (Fig. 5.3b) is negative, indicating electron-like transport, with a kink at about 1 T. A nonlinear component in the Hall effect of STO-based systems is typically related to multiple conduction channels contributing to the transport [145, 158–160]. In the two-channel system, the sheet resistance (ρ_{xx}) and the Hall resistance (ρ_{xy}) are given by

$$\rho_{xx} = \frac{(n_I \mu_I + n_{II} \mu_{II}) + (n_I \mu_{II} + n_{II} \mu_I) \mu_I \mu_{II} B^2}{(n_I \mu_I + n_{II} \mu_{II})^2 + (n \mu_I \mu_{II} B)^2} \cdot \frac{1}{e}, \quad (5.1a)$$

$$\rho_{xy} = \frac{(\pm n_I \mu_I^2 \pm n_{II} \mu_{II}^2) + n (\mu_I \mu_{II} B)^2}{(n_I \mu_I + n_{II} \mu_{II})^2 + (n \mu_I \mu_{II} B)^2} \cdot \frac{B}{e}, \quad (5.1b)$$

where n_i , μ_i are the carrier density and mobility of the i -th channel and $n = (\pm n_I \pm n_{II})$, with the \pm sign indicating hole or electron carriers, respectively. The nonlinearity in the Hall effect is well captured after fitting the data to Eq. (5.1b) (dashed line in Fig. 5.3b). The extracted transport parameters are presented in Table 5.1 (see Methods for details). The (4,2) heterostructure presents two channels of electrons: one with lower mobility $\mu_I = 3600 \text{ cm}^2 \text{ V}^{-1} \text{ s}^{-1}$, $n_I = 1.7 \times 10^{13} \text{ cm}^{-2}$ and one with higher mobility $\mu_{II} = 80000 \text{ cm}^2 \text{ V}^{-1} \text{ s}^{-1}$, $n_{II} = 9.3 \times 10^{12} \text{ cm}^{-2}$. Higher mobility values are observed for lower carrier densities, consistently with previous studies of STO-based 2DES [159, 160]. We note that the sheet resistance of the higher mobility channel ρ_{II} is one order of magnitude smaller than ρ_I , indicating that it dominates the low-temperature transport. The (4,2) mobility is about 2 orders of magnitude higher than what was observed in the reference (0,4) sample ($\mu_I = 840 \text{ cm}^2 \text{ V}^{-1} \text{ s}^{-1}$), which is consistent with the higher resistivity at 1.5 K and the lower RRR value usually found in LAO/STO heterostructures.

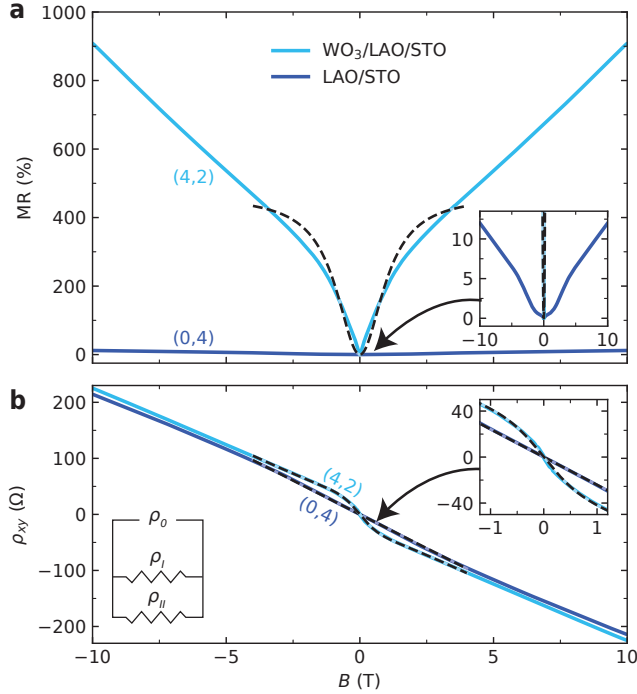


Figure 5.3: **Comparison of $\text{WO}_3/\text{LAO}/\text{STO}$ and LAO/STO magnetotransport.** (a) Magnetoresistance and (b) Hall effect measured at 1.5 K in van der Pauw geometry, with respective zoom-in (insets). The Hall data is fitted (dashed lines) with Eq. (5.1b) and used to extract the values in Table 5.1. The classical MR (dashed line in (a)) is calculated from these values using Eq. (5.1a).

Using n_i , μ_i extracted from the Hall effect, we calculate with Eq. (5.1a) the classical two-channel MR (dashed line in Fig. 5.3a). The resulting curve has the same order of magnitude as that of the measured signal, signalling that the classical component is the dominant MR contribution, in particular for small magnetic fields. The residual MR is much larger than the typical magnitude of quantum correction effects, which are thus negligible in this case. The additional MR signal can be explained considering Boltzmann transport contributions for mixed orbital states [52], or disorder, which can lead to a linear high MR (Fig. 5.11) [161, 162].

Table 5.1: **Transport parameters.** Mobility, carrier density, sheet resistance, and mean free path of the conductive channels extracted from the fits in Fig. 5.3b.

	μ ($\text{cm}^2 \text{V}^{-1} \text{s}^{-1}$)	$n_{2\text{D}}$ (cm^{-2})	ρ_0 (Ω)	λ (nm)
$(4,2)_{\text{II}}$	80 000	9.3×10^{12}	8	4100
$(4,2)_{\text{I}}$	3600	1.7×10^{13}	100	250
$(0,4)_{\text{I}}$	840	2.6×10^{13}	290	70

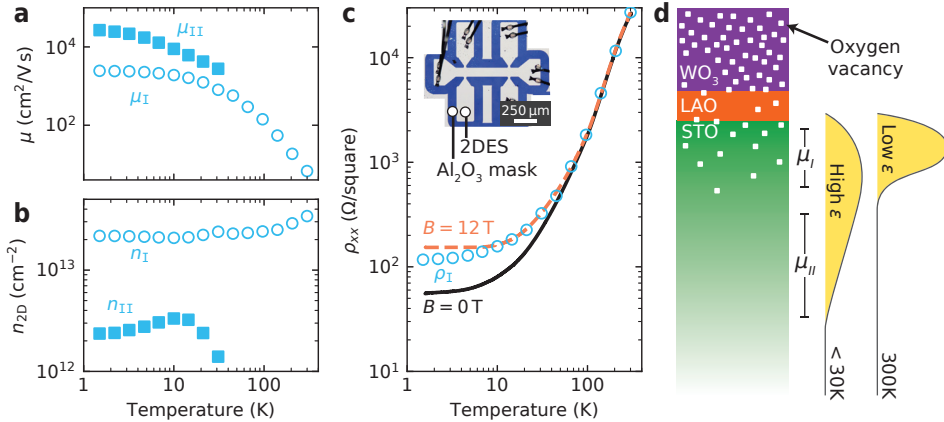


Figure 5.4: **Temperature dependence of the magnetotransport.** (a) Mobility and (b) carrier density as a function of temperature for a (4, 2) $\text{WO}_3/\text{LAO}/\text{STO}$ heterostructure. The parameters for the two channels (squares and circles) are extracted by fitting the Hall effect with Eq. (5.1b). (c) Resistance vs temperature with applied perpendicular magnetic field $B = 0$ and 12 T compared to the resistivity of the lower mobility channel (circles). The inset shows an optical image of a $100\ \mu\text{m} \times 500\ \mu\text{m}$ Hall bar used for electrical characterisation. (d) Proposed mechanism for the formation of two parallel conduction channels in STO below 30 K. The lower mobility Channel I is closer to the defect-rich interface region, while Channel II extends deep in the less-defected material. The temperature-dependent STO dielectric constant ϵ changes the electron charge distribution (indicated in yellow), determining a crossover from multichannel ($T < 30\ \text{K}$) to single channel transport.

5

5.4. TEMPERATURE-DEPENDENT MAGNETOTRANSPORT

Additional insight into the effects of these parallel conduction channels is obtained by tracking them as a function of temperature. The measurements are performed on a (4, 2) heterostructure in a $100\ \mu\text{m} \times 500\ \mu\text{m}$ Hall bar geometry (inset of Fig. 5.4c), as described in the Methods. We observe a nonlinear Hall effect below 30 K, whereas it is linear at higher temperatures (Fig. 5.12). The temperature dependence of mobility and carrier density for the two channels are extracted in Figs. 5.4a and 5.4b. For the higher mobility channel we find that both μ_{II} , n_{II} decrease and then completely disappear above 30 K. The lower mobility Channel I shows an almost temperature-independent carrier density and a mobility decreasing several orders of magnitude upon warming, similar to what previously reported for conventional LAO/STO heterostructures [163]. Interestingly, above 30 K, where the high-mobility electrons disappear, the resistivity curves in Fig. 5.2a overlap with LAO/STO, indicating that Channel II is a peculiar characteristic of $\text{WO}_3/\text{LAO}/\text{STO}$ heterostructures.

The presence of two distinct conduction channels can be explained considering a different spatial confinement of the charge carriers in the STO (Fig. 5.4d). The electrons of Channel I, closer to the LAO layer, experience a stronger polar electric field and a higher concentration of defects, resulting in lower mobility. Channel II, instead, arises from electrons that extend deeper into the substrate, where a less-defected STO determines a higher mobility. In this scenario, the spatial extent of the conductive channels is related to the STO dielectric constant, which drops sharply upon warming, determining the depopulation of Channel II [164] (see also Fig. 5.13). A similar mechanism and tem-

perature dependence have been previously reported for other STO-based heterostructures [159, 160, 165, 166]. This interpretation is further supported by field-effect measurements performed in a back-gate configuration (Fig. 5.14).

We study the effect of a magnetic field on the higher mobility Channel II, and show that it dominates the transport only at small values of B . In Fig. 5.4c we compare the resistivity versus temperature curve measured with $B = 0$ and 12 T applied perpendicular to the interface plane. At 1.5 K the curves are well separated, determining a strong positive MR of 200%. On warming, the MR decreases and the curves overlap. The strong MR in our system can be explained by considering the high mobility of Channel II and the large resistivity ratio of the two channels. In general, classical MR predicts a strong resistivity increase with applied magnetic field whenever the charge carriers possess high mobility. In systems with multiple channels high MR is observed only if the high-mobility channel is dominant in the electronic conduction (i.e., $\rho_{II}/\rho_I \ll 1$). Both conditions are met in $\text{WO}_3/\text{LAO}/\text{STO}$, where we find a direct correlation between the ratio ρ_{II}/ρ_I and the MR magnitude at 10 T: with $\rho_{II}/\rho_I \sim 10^{-1}$ in Fig. 5.3 we measure $\text{MR} \sim 900\%$, and with $\rho_{II}/\rho_I \sim 1$ in Fig. 5.4 we have a lower $\text{MR} \sim 200\%$. A confirmation of this behaviour is given by considering that ρ_I values in Fig. 5.4c well represent the resistivity versus temperature curve at $B = 12$ T. This indicates that the transport response is dominated by the low-mobility channel at high magnetic field.

5.5. QUANTUM OSCILLATIONS OF CONDUCTANCE

The electronic state confined in our (4,2) $\text{WO}_3/\text{LAO}/\text{STO}$ heterostructures shows Shubnikov–de Haas (SdH) oscillations superimposed on the background of strong positive MR. The SdH as a function of temperature are shown in Fig. 5.5a, where their signal was extracted by fitting the background with a third-order polynomial (dashed line in Fig. 5.5b). The oscillations disappear when the magnetic field is applied parallel to the interface plane, as expected for a two-dimensional system. SdH oscillations in 2DESs can be modelled by

$$\Delta\rho_{xx} = 4\rho_c e^{-\alpha T_D} \frac{\alpha T}{\sinh(\alpha T)} \sin\left(2\pi \frac{\omega_{\text{SdH}}}{B}\right), \quad (5.2)$$

where ρ_c is the classical sheet resistance in zero magnetic field, $\alpha = 2\pi^2 k_B/\hbar\omega_c$ with cyclotron frequency $\omega_c = eB/m^*$, Boltzmann constant k_B , reduced Planck's constant \hbar , carrier effective mass m^* and Dingle temperature T_D [167]. Fourier analysis in Fig. 5.5c reveals that the oscillations are periodic in B^{-1} , with a main frequency peak at $\omega_{\text{SdH}} = 50$ T. Assuming a 2DES with circular sections of the Fermi surface, we can estimate the carrier density as $n_{\text{SdH}} = \frac{\nu_s e}{h} \omega_{\text{SdH}}$, where ν_s indicates the spin degeneracy. By considering $\nu_s = 2$ we find $n_{\text{SdH}} = 2.5 \times 10^{12} \text{ cm}^{-2}$.

To extract the mass of the electrons showing the SdH effect, in Fig. 5.5d we track the oscillation amplitude at $B = 11.85$ T as a function of temperature (similar results are obtained using different values of B). Fitting the trend with Eq. (5.2), we find $m^* = 5.6 m_e$. From the Dingle plot in Fig. 5.5e we extract $T_D = 0.45$ K. This value points to an ordered electronic system with sharp Landau levels, considering that their energy smearing $k_B T_D \sim 40 \mu\text{eV}$ is much smaller than their spacing $\hbar\omega_c \sim 250 \mu\text{eV}$. The extracted value

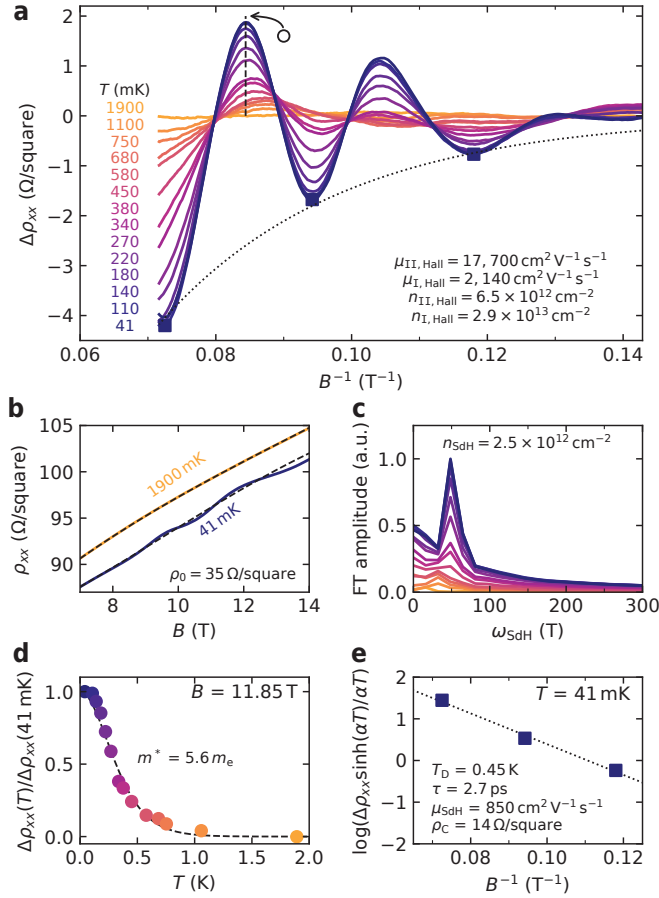


Figure 5.5: **Quantum oscillations of conductance.** (a) Temperature dependence of the SdH oscillations after the removal of a third order polynomial background for a (4,2) WO₃/LAO/STO heterostructure. The dashed and dotted lines indicate the data in (d) and (e), respectively. (b) Raw ρ_{xx} data at two different temperatures showing the fit of the polynomial background (dashed lines). (c) Fourier spectra of the oscillation in the range 7–14 T. (d) Temperature dependence of the oscillation amplitude at $B = 11.85 \text{ T}$ and fit to Eq. (5.2) (dashed line) from which the carrier effective mass m^* is extracted. (e) Dingle plot of the SdH oscillations minima at $T = 41 \text{ mK}$ and fit to Eq. (5.2) (dotted line) from which the Dingle temperature T_D , elastic scattering time τ , mobility μ_{SdH} and the classical sheet resistance ρ_c are extracted.

$\rho_c = 14 \Omega/\text{square}$ is in good agreement with $\rho_0 = 35 \Omega/\text{square}$, corroborating the performed analysis. Using $T_D = \hbar/2\pi k_B \tau$ and $\tau = m^* \mu_{\text{SdH}}/e$ we calculate the elastic scattering time $\tau = 2.7 \text{ ps}$ and the quantum mobility $\mu_{\text{SdH}} = 850 \text{ cm}^2 \text{ V}^{-1} \text{ s}^{-1}$.

It is worth to compare the results of the SdH analysis with the Hall effect measurements (values for this sample in Fig. 5.5a). Although the Hall effect shows the presence of two conduction channels, a single oscillation frequency dominates the SdH signal. We identify the lower mobility Channel I as the source of the observed SdH. This conclusion stems from two considerations: in STO-based materials n_{SdH} is usually about an

order of magnitude smaller than n_{Hall} [168–170], and, similarly, quantum mobility μ_{sdH} is a factor 2–5 smaller than μ_{Hall} [145, 171]. The properties of Channel I fulfil these conditions. This naturally raises the question as to why the higher mobility channel is not visible in the SdH signal. We show in Fig. 5.15 and Table 5.2 that the quantum oscillations of Channel II have low visibility due to its high classical MR, and that this is well explained within the two-channel model. Furthermore, this observation is in agreement with Fig. 5.4c, where we showed that transport at high magnetic field is dominated by the lower mobility channel.

Quite unusual is the effective mass value $m^* = 5.6 m_e$, which is 2–3 times larger than what is typically observed in LAO/STO heterostructures [145, 157]. Possible explanations for this electron mass renormalization are the modified defect profile with respect to conventional LAO/STO interfaces [172], large phonon-drag due to tight spatial electron confinement [173, 174], or strong polaronic effects which have been reported in both LAO/STO interfaces and amorphous WO_3 thin films [175, 176]. Further studies are required to reveal the origin of this phenomenon.

5.6. CONCLUSIONS

To conclude, we have demonstrated that amorphous WO_3 is an effective overlayer to induce an insulator-to-metal transition in $\text{WO}_3/\text{LAO}/\text{STO}$ heterostructures. Reducing the crystalline LAO critical thickness from 4 to 2 uc, the WO_3 overlayer determined a metallic system with large RRR and high electron mobility. We ascribed the appearance of a strong classical magnetoresistance to the large resistivity ratio and high mobility of the multiple conduction channels observed in the system. Quantum oscillations of conductance confirmed the realisation of high-quality $\text{WO}_3/\text{LAO}/\text{STO}$ heterostructures, where a strong two-dimensional confinement of carriers is observed. All of these results are obtained using an amorphous WO_3 overlayer, which does not require crystal matching and could thus be exploited to induce 2DES in other oxide materials.

5.7. METHODS

SAMPLE GROWTH

$\text{WO}_3/\text{LaAlO}_3/\text{SrTiO}_3$ heterostructures were grown by pulsed laser deposition on commercially available 5 mm × 5 mm SrTiO_3 (001) substrates, with TiO_2 surface termination. The laser ablation was performed using a KrF excimer laser (Coherent COMPexPro 205, $\lambda = 248\text{ nm}$) with a 1 Hz repetition rate and 1 J cm^{-2} fluence. The target-substrate distance was fixed at 55 mm. For the LaAlO_3 thin films a crystalline target was employed and the deposition performed at 800 °C substrate temperature and 3×10^{-5} mbar oxygen pressure. LaAlO_3 film thickness was monitored *in situ* during growth by intensity oscillations of reflection high-energy electron diffraction (RHEED). The samples were annealed for 1 h at 600 °C in 300 mbar of O_2 atmosphere to compensate for the possible formation of oxygen vacancies. The amorphous WO_3 thin films were deposited from a WO_3 sintered target at 500 °C substrate temperature and 5×10^{-3} mbar oxygen pressure. WO_3 film thickness was calibrated by depositing crystalline WO_3 on SrTiO_3 and monitoring the growth by RHEED. The thickness value was then confirmed by X-ray diffraction (XRD) and transmission electron microscopy (TEM) measurements (further details in

Chapter 4). At the end of the growth the heterostructures were cooled down to ambient temperature in 5×10^{-3} mbar oxygen pressure (further details in Fig. 5.6).

HALL BAR GEOMETRY FABRICATION

SrTiO_3 substrates were patterned prior to $\text{WO}_3/\text{LaAlO}_3$ thin-film deposition with standard e-beam lithography, followed by the deposition of an insulating Al_2O_3 mask. The mask was deposited at room temperature by radio frequency sputtering in a 5 μbar Ar atmosphere, resulting in amorphous alumina.

ELECTRICAL MEASUREMENTS

The measurements in Figs. 5.2 and 5.3 were carried out in van der Pauw configuration, whereas for the ones in Figs. 5.4 and 5.5 a Hall bar geometry was used. In both measurement configurations, the metallic interface was directly contacted by ultrasonically wire-bonded Al.

NONLINEAR HALL EFFECT FITS

The fits are performed with the least squares method using data in the magnetic field range -4 to 4 T. The constraint $1/\rho_0 = 1/\rho_{\text{I}} + 1/\rho_{\text{II}}$ is applied to the fitting parameters, and ρ_0 is extracted from the $\rho_{xx}(B)$ measurement. With the assumption $1/\rho_i = n_i e \mu_i$, only three free parameters among ρ_i , n_i , μ_i , with $i = \text{I}$ and II , are varied in the fitting procedure.

5.8. SUPPLEMENTARY INFORMATION

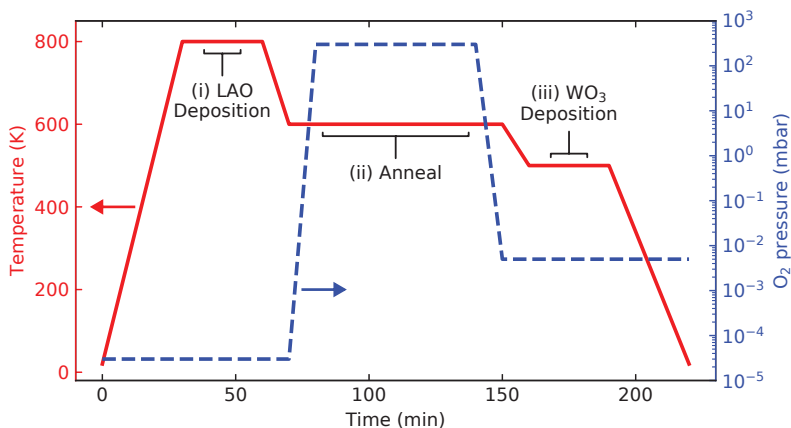


Figure 5.6: **Schematic of the growth conditions.** Cycle of sample temperature and oxygen pressure used for the growth of all the (m, n) heterostructures: (i) heating to 800 °C in 5×10^{-4} mbar followed by possible LaAlO_3 deposition, (ii) post-growth anneal step for 1 h at 600 °C and 300 mbar, (iii) cool-down to 500 °C and 5×10^{-3} mbar followed by possible WO_3 deposition, final cool-down to room temperature. A rate of $20 \text{ }^\circ\text{C min}^{-1}$ was used for all temperature ramps. The $(m, 0)$ and $(0, n)$ samples underwent the same T, p cycle, where the LAO or WO_3 deposition steps were substituted by an idling stage of a few minutes.

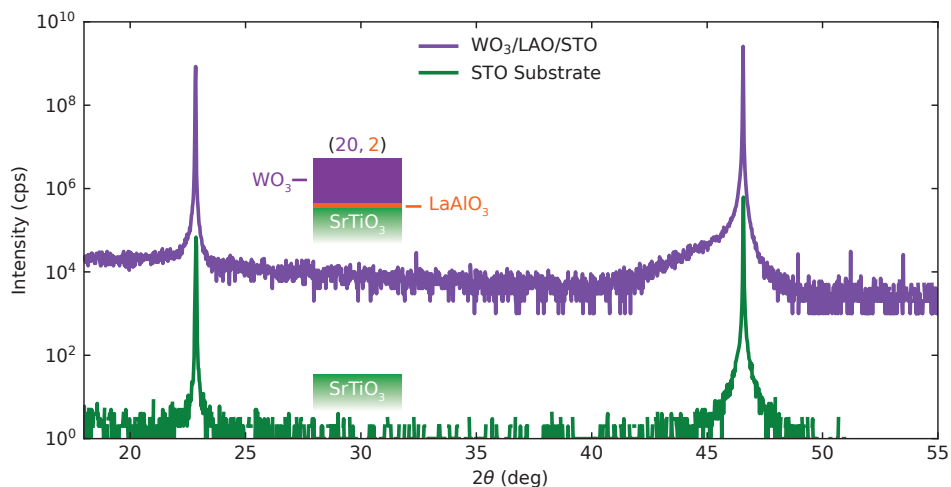


Figure 5.7: **XRD comparison of an STO substrate and a $(20, 2)$ $\text{WO}_3/\text{LAO}/\text{STO}$ heterostructure.** The $\theta-2\theta$ X-ray diffraction scan around the (001) and (002) substrate peak shows no clear diffraction peak coming from the heterostructure, further confirming the amorphous nature of our WO_3 overlayer.

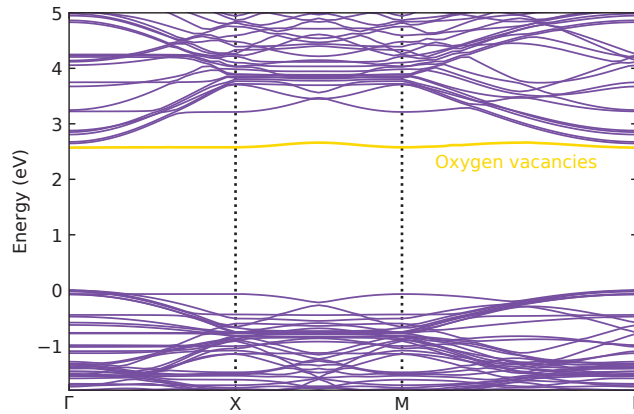


Figure 5.8: **Band structure of bulk WO_3 with oxygen vacancies.** Self-interaction-free density functional theory calculations of a defected WO_3 structure with 2% oxygen vacancies. The computations are performed using plane-waves and ultrasoft pseudopotentials, with cut-off energy of 35 Ryd, and $2 \times 2 \times 4$ supercells with triclinic symmetry and fully relaxed atomic structure. Vacancies are introduced by removing oxygen atoms from WO_2 crystal planes. We find a 2.6 eV band gap for the bulk WO_3 structure. The oxygen-vacant donor sites form energy levels about 0.1 eV below the conduction band bottom. This analysis holds for a crystalline system, but the alignment of these energy levels in our amorphous WO_3 overlayers is likely to be similar. Considering this electronic structure, the electric field provided by the LAO interlayer determines, above the critical thickness of 2 uc, an electron transfer from the oxygen vacancy levels to STO conduction band. This mechanism, discussed in Fig. 5.2c of the main text, is responsible for the formation of a metallic 2DES in $\text{WO}_3/\text{LAO}/\text{STO}$ heterostructures and explains how our experimental results depend on LAO thickness. The dependence on WO_3 thickness, instead, can be explained considering that thicker WO_3 provides a higher number of oxygen-vacant donor states. In this picture, the 2DES forms when the number of carriers overcomes the limit for metallic conductivity in 2D.

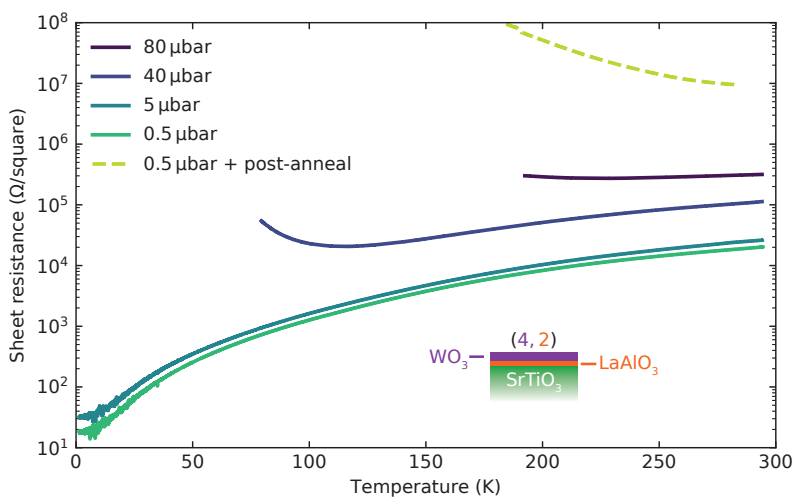


Figure 5.9: **Transport of a (4,2) $\text{WO}_3/\text{LAO}/\text{STO}$ heterostructures where WO_3 is grown in different oxygen pressures.** We measure the metallic trend discussed in the paper only when the WO_3 overlayer is grown in a low oxygen pressure ($p_{\text{O}_2} < 40 \mu\text{bar}$). Furthermore, post-annealing of metallic samples in O_2 atmosphere ($p_{\text{O}_2} = 300 \text{ mbar}$, $T = 500^\circ\text{C}$) turns them insulating (dashed line). This shows the important role of defect formation, such as oxygen vacancies, in the WO_3 overlayer to obtain the high-mobility 2DES at $\text{WO}_3/\text{LAO}/\text{STO}$ heterostructures.

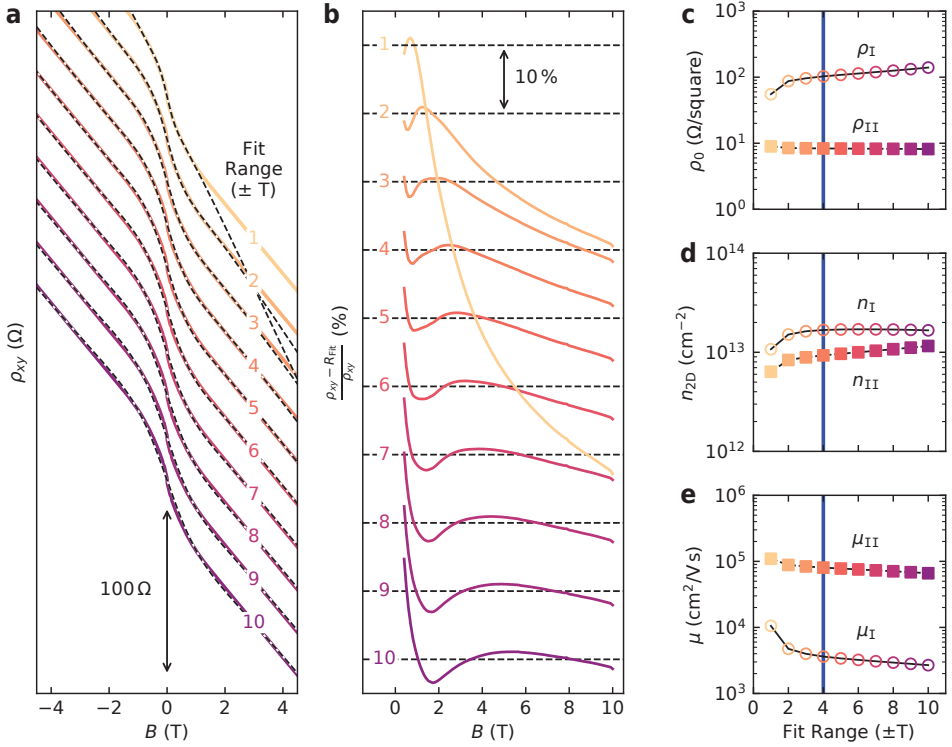


Figure 5.10: Hall effect fits performed on different data ranges. (a) Hall effect measured at 1.5 K on the (4,2) WO_3 /LAO/STO heterostructure of Fig. 5.3 in the main text. The same curve is repeated several times (coloured lines), with vertical offsets of 20Ω . Fits with the two-channel model (Eq. (5.1b) of the main text) are performed in the magnetic field range $-B^* < B < B^*$, where the value of B^* for each curve is indicated by the number in colour. Using the parameters extracted from each fit, the two-channel Hall effect is then calculated for the full data range (dashed lines). (b) Percentage deviation of the calculated curves with respect to the measured data. The curves are vertically offset by 10% and the horizontal dashed lines indicate 0% deviation. For fits with $B^* \leq 3 \text{ T}$ we observe a deviation larger than 10% at high magnetic field. For $B^* \geq 8 \text{ T}$, instead, a deviation larger than 10% is observed in the low-magnetic field range. Based on these observations, we choose the optimal value $B^* = 4 \text{ T}$ to fit the data in the main text because it provides the best fit of the low-field data while guaranteeing a deviation smaller than 10% in the high-field range. (c) Sheet resistance, (d) carrier density and (e) mobility extracted from the two-channel model. The vertical blue line indicates the results for the optimal fit range $B^* = 4 \text{ T}$. We note that the extracted parameters do not have a strong dependence on the choice of B^* . To estimate the reliability of the values extracted by the fits, we consider that for $B^* = 2 \text{ T}$ the high-mobility is $\mu_{\text{II}} = 66000 \text{ cm}^2 \text{ V}^{-1} \text{ s}^{-1}$, and for $B^* = 10 \text{ T}$ is $\mu_{\text{II}} = 88000 \text{ cm}^2 \text{ V}^{-1} \text{ s}^{-1}$. The two values show a discrepancy of about 20%, which provides an indication of the upper limit confidence range of the parameters extracted from the fits. This error is compatible with the observed sample-to-sample variations and does not change the order of magnitude of the extracted values.

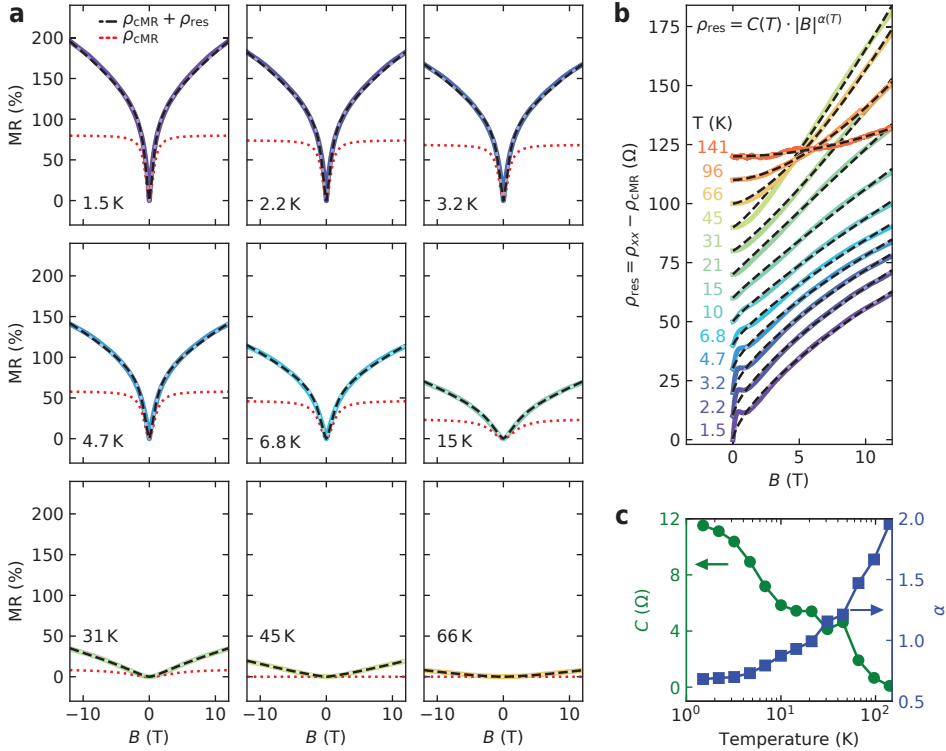


Figure 5.11: **Phenomenological magnetoresistance fits.** (a) Experimental magnetoresistance (solid lines) at different temperatures, classical magnetoresistance ρ_{cMR} (red dotted lines) calculated with Eq. (5.1a) of the main text using the parameters extracted from the Hall effect, and total magnetoresistance (black dashed lines) obtained summing ρ_{cMR} with the fit of the residual magnetoresistance ρ_{res} . (b) Residual magnetoresistance curves (offset for clarity) fitted with a power law function (dashed black lines), and (c) extracted parameters. The fits, performed in the 3–12 T range, represent well the high-field part of the experimental curves. The amplitude factor $C(T)$ shows a decreasing trend as a function of temperature, consistent with the decreasing magnetoresistance effect. The exponent $\alpha(T)$ grows with increasing temperature, and evolves from $\alpha < 1$ (curve of ρ_{res} concave down) to $\alpha > 1$ (concave up) at about 30 K. We note that this temperature corresponds to the crossover from the presence of two to one conduction channels observed in the Hall measurements. In this framework, the power-law dependence of the residual magnetoresistance might be related to spatial inhomogeneities of $n_{2\text{D}}$ and μ , or to disorder.

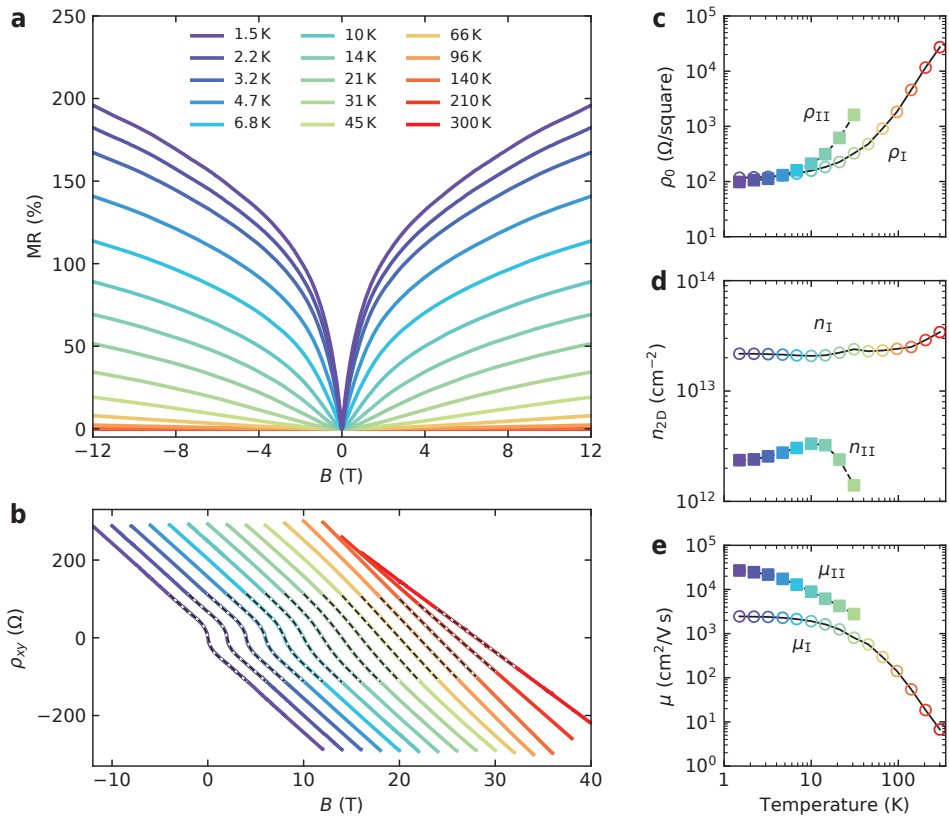


Figure 5.12: **Temperature dependent magnetotransport of a (4,2) $\text{WO}_3/\text{LAO}/\text{STO}$ heterostructure.** (a) Magnetoresistance and (b) Hall effect measured at different temperatures in a Hall bar configuration (curves shifted horizontally by 2 T for clarity). Fits of the Hall curves (dashed lines) allow to extract (c) sheet resistance, (d) carrier density and (e) mobility of the two conduction channels.

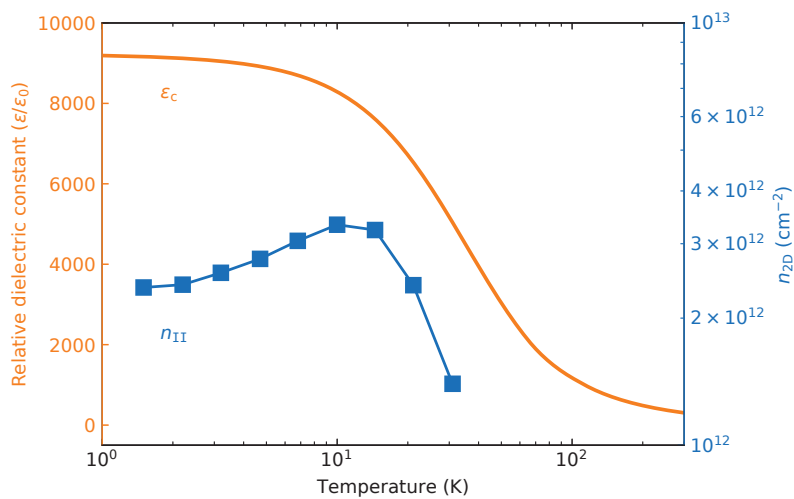


Figure 5.13: **Comparison of STO dielectric constant with high-mobility carrier density.** Temperature dependence of STO relative dielectric constant along the c -axis (orange) from ref. [164] and carrier density of the high mobility channel in the (4,2) $\text{WO}_3/\text{LAO}/\text{STO}$ heterostructure of Fig. 5.4 of the main text. We note that n_{II} decreases sharply and then disappears in the same temperature range where the STO dielectric constant presents a sharp drop. This suggests that the loss of the high-mobility carriers above 30 K is related to a change in the STO dielectric environment.

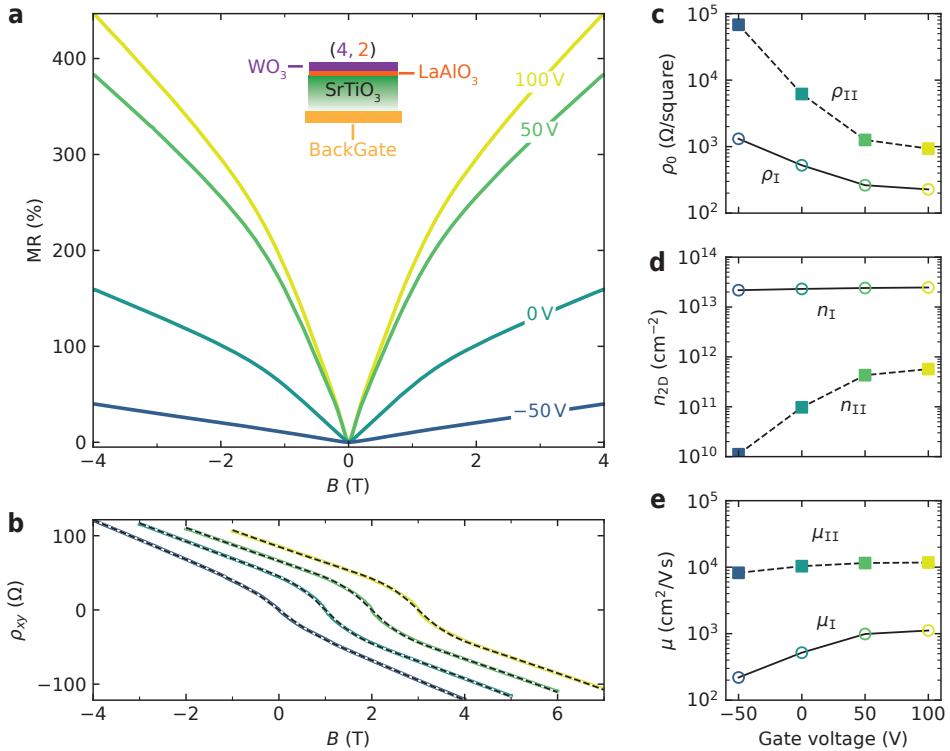


Figure 5.14: **Back-gate modulation of the magnetotransport of a (4,2) heterostructure at 1.5 K.** (a) Magnetoconductance curves showing that a positive gate voltage determines stronger MR signal. (b) Hall effect curves under field-effect (horizontally shifted by 1 T for clarity) fitted with the two-channel model (dashed lines). (c) Sheet resistance, (d) carrier density and (e) mobility of the two electron channels as a function of back-gate voltage extracted from the fits. The measurements are performed on a $100 \mu\text{m} \times 500 \mu\text{m}$ Hall bar device, similar to the one used in Fig. 5.4 of the main text. The sample is glued with silver paint on a homogeneous metallic plate which is used as a back-gate. The back-gate has a strong effect on the carrier density of the higher mobility band, with a negative voltage determining lower n_{II} . Because a negative back-gate voltage enhances the electron gas confinement to the LAO/STO interfacial region, reducing the depth of the electron distribution in the STO substrate, these measurements support our interpretation of a different spatial confinement of the two conduction channels given in Fig. 5.4 of the main text.

5.8.1. SDH OSCILLATIONS WITH TWO-CHANNEL MAGNETORESISTANCE

While the Hall data indicates the presence of two parallel conduction channels, SdH measurements present only one oscillatory signal. Here we show that this apparent discrepancy is well explained in the framework of the two-channel model. In Fig. 5.15a we compare the experimental SdH data at 41 mK with the one calculated with the expression

$$\Delta\rho_{\text{SdH}} = 4\rho_{\text{c}}e^{-\alpha T_{\text{D}}} \frac{\alpha T}{\sinh(\alpha T)} \sin\left(2\pi \frac{\omega_{\text{SdH}}}{B}\right), \quad (5.3)$$

using the experimental parameters from Fig. 5.5 of the main text. We note that the subtraction of the MR background is crucial in order to extract a clear oscillatory component. The agreement between the calculated curve and the experimental data above 8 T indicates that, despite the strong MR background, the procedure used in Fig. 5.5 of the main text provides the correct representation of the experimental SdH signal.

In the presence of multiple conduction channels, ρ_{xx} is given by the combination of the contributions of both the classical MR and the SdH. Here, we derive an expression for the total ρ_{xx} in the case of transport dominated by multiple channels with SdH oscillations. In the presence of SdH, the single channel resistivity tensor in 2D for electron carriers is

$$\underline{\rho} = \begin{pmatrix} \rho_0 + \Delta\rho_{\text{SdH}} & \rho_0\mu B \\ -\rho_0\mu B & \rho_0 + \Delta\rho_{\text{SdH}} \end{pmatrix}. \quad (5.4)$$

Considering that $\underline{\sigma} = \underline{\rho}^{-1}$, the expression for the conductance tensor is

$$\underline{\sigma} = \frac{1}{(\rho_0 + \Delta\rho_{\text{SdH}})^2 + (\rho_0\mu B)^2} \begin{pmatrix} \rho_0 + \Delta\rho_{\text{SdH}} & -\rho_0\mu B \\ \rho_0\mu B & \rho_0 + \Delta\rho_{\text{SdH}} \end{pmatrix}. \quad (5.5)$$

In the case of two (or multiple) parallel conduction channels, the total conductance is given by $\sigma_{\text{tot}} = \sum_i \sigma_i$, that is the sum of Eq. (5.5) for each channel. Inverting the last expression, it is possible to obtain the total two-channel resistivity tensor $\underline{\rho}_{\text{tot}}$. The xx component of this tensor is measured by low-temperature transport, and shows the experimental SdH oscillations. Because the analytic expression of $[\underline{\rho}_{\text{tot}}]_{xx}$ is quite cumbersome, we limit ourselves to compute it numerically.

In Fig. 5.15b we show the experimental ρ_{xx} with the strong MR background (black curve). Using Eq. (5.5), we calculate ρ_{xx} by associating the SdH contribution to either Channel I or to Channel II, independently. When the SdH are on Channel I (orange curve in Fig. 5.15b), the total MR shows oscillations that resemble the experimental curve. When, instead, the SdH are associated to Channel II (green curve), the MR shows a flat trend at high field, without detectable oscillations. Because of its strong classical MR, in fact, Channel II is mostly suppressed in the high-field regime so that its SdH do not appear. This is better seen considering that the factor $\rho_0\mu B$ in the denominator of Eq. (5.5) dominates over $\Delta\rho_{\text{SdH}}$ for high values of electron mobility. This corroborates our association of the experimentally observed SdH with the lower mobility Channel I.

We now discuss how the presence of two different SdH signals (i.e. for Channel I and II) would appear in ρ_{xx} measurements. For this purpose, we consider in Table 5.2 the transport parameters obtained by Hall (Channels I and II) and SdH measurements (Channel I), and calculate the ratio between the experimental parameters for Channel

Table 5.2: **Transport parameters from Hall and SdH measurements.** The Hall data for Channels I and II is extracted fitting the two-channel Hall effect on the experimental data of the sample in Fig. 5.5 of the main text (Hall effect not shown). The parameters extracted from the SdH measurements in Fig. 5.5 are assigned to Channel I, assuming $\rho_0 \sim \rho_c$. The ratio of the transport parameters extracted from the Hall and SdH measurements is then computed for Channel I. The same ratios are assumed to be valid also for Channel II, and are used to calculate the expected SdH parameters for Channel II (last column, data in gray).

	Channel I			Channel II	
	Hall	SdH	Ratio (Hall/SdH)	Hall	SdH
n (cm ⁻²)	2.90E+13	2.50E+12	11.6	6.50E+12	5.60E+11
μ (cm ² V ⁻¹ s ⁻¹)	2140	850	2.5	17700	7030
ρ_0 (Ω /square)	101	14	7.2	55	8

I. As discussed in the main text, the Hall parameters set a higher bound for the SdH parameters, which usually have a smaller value, as evidenced by the calculated ratios. Assuming the same ratios are valid also for Channel II, we calculate the SdH parameters expected for Channel II (Table 5.2). At very low temperatures ($T \rightarrow 0$), Eq. (5.2) reduces to the expression

$$\Delta\rho_{\text{SdH}} \sim 4\rho_c e^{-\pi/B\mu_{\text{SdH}}} \sin\left(2\pi \frac{\omega_{\text{SdH}}}{B}\right), \quad (5.6)$$

which is independent from the value of the effective mass m^* . In this regime, a very sensitive parameter is the classical sheet resistance in zero magnetic field ρ_c , which determines the scaling of the SdH signal. Because our SdH parameters for Channel II are only an estimation, in Fig. 5.15c we plot the oscillations using the parameters in Table 5.2 and several values of ρ_c . This provides an indication of the sensitivity of our analysis to the choice of SdH parameters for Channel II. Figure 5.15d shows the total ρ_{xx} , which includes the SdH contributions of both conduction channels. Just a small difference is observed between the orange and grey curves above 8 T, confirming that the oscillatory signal is dominated by the SdH of Channel II, independently of the value chosen for ρ_c .

To conclude, our analysis shows that the SdH signal of the high-mobility carriers is suppressed by the high classical MR, consistent with our experimental SdH measurements that show a single oscillatory signal.

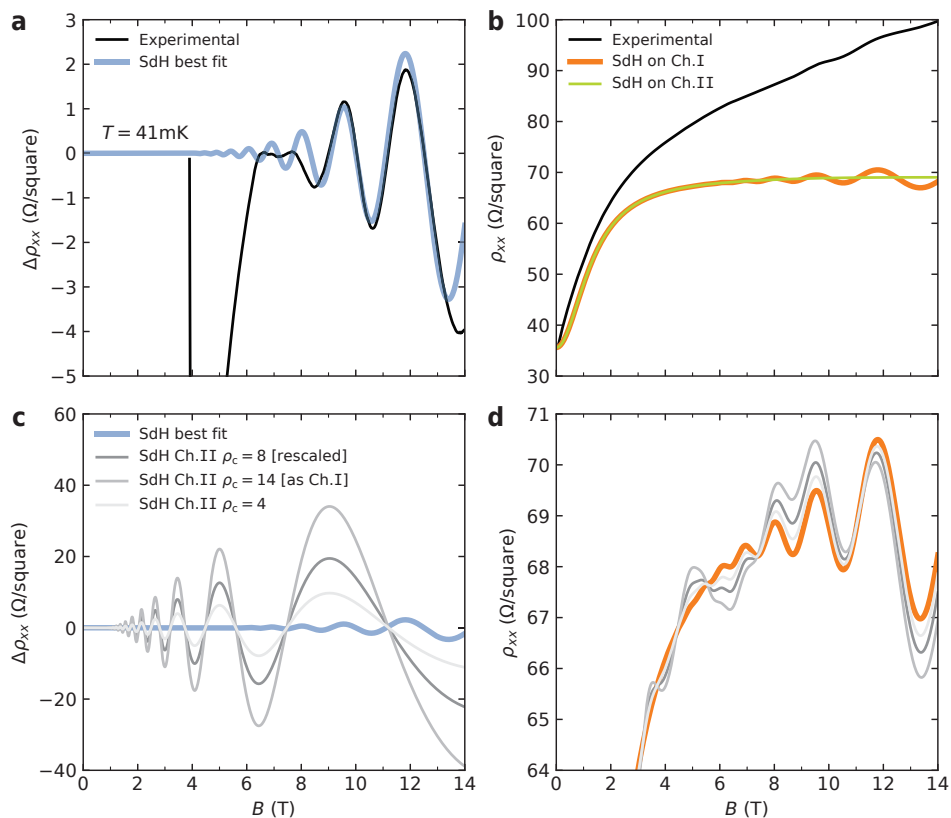


Figure 5.15: **Calculated Shubnikov-de Haas oscillations with two-channel magnetoresistance at 41 mK.** (a) Experimental oscillatory component of ρ_{xx} (black curve) and its best fit (blue curve) calculated with Eq. (5.2) using the parameters from Fig. 5.5 of the main text. (b) Experimental ρ_{xx} prior to the removal of the MR background (black curve). Using the two-channel model with SdH oscillations discussed in the following section, we calculate the total ρ_{xx} adding the SdH contribution to Channel I only (orange curve), or to Channel II only (green curve). (c) Single channel SdH oscillatory components calculated with Eq. (5.2) and the parameters in Table 5.2. (d) Total ρ_{xx} calculated with Eq. (5.5) summing the SdH contributions of both Channels I and II.

6

HYDROGEN SENSING WITH HETEROEPITAXIAL WO_3

Hydrogen-related technologies are rapidly developing, driven by the necessity of efficient and high-density energy storage. This poses new challenges to the sensing of dangerous gases, in particular the realisation of cheap, sensitive and fast sensors is a crucial requirement for the upcoming hydrogen-based economy. While several materials are being studied for such applications, most devices have critical bottlenecks, such as complex fabrication procedures, high operational temperature, slow response time or low sensitivity. Here, we demonstrate hydrogen sensing with single-crystal WO_3 ultra-thin films. The long range crystal order together with the high surface-to-volume ratio make our material an ideal candidate for hydrogen sensing, showing detection limits down to 1 ppm near room temperature, response times as low as 1 s and high reproducibility. We successfully model hydrogen intercalation and deintercalation dynamics by means of coupled rate equations, and extract the associated energy barriers. Our results demonstrate the potential of crystalline WO_3 thin films for hydrogen sensing within a simple but powerful theoretical background of incorporation dynamics.

Parts of this chapter have been submitted for peer review (2017), by G. Mattoni, B. de Jong, N. Manca, M. Tomellini, and A. D. Caviglia.

COMPLEX oxides are a class of materials whose properties can be tuned by several external parameters, such as heteroepitaxial strain [177], electrostatic doping [50, 178], intercalation of other species [179], or oxygen vacancies [140, 180, 181]. This versatility recently triggered a broad technological interest, which goes from the use in oxide-based fuel cells [182, 183], memristive systems [184–186], neuromorphic architectures [187, 188], chemical actuators [189], and gas sensors [190]. In this framework, sensing of hydrogen is an application of raising importance, linked to the growing demand of H_2 gas as energy carrier and for chemical reactions, and the safety concerns originating from that [191, 192]. Several complex oxide materials have been employed for resistive hydrogen sensing, with TiO_2 , SnO_2 , VO_2 and WO_3 being among the most prominent ones [37, 193–195]. WO_3 , in particular, is regarded as a very promising candidate because incorporation of hydrogen changes its electrical resistance by several orders of magnitude [104, 196]. Hydrogen sensing has been demonstrated with various forms of WO_3 , such as amorphous layers and nanostructured materials [197–200]. These sensors, however, usually suffer from high operational temperature, resulting in high-power consumption and poor long-term stability, together with a sensitivity limited to hydrogen concentrations of tens of ppm.

In this work we show that single crystal WO_3 ultra-thin films can detect ultra-low H_2 concentrations down to 1 ppm, with a fast response time, while working at or nearby room temperature. Hydrogen intercalation in WO_3 crystal lattice is a fully reversible process, determining more than 5 orders of magnitude changes in the electrical resistivity. Response time and sensitivity can be tuned with temperature, and improve by one order of magnitude from 25 °C to 65 °C. We study the hydrogen dynamics by modelling the intercalation and deintercalation processes with a series of coupled rate equations, and extract the characteristic energy scales related to H_2 dissociation, incorporation and recombination phenomena. We also demonstrate that hydrogen doping is a powerful control parameter to modulate WO_3 physical state, which can be stabilised in kinetically-arrested configurations just below room temperature. Our results show that WO_3 ultra-thin films are ideal candidates for next-generation sensing devices, combining high sensitivity, fast response time and device scalability.

6.1. MATERIAL PREPARATION

We grow a 24 unit cell (uc) crystalline WO_3 film on a SrTiO_3 (001) substrate by pulsed laser deposition (growth details in Methods and [103]). The WO_3 structural properties are investigated by X-ray diffraction (XRD) and presented in Fig. 6.1a, where finite size oscillations indicate high crystal quality and confirms the expected film thickness of 9 nm. The reciprocal space map in Fig. 6.1b shows that the material is a single crystal, coherently oriented to the substrate lattice. Surface topography, investigated by atomic force microscopy (AFM) in Fig. 6.1c, shows a step and terrace structure which mimics the underlying substrate morphology. The hydrogen reaction is made possible by the presence of a catalyst, whose function is to facilitate the splitting of H_2 molecules into atomic hydrogen, which then enters WO_3 lattice. For this purpose, we use platinum, which has the advantage of a high catalytic efficiency together with a low reactivity with oxide materials [45, 46]. A Pt layer having nominal thickness of 1 nm is deposited at

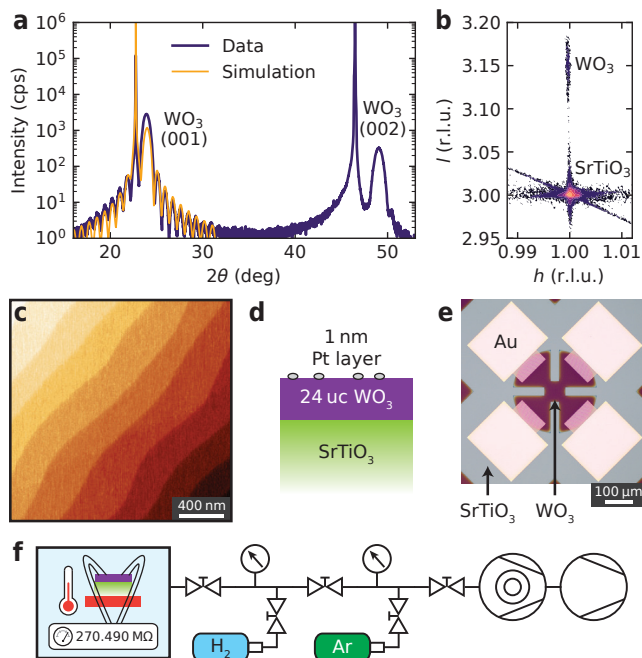


Figure 6.1: **Characterisation of WO₃ thin films.** (a) θ - 2θ X-ray diffraction scan showing the (001) and (002) peaks of the WO₃ thin film with finite size oscillations around the sharp peaks of the SrTiO₃ substrate. By simulating the experimental data with a kinematic scattering model, we extract a film c -axis of 3.71 Å and a thickness of 24 uc. (b) Reciprocal space map around the (103) peak of the substrate showing the WO₃ peak (top) aligned with the more intense SrTiO₃ peak (bottom). (c) Atomic force microscopy of the WO₃ surface. (d) Schematic of the WO₃/SrTiO₃ heterostructure after the evaporation of the Pt catalyst. (e) Optical image of the WO₃ sample patterned in Van der Pauw geometry (for better contrast, the image is taken before the removal of the resist). (f) Schematic of the experimental setup.

room temperature by evaporation in vacuum (Fig. 6.1d). Deposition of this low amount of material is expected to form sparse droplets of a few nanometres. Although we do not detect these droplets in our AFM measurements, their catalytic activity is confirmed by the data discussed in the following section. Electrical measurements are performed on devices patterned in van der Pauw configuration, as shown in the optical image of Fig. 6.1e (details in Methods). The experimental setup is sketched in Fig. 6.1f, where the sample in a vacuum chamber (base pressure $p < 1 \times 10^{-4}$ mbar), which is placed in a dark environment. Mixtures of H₂ in argon carrying gas, with concentration ranging from pure hydrogen down to $C_{\text{H}_2} = 1$ ppm at 1 bar, are prepared in a mixing chamber before exposing the sample.

6.2. WO₃ RESPONSE TO HYDROGEN

The electrical resistance of the pristine sample measured at room temperature is $R = 400$ MΩ, corresponding to a resistivity of about 400 Ω cm, consistent with previous reports of high quality WO₃ thin films grown in optimal oxygen pressure [103]. In Fig. 6.2

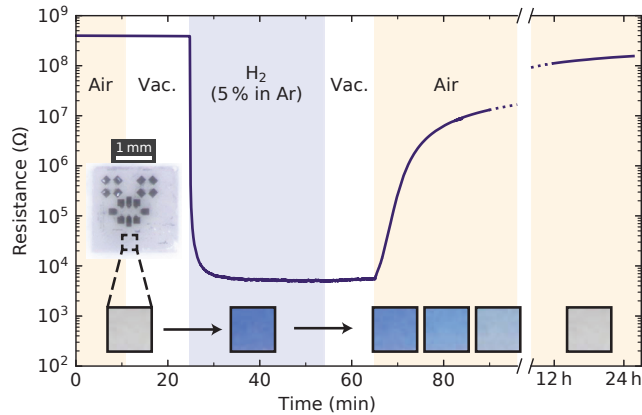


Figure 6.2: **Electrical and optical changes with hydrogen gas.** The WO_3 thin film is exposed to different gas at 1 bar pressure and to vacuum ($p < 1 \times 10^{-4}$ mbar) as indicated by the labels. Both electrical resistance and sample colour (photographs) change upon exposure to H_2 , and recover their initial state once in air.

we show that, upon room temperature exposure to a high hydrogen concentration ($C_{\text{H}_2} = 5\%$ in 1 bar), R drops by 5 orders of magnitude, and after a few minutes it saturates to a constant value. When the sample chamber is evacuated, the resistance shows no significant variation, indicating that hydrogen doping is thermodynamically stable. As shown in Fig. 6.2, if the doped sample is exposed to air the electrical resistance increases over time, recovering more than 3 orders of magnitude in the first 10 min, and reaching the initial state after several hours.

During the electrical measurement, we took a series of photographs of an unpatterned WO_3 region that is shown in Fig. 6.2 below the resistance curves, at the corresponding time. Exposure to hydrogen determines a change of WO_3 optical properties, which acquires a blue colouration in high-doping conditions, and then goes back to its initial transparency when the resistance recovers its original value. This colour change is a well-known effect of hydrogen doping in WO_3 [198, 201, 202]. Both the resistance and optical data indicate that the measured changes in the sample properties are due to hydrogen intercalation and deintercalation into the WO_3 lattice [203]. Moreover, the doping is a reversible process, and the deintercalation is facilitated by the presence of air.

Although a precise description of the doping mechanism is still a matter of debate, several reports show that incorporation of atomic hydrogen in WO_3 determines electron doping [196, 204, 205]. In this picture, the Pt catalyst plays a primary role, as without it no intercalation occurs and the resistance stays constant (Fig. 6.6). The influence of the carrier gas on hydrogen intercalation is discussed in Fig. 6.7. The Ar gas has no direct effect, and the use of other carrier gases, such as He or N_2 , produces results similar to what reported in Fig. 6.2. A different response is observed when the carrier gas is air, since in that case the intercalation has a slower rate. We ascribe this difference to the presence of O_2 molecules that can react with the split H atoms to form water, reducing the amount of hydrogen entering WO_3 crystal lattice [203]. The rate of the deintercalation process

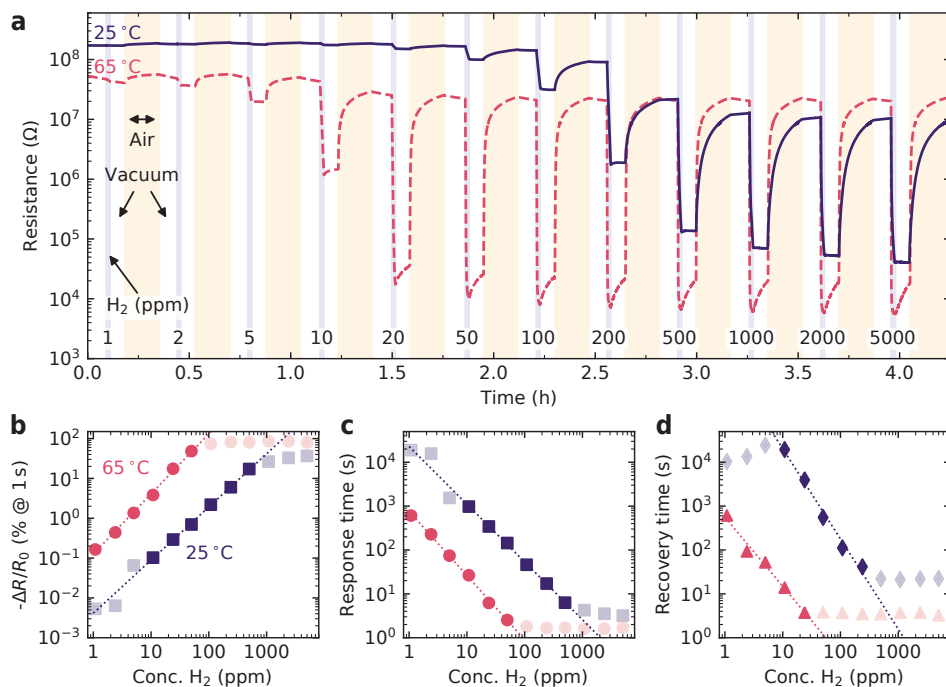


Figure 6.3: **Resistive sensing of different hydrogen concentrations.** (a) Resistance variation upon 1 min exposure to different concentrations of H₂ gas in Ar (1 bar total pressure), followed by recovery in air. The curves are measured at a sample temperature of 25 °C (solid blue) and 65 °C (dashed red). Between the different exposures, the sample chamber is evacuated to $p < 1 \times 10^{-4}$ mbar for about 5 min. (b) Percentage resistive variation 1 s after the exposure to H₂ and (c) corresponding exponential response time τ . (d) Recovery time upon exposure to air. The dotted lines are linear fits to the solid markers, while the greyed out data points are either below the sensor sensitivity (low ppm) or in its saturation regime (high ppm).

is quite slow in vacuum or inert gas atmosphere, but it is significantly enhanced in the presence of O₂ molecules in the gas phase (further details in Fig. 6.8).

6.3. HYDROGEN SENSING

The strong and fast response of heteroepitaxial WO₃ thin films to hydrogen makes them interesting candidates to develop H₂ gas sensors. A good sensor requires high sensitivity, fast response time and a direct relationship between hydrogen concentration and its output signal. For this purpose, we characterised WO₃ resistive changes for different C_{H₂} as reported in Fig. 6.3a. The measurements were performed with the following experimental procedure: (i) sample chamber evacuation ($p < 1 \times 10^{-4}$ mbar), (ii) exposure to the H₂/Ar mixture at 1 bar for 1 min, (iii) chamber evacuation, (iv) exposure to air at 1 bar for 10 min. This procedure is repeated for different hydrogen concentrations in the range 1–4000 ppm and for two sample temperatures, namely 25 °C and 65 °C. Initially, the resistance drop ΔR is small, and it becomes progressively larger upon increasing

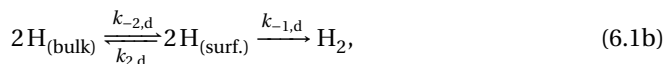
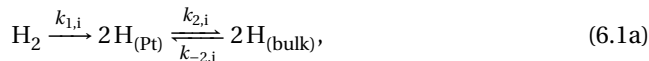
C_{H_2} . At the highest concentrations, ΔR gets almost independent of C_{H_2} indicating a saturation regime. Upon exposure to air, the resistance recovers towards the initial value. Raising the temperature determines a faster response, without affecting the overall sample behaviour.

We quantitatively evaluate the performance of WO₃ as hydrogen sensor by considering the relative resistance change $\frac{\Delta R}{R_0}$ after 1 s from the introduction of H₂ gas. This analysis is reported in Fig. 6.3b, where we show that at intermediate concentrations (solid markers) the response depends on C_{H_2} according to the power law $\Delta R/R_0 \sim (C_{\text{H}_2})^\alpha$. We find $\alpha = 1.33$ at 25 °C, and $\alpha = 1.51$ at 65 °C, indicating that akin laws regulate the trend at both temperatures. The onset of the saturating response of the WO₃ device depends on its operational temperature. At 25 °C the response follows the power law in the range 10–1000 ppm, while at 65 °C this window is shifted to lower concentrations 1–100 ppm. This indicates that by increasing the sensor temperature of a few tens of degrees, it is possible to enhance its detection limit by 1 order of magnitude or, similarly, that the detection limits can be tuned by controlling the sample temperature.

To evaluate the response time of WO₃, we consider a simplified model describing the time-dependent resistance change as $\Delta R/R_0 \sim e^{-t/\tau}$, where the response time τ is the fitting parameter. We find decreasing τ values for higher concentration and temperature, reaching $\tau = 1$ s for $C_{\text{H}_2} = 100$ ppm at 65 °C (Fig. 6.3c). We note that, independently from the value of τ and in the whole range of explored parameters, the presence of hydrogen was always detected within the 1 min time frame used in the experiments. Figure 6.3d shows the recovery time of doped WO₃ after exposing the device to air. Again, lower τ is measured at higher temperature and higher initial hydrogen concentration in WO₃. In all cases, most of the pristine resistivity is recovered after 10 min. Finally, we note that the sensor response is independent from the initial resistance value R_0 (Fig. 6.10), meaning that in the explored range of parameters WO₃ works as a differential sensor, with a response depending only on C_{H_2} and not on the material doping state. Also, we show in Fig. 6.9 that the sensor preserves its functionality in pure, low-pressure H₂ (i.e., without the carrier gas). These characteristics make WO₃ an ideal material for H₂ sensing that can be exploited in a large variety of environments.

6.4. KINETIC MODEL

To obtain insight into the reactions responsible for the doping of WO₃ thin films, we study the intercalation and deintercalation kinetics in a controlled atmosphere. For this purpose, we consider the simple model of two-step reactions schematically illustrated in Fig. 6.4a, where each step is described by a rate constant k_a , and its reverse by k_{-a} . We model the intercalation and deintercalation processes, respectively, with the balance equations



where $\text{H}_{(\text{Pt})}$ indicates a hydrogen atom on a catalyst site, $\text{H}_{(\text{surf.})}$ anywhere on WO₃ or Pt surface, and $\text{H}_{(\text{bulk})}$ intercalated in the WO₃ lattice. Our model describes the inter-

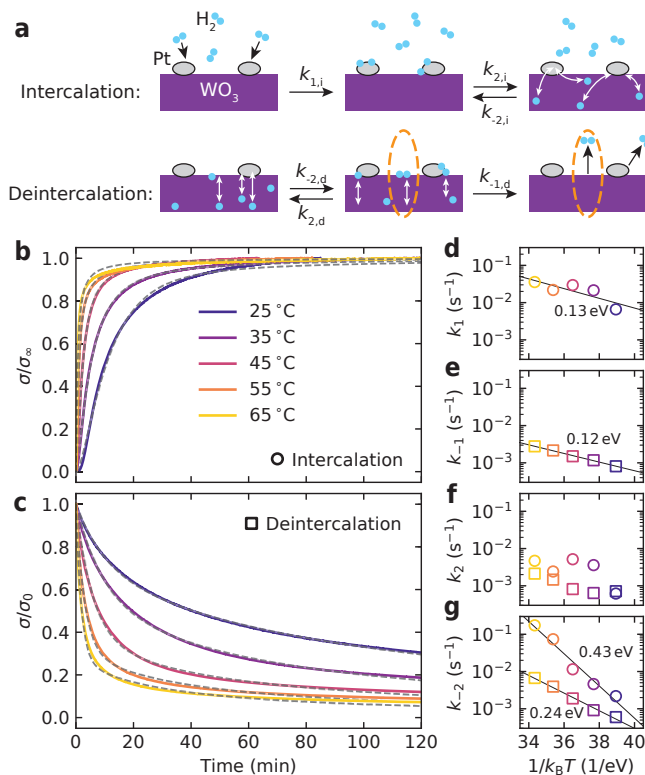


Figure 6.4: **Kinetics of hydrogen intercalation and deintercalation.** (a) Schematics of the processes involved in H₂ exchange with WO₃. The rate constants associated with each process are indicated on the relative reaction arrow. Intercalation: H₂ molecules adsorption on Pt from the gas atmosphere, splitting of H₂ and spillover of atomic H to the film, diffusion in the WO₃ lattice. Deintercalation: diffusion of H atoms in WO₃ towards its surface (vacuum atmosphere), recombination to form H₂ gas that happens both on Pt and on WO₃ surface (highlighted by the orange dashed lines), H₂ desorption and evacuation. (b) Experimental curves of intercalation in a low-pressure mixture of 1 mbar H₂ and 4 mbar Ar. (c) Deintercalation curves (vacuum atmosphere) at different temperatures. The conductance is divided by its final (σ_∞) or initial (σ_0) value for intercalation and deintercalation curves, respectively. Dashed lines are fits obtained from numerical solutions of Eqs. (6.1a) and (6.1b). Rate constants extracted from the fits (circles for intercalation, squares for deintercalation): (d) k_1 adsorption and (e) k_{-1} desorption of H₂, (f) k_2 intercalation and (g) k_{-2} deintercalation of hydrogen in WO₃ crystal lattice. The solid lines are Arrhenius fits used to extract the activation energy of the processes.

calation and deintercalation considering different initial conditions. The intercalation starts with undoped WO₃ and an infinite reservoir of H₂ in gas phase, allowing to consider the dissociative adsorption of H₂ on Pt as an irreversible process ($k_{1,i}$). The subsequent hydrogen exchange between WO₃ surface and WO₃ bulk is an equilibrium reaction, regulated by rate constants $k_{2,i}$ and $k_{-2,i}$. The deintercalation, instead, is modelled considering an initial condition where WO₃ is in a saturated-doping state, in vacuum atmosphere. Hydrogen atoms in the crystal lattice migrate towards and from the surface (rate constants $k_{-2,d}$ and $k_{2,d}$) where they can recombine to form H₂. This step is different from the intercalation process, because hydrogen recombination is a spontaneous

reaction that does not require a catalyst, and thus H₂ molecules can form anywhere on WO₃ surface. Subsequently, hydrogen molecules desorb and are pumped away in an irreversible process ($k_{-1,d}$).

Hydrogen intercalation is experimentally studied starting from an undoped, low-conductance state. In Fig. 6.4b, we show intercalation curves performed in a 5 mbar gas mixture with $C_{H_2} = 20\%$ at different sample temperatures. Higher temperatures determine faster intercalation, with the conductance reaching a saturation value after a few tens of minutes. The deintercalation process in Fig. 6.4c, instead, is studied starting with WO₃ in a high-conductance state. At the beginning of the measurement, WO₃ is exposed to a vacuum atmosphere and the conductance decreases over time, with a faster rate at higher temperatures. We note that in vacuum the deintercalation process is much slower than in air, so that the curves do not reach full saturation in the duration of the experiment (2 h), in agreement with our interpretation of the role played by oxygen in accelerating the desorption process (Fig. 6.8).

The kinetic equations associated with the reactions in Eqs. (6.1a) and (6.1b) (derivation in Section 6.8.1) are solved numerically and used to fit the experimental data (dashed lines in Figs. 6.4b and 6.4c). Our model shows good agreement with the measurements and allows to extract the rate constants of the different processes (Figs. 6.4d to 6.4g). We find that k_1 is, at all temperatures, an order of magnitude larger than k_{-1} , signalling a faster rate of H₂ splitting compared to its recombination. This difference supports our assumption of an irreversible reaction, since with $k_{-1} \ll k_1$ the recombination is negligible in the intercalation process, while it occurs in the deintercalation process because the vacuum atmosphere prevents the splitting reaction, carrying away the H₂ molecules once recombined. We fit the temperature dependence of the rate constants with an Arrhenius model, finding activation energies of 0.13 eV for k_1 and 0.12 eV for k_{-1} . These results can be compared with *ab initio* computations that find activation energies in the range 0.06–0.42 eV for the dissociative chemisorption on Pt surfaces, with lower values expected for smaller particles [206, 207]. Similarly, recombinative desorption at oxide surfaces entails activation energies in the range 0.05–0.9 eV, which depend on the hydrogen binding energy at the adsorption site [208].

The surface-to-bulk diffusion rate constant k_2 has a weak temperature dependence (Fig. 6.4f). The bulk-to-surface rate k_{-2} in Fig. 6.4g, instead, shows a linear trend which allows to extract activation energies of 0.43 eV and 0.24 eV for intercalation and deintercalation, respectively. The higher activation energy required during intercalation can be explained considering that hydrogen splitting can only happen on the catalyst particles, so that the hydrogen atoms have to overcome two energy barriers: the diffusion on WO₃ surface and then the diffusion in WO₃ bulk. During deintercalation, instead, k_{-2} is only related to the hydrogen diffusion in WO₃ bulk, because recombination can happen anywhere on WO₃ surface. Previous experimental and density functional theory calculations reported energy barriers in the range 0.26–0.37 eV for hydrogen migration from the Pt sites to WO₃ surface [209, 210], which are compatible with our experimental findings. This analysis shows that both intercalation and deintercalation are thermally activated processes, so that their rates can be controlled changing the sample temperature.

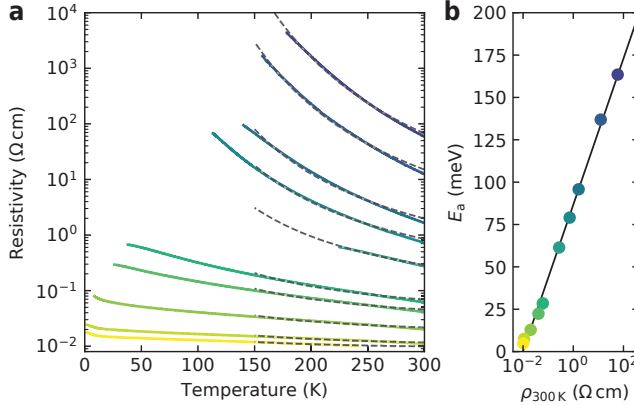


Figure 6.5: **Low-temperature transport at different dopings.** (a) Resistance vs temperature curves of a WO₃ device at different levels of H₂ doping. The data is fit with the Arrhenius model for activated transport (dashed lines). (b) Activation energy as a function of room temperature resistivity $\rho_{300\text{K}}$. The solid line is a linear regression to the data points.

6.5. TEMPERATURE-DEPENDENT ELECTRICAL TRANSPORT

We showed that the room temperature resistivity of WO₃ films can be continuously tuned by H₂ intercalation, and that both the intercalation and deintercalation are thermally activated processes. As a result, hydrogen kinetics in the WO₃ lattice can be arrested by cooling down the material. This allows to measure the transport activation energy of the free carriers in WO₃ induced by H₂ doping, giving insight into the doping mechanism. In Fig. 6.5a, we show a series of resistance vs temperature curves measured on a single WO₃ device under different H₂ doping conditions. Before each measurement, the sample is exposed to hydrogen gas at room temperature. Once the desired sheet resistance $\rho_{300\text{K}}$ is obtained, the sample chamber is evacuated and the temperature ramp is started. All curves show a semiconducting trend, where higher doping determines a shallower temperature dependence. The measured curves have a strong similarity with what previously reported for oxygen-deficient WO₃ thin films [34, 103], suggesting the occurrence of a similar mechanism of extrinsic doping. This interpretation is supported by recent experiments on WO₃ nanowires which showed that H₂ intercalation is accompanied by the formation of interstitial H₂O molecules and oxygen vacancies [203, 211].

We consider a simple Arrhenius mechanism $\sigma = 1/\rho \sim e^{-E_a/k_B T}$ to characterise the electrical transport, where E_a is the activation energy. The resulting fits in the high-temperature regime (above 150 K, dashed lines in Fig. 6.5a) show good agreement with the experimental data, and allows us to extract the relationship between E_a and $\rho_{300\text{K}}$, which is reported in Fig. 6.5b. The data shows a logarithmic dependence which is well-fit by $E_a = A \log \rho_{300\text{K}} + B$, with $A = 19 \text{ meV}$ and $B = 90 \text{ meV}$. We show in Section 6.8.2 that the activation energy can be expressed as

$$E_a = k_B T_{300\text{K}} [\log \rho_{300\text{K}} + \gamma \log C_H] + \gamma T_{300\text{K}} \Delta S^\circ, \quad (6.2)$$

where γ is related to the extrinsic donor charge, ΔS° is the reaction entropy and C_H is the

hydrogen concentration inside the WO₃ lattice. Equation (6.2) provides a direct relationship between E_a and $\rho_{300\text{K}}$ through the coefficient $k_B T_{300\text{K}} \sim 26\text{meV}$. However, $\rho_{300\text{K}}$ is also a function of C_H , and by comparing Eq. (6.2) with the experimental fit, we find the expression for the resistivity $\rho_{300\text{K}} \sim (C_H)^{-\gamma/0.3}$. We show in Section 6.8.2 that $\gamma = \frac{1}{3}$ if the electron donors are oxygen vacancies. Substituting this value, we obtain an almost linear relationship between the conductance and hydrogen concentration in the material $\sigma_{300\text{K}} = 1/\rho_{300\text{K}} \sim C_H$, in agreement with the assumption we used to treat the experimental intercalation and deintercalation curves with the kinetic model. The linear dependence between gas concentration and resistivity constitutes a powerful transduction scheme for the electrical sensing of H₂.

6.6. CONCLUSIONS

To conclude, single-crystal WO₃ thin films have found to be extremely sensitive probes for solid state hydrogen gas sensors. Our devices show resistance variations up to 5 orders of magnitude upon exposure to H₂ at room temperature. The device response can be tuned by controlling the temperature, achieving high sensitivity down to concentrations of 10 ppm at room temperature and to as low as 1 ppm at 65 °C, where we measured fast response times down to 2 s. We successfully modelled the intercalation and deintercalation of hydrogen in the WO₃ lattice with a simple kinetic of thermally activated processes. Our analysis allowed us to extract the activation energies of the different reactions, which are in good agreement with previous reports based on *ab initio* calculations. Finally, low temperature measurements indicated that the doping is consistent with a mechanism involving the formation of oxygen vacancies as electron donors in the oxide. These results show that heteroepitaxial WO₃ films hold great potential for next-generation hydrogen gas sensors, providing high sensitivity, fast response time, high dynamic range and simple read-out.

6.7. METHODS

SAMPLE GROWTH

WO₃ thin films were grown by pulsed laser deposition on commercially available SrTiO₃ (001) substrates, with TiO₂ surface termination. The laser ablation was performed using a KrF excimer laser (Coherent COMPexPro 205, $\lambda = 248\text{nm}$) with a 1 Hz repetition rate and 1Jcm^{-2} fluence. The target-substrate distance was fixed at 55 mm. The WO₃ films were deposited from a WO₃ sintered target at 500 °C substrate temperature and 8×10^{-2} mbar oxygen pressure. Film thickness was monitored *in-situ* during growth by intensity oscillations of reflection high-energy electron diffraction (RHEED). At the end of the growth, the films were cooled down to room temperature in the same oxygen pressure used during deposition.

VAN DER PAUW GEOMETRY FABRICATION

Standard e-beam lithography with PMMA resist was used to pattern WO₃ heteroepitaxial films. The metal contacts were deposited by evaporation of 5 nm Ti and 45 nm Au at room temperature, followed by lift-off. Ar ion etching was used prior to metal deposition to etch 5 nm of WO₃ in order to provide edge contacts to the film, which ensure a

low contact resistance. The WO_3 mesa was defined by a subsequent etching step which fully removes the WO_3 film from the regions surrounding the van der Pauw geometry. The etching was performed using $V_{\text{discharge}} = 44 \text{ V}$, $V_{\text{beam}} = 500 \text{ V}$, $V_{\text{accelerator}} = 70 \text{ V}$ and a beam current of 2 mA , corresponding to an Ar ion flux of 0.25 mA cm^{-2} . These parameters produce etched regions which are insulating at all temperatures.

ELECTRICAL MEASUREMENTS

The resistive measurements were performed with a Keithley 6430 sourcemeter using a four-probe configuration with an excitation current of 100 nA .

AIR CONDITIONS

Air from the environment (relative humidity 50%) was used in the sensing measurements.

NUMERICAL SOLUTION OF KINETIC EQUATIONS

The kinetic model in the Supplementary Information was solved using the NDSolve function of Wolfram Mathematica.

6.8. SUPPLEMENTARY INFORMATION

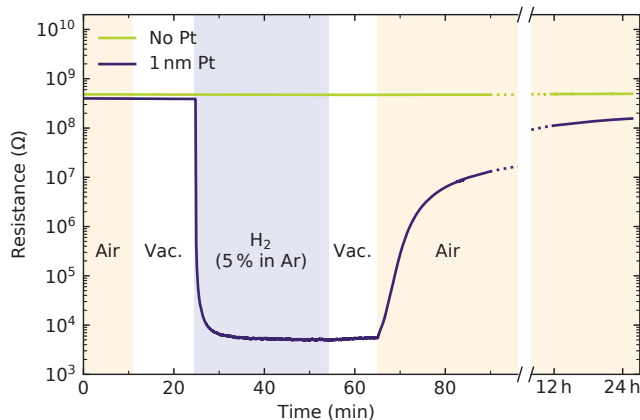


Figure 6.6: **WO_3 response with and without catalyst.** We compare the resistance change of two WO_3 devices, one without catalyst and one with 1 nm of Pt. The samples have comparable resistance in pristine conditions. Upon exposure to $5\% \text{ H}_2$ in Ar carrier gas, the bare WO_3 sample shows no change in resistance, while the one with Pt shows a sharp drop. This underscores the crucial role of the noble metal in catalysing the hydrogen intercalation reaction.

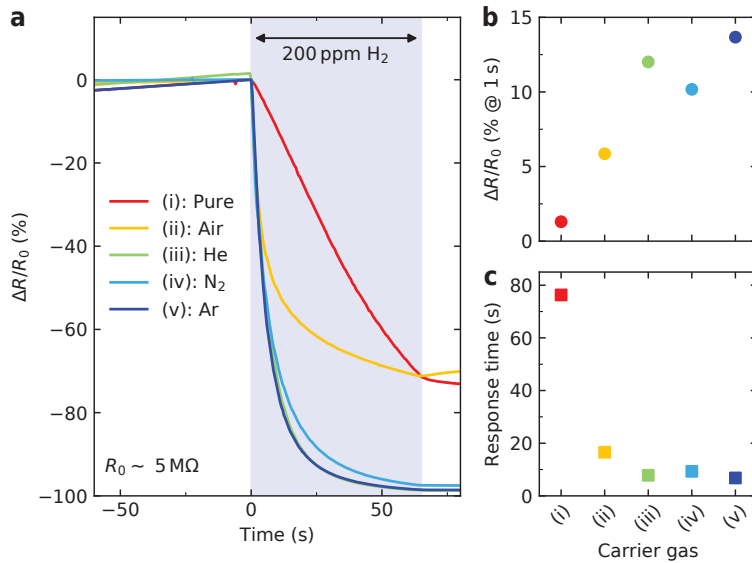


Figure 6.7: **Hydrogen intercalation with different carrier gases.** (a) At $t = 0$ the material is exposed to 200 ppm of H_2 in 1 bar atmosphere of a carrying gas, as indicated in the legend. In the case labelled as "pure" (red curve), a low-pressure (1 mbar) mixture of 20% H_2 in Ar is used. (b) Percentage variation after 1 s exposure and (c) exponential response time. The intercalation rates in He, N_2 and Ar carrying gases are comparable, indicating that these gases do not affect the intercalation process. We observe a reduced intercalation rate in air. This can be related to the recombination of H_2 and O_2 molecules to form water on the surface of WO_3 , thus reducing the H_2 concentration entering the WO_3 lattice, as previously reported in ref. [203]. Interestingly, an even lower intercalation rate is observed when using "pure" hydrogen. This can be explained considering the lower scattering rate of molecules in gas phase at low pressure, which determines a reduced H_2 adsorption rate on the Pt catalyst sites. This data highlights the versatility of our WO_3 device, which can be used for H_2 sensing in several gaseous atmospheres.

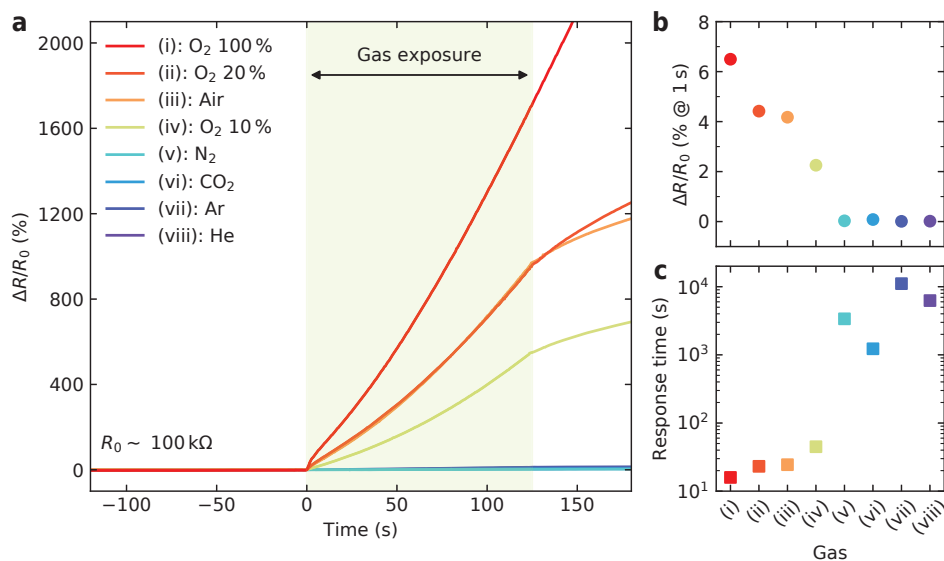


Figure 6.8: **Recovery in different gases.** (a) Before the measurement, the WO₃ device is doped with H₂ to an initial state with $R_0 \sim 100 \text{ k}\Omega$, value that is approximately constant in vacuum for the few minutes prior to the gas exposure. At $t = 0$, the indicated gas is introduced in the sample chamber with a pressure of 1 bar. Partial pressures of oxygen are obtained by mixing pure O₂ gas with Ar. (b) Percentage variation after 1 s exposure and (c) exponential response time. The resistance does not change upon exposure to N₂, CO₂ and the inert gases Ar, He. We note that these gases, together with O₂, are the main components of air. An enhanced deintercalation rate is observed upon exposure to O₂ gas. Remarkably, the response to 20% O₂ in Ar and to pure air (where the oxygen concentration is also approximately 20%) is comparable, indicating that O₂ is the agent responsible for the enhanced hydrogen deintercalation rates.

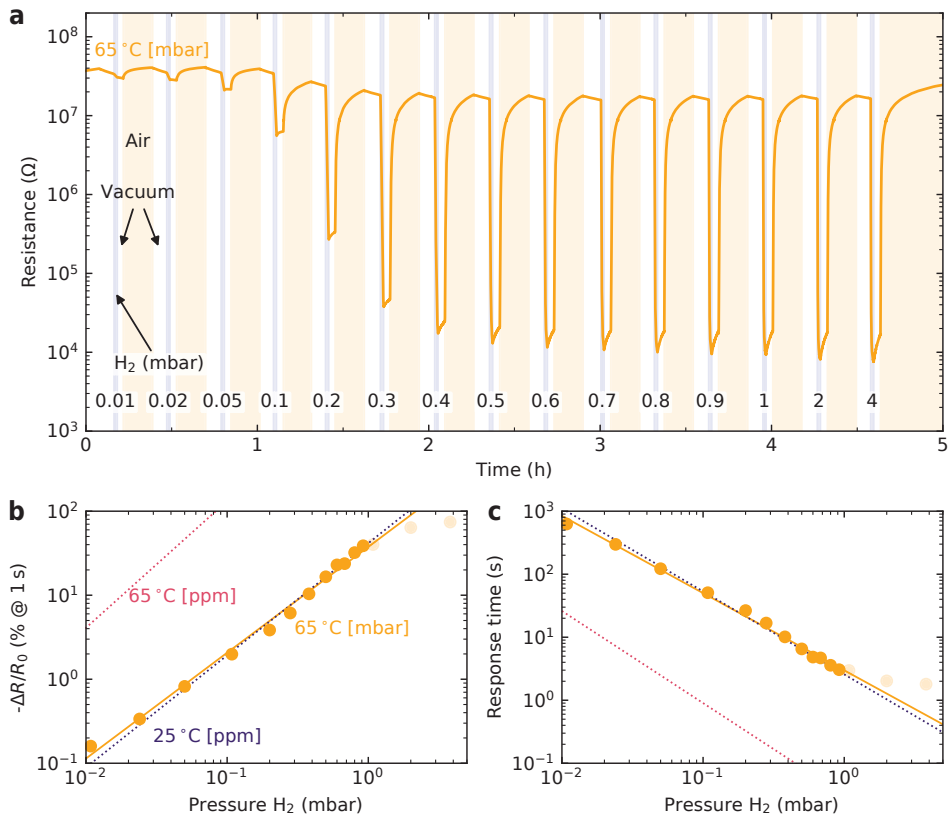


Figure 6.9: **Hydrogen sensing in low-pressure.** (a) Resistance variations upon exposure to a mixture of 20% H_2 in Ar, where the H_2 partial pressure is indicated in the figure. The sample is kept at 65°C during the experiment. (b) Percentage variation after 1 s gas exposure and (c) exponential response time. The orange line is a linear fit to the experimental data. For comparison purposes, we report as dotted lines the fits relative to the ambient pressure data of Figs. 6.3b and 6.3c in the main text, where the H_2 partial pressure values are a conversion of the concentration values in ppm. Because the H_2 intercalation rate is reduced at lower pressures, the WO_3 sensor shows an overall lower sensitivity to H_2 in the low-pressure regime presented here.

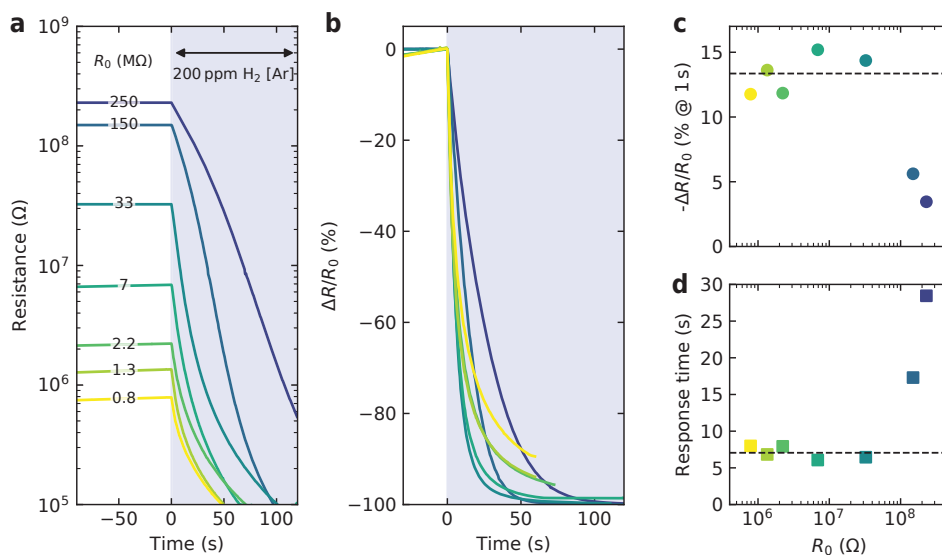


Figure 6.10: **Hydrogen sensing with different initial resistance.** (a) Resistance and (b) percentage variation upon exposure to 200 ppm of H₂ in 1 bar total pressure of Ar. (c) Percentage variation after 1 s exposure and (d) exponential response time. For $R_0 < 1 \times 10^8 \Omega$, the sensor response to 200 ppm H₂ is constant at its average value (dashed horizontal lines), within experimental error. A deviation from this trend is observed for the highest R_0 values, for which WO₃ is in a state of very low doping. In such state, the doping might be inhomogeneous and changes in amount of intercalated H₂ might result in smaller changes of material resistance. We note that the variations observed here, where a fixed $C_{H_2} = 200$ ppm was used, are much smaller than the ones observed for different C_{H_2} in Fig. 6.3 of the main text. This indicates that WO₃ sensing properties are only slightly affected by the value of R_0 , which can be safely neglected.

6.8.1. MODEL FOR HYDROGEN REACTION KINETICS

INTERCALATION

We assume an infinite reservoir of hydrogen in gas phase which adsorbs on catalyst sites A , out of which a are full (molar fraction $\alpha = a/A$) and $(A - a)$ are empty. The WO₃ material has B bulk sites that can accommodate hydrogen, out of which b are full (molar fraction $\beta = b/B$). The first reaction step is irreversible (i.e. $k_{-1,i} = 0$). The rates for the concentrations are:

$$\begin{cases} \dot{a} = k_{1,i}(A - a)^2 + k_{-2,i}b - k_{2,i}a \\ \dot{b} = k_{2,i}a - k_{-2,i}b \end{cases} \quad (6.3)$$

Transforming to molar fractions:

$$\begin{cases} \dot{\alpha} = k_{1,i}A(1 - \alpha)^2 + k_{-2,i}\frac{B}{A}\beta - k_{2,i}\alpha \\ \dot{\beta} = k_{2,i}\frac{A}{B}\alpha - k_{-2,i}\beta \end{cases} \quad (6.4)$$

We can now assume that the system reaches a stationary condition ($\dot{\alpha} = \dot{\beta} = 0$) when $t \rightarrow \infty$:

$$\begin{cases} 0 = k_{1,i}A(1 - \alpha_\infty)^2 + k_{-2,i}\frac{B}{A}\beta_\infty - k_{2,i}\alpha_\infty \\ 0 = k_{2,i}\frac{A}{B}\alpha_\infty - k_{-2,i}\beta_\infty \end{cases} \quad (6.5)$$

Multiplying the second equation by $\frac{B}{A}$ and summing it to the first, we find that $\alpha_\infty = 1$. From the second equation we then have $k_{2,i} = \frac{B}{A}\beta_\infty k_{-2,i}$. We can simplify the rate equations by keeping $k_{2,i}$ in the first and $k_{-2,i}$ in the second, and using the normalised quantity $\sigma(t) = \frac{\beta(t)}{\beta_\infty}$:

$$\begin{cases} \dot{\alpha} = k_{1,i}A(1 - \alpha)^2 + k_{2,i}(\sigma - \alpha) \\ \dot{\sigma} = k_{-2,i}(\alpha - \sigma) \end{cases} \quad (6.6)$$

The last set of equations can be solved numerically. We identify $\sigma(t)$ with the experimentally measured conductance, normalised on its final value. This is valid with the assumption that σ is proportional to the hydrogen concentration in the material, as discussed in the main text.

DEINTERCALATION

In this case the removal of hydrogen from WO₃ is an irreversible step (i.e. $k_{1,d} = 0$) because of the vacuum atmosphere. We can write:

$$\begin{cases} \dot{a} = -k_{-1,d}a^2 + k_{-2,d}b - k_{2,d}a \\ \dot{b} = k_{2,d}a - k_{-2,d}b \end{cases} \quad (6.7)$$

Using molar fractions:

$$\begin{cases} \dot{\alpha} = -k_{-1,d}A\alpha^2 + k_{-2,d}\frac{B}{A}\beta - k_{2,d}\alpha \\ \dot{\beta} = k_{2,d}\frac{A}{B}\alpha - k_{-2,d}\beta \end{cases} \quad (6.8)$$

We consider a stationary state ($\dot{\alpha} = \dot{\beta} = 0$) before the deintercalation beginning (i.e. before the evacuation of H₂ gas), with catalyst particles saturated by hydrogen ($\alpha_0 = 1$), and

some hydrogen in the WO_3 lattice ($\beta_0 > 0$). This considerations lead to $k_{2,d} = \frac{B}{A}\beta_0 k_{-2,d}$, which allows us to rewrite the system as:

$$\begin{cases} \dot{\alpha} = -k_{-1,d}A\alpha^2 + k_{2,d}(\sigma - \alpha) \\ \dot{\sigma} = k_{-2,d}(\alpha - \sigma) \end{cases} \quad (6.9)$$

where, as before, we take $\sigma(t) = \frac{\beta(t)}{\beta_0}$. In order to simplify the last system, new rate constants can be defined as $\bar{k}_{-1,d} = k_{-1,d}A$. Furthermore, we note that the relation $k_{2,d} = \frac{B}{A}\beta_0 k_{-2,d}$ holds only for fixed values of T and p , because both A and B depend on temperature and pressure. It is thus not possible to derive the temperature dependence of $k_{2,d}$ from the one of $k_{-2,d}$, or vice-versa.

6.8.2. MODEL FOR ACTIVATED ELECTRICAL TRANSPORT

In the following, we develop a simple thermodynamic model to express the Arrhenius activation energy for the electrical transport as a function of sample resistivity at $T = 300\text{K}$. The WO_3 is doped with hydrogen, which intercalates in the crystal lattice to form electron donor sites, such as oxygen vacancies. We consider the existence of an equilibrium for the ionisation of the donor site as



where, in Kröger–Vink notation, V_O^\times represents a neutral oxygen vacancy and $\text{V}_\text{O}^{\bullet\bullet}$ a double ionised one. The corresponding equilibrium constant is¹

$$k_{\text{eq}} = \frac{[\text{V}_\text{O}^{\bullet\bullet}]n^2}{[\text{V}_\text{O}^\times]} = \frac{n^3}{2[\text{V}_\text{O}^\times]}, \quad (6.11)$$

where n is the concentration of electrons in the material, and $[\text{V}_\text{O}^{\bullet\bullet}] = \frac{n}{2}$ for the reaction equation. We can solve for the electron density

$$n = (2[\text{V}_\text{O}^\times]k_{\text{eq}})^{\frac{1}{3}}. \quad (6.12)$$

In general, the concentration of donor sites will depend on the hydrogen concentration in WO_3 , so that we can assume $[\text{V}_\text{O}^\times] \sim C_\text{H}$. Furthermore, there could be additional ionisation equilibria that affect the experimental value of n (i.e. the single ionisation of the oxygen vacancy, or the ionisation of an interstitial hydrogen radical). For this reason, we generalise Eq. (6.12) by introducing an exponent γ and, disregarding the constant terms, we obtain

$$n \sim (C_\text{H}k_{\text{eq}})^\gamma. \quad (6.13)$$

We now consider that the temperature dependence of an equilibrium constant can be written as a function of the associated variation of Gibbs free energy ΔG as

$$k_{\text{eq}} \sim e^{-\frac{\Delta G}{k_\text{B}T}}. \quad (6.14)$$

¹Here k_{eq} is an effective rate constant because it is written in terms of concentrations rather than thermodynamic activities.

The free energy can be expressed as

$$\Delta G = \Delta G^\circ + g(C_H) = \Delta H^\circ - T\Delta S^\circ + g(C_H), \quad (6.15)$$

where ΔH° and ΔS° are, respectively, the standard enthalpy and entropy variations of the reaction, and $g(C_H)$ is a function that takes into account the non-ideality of the donor ionisation process, comprising, for example, the interaction between the reaction species (both electrons and donor sites). We note that, apart from $T\Delta S^\circ$, all terms in Eq. (6.15) are temperature independent. In general, the electrical conductance σ is proportional to the carrier density, so that we can write

$$\log \sigma \sim \log n = \gamma [\log C_H + \log k_{\text{eq}}], \quad (6.16)$$

and substitute $\rho = 1/\sigma$, Eqs. (6.14) and (6.15) to obtain

$$\log \rho = \gamma \left[-\log C_H - \frac{\Delta S^\circ}{k_B} + \frac{\Delta H^\circ + g(C_H)}{k_B T} \right]. \quad (6.17)$$

Considering that C_H does not depend on temperature, at $T = T_0 \equiv 300\text{K}$ we have

$$\log \rho_0 = \gamma \left[-\log C_H - \frac{\Delta S^\circ}{k_B} + \frac{\Delta H^\circ + g(C_H)}{k_B T_0} \right]. \quad (6.18)$$

According to the Arrhenius activated mechanism for electrical transport, which we used in the main text to describe the data of Fig. 6.5a, we have

$$\log \rho \sim \frac{E_a}{k_B T}. \quad (6.19)$$

By comparing the temperature dependences of Eq. (6.17) and Eq. (6.19) we find

$$\gamma \frac{\Delta H^\circ + g(C_H)}{k_B T} = \frac{E_a}{k_B T}, \quad (6.20)$$

from which, substituting Eq. (6.18), we obtain the following expression for the activation energy

$$E_a = k_B T_0 [\log \rho_0 + \gamma \log C_H] + \gamma T_0 \Delta S^\circ. \quad (6.21)$$

7

CONCLUSIONS AND PERSPECTIVES

Hey [...] I would say that this is the end!
Wait a moment: I am the boss, I say when it's the end.
[...]
It's the end!

Napoleon & Lafayette

THIS thesis covered experimental work on metal–insulator transitions (MITs) in different systems of quantum materials. In the first part, nanoscale microscopy allowed us to visualise for the first time the formation of nanoscale phase separation in the proximity of the temperature-driven MIT in nickelates. In the second part, we induced the formation of different defect profiles to trigger an MIT both in single-crystal WO_3 thin films and in $\text{WO}_3/\text{LAO}/\text{STO}$ heterostructures. These solid state phase transitions are one of the most promising routes for next-generation nanoscale functional devices and, at the same time, a great body of experimental and theoretical work is devoted to the understanding of their fundamental mechanism. In the following, we summarise the key results of the research presented in the various chapters, discussing the many open challenges, providing indications for future developments and presenting some preliminary results of our on-going work.

7.1. NICKELATES FOR NEURAL NETWORKS AND ULTRA-FAST SWITCHES

In [Chapter 2](#), we imaged the nanoscale phase separation occurring during the MIT in heteroepitaxial nickelates. We found out that the phase transition is regulated by the surface morphology, and that insulating nanodomains nucleate along the surface terraces. These findings provide a direct link between structural and electronic properties in nickelate materials, allowing the engineering of devices where the domain formation pathway is predefined. An important question that is yet unanswered is how the nanodomain structure is reflected in electrical transport. Because of the strongly anisotropic shape of the domains, a strong in-plane anisotropy is expected to appear in the vicinity of the MIT. Furthermore, it would be very appealing for technological applications to fabricate nanodevices comprising a single nanodomain, where a discrete bit-like transition from metal to insulator is expected to occur in a narrow temperature range. In addition, because the phase transition is sensitive to local strain fields, nanopatterning techniques could be used to locally control the transition temperature, and tailor it by design. Finally, by connecting multiple nanodevices in a network one could engineer neuromorphic architectures, where the memory properties of the MIT could be exploited to realise solid-state machine learning algorithms.

We showed in [Chapter 3](#) that the phase transition can be triggered by external illumination with laser light. The advantage of using a laser for this purpose is that a large amount of energy can be delivered to the material in a very short timescale. This can be used to trigger ultra-fast phase transitions, which set the material in a metallic or insulating state. By conveniently regulating the material temperature, it would then be possible to engineer ultra-fast switches, or devices whose memory state can be initialised by a light pulse. This paves the way towards ultra-fast electronic circuits that take advantage of the ultra-fast electro-optical coupling.

A first step towards the proposed developments involves probing the properties of heteroepitaxial nickelates at a scale comparable to the nanodomain dimensions. Since the domains are oriented along the surface terraces, it is possible to pattern devices where the electrical current flow is aligned perpendicular or parallel to the domains.

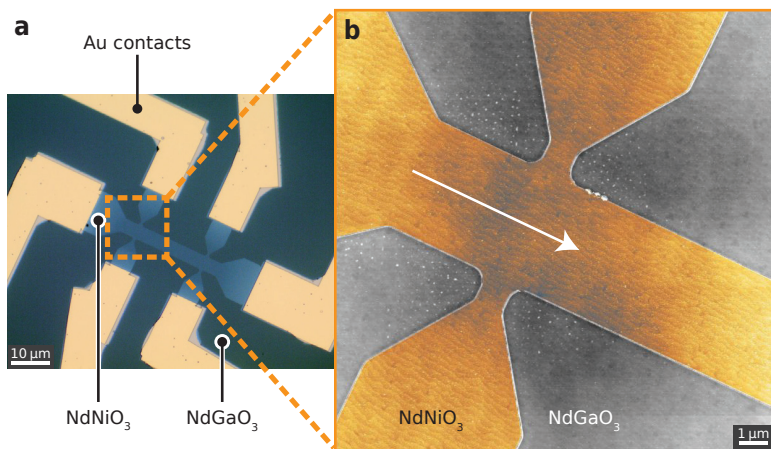


Figure 7.1: **Hall bar device patterned in NdNiO₃ along the surface terraces.** (a) Optical image of the device and (b) false colour atomic force microscopy image showing the conductive NdNiO₃ film (orange) and the insulating NdGaO₃ substrate (grey). The white arrow indicates the direction of the surface terraces, which corresponds to the direction of the striped nanodomains that form during the MIT.

In Fig. 7.1, we show a Hall bar device with the channel oriented parallel to the surface terraces. The fabrication involved use of electron beam lithography to define the structures, Ar ion milling to etch away the conductive NdNiO₃ and form a Hall bar mesa, and gold evaporation to lay down contact pads (details of a similar fabrication were further discussed in Section 6.7). The direction of the surface terraces was identified by AFM imaging before the lithographic fabrication, and the Hall bar device oriented accordingly. As shown in Fig. 7.1b, the 4 μm-wide device channel contains about ten surface terraces, indicating that as many insulating nanodomains are expected to form in the proximity of the MIT. With such a small number of nanodomains, anisotropy effects are expected to arise in the electronic transport behaviour. Contrary to our expectations, measurements on the patterned device showed semiconducting behaviour at all temperatures. Preliminary investigations revealed that the NdNiO₃ thin film degraded during the fabrication process, most likely due to the formation of oxygen vacancies induced by curing the lithographic resists at high temperature. These results indicate that special care should be taken when performing device fabrication on nickelate materials. In future work, one could avoid exposing the material to high temperatures, and possibly use alternative resists which have low reactivity with oxide materials.

7.2. TOWARDS BALLISTIC TRANSPORT AT OXIDE INTERFACES

In the second part of this dissertation, our research focused on WO₃, an interesting semiconductor material with strong chemical reactivity. We showed in Chapter 5 how the reactivity of amorphous WO₃ thin films can be exploited to induce an insulator-to-metal transition in WO₃/LAO/STO heterostructures, determining the formation of a metallic 2DES. This conductive system showed very high electron mobility of 80 000 cm² V⁻¹ s⁻¹, that we characterised by low-temperature magnetotransport and quantum oscillations

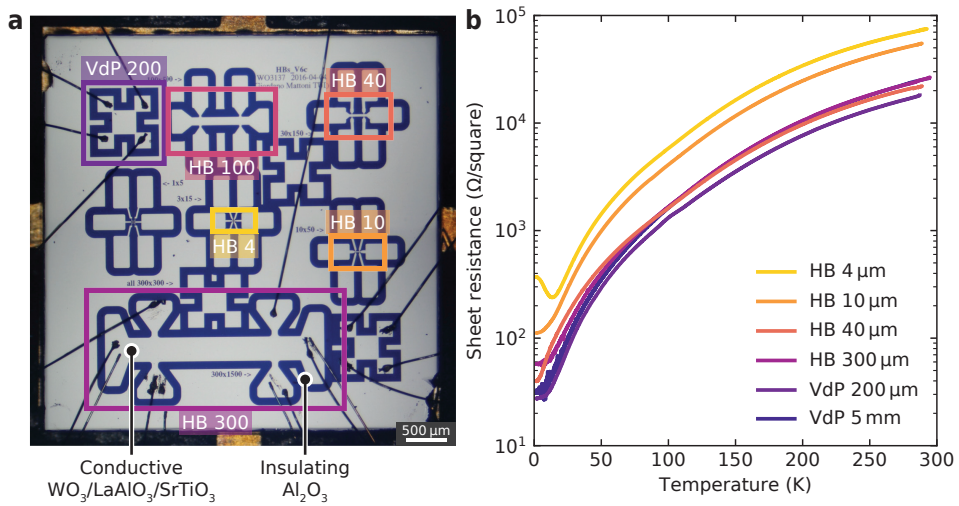


Figure 7.2: **Devices of different size in $\text{WO}_3/\text{LAO}/\text{STO}$ heterostructures.** (a) Optical image showing patterned van der Pauw (VdP) and Hall bar (HB) devices. The heterostructure is made of 4 uc of amorphous WO_3 and 2 uc of crystalline LAO. All the HB devices have an aspect ratio of 5, and the labels in the image indicate the channel width in μm . (b) Resistance vs temperature curves measured on the different devices. The 5 mm VdP device is obtained by bonding an unpatterned $5\ \mu\text{m} \times 5\ \mu\text{m}$ sample in its four corners.

of conductance. Our results are an important step towards future oxide-based electronics, where oxide materials such as superconductors, ferromagnets and ferroelectrics could be combined in the same platform of highly conductive materials.

A natural extension of this research would be the demonstration of ballistic transport at oxide interfaces. Considering that the electrons confined in our highly-mobile $\text{WO}_3/\text{LAO}/\text{STO}$ heterostructures possess mean free paths up to $4\ \mu\text{m}$, fabrication of devices smaller than such critical dimension constitutes a very interesting development. Another intriguing research question is the effect of the WO_3 overlayers on the superconducting state at LAO/STO interface. While the authors did not observe a superconducting state upon zero-field cooling, in fact, the heterostructures showed hints of unconventional superconductivity when a negative back-gate voltage was applied. Within this framework, the control of oxygen defects provided by the WO_3 overlayers could be combined with electrostatic gating to form a basis for new experiments on the 2DES at LAO/STO interfaces.

For the reasons discussed above, a first research step is the fabrication of micron-scale devices in $\text{WO}_3/\text{LAO}/\text{STO}$ heterostructures. In the following, we discuss some preliminary results involving the fabrication of devices of different size obtained using the procedure detailed in Section 5.7. Our pre-patterning scheme involves the use of an insulating Al_2O_3 layer that is laid down on the bare STO substrate to define the insulating regions. Upon deposition of the LAO and WO_3 layers, the conductive devices are readily formed and can be directly bonded and measured without the need of additional preparation. This procedure preserves the delicate transport properties of the $\text{WO}_3/\text{LAO}/\text{STO}$ heterostructures, which could be destroyed by performing device fabrication after mate-

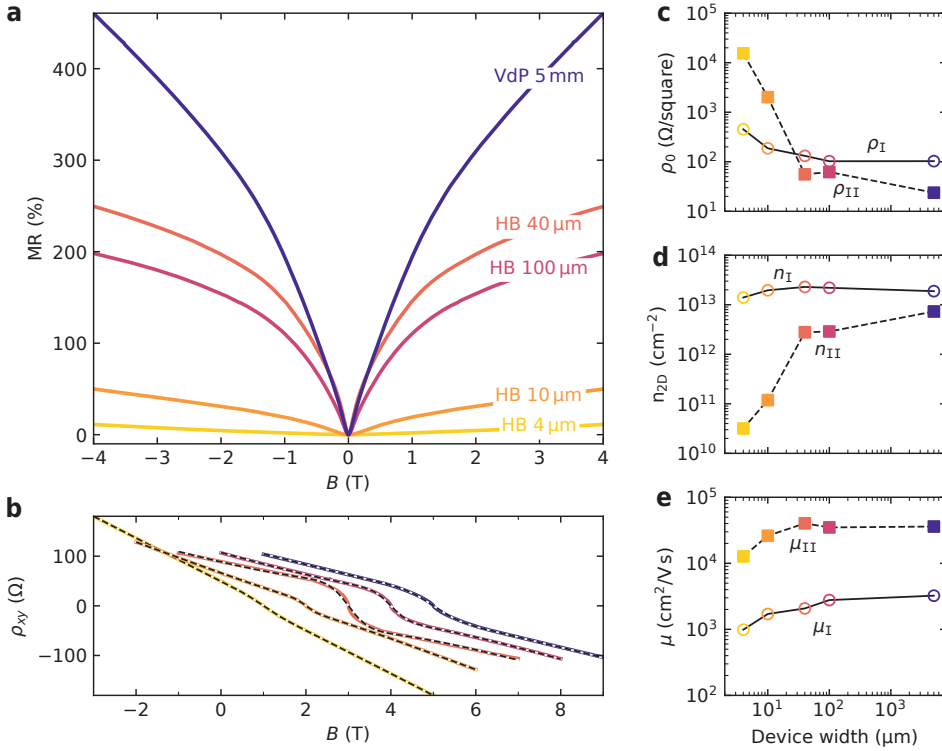


Figure 7.3: **Magnetotransport as a function of lateral device size.** (a) Magnetoresistance and (b) Hall effect measured on the devices of Fig. 7.2 at 1.5 K. Fits with the two-channel model of Eq. (5.1b) allow to extract (c) the sheet resistance, (d) the carrier density, and (e) the mobility of the two conduction channels.

rial growth. In Fig. 7.2a we show a series of van der Pauw (VdP) and Hall bar (HB) devices with channel widths ranging from 5 mm to 4 μm. The resistance vs temperature characteristics of several devices are presented in Fig. 7.2b. We find a critical thickness of about 20 μm separating two different transport characteristics: the larger devices show nearly overlapping curves, while the smaller ones have a higher sheet resistance and display charge localisation effects below 50 K.

To further investigate the difference between large and small devices, we perform MR and Hall effect measurements at 1.5 K (Fig. 7.3). Above the critical thickness of 20 μm, the devices have comparable properties, which are consistent with sample-to-sample variations. The smallest devices, instead, show a strong depletion of the high-mobility carriers, signalled by an almost linear Hall effect and a smaller MR. The origin of the observed behaviour is still under investigation and might be related to our fabrication procedure. Considering that metallic conductivity in WO₃/LAO/STO heterostructures is regulated by the delicate chemistry of oxygen defects, it is possible that the insulating Al₂O₃ material determines a rearrangement of oxygen defects. For instance, the oxygen-deficient WO₃ overlayers could absorb oxygen atoms from the oxygen-rich Al₂O₃ mate-

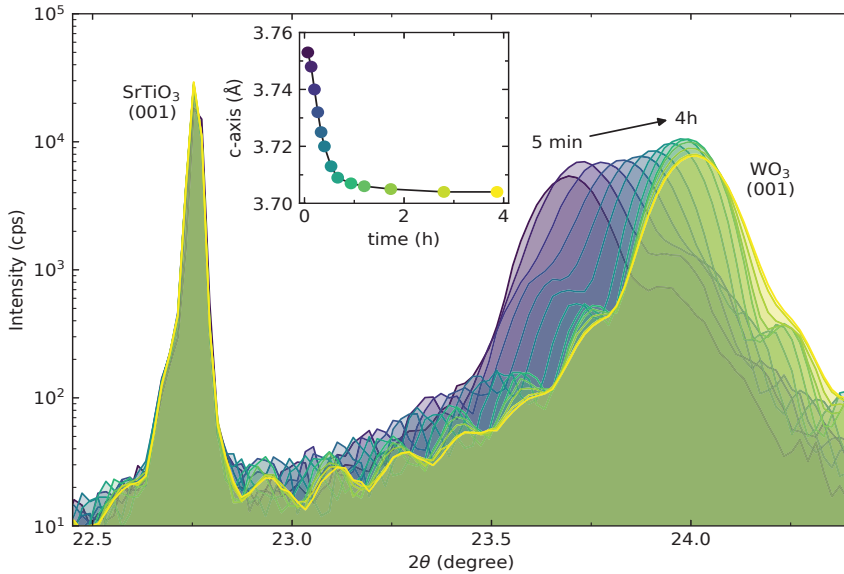


Figure 7.4: **WO₃ lattice expansion with H₂ doping.** X-ray diffraction measurement of a 50 nm WO₃ thin film on SrTiO₃ (001). Initially, the film is in a saturated hydrogen-doped state, with maximum lattice expansion. Upon exposure to air, the undoped state is gradually recovered, while θ - 2θ scans are acquired. The inset shows the change of WO₃ *c*-axis parameter as a function of time, extracted from the 2θ position of the WO₃ (001) diffraction peak.

7

rial. In this picture, replenished oxygen vacancy states of WO₃ would reduce the charge transfer to the conductive LAO/STO interface, hence explaining the lower values found for n_{II} in Fig. 7.3d. Because this process involves an in-plane exchange of oxygen atoms between the two materials, which occurs at the edges of the devices, it is reasonable that a stronger effect is observed in smaller devices. Further studies are required to better understand the origin of this effect, which constitutes an obstacle to the downscaling of WO₃/LAO/STO devices. A possible way to overcome this limitation could rely on the use of another insulating material, or different patterning strategies. Finally, we also note that small devices benefit from electric field focusing effects in a back-gate configuration. This advantage could be exploited to achieve a strong device tunability, which could overcome the localisation effects observed so far.

7.3. WO₃ FOR HYDROGEN SENSING, NANO-IONICS AND BEYOND

The systematic study performed in Chapter 4 allowed us to identify the deposition parameters to achieve high-quality growth of WO₃ single-crystal thin films. We showed that the oxygen stoichiometry can be tuned by regulating the oxygen pressure during pulsed laser deposition. As a function of oxygen content, the single-crystal WO₃ thin films undergo a large lattice expansion up to 10%, and display an insulator-to-metal transition. In Chapter 6 we demonstrated another approach for the doping of WO₃ thin films, namely the catalyst-mediated intercalation of hydrogen. By monitoring the change in

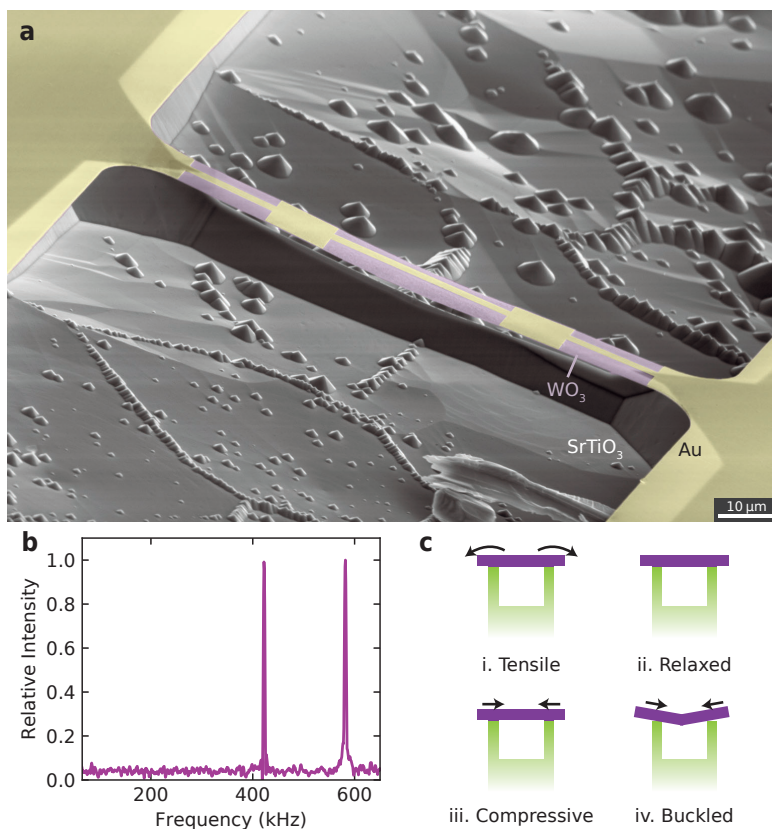


Figure 7.5: **Free-standing WO₃ microbridge.** (a) False colour scanning electron microscopy (SEM) image of a WO₃ microbridge (50 nm in thickness, and 110 μm × 5 μm in surface area) clamped on the SrTiO₃ substrate. The WO₃ film (violet) is covered by a 50 nm gold layer (yellow) that allows a current to flow through the structure, which is used for electromotive actuation. Two 5 μm × 5 μm gold mirrors allow detection of the mechanical vibration of the microbridge by using a laser in an optical lever geometry. (b) First and second vibrational modes of the microbridge at room temperature in its undoped state, measured in a vacuum atmosphere ($p < 1 \times 10^{-4}$ mbar). (c) Possible evolution of the microbridge strain state upon doping with H₂.

resistivity, WO₃-based devices have been employed for hydrogen gas sensing, showing fast response and unprecedented sensitivity with a detection limit as low as H₂ concentrations of 1 ppm nearby room temperature. Owing to the simple device architecture, we envision WO₃ as a promising candidate for future on-chip hydrogen detectors, which could be integrated in present CMOS technology. Furthermore, the high permeability to H₂ gas makes WO₃ a very appealing material to build semipermeable membranes, with potential use in solid oxide fuel cells, water splitting and recombination technologies and catalysis applications. However, before such devices can be developed, a more in-depth fundamental understanding of hydrogen intercalation and bulk diffusion in WO₃ is required.

At the end of [Chapter 6](#), we discussed how hydrogen intercalation in WO₃ deter-

mines the formation of oxygen vacancies in the material lattice. Considering that a large WO_3 lattice expansion induced by oxygen vacancies was observed in [Chapter 4](#), a natural question is how the material structural properties are affected by the intercalation of hydrogen. We investigate this aspect in [Fig. 7.4](#), where we measure the WO_3 c -axis parameter with X-ray diffraction. When Pt-catalysed WO_3 thin films are doped with H_2 gas, we observe a crystal lattice expansion up to 1.5%. This change is fully reversible and it indicates that WO_3 structural properties can be controlled by an external gas.

These findings open up interesting perspectives such as the fabrication of devices whose mechanical properties could be reversibly modified by chemical reactions. This is a very appealing research direction for micro- and nanoelectromechanical systems, where tunability of the resonance frequency of suspended structures is a highly desirable property. In [Fig. 7.5a](#) we show a preliminary result in this research direction, where a 50 nm-thick free-standing WO_3 microbridge is fabricated. Detailed discussion on the fabrication of this device is beyond the scope of this thesis, and here we limit ourselves to illustrate some of its properties. As shown in [Fig. 7.5b](#), the free-standing structure has a main vibrational mode around 400 kHz, with a Q -factor of about 5000. The heteroepitaxial strain imposed by the STO substrate, which clamps the structure at its ends, determines an initial tensile strain in the microbridge. Upon doping with H_2 , the WO_3 lattice expansion can determine a crossover from tensile, to relaxed, compressed and, finally, buckled state of the microbridge, as illustrated in [Fig. 7.5c](#). In this framework, doping with hydrogen gas adds a very unique degree of tunability to this mechanical resonator, with possible applications spanning from fundamental studies on mechanics at the micro- and nanoscale, to the development of novel actuators and detectors.

A

DERIVATION OF CLASSICAL MAGNETOTRANSPORT FORMULAS

In the following, we derive a series of formulas to describe magnetoresistance and Hall effect measurements. We begin by considering a single channel of charge carriers, and then extend the discussion to multiple parallel channels. Finally, we plot the obtained equations for a set of parameters corresponding to the typical values of the systems studied in this thesis.

A.1. CHARGE TRANSPORT FOR A SINGLE CONDUCTION CHANNEL

In general, in the approximation that the current density \mathbf{j} is a simple function of the electric field \mathbf{E} , it is possible to write

$$\mathbf{j} = \underline{\sigma}\mathbf{E}, \quad (\text{A.1})$$

$$\underline{\rho} = \underline{\sigma}^{-1}, \quad (\text{A.2})$$

$$\mathbf{E} = \underline{\rho}\mathbf{j}, \quad (\text{A.3})$$

where $\underline{\sigma}$ is the electrical conductivity tensor, and its inverse $\underline{\rho}$ is the electrical resistivity tensor. In a conductive material, the charge carriers move with an average drift velocity \mathbf{v} , which can be expressed as

$$\mathbf{v} = \mu\mathbf{E}, \quad (\text{A.4})$$

where μ is the carrier electrical mobility. In a classical picture, the conductivity of a homogeneous material is determined by Drude's formula

$$\sigma_0 = n|Q|\mu, \quad (\text{A.5})$$

where n is the carrier density and Q is its charge.

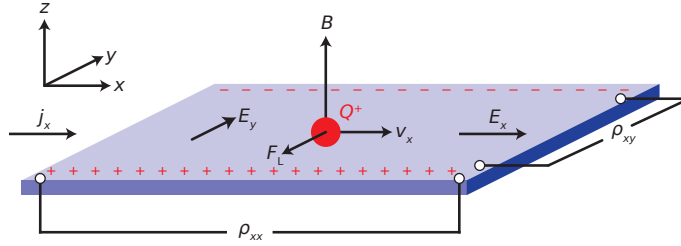


Figure A.1: **Schematic of a 2D conductor.** A current flow in the positive x -direction (j_x) is carried by positive charge carriers Q^+ which move with velocity v_x . The magnetic field B , applied in the positive z -direction, determines a Lorentz force (F_L) on the charge carriers, which induces the accumulation of positive and negative charge at the conductor edges (indicated in red). This charge is responsible for the insurgence of the transversal electric field E_y , or Hall voltage.

In a typical electrical transport experiment, the current direction and intensity \mathbf{j} is fixed, and the resulting electric field \mathbf{E} is determined by the voltage drop across a known current path. As a result, transport experiments allow the measurement of the resistivity tensor in Eq. (A.3), rather the conductivity one. In the case of a two-dimensional (2D) conductor, we can write explicitly

$$\begin{pmatrix} E_x \\ E_y \end{pmatrix} = \begin{pmatrix} \rho_{xx} & \rho_{xy} \\ \rho_{yx} & \rho_{yy} \end{pmatrix} \begin{pmatrix} j_x \\ j_y \end{pmatrix} = \begin{pmatrix} \rho_{xx} j_x + \rho_{xy} j_y \\ \rho_{yx} j_x + \rho_{yy} j_y \end{pmatrix}. \quad (\text{A.6})$$

As illustrated in Fig. A.1 for the case of a positive charge Q^+ , when a homogeneous current flows in the x -direction, the current density $\mathbf{j} = (j_x, 0, 0)$ can be expressed with Drude's formula as

$$j_x = \sigma_0 E_x \quad \rightarrow \quad E_x = \frac{1}{n|Q|\mu} j_x. \quad (\text{A.7})$$

If a magnetic field \mathbf{B} is applied, the Lorentz force deflects the moving carriers according to

$$\mathbf{F}_L = Q\mathbf{v} \wedge \mathbf{B}. \quad (\text{A.8})$$

In case the magnetic field is perpendicular to the conduction plane $\mathbf{B} = (0, 0, B)$, some charge carriers accumulate at the material edges along the y -direction, giving rise to an electric field E_y which counterbalances the Lorentz force

$$Qv_x B = QE_y \quad \rightarrow \quad E_y = \frac{B}{nQ} j_x. \quad (\text{A.9})$$

This mechanism is better known as Hall effect. We can identify the matrix elements of the resistivity tensor in Eq. (A.6) from the Equations (A.7) and (A.9) as

$$\rho_{xx} = \frac{1}{n|Q|\mu}, \quad (\text{A.10a})$$

$$\rho_{yx} = +\frac{B}{nQ}. \quad (\text{A.10b})$$

Repeating the considerations above for a current flowing in the y -direction, we can obtain the remaining matrix elements

$$\rho_{yy} = \frac{1}{n|Q|\mu}, \quad (\text{A.11a})$$

$$\rho_{xy} = -\frac{B}{nQ}, \quad (\text{A.11b})$$

where the minus sign in the second equation comes from the negative direction of the Lorentz force along the x -axis. The full resistivity matrix in 2D is thus

$$\underline{\rho} = \frac{1}{n|Q|\mu} \begin{pmatrix} 1 & \mp\mu B \\ \pm\mu B & 1 \end{pmatrix}, \quad (\text{A.12})$$

where the \pm sign accounts for the sign of the charge carriers. Inverting the previous expression, the conductance matrix is readily obtained

$$\underline{\sigma} = \frac{\sigma_0}{1 + (\mu B)^2} \begin{pmatrix} 1 & \pm\mu B \\ \mp\mu B & 1 \end{pmatrix}. \quad (\text{A.13})$$

We note that the quadratic dependence on B appearing in the diagonal matrix element σ_{xx} is the classical magnetoresistance.

A.2. MULTICHANNEL TRANSPORT

In a material where multiple parallel conduction channels $\{i\}$ contribute to transport, and in the approximation that they do not interact, the conductivity matrix is obtained by summing the contributions of the single channels as

$$\underline{\sigma} = \sum_i \underline{\sigma}_i = \sum_i \frac{\sigma_i}{1 + (\mu_i B)^2} \begin{pmatrix} 1 & \pm\mu_i B \\ \mp\mu_i B & 1 \end{pmatrix}, \quad (\text{A.14})$$

where μ_i , σ_i are the mobility and 2D conductivity at $B = 0$ for the i -th channel, respectively. By inverting this expression, we obtain the matrix elements of the resistivity tensor, which are the quantities measured by electrical transport. In the case of two parallel channels (I and II), the resulting analytic expressions are

$$\rho_{xx} = \frac{(\sigma_I + \sigma_{II}) + (\sigma_I \mu_{II}^2 + \sigma_{II} \mu_I^2) B^2}{(\sigma_I + \sigma_{II})^2 + (\pm\sigma_I \mu_{II} \pm \sigma_{II} \mu_I)^2 B^2}, \quad (\text{A.15a})$$

$$\rho_{xy} = \frac{(\pm\sigma_I \mu_I \pm \sigma_{II} \mu_{II}) + (\pm\sigma_I \mu_{II} \pm \sigma_{II} \mu_I) \mu_I \mu_{II} B^2}{(\sigma_I + \sigma_{II})^2 + (\pm\sigma_I \mu_{II} \pm \sigma_{II} \mu_I)^2 B^2} \cdot B, \quad (\text{A.15b})$$

where the \pm indicates the sign of the charge carriers in the i -th channel.

By using Eq. (A.5), the expressions above can be rewritten in terms of the carrier densities $\{n_i\}$ and the elementary electric charge $Q = \pm e$ as

$$\rho_{xx} = \frac{(n_I \mu_I + n_{II} \mu_{II}) + (n_I \mu_{II} + n_{II} \mu_I) \mu_I \mu_{II} B^2}{(n_I \mu_I + n_{II} \mu_{II})^2 + (n \mu_I \mu_{II} B)^2} \cdot \frac{1}{e}, \quad (\text{A.16a})$$

$$\rho_{xy} = \frac{(\pm n_I \mu_I^2 \pm n_{II} \mu_{II}^2) + n(\mu_I \mu_{II} B)^2}{(n_I \mu_I + n_{II} \mu_{II})^2 + (n \mu_I \mu_{II} B)^2} \cdot \frac{B}{e}, \quad (\text{A.16b})$$

where $n = (\pm n_I \pm n_{II})$ is the total carrier density.

It is interesting to consider the limits of Eqs. (A.16a) and (A.16b) for small and large B . For the longitudinal resistivity we find

$$\lim_{B \rightarrow 0} \rho_{xx} = \frac{1}{(n_I \mu_I + n_{II} \mu_{II})} \cdot \frac{1}{e} = \frac{1}{\sigma_I + \sigma_{II}}, \quad (\text{A.17a})$$

$$\lim_{B \rightarrow \infty} \rho_{xx} = \frac{(n_I \mu_{II} + n_{II} \mu_I)}{n^2 \mu_I \mu_{II}} \cdot \frac{1}{e}. \quad (\text{A.17b})$$

Equation (A.17a) indicates that at small B -field, when the classical magnetoresistance contribution is negligible, the longitudinal resistivity is the reciprocal of the sum of the two channels conductivity. Upon increasing magnetic field, ρ_{xx} increases monotonously and then reaches the constant saturation value indicated by Eq. (A.17b). The limits of the transverse resistivity yield

$$\lim_{B \rightarrow 0} \rho_{xy} = \frac{(\pm n_I \mu_I^2 \pm n_{II} \mu_{II}^2)}{(n_I \mu_I + n_{II} \mu_{II})^2} \cdot \frac{B}{e}, \quad (\text{A.18a})$$

$$\lim_{B \rightarrow \infty} \rho_{xy} = \frac{1}{n} \cdot \frac{B}{e}. \quad (\text{A.18b})$$

In the special case that one channel shows a much larger mobility (i.e., $\mu_{II} \gg \mu_I$) while having comparable carrier density (i.e., $n_I \approx n_{II}$), the low-field value of Eq. (A.18a) reduces to $\rho_{xy} \sim \frac{1}{n_{II}} \frac{B}{e}$. The slope of the Hall effect at small magnetic field, thus, would provide direct information concerning the carrier density of the high-mobility channel. These conditions are often not met in STO-based oxide interfaces, where it is common to find low-mobility carriers with high-density and high-mobility carriers with low-density (i.e., $n_I \mu_I \approx n_{II} \mu_{II}$). In this other case, thus, it is not possible to further simplify Eq. (A.18a) and no direct information can be extracted by the low-field slope of the Hall effect. In the large B -field limit of Eq. (A.18b), instead, the slope of ρ_{xy} always gives information regarding the total carrier density n .

Finally, we note that the model of multiple parallel conduction channels does not take into account any possible field-dependent variations of μ_i and σ_i , which could be determined by a change in band structure for strong magnetic fields. This is usually a valid assumption for magnetic field in the range of a few Tesla, limiting the usability of the model to relatively small values of B .

A.3. CALCULATED HALL EFFECT AND MAGNETORESISTANCE

A

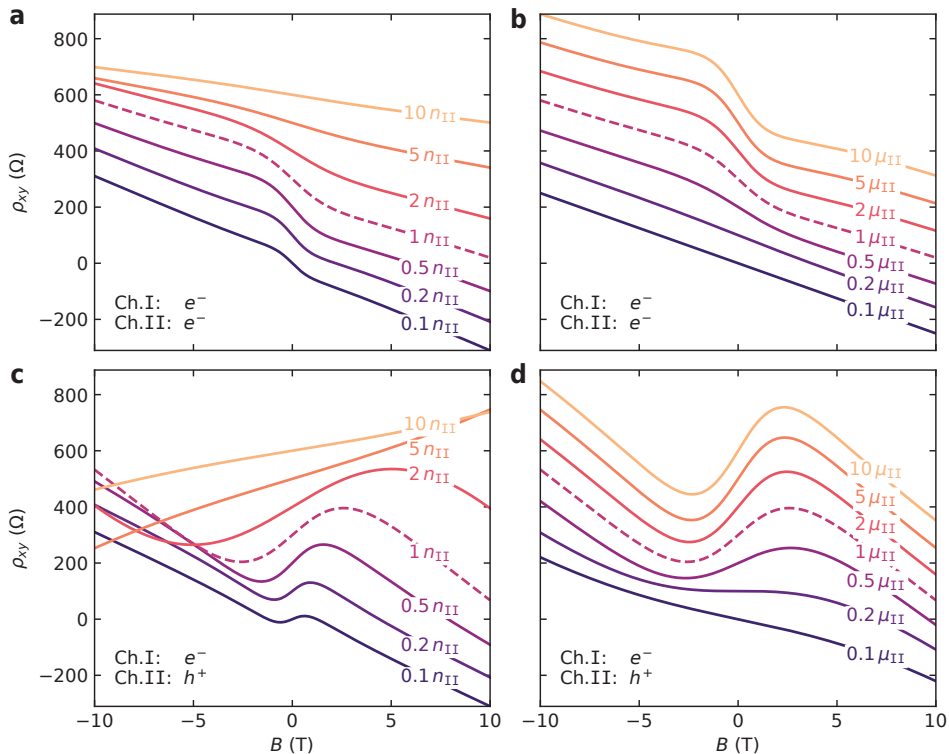


Figure A.2: **Hall effect curves with two parallel conduction channels.** Transverse resistivity curves calculated with Eq. (A.16b) using the carrier density and mobility parameters of Channels I and II from Table A.1. For each curve, one of the four parameters is varied as indicated in the legend (curves vertically offset by 100 Ω for clarity). The top panels (a) and (b) show the case of two electron channels, while the bottom panels (c) and (d) are calculated in the case of one electron, and one hole channel.

To illustrate the magnetotransport curves resulting from the multichannel model discussed in the previous section, we consider a few conduction channels whose carrier density, mobility, and sheet resistance are reported in Table A.1. The chosen values are compatible with what we measured experimentally in $\text{WO}_3/\text{LAO}/\text{STO}$ heterostructures,

Table A.1: **Transport parameters.** Carrier density, mobility, and sheet resistance of the multiple channels used to calculate the curves in Figs. A.2 and A.3.

Ch.	n_{2D} (cm^{-2})	μ ($\text{cm}^2 \text{V}^{-1} \text{s}^{-1}$)	ρ_0 (Ω)
I	2×10^{13}	1×10^3	313
II	5×10^{12}	1×10^4	125
III	1×10^{12}	1×10^5	63

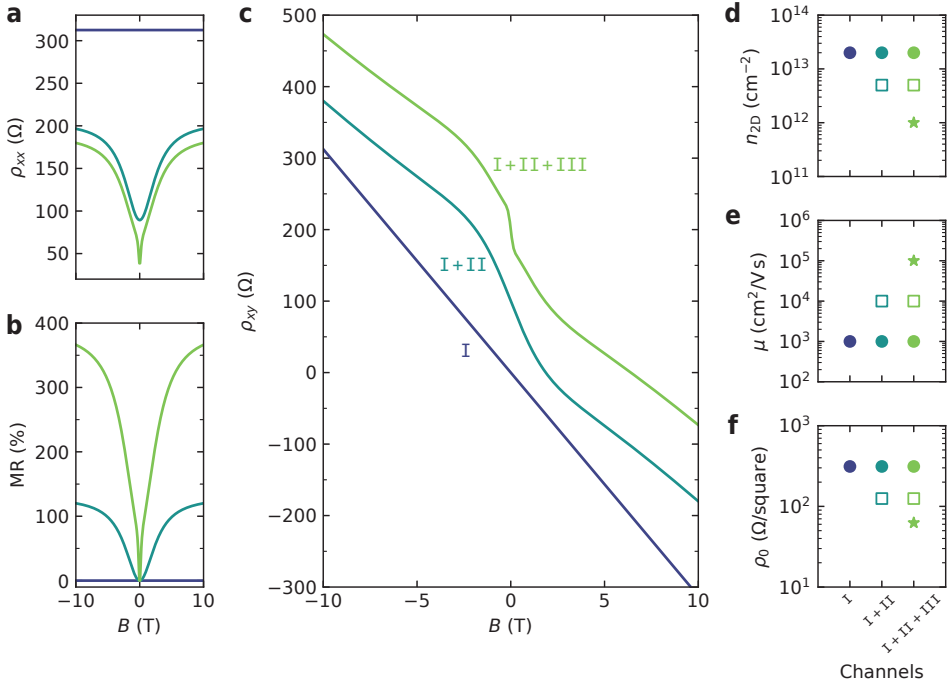


Figure A.3: **Magnetotransport for multiple electron channels.** (a) Sheet resistance, (b) magnetoresistance, and (c) transverse resistivity calculated with Eq. (A.14) for one, two or three parallel conduction channels (Hall curves vertically offset by $100\ \Omega$ for clarity). The curves are calculated with the parameters from Table A.1: (d) carrier density, (e) mobility, and (f) sheet resistance.

as discussed in Chapter 5. In Fig. A.2 we plot the Hall effect curves determined by two channels in parallel, where Channel II is the high-mobility one. When both channels have electron-like carriers (Figs. A.2a and A.2b), the Hall effect has a negative slope at all magnetic fields. As in the legend, we vary the properties of the high-mobility channel to show how they affect the Hall curves. In particular, the nonlinearity at small B -values is sharper for small n_{II} and high μ_{II} , while the Hall effect becomes linear for large n_{II} and small μ_{II} values. In Figs. A.2c and A.2d we show the case when Channel I has electrons and Channel II has hole-like carriers. In this case, the curves present both a positive and a negative slope, and show a more intense nonlinearity with smaller carrier density and larger mobility of Channel II, the one with higher mobility.

Figure A.3 shows how the longitudinal and transverse resistivity evolve in the case one, two or three parallel conduction channels of electrons contribute to the transport. With more than two conduction channels, it is complex to determine the analytic expression for ρ_{xx} and ρ_{xy} , which are here computed by inverting numerical calculations of Eq. (A.14). The classical magnetoresistance in Fig. A.3b changes from a flat curve, when only one channel is present, to a rounded shape, when the higher mobility Channel II is added, to a sharp cusp-like trend, when also Channel III is added. An important change is observed also in the Hall effect in Fig. A.3c, which goes from linear, with only

one channel, to a single or double nonlinearity when two or three channels are present, respectively. We note that the features of multichannel conduction are well-evident in the presented curves because the parameters in [Table A.1](#) are remarkably different from each other. In materials where multichannel conduction occurs, these parameters can often be quite similar in value, so that nonlinearities in experimental curves are not so sharp. Precise determination of experimental carrier densities and mobilities can thus be a quite tedious process, which needs to be complemented with additional measurement techniques.

REFERENCES

- [1] J. Bardeen and W. H. Brattain, *The transistor, a semi-conductor triode*, *Physical Review* **74**, 230 (1948).
- [2] D. Basov, R. Averitt, and D. Hsieh, *Towards properties on demand in quantum materials*, *Nature Materials* **16**, 1077 (2017).
- [3] B. Keimer and J. Moore, *The physics of quantum materials*, *Nature Physics* (2017).
- [4] K. A. Moler, *Imaging quantum materials*, *Nature Materials* **16** (2017).
- [5] A. Soumyanarayanan, M. M. Yee, Y. He, J. van Wezel, D. J. Rahn, K. Rossnagel, E. Hudson, M. R. Norman, and J. E. Hoffman, *Quantum phase transition from triangular to stripe charge order in $NbSe_2$* , *Proceedings of the National Academy of Sciences* **110**, 1623 (2013).
- [6] P. Milde, D. Köhler, J. Seidel, L. Eng, A. Bauer, A. Chacon, J. Kindervater, S. Mühlbauer, C. Pfleiderer, S. Buhrandt, *et al.*, *Unwinding of a skyrmion lattice by magnetic monopoles*, *Science* **340**, 1076 (2013).
- [7] J. Hoffman, E. Hudson, K. Lang, V. Madhavan, H. Eisaki, S. Uchida, and J. Davis, *A four unit cell periodic pattern of quasi-particle states surrounding vortex cores in $Bi_2Sr_2CaCu_2O_{8+\delta}$* , *Science* **295**, 466 (2002).
- [8] D. B. Strukov, G. S. Snider, D. R. Stewart, and R. S. Williams, *The missing memristor found*, *Nature* **453**, 80 (2008).
- [9] A. Drozdov, M. Erements, I. Troyan, V. Ksenofontov, and S. Shylin, *Conventional superconductivity at 203 Kelvin at high pressures in the sulfur hydride system*, *Nature* **525**, 73 (2015).
- [10] S. Gerber, H. Jang, H. Nojiri, S. Matsuzawa, H. Yasumura, D. Bonn, R. Liang, W. Hardy, Z. Islam, A. Mehta, *et al.*, *Three-dimensional charge density wave order in $YBa_2Cu_3O_{6.67}$ at high magnetic fields*, *Science* **350**, 949 (2015).
- [11] R. Mankowsky, A. Subedi, M. Först, S. Mariager, M. Chollet, H. Lemke, J. Robinson, J. Glowia, M. Minitti, A. Frano, *et al.*, *Nonlinear lattice dynamics as a basis for enhanced superconductivity in $YBa_2Cu_3O_{6.5}$* , *Nature* **516**, 71 (2014).
- [12] M. Forst, A. D. Caviglia, R. Scherwitzl, R. Mankowsky, P. Zubko, V. Khanna, H. Bromberger, S. B. Wilkins, Y.-D. Chuang, W. S. Lee, W. F. Schlotter, J. J. Turner, G. L. Dakovski, M. P. Minitti, J. Robinson, S. R. Clark, D. Jaksch, J.-M. Triscone, J. P. Hill, S. S. Dhesi, and A. Cavalleri, *Spatially resolved ultrafast magnetic dynamics initiated at a complex oxide heterointerface*, *Nature Materials* **14**, 883 (2015).
- [13] J. Chakhalian, J. W. Freeland, A. J. Millis, C. Panagopoulos, and J. M. Rondinelli, *Colloquium: Emergent properties in plane view: Strong correlations at oxide interfaces*, *Reviews of Modern Physics* **86**, 1189 (2014).
- [14] M. Gibert, P. Zubko, R. Scherwitzl, J. Íñiguez, and J.-M. Triscone, *Exchange bias in $LaNiO_3$ - $LaMnO_3$ superlattices*, *Nature Materials* **11**, 195 (2012).
- [15] G. Catalan, *Progress in perovskite nickelate research*, *Phase Transitions* **81**, 729 (2008).
- [16] D. G. Schlom, *Perspective: Oxide molecular-beam epitaxy rocks!* *APL Materials* **3**, 062403 (2015).
- [17] H. M. Christen and G. Eres, *Recent advances in pulsed-laser deposition of complex oxides*, *Journal of Physics: Condensed Matter* **20**, 264005 (2008).
- [18] A. Biswas, K.-S. Kim, and Y. H. Jeong, *Metal-insulator transitions and non-Fermi liquid behaviors in 5d perovskite iridates*, in *Perovskite Materials - Synthesis, Characterisation, Properties, and Applications*, edited by L. Pan and G. Zhu (InTech, Rijeka, 2016) Chap. 07.
- [19] N. Mott and R. Peierls, *Discussion of the paper by de Boer and Verwey*, *Proceedings of the Physical Society* **49**, 72 (1937).

- [20] J. Slater, *Magnetic effects and the Hartree-Fock equation*, *Physical Review* **82**, 538 (1951).
- [21] P. W. Anderson, *Absence of diffusion in certain random lattices*, *Physical Review* **109**, 1492 (1958).
- [22] M. Imada, A. Fujimori, and Y. Tokura, *Metal-insulator transitions*, *Reviews of Modern Physics* **70**, 1039 (1998).
- [23] P.-H. Xiang, N. Zhong, C.-G. Duan, X. Tang, Z. Hu, P. Yang, Z. Zhu, and J. Chu, *Strain controlled metal-insulator transition in epitaxial NdNiO₃ thin films*, *Journal of Applied Physics* **114**, 243713 (2013).
- [24] R. Scherwitzl, P. Zubko, I. G. Lezama, S. Ono, A. F. Morpurgo, G. Catalan, and J.-M. Triscone, *Electric-field control of the metal-insulator transition in ultrathin NdNiO₃ films*, *Advanced Materials* **22**, 5517 (2010).
- [25] M. L. Medarde, *Structural, magnetic and electronic properties of RNiO₃ perovskites (R = rare earth)*, *Journal of Physics: Condensed Matter* **9**, 1679 (1997).
- [26] T. Mizokawa, D. Khomskii, and G. Sawatzky, *Spin and charge ordering in self-doped Mott insulators*, *Physical Review B* **61**, 11263 (2000).
- [27] S. Lee, R. Chen, and L. Balents, *Metal-insulator transition in a two-band model for the perovskite nickelates*, *Physical Review B* **84**, 165119 (2011).
- [28] H. Park, A. J. Millis, and C. A. Marianetti, *Site-selective Mott transition in rare-earth-element nickelates*, *Physical Review Letters* **109**, 156402 (2012).
- [29] A. Subedi, O. E. Peil, and A. Georges, *Low-energy description of the metal-insulator transition in the rare-earth nickelates*, *Physical Review B* **91**, 075128 (2015).
- [30] V. Bisogni, S. Catalano, R. J. Green, M. Gibert, R. Scherwitzl, Y. Huang, V. N. Strocov, P. Zubko, S. Balandeh, J.-M. Triscone, *et al.*, *Ground-state oxygen holes and the metal-insulator transition in the negative charge-transfer rare-earth nickelates*, *Nature Communications* **7**, 13017 (2016).
- [31] X. Obradors, L. Paulius, M. Maple, J. Torrance, A. Nazzal, J. Fontcuberta, and X. Granados, *Pressure dependence of the metal-insulator transition in the charge-transfer oxides RNiO₃ (R = Pr, Nd, Nd_{0.7}La_{0.3})*, *Physical Review B* **47**, 12353 (1993).
- [32] P. Canfield, J. Thompson, S. Cheong, and L. Rupp, *Extraordinary pressure dependence of the metal-to-insulator transition in the charge-transfer compounds NdNiO₃ and PrNiO₃*, *Physical Review B* **47**, 12357 (1993).
- [33] K. Yoshimatsu, T. Soma, and A. Ohtomo, *Insulator-to-metal transition of WO₃ epitaxial films induced by electrochemical Li-ion intercalation*, *Applied Physics Express* **9**, 075802 (2016).
- [34] S. G. Altendorf, J. Jeong, D. Passarello, N. B. Aetukuri, M. G. Samant, and S. S. Parkin, *Facet-independent electric-field-induced volume metallization of tungsten trioxide films*, *Advanced Materials* **28**, 5284 (2016).
- [35] D. W. Bullett, *Bulk and surface electron states in WO₃ and tungsten bronzes*, *Journal of Physics C: Solid State Physics* **16**, 2197 (1983).
- [36] S. K. Deb, *Opportunities and challenges in science and technology of WO₃ for electrochromic and related applications*, *Solar Energy Materials and Solar Cells* **92**, 245 (2008).
- [37] H. Long, W. Zeng, and H. Zhang, *Synthesis of WO₃ and its gas sensing: A review*, *Journal of Materials Science: Materials in Electronics* **26**, 4698 (2015).
- [38] S. Cong, F. Geng, and Z. Zhao, *Tungsten oxide materials for optoelectronic applications*, *Advanced Materials* **28**, 10518 (2016).
- [39] H. Zheng, J. Z. Ou, M. S. Strano, R. B. Kaner, A. Mitchell, and K. Kalantar-zadeh, *Nanostructured tungsten oxide – properties, synthesis, and applications*, *Advanced Functional Materials* **21**, 2175 (2011).
- [40] H. Hamdi, E. K. Salje, P. Ghosez, and E. Bousquet, *First-principles reinvestigation of bulk WO₃*, *Physical Review B* **94**, 245124 (2016).
- [41] Y. Du, M. Gu, T. Varga, C. Wang, M. E. Bowden, and S. A. Chambers, *Strain accommodation by facile WO₆ octahedral distortion and tilting during WO₃ heteroepitaxy on SrTiO₃ (001)*, *ACS Applied Materials*

- & Interfaces **6**, 14253 (2014).
- [42] X. Leng, J. Pereira, J. Strle, A. T. Bollinger, and I. Božović, *Epitaxial growth of high quality WO_3 thin films*, *APL Materials* **3**, 096102 (2015).
- [43] H. Kalthori, S. B. Porter, A. S. Esmaily, M. Coey, M. Ranjbar, and H. Salamati, *Morphology and structural studies of WO_3 films deposited on $SrTiO_3$ by pulsed laser deposition*, *Applied Surface Science* **390**, 43 (2016).
- [44] A. Herklotz, S. F. Rus, S. Kc, V. R. Cooper, A. Huon, E.-J. Guo, and T. Z. Ward, *Symmetry driven control of optical properties in WO_3 films*, *APL Materials* **5**, 066106 (2017).
- [45] P. Sermon and G. Bond, *Hydrogen spillover*, *Catalysis Reviews* **8**, 211 (1974).
- [46] H. Yoon, M. Choi, T.-W. Lim, H. Kwon, K. Ihm, J. K. Kim, S.-Y. Choi, and J. Son, *Reversible phase modulation and hydrogen storage in multivalent VO_2 epitaxial thin films*, *Nature Materials* **15**, 1113 (2016).
- [47] N. Nakagawa, H. Y. Hwang, and D. A. Muller, *Why some interfaces cannot be sharp*, *Nature Materials* **5**, 204 (2006).
- [48] S. Thiel, G. Hammerl, A. Schmehl, C. Schneider, and J. Mannhart, *Tunable quasi-two-dimensional electron gases in oxide heterostructures*, *Science* **313**, 1942 (2006).
- [49] N. Reyren, S. Thiel, A. Caviglia, L. F. Kourkoutis, G. Hammerl, C. Richter, C. Schneider, T. Kopp, A.-S. Rüetschi, D. Jaccard, *et al.*, *Superconducting interfaces between insulating oxides*, *Science* **317**, 1196 (2007).
- [50] A. Caviglia, S. Gariglio, N. Reyren, D. Jaccard, T. Schneider, M. Gabay, S. Thiel, G. Hammerl, J. Mannhart, and J.-M. Triscone, *Electric field control of the $LaAlO_3/SrTiO_3$ interface ground state*, *Nature* **456**, 624 (2008).
- [51] A. Caviglia, M. Gabay, S. Gariglio, N. Reyren, C. Cancellieri, and J.-M. Triscone, *Tunable Rashba spin-orbit interaction at oxide interfaces*, *Physical Review Letters* **104**, 126803 (2010).
- [52] M. Diez, A. Monteiro, G. Mattoni, E. Cobanera, T. Hyart, E. Mulazimoglu, N. Bovenzi, C. Beenakker, and A. Caviglia, *Giant negative magnetoresistance driven by spin-orbit coupling at the $LaAlO_3/SrTiO_3$ interface*, *Physical Review Letters* **115**, 016803 (2015).
- [53] J. A. Bert, B. Kalisky, C. Bell, M. Kim, Y. Hikita, H. Y. Hwang, and K. A. Moler, *Direct imaging of the coexistence of ferromagnetism and superconductivity at the $LaAlO_3/SrTiO_3$ interface*, *Nature Physics* **7**, 767 (2011).
- [54] L. Li, C. Richter, J. Mannhart, and R. Ashoori, *Coexistence of magnetic order and two-dimensional superconductivity at $LaAlO_3/SrTiO_3$ interfaces*, *Nature Physics* **7**, 762 (2011).
- [55] A. Ohtomo and H. Hwang, *A high-mobility electron gas at the $LaAlO_3/SrTiO_3$ heterointerface*, *Nature* **427**, 423 (2004).
- [56] J. Nishimura, A. Ohtomo, A. Ohkubo, Y. Murakami, and M. Kawasaki, *Controlled carrier generation at a polarity-discontinued perovskite heterointerface*, *Japanese Journal of Applied Physics* **43**, L1032 (2004).
- [57] A. Kalabukhov, R. Gunnarsson, J. Börjesson, E. Olsson, T. Claeson, and D. Winkler, *Effect of oxygen vacancies in the $SrTiO_3$ substrate on the electrical properties of the $LaAlO_3/SrTiO_3$ interface*, *Physical Review B* **75**, 121404 (2007).
- [58] F. Gunkel, P. Brinks, S. Hoffmann-Eifert, R. Dittmann, M. Huijben, J. Kleibeuker, G. Koster, G. Rijnders, and R. Waser, *Influence of charge compensation mechanisms on the sheet electron density at conducting $LaAlO_3/SrTiO_3$ interfaces*, *Applied Physics Letters* **100**, 052103 (2012).
- [59] M. Warusawithana, C. Richter, J. Mundy, P. Roy, J. Ludwig, S. Paetel, T. Heeg, A. Pawlicki, L. Kourkoutis, M. Zheng, *et al.*, *$LaAlO_3$ stoichiometry is key to electron liquid formation at $LaAlO_3/SrTiO_3$ interfaces*, *Nature Communications* **4** (2013).
- [60] L. Yu and A. Zunger, *A polarity-induced defect mechanism for conductivity and magnetism at polar-nonpolar oxide interfaces*, *Nature Communications* **5** (2014).

- [61] G. Mattoni, P. Zubko, F. Maccherozzi, A. J. van der Torren, D. B. Boltje, M. Hadjimichael, N. Manca, S. Catalano, M. Gibert, Y. Liu, *et al.*, *Striped nanoscale phase separation at the metal–insulator transition of heteroepitaxial nickelates*, *Nature Communications* **7** (2016).
- [62] J. Garcia-Munoz, J. Rodriguez-Carvajal, P. Lacorre, and J. Torrance, *Neutron-diffraction study of $R\text{NiO}_3$ ($R = \text{La}, \text{Pr}, \text{Nd}, \text{Sm}$): Electronically induced structural changes across the metal–insulator transition*, *Physical Review B* **46**, 4414 (1992).
- [63] J. García-Muñoz, J. Rodriguez-Carvajal, and P. Lacorre, *Neutron-diffraction study of the magnetic ordering in the insulating regime of the perovskites $R\text{NiO}_3$ ($R = \text{Pr}$ and Nd)*, *Physical Review B* **50**, 978 (1994).
- [64] V. Scagnoli, U. Staub, Y. Bodenthin, M. Garcia-Fernandez, A. Mulders, G. Meijer, and G. Hammerl, *Induced noncollinear magnetic order of Nd_3^+ in NdNiO_3 observed by resonant soft X-ray diffraction*, *Physical Review B* **77**, 115138 (2008).
- [65] A. Caviglia, M. Först, R. Scherwitzl, V. Khanna, H. Bromberger, R. Mankowsky, R. Singla, Y.-D. Chuang, W. Lee, O. Krupin, *et al.*, *Photoinduced melting of magnetic order in the correlated electron insulator NdNiO_3* , *Physical Review B* **88**, 220401 (2013).
- [66] S. Johnston, A. Mukherjee, I. Elfimov, M. Berciu, and G. A. Sawatzky, *Charge disproportionation without charge transfer in the rare-earth-element nickelates as a possible mechanism for the metal–insulator transition*, *Physical Review Letters* **112**, 106404 (2014).
- [67] W. J. Hardy, H. Ji, E. Mikheev, S. Stemmer, and D. Natelson, *Nanostructure investigations of nonlinear differential conductance in NdNiO_3 thin films*, *Physical Review B* **90**, 205117 (2014).
- [68] M. H. Upton, Y. Choi, H. Park, J. Liu, D. Meyers, J. Chakhalian, S. Middey, J.-W. Kim, and P. J. Ryan, *Novel electronic behavior driving NdNiO_3 metal–insulator transition*, *Physical Review Letters* **115**, 036401 (2015).
- [69] G. Catalan, R. Bowman, and J. Gregg, *Metal–insulator transitions in NdNiO_3 thin films*, *Physical Review B* **62**, 7892 (2000).
- [70] A. Caviglia, R. Scherwitzl, P. Popovich, W. Hu, H. Bromberger, R. Singla, M. Mitrano, M. Hoffmann, S. Kaiser, P. Zubko, *et al.*, *Ultrafast strain engineering in complex oxide heterostructures*, *Physical Review Letters* **108**, 136801 (2012).
- [71] J. Liu, M. Kargarian, M. Kareev, B. Gray, P. J. Ryan, A. Cruz, N. Tahir, Y.-D. Chuang, J. Guo, J. M. Rondinelli, *et al.*, *Heterointerface engineered electronic and magnetic phases of NdNiO_3 thin films*, *Nature Communications* **4** (2013).
- [72] S. Catalano, M. Gibert, V. Bisogni, F. He, R. Sutarto, M. Viret, P. Zubko, R. Scherwitzl, G. Sawatzky, T. Schmitt, *et al.*, *Tailoring the electronic transitions of NdNiO_3 films through $(111)_{pc}$ oriented interfaces*, *APL Materials* **3**, 062506 (2015).
- [73] A. J. Hauser, E. Mikheev, N. E. Moreno, J. Hwang, J. Y. Zhang, and S. Stemmer, *Correlation between stoichiometry, strain, and metal–insulator transitions of NdNiO_3 films*, *Applied Physics Letters* **106**, 092104 (2015).
- [74] D. Kumar, K. Rajeev, A. Kushwaha, and R. Budhani, *Heterogeneous nucleation and metal–insulator transition in epitaxial films of NdNiO_3* , *Journal of Applied Physics* **108**, 063503 (2010).
- [75] D. Kumar, K. Rajeev, J. Alonso, and M. Martinez-Lope, *Slow dynamics in hard condensed matter: A case study of the phase separating system NdNiO_3* , *Journal of Physics: Condensed Matter* **21**, 185402 (2009).
- [76] S. Asanuma, P.-H. Xiang, H. Yamada, H. Sato, H. Inoue, H. Akoh, A. Sawa, K. Ueno, H. Shimotani, H. Yuan, *et al.*, *Tuning of the metal–insulator transition in electrolyte-gated NdNiO_3 thin films*, *Applied Physics Letters* **97**, 142110 (2010).
- [77] J. Son, B. Jalan, A. P. Kajdos, L. Balents, S. J. Allen, and S. Stemmer, *Probing the metal–insulator transition of NdNiO_3 by electrostatic doping*, *Applied Physics Letters* **99**, 192107 (2011).
- [78] J. Shi, Y. Zhou, and S. Ramanathan, *Colossal resistance switching and band gap modulation in a perovskite nickelate by electron doping*, *Nature Communications* **5** (2014).

- [79] C. Cen, S. Thiel, J. Mannhart, and J. Levy, *Oxide nanoelectronics on demand*, *Science* **323**, 1026 (2009).
- [80] R. Jany, C. Richter, C. Woltmann, G. Pfanzelt, B. Förg, M. Rommel, T. Reindl, U. Waizmann, J. Weis, J. A. Mundy, *et al.*, *Monolithically integrated circuits from functional oxides*, *Advanced Materials Interfaces* **1** (2014).
- [81] M. Fäth, S. Freisem, A. Menovsky, Y. Tomioka, J. Aarts, and J. Mydosh, *Spatially inhomogeneous metal-insulator transition in doped manganites*, *Science* **285**, 1540 (1999).
- [82] M. M. Qazilbash, M. Brehm, B.-G. Chae, P.-C. Ho, G. O. Andreev, B.-J. Kim, S. J. Yun, A. Balatsky, M. Maple, F. Keilmann, *et al.*, *Mott transition in VO_2 revealed by infrared spectroscopy and nano-imaging*, *Science* **318**, 1750 (2007).
- [83] T.-H. Kim, M. Angst, B. Hu, R. Jin, X.-G. Zhang, J. Wendelken, E. Plummer, and A.-P. Li, *Imaging and manipulation of the competing electronic phases near the Mott metal-insulator transition*, *Proceedings of the National Academy of Sciences* **107**, 5272 (2010).
- [84] Y. Choi, D. J. Keavney, M. V. Holt, V. Uhlir, D. Arena, E. E. Fullerton, P. J. Ryan, and J.-W. Kim, *Critical phenomena of nano phase evolution in a first order transition*, preprint arXiv:1405.4319 (2014).
- [85] D. Siegel, F. El Gabaly, K. McCarty, and N. Bartelt, *In situ characterization of the formation of a mixed conducting phase on the surface of yttria-stabilized zirconia near Pt electrodes*, *Physical Review B* **92**, 125421 (2015).
- [86] J. Liu, S. Okamoto, M. Van Veenendaal, M. Kareev, B. Gray, P. Ryan, J. Freeland, and J. Chakhalian, *Quantum confinement of Mott electrons in ultrathin $LaNiO_3/LaAlO_3$ superlattices*, *Physical Review B* **83**, 161102 (2011).
- [87] V. Kiryukhin, D. Casa, J. Hill, B. Keimer, A. Vigliante, Y. Tomioka, and Y. Tokura, *An X-ray-induced insulator-metal transition in a magnetoresistive manganite*, *Nature* **386**, 813 (1997).
- [88] I. Tung, P. Balachandran, J. Liu, B. Gray, E. Karapetrova, J. Lee, J. Chakhalian, M. Bedzyk, J. Rondinelli, and J. Freeland, *Connecting bulk symmetry and orbital polarization in strained $RNiO_3$ ultrathin films*, *Physical Review B* **88**, 205112 (2013).
- [89] D. P. Kumah, A. S. Disa, J. H. Ngai, H. Chen, A. Malashevich, J. W. Reiner, S. Ismail-Beigi, F. J. Walker, and C. H. Ahn, *Tuning the structure of nickelates to achieve two-dimensional electron conduction*, *Advanced Materials* **26**, 1935 (2014).
- [90] M. Grisolia, J. Varignon, G. Sanchez-Santolino, A. Arora, S. Valencia, M. Varela, R. Abrudan, E. Weschke, E. Schierle, J. Rault, *et al.*, *Hybridization-controlled charge transfer and induced magnetism at correlated oxide interfaces*, *Nature Physics* **12**, 484 (2016).
- [91] J. Fowlie, M. Gibert, G. Tieri, A. Gloter, J. Íñiguez, A. Filippetti, S. Catalano, S. Gariglio, A. Schober, M. Guennou, *et al.*, *Conductivity and local structure of $LaNiO_3$ thin films*, *Advanced Materials* **29** (2017).
- [92] A. Tiwari, C. Jin, and J. Narayan, *Strain-induced tuning of metal-insulator transition in $NdNiO_3$* , *Applied Physics Letters* **80**, 4039 (2002).
- [93] A. Boris, Y. Matiks, E. Benckiser, A. Frano, P. Popovich, V. Hinkov, P. Wochner, M. Castro-Colin, E. Detemple, V. K. Malik, *et al.*, *Dimensionality control of electronic phase transitions in nickel-oxide superlattices*, *Science* **332**, 937 (2011).
- [94] G. Berner, M. Sing, F. Pfaff, E. Benckiser, M. Wu, G. Christiani, G. Logvenov, H.-U. Habermeier, M. Kobayashi, V. Strocov, *et al.*, *Dimensionality-tuned electronic structure of nickelate superlattices explored by soft-X-ray angle-resolved photoelectron spectroscopy*, *Physical Review B* **92**, 125130 (2015).
- [95] P. Ruello, S. Zhang, P. Laffez, B. Perrin, and V. Gusev, *Ultrafast electronic dynamics in the metal-insulator transition compound $NdNiO_3$* , *Physical Review B* **76**, 165107 (2007).
- [96] M. Först, K. Beyerlein, R. Mankowsky, W. Hu, G. Mattoni, S. Catalano, M. Gibert, O. Yefanov, J. Clark, A. Frano, *et al.*, *Multiple supersonic phase fronts launched at a complex-oxide heterointerface*, *Physical Review Letters* **118**, 027401 (2017).
- [97] X. Granados, J. Fontcuberta, X. Obradors, L. Manosa, and J. Torrance, *Metallic state and the metal-*

- insulator transition of NdNiO₃*, *Physical Review B* **48**, 11666 (1993).
- [98] L. Pellegrino, N. Manca, T. Kanki, H. Tanaka, M. Biasotti, E. Bellingeri, A. S. Siri, and D. Marré, *Multistate memory devices based on free-standing VO₂/TiO₂ microstructures driven by Joule self-heating*, *Advanced Materials* **24**, 2929 (2012).
- [99] V. Franco, F. Béron, K. Pirota, M. Knobel, and M. Willard, *Characterization of the magnetic interactions of multiphase magnetocaloric materials using first-order reversal curve analysis*, *Journal of Applied Physics* **117**, 17C124 (2015).
- [100] V. Orera, L. Trinkler, R. Merino, and A. Larrea, *The optical properties of the Nd₃⁺ ion in NdGaO₃ and LaGaO₃:Nd: Temperature and concentration dependence*, *Journal of Physics: Condensed Matter* **7**, 9657 (1995).
- [101] W. Schnelle, R. Fischer, and E. Gmelin, *Specific heat capacity and thermal conductivity of NdGaO₃ and LaAlO₃ single crystals at low temperatures*, *Journal of Physics D: Applied Physics* **34**, 846 (2001).
- [102] M. Hooda and C. Yadav, *Electronic properties and the nature of metal–insulator transition in NdNiO₃ prepared at ambient oxygen pressure*, *Physica B: Condensed Matter* **491**, 31 (2016).
- [103] G. Mattoni, A. Filippetti, N. Manca, P. Zubko, and A. D. Caviglia, *Charge doping and large lattice expansion in oxygen-deficient heteroepitaxial WO₃*, arXiv preprint arXiv:1711.05106 (2017).
- [104] C. G. Granqvist, *Electrochromic tungsten oxide films: Review of progress 1993–1998*, *Solar Energy Materials and Solar Cells* **60**, 201 (2000).
- [105] D. Hirai, E. Climent-Pascual, and R. J. Cava, *Superconductivity in WO_{2.6}F_{0.4} synthesized by reaction of WO₃ with teflon*, *Physical Review B* **84**, 174519 (2011).
- [106] N. Haldolaarachchige, Q. Gibson, J. Krizan, and R. J. Cava, *Superconducting properties of the K_xWO₃ tetragonal tungsten bronze and the superconducting phase diagram of the tungsten bronze family*, *Physical Review B* **89**, 104520 (2014).
- [107] T. Soma, K. Yoshimatsu, and A. Ohtomo, *Epitaxial growth of hexagonal tungsten bronze Cs_xWO₃ films in superconducting phase region exceeding bulk limit*, *Applied Physics Express* **9**, 075801 (2016).
- [108] L. J. LeGore, O. D. Greenwood, J. W. Paulus, D. J. Frankel, and R. J. Lad, *Controlled growth of WO₃ films*, *Journal of Vacuum Science & Technology A: Vacuum, Surfaces, and Films* **15**, 1223 (1997).
- [109] P. Tägtström and U. Jansson, *Chemical vapour deposition of epitaxial WO₃ films*, *Thin Solid Films* **352**, 107 (1999).
- [110] W. Sahle and M. Nygren, *Electrical conductivity and high resolution electron microscopy studies of WO_{3-x} crystals with 0 ≤ x ≤ 0.28*, *Journal of Solid State Chemistry* **48**, 154 (1983).
- [111] X. He, Y. Yin, J. Guo, H. Yuan, Y. Peng, Y. Zhou, D. Zhao, K. Hai, W. Zhou, and D. Tang, *Memristive properties of hexagonal WO₃ nanowires induced by oxygen vacancy migration*, *Nanoscale Research Letters* **8**, 50 (2013).
- [112] X. Meng, F. Quenneville, F. Venne, E. Di Mauro, D. Işık, M. Barbosa, Y. Drolet, M. M. Natile, D. Rochefort, F. Soavi, et al., *Electrolyte-gated WO₃ transistors: Electrochemistry, structure, and device performance*, *The Journal of Physical Chemistry C* **119**, 21732 (2015).
- [113] S. Wicklein, A. Sambri, S. Amoruso, X. Wang, R. Bruzzese, A. Koehl, and R. Dittmann, *Pulsed laser ablation of complex oxides: The role of congruent ablation and preferential scattering for the film stoichiometry*, *Applied Physics Letters* **101**, 131601 (2012).
- [114] D. J. Groenendijk, N. Manca, G. Mattoni, L. Kootstra, S. Gariglio, Y. Huang, E. van Heumen, and A. D. Caviglia, *Epitaxial growth and thermodynamic stability of SrIrO₃/SrTiO₃ heterostructures*, *Applied Physics Letters* **109**, 041906 (2016).
- [115] J. H. Haeni, C. D. Theis, and D. G. Schlom, *RHEED intensity oscillations for the stoichiometric growth of SrTiO₃ thin films by reactive molecular beam epitaxy*, *Journal of Electroceramics* **4**, 385 (2000).
- [116] Y. He, M. Gu, H. Xiao, L. Luo, Y. Shao, F. Gao, Y. Du, S. X. Mao, and C. Wang, *Atomistic conversion reaction mechanism of WO₃ in secondary ion batteries of Li, Na, and Ca*, *Angewandte Chemie International*

- Edition **55**, 6244 (2016).
- [117] Z. Wang, Y. He, M. Gu, Y. Du, S. X. Mao, and C. Wang, *Electron transfer governed crystal transformation of tungsten trioxide upon Li ions intercalation*, *ACS Applied Materials & Interfaces* **8**, 24567 (2016).
- [118] S. McIntosh, J. F. Vente, W. G. Haije, D. H. Blank, and H. J. Bouwmeester, *Oxygen stoichiometry and chemical expansion of $Ba_{0.5}Sr_{0.5}Co_{0.8}Fe_{0.2}O_{3-\delta}$ measured by in situ neutron diffraction*, *Chemistry of Materials* **18**, 2187 (2006).
- [119] E. Choi, J. Kim, D. Cuong, and J. Lee, *Oxygen vacancies in $SrTiO_3$* , in *17th IEEE International Symposium on the Applications of Ferroelectrics, 2008*, Vol. 1 (IEEE, 2008) pp. 1–2.
- [120] M. Lorenz, G. Wagner, V. Lazenka, P. Schwinkendorf, M. Bonholzer, M. J. Van Bael, A. Vantomme, K. Temst, O. Oeckler, and M. Grundmann, *Correlation of high magnetoelectric coupling with oxygen vacancy superstructure in epitaxial multiferroic $BaTiO_3$ – $BiFeO_3$ composite thin films*, *Materials* **9**, 44 (2016).
- [121] E. Enriquez, A. Chen, Z. Harrell, P. Dowden, N. Koskelo, J. Roback, M. Janoschek, C. Chen, and Q. Jia, *Oxygen vacancy-tuned physical properties in perovskite thin films with multiple B-site valence states*, *Scientific Reports* **7** (2017).
- [122] A. Filippetti, C. D. Pemmaraju, S. Sanvito, P. Delugas, D. Puggioni, and V. Fiorentini, *Variational pseudo-self-interaction-corrected density functional approach to the ab initio description of correlated solids and molecules*, *Physical Review B* **84**, 195127 (2011).
- [123] T. Archer, C. D. Pemmaraju, S. Sanvito, C. Franchini, J. He, A. Filippetti, P. Delugas, D. Puggioni, V. Fiorentini, R. Tiwari, and P. Majumdar, *Exchange interactions and magnetic phases of transition metal oxides: Benchmarking advanced ab initio methods*, *Physical Review B* **84**, 115114 (2011).
- [124] D. Puggioni, A. Filippetti, and V. Fiorentini, *Ordering and multiple phase transitions in ultrathin nickelate superlattices*, *Physical Review B* **86**, 195132 (2012).
- [125] P. Delugas, A. Filippetti, A. Gadaleta, I. Pallecchi, D. Marré, and V. Fiorentini, *Large band offset as driving force of two-dimensional electron confinement: The case of $SrTiO_3/SrZrO_3$ interface*, *Physical Review B* **88**, 115304 (2013).
- [126] D. Marrocchelli, S. Bishop, H. Tuller, G. Watson, and B. Yildiz, *Charge localization increases chemical expansion in cerium-based oxides*, *Physical Chemistry Chemical Physics* **14** (2012).
- [127] D. Marrocchelli, S. Bishop, and J. Kilner, *Chemical expansion and its dependence on the host cation radius*, *Journal of Materials Chemistry A* **1** (2013).
- [128] A. Glensk, B. Grabowski, T. Hickel, and J. Neugebauer, *Breakdown of the Arrhenius law in describing vacancy formation energies: The importance of local anharmonicity revealed by ab initio thermodynamics*, *Physical Review X* **4**, 011018 (2014).
- [129] K. Bange, *Colouration of tungsten oxide films: A model for optically active coatings*, *Solar Energy Materials and Solar Cells* **58**, 1 (1999).
- [130] A. Filippetti, P. Delugas, M. J. Verstraete, I. Pallecchi, A. Gadaleta, D. Marré, D. F. Li, S. Gariglio, and V. Fiorentini, *Thermopower in oxide heterostructures: The importance of being multiple-band conductors*, *Physical Review B* **86**, 195301 (2012).
- [131] P. Delugas, A. Filippetti, M. J. Verstraete, I. Pallecchi, D. Marré, and V. Fiorentini, *Doping-induced dimensional crossover and thermopower burst in Nb-doped $SrTiO$ superlattices*, *Physical Review B* **88**, 045310 (2013).
- [132] P. González-Borrero, F. Sato, A. Medina, M. L. Baesso, A. C. Bento, G. Baldissera, C. Persson, G. A. Niklasson, C. G. Granqvist, and A. Ferreira da Silva, *Optical band-gap determination of nanostructured WO_3 film*, *Applied Physics Letters* **96**, 061909 (2010).
- [133] M. B. Johansson, G. Baldissera, I. Valyukh, C. Persson, H. Arwin, G. A. Niklasson, and L. Österlund, *Electronic and optical properties of nanocrystalline WO_3 thin films studied by optical spectroscopy and density functional calculations*, *Journal of Physics: Condensed Matter* **25**, 205502 (2013).

- [134] F. Wang, C. Di Valentin, and G. Pacchioni, *Electronic and structural properties of WO_3 : A systematic hybrid DFT study*, *The Journal of Physical Chemistry C* **115**, 8345 (2011).
- [135] P. Woodward, A. Sleight, and T. Vogt, *Structure refinement of triclinic tungsten trioxide*, *Journal of Physics and Chemistry of Solids* **56**, 1305 (1995).
- [136] A. Van de Walle and G. Ceder, *Correcting overbinding in local-density-approximation calculations*, *Physical Review B* **59**, 14992 (1999).
- [137] P. Haas, F. Tran, and P. Blaha, *Calculation of the lattice constant of solids with semilocal functionals*, *Physical Review B* **79**, 085104 (2009).
- [138] D. G. Barton, M. Shtein, R. D. Wilson, S. L. Soled, and E. Iglesia, *Structure and electronic properties of solid acids based on tungsten oxide nanostructures*, *The Journal of Physical Chemistry B* **103**, 630 (1999).
- [139] R. Vemuri, M. H. Engelhard, and C. Ramana, *Correlation between surface chemistry, density, and band gap in nanocrystalline WO_3 thin films*, *ACS Applied Materials & Interfaces* **4**, 1371 (2012).
- [140] G. Mattoni, D. J. Baek, N. Manca, N. Verhagen, D. Groenendijk, L. F. Kourkoutis, A. Filippetti, and A. D. Caviglia, *Insulator-to-metal transition at oxide interfaces induced by WO_3 overlayers*, *ACS Applied Materials & Interfaces* (2017).
- [141] N. Bristowe, P. Littlewood, and E. Artacho, *Surface defects and conduction in polar oxide heterostructures*, *Physical Review B* **83**, 205405 (2011).
- [142] M. Huijben, G. Koster, M. K. Kruijze, S. Wenderich, J. Verbeeck, S. Bals, E. Slooten, B. Shi, H. J. Molegraaf, J. E. Kleibeuker, *et al.*, *Defect engineering in oxide heterostructures by enhanced oxygen surface exchange*, *Advanced Functional Materials* **23**, 5240 (2013).
- [143] Y. Chen, F. Trier, T. Wijnands, R. Green, N. Gauquelin, R. Egoavil, D. V. Christensen, G. Koster, M. Huijben, N. Bovet, *et al.*, *Extreme mobility enhancement of two-dimensional electron gases at oxide interfaces by charge-transfer-induced modulation doping*, *Nature Materials* **14**, 801 (2015).
- [144] Y. Xie, C. Bell, Y. Hikita, S. Harashima, and H. Y. Hwang, *Enhancing electron mobility at the $LaAlO_3/SrTiO_3$ interface by surface control*, *Advanced Materials* **25**, 4735 (2013).
- [145] Y. Chen, N. Bovet, F. Trier, D. Christensen, F. Qu, N. H. Andersen, T. Kasama, W. Zhang, R. Giraud, J. Dufouleur, *et al.*, *A high-mobility two-dimensional electron gas at the spinel/perovskite interface of γ - $Al_2O_3/SrTiO_3$* , *Nature Communications* **4**, 1371 (2013).
- [146] S. Wu, X. Luo, S. Turner, H. Peng, W. Lin, J. Ding, A. David, B. Wang, G. Van Tendeloo, J. Wang, *et al.*, *Nonvolatile resistive switching in $Pt/LaAlO_3/SrTiO_3$ heterostructures*, *Physical Review X* **3**, 041027 (2013).
- [147] E. Lesne, N. Reyren, D. Doennig, R. Mattana, H. Jaffrès, V. Cros, F. Petroff, F. Choueikani, P. Ohresser, R. Pentcheva, *et al.*, *Suppression of the critical thickness threshold for conductivity at the $LaAlO_3/SrTiO_3$ interface*, *Nature Communications* **5** (2014).
- [148] M. Arab, A. L. Lopes-Moriyama, T. R. dos Santos, C. P. de Souza, J. R. Gavarri, and C. Leroux, *Strontium and cerium tungstate materials $SrWO_4$ and $Ce_2(WO_4)_3$: Methane oxidation and mixed conduction*, *Catalysis Today* **208**, 35 (2013).
- [149] N. Mott, *Conduction in non-crystalline systems IX. The minimum metallic conductivity*, *Philosophical Magazine* **26**, 1015 (1972).
- [150] D. Licciardello and D. Thouless, *Constancy of minimum metallic conductivity in two dimensions*, *Physical Review Letters* **35**, 1475 (1975).
- [151] S. Kravchenko and M. Sarachik, *Metal-insulator transition in two-dimensional electron systems*, *Reports on Progress in Physics* **67**, 1 (2003).
- [152] S. Gariglio, N. Reyren, A. Caviglia, and J.-M. Triscone, *Superconductivity at the $LaAlO_3/SrTiO_3$ interface*, *Journal of Physics: Condensed Matter* **21**, 164213 (2009).
- [153] D. C. Vaz, E. Lesne, A. Sander, H. Naganuma, E. Jacquet, J. Santamaria, A. Barthélémy, and M. Bibes, *Tuning up or down the critical thickness in $LaAlO_3/SrTiO_3$ through in situ deposition of metal overlayers*, *Advanced Materials* (2017).

- [154] F. Gunkel, S. Hoffmann-Eifert, R. A. Heinen, D. V. Christensen, Y. Chen, N. Pryds, R. Waser, and R. Dittmann, *Thermodynamic ground states of complex oxide heterointerfaces*, *ACS Applied Materials & Interfaces* **9**, 1086 (2016).
- [155] Y. Chen, N. Pryds, J. E. Kleibecker, G. Koster, J. Sun, E. Stamate, B. Shen, G. Rijnders, and S. Linderoth, *Metallic and insulating interfaces of amorphous SrTiO₃-based oxide heterostructures*, *Nano Letters* **11**, 3774 (2011).
- [156] A. Joshua, S. Pecker, J. Ruhman, E. Altman, and S. Ilani, *A universal critical density underlying the physics of electrons at the LaAlO₃/SrTiO₃ interface*, *Nature Communications* **3**, 1129 (2012).
- [157] A. McCollam, S. Wenderich, M. Kruize, V. Guduru, H. Molegraaf, M. Huijben, G. Koster, D. Blank, G. Rijnders, A. Brinkman, *et al.*, *Quantum oscillations and subband properties of the two-dimensional electron gas at the LaAlO₃/SrTiO₃ interface*, *APL Materials* **2**, 022102 (2014).
- [158] R. Pentcheva, M. Huijben, K. Otte, W. E. Pickett, J. Kleibecker, J. Huijben, H. Boschker, D. Kockmann, W. Siemons, G. Koster, *et al.*, *Parallel electron-hole bilayer conductivity from electronic interface reconstruction*, *Physical Review Letters* **104**, 166804 (2010).
- [159] F. Gunkel, C. Bell, H. Inoue, B. Kim, A. G. Swart, T. A. Merz, Y. Hikita, S. Harashima, H. K. Sato, M. Minohara, *et al.*, *Defect control of conventional and anomalous electron transport at complex oxide interfaces*, *Physical Review X* **6**, 031035 (2016).
- [160] J. S. Kim, S. S. A. Seo, M. F. Chisholm, R. Kremer, H.-U. Habermeier, B. Keimer, and H. N. Lee, *Nonlinear Hall effect and multichannel conduction in LaTiO₃/SrTiO₃ superlattices*, *Physical Review B* **82**, 201407 (2010).
- [161] A. Mirlin, J. Wilke, F. Evers, D. Polyakov, and P. Wölfle, *Strong magnetoresistance induced by long-range disorder*, *Physical Review Letters* **83**, 2801 (1999).
- [162] M. M. Parish and P. B. Littlewood, *Non-saturating magnetoresistance in heavily disordered semiconductors*, *Nature* **426**, 162 (2003).
- [163] A. Fête, C. Cancellieri, D. Li, D. Stornaiuolo, A. Caviglia, S. Gariglio, and J.-M. Triscone, *Growth-induced electron mobility enhancement at the LaAlO₃/SrTiO₃ interface*, *Applied Physics Letters* **106**, 051604 (2015).
- [164] T. Sakudo and H. Unoki, *Dielectric properties of SrTiO₃ at low temperatures*, *Physical Review Letters* **26**, 851 (1971).
- [165] P. Delugas, A. Filippetti, V. Fiorentini, D. I. Bilc, D. Fontaine, and P. Ghosez, *Spontaneous 2-dimensional carrier confinement at the n-type SrTiO₃/LaAlO₃ interface*, *Physical Review Letters* **106**, 166807 (2011).
- [166] P. Schütz, D. Christensen, V. Borisov, F. Pfaff, P. Scheiderer, L. Dudy, M. Zapf, J. Gabel, Y. Chen, N. Pryds, *et al.*, *Microscopic origin of the mobility enhancement at a spinel/perovskite oxide heterointerface revealed by photoemission spectroscopy*, *Physical Review B* **96**, 161409 (2017).
- [167] D. Shoenberg, *Magnetic oscillations in metals*, Press, Cambridge (1984).
- [168] J. Son, P. Moetakef, B. Jalan, O. Bierwagen, N. J. Wright, R. Engel-Herbert, and S. Stemmer, *Epitaxial SrTiO₃ films with electron mobilities exceeding 30 000 cm² V⁻¹ s⁻¹*, *Nature Materials* **9**, 482 (2010).
- [169] A. Caviglia, S. Gariglio, C. Cancellieri, B. Sacepe, A. Fête, N. Reyren, M. Gabay, A. Morpurgo, and J.-M. Triscone, *Two-dimensional quantum oscillations of the conductance at LaAlO₃/SrTiO₃ interfaces*, *Physical Review Letters* **105**, 236802 (2010).
- [170] M. B. Shalom, A. Ron, A. Palevski, and Y. Dagan, *Shubnikov-de Haas oscillations in SrTiO₃/LaAlO₃ interface*, *Physical Review Letters* **105**, 206401 (2010).
- [171] Y. Kozuka, M. Kim, C. Bell, B. G. Kim, Y. Hikita, and H. Hwang, *Two-dimensional normal-state quantum oscillations in a superconducting heterostructure*, *Nature* **462**, 487 (2009).
- [172] W. Wunderlich, H. Ohta, and K. Koumoto, *Enhanced effective mass in doped SrTiO₃ and related perovskites*, *Physica B: Condensed Matter* **404**, 2202 (2009).
- [173] I. Pallecchi, F. Telesio, D. Li, A. Fête, S. Gariglio, J.-M. Triscone, A. Filippetti, P. Delugas, V. Fiorentini, and

- D. Marré, *Giant oscillating thermopower at oxide interfaces*, *Nature Communications* **6** (2015).
- [174] I. Pallecchi, F. Telesio, D. Marré, D. Li, S. Gariglio, J.-M. Triscone, and A. Filippetti, *Large phonon-drag enhancement induced by narrow quantum confinement at the $\text{LaAlO}_3/\text{SrTiO}_3$ interface*, *Physical Review B* **93**, 195309 (2016).
- [175] C. Cancellieri, A. Mishchenko, U. Aschauer, A. Filippetti, C. Faber, O. Barišić, V. Rogalev, T. Schmitt, N. Nagaosa, and V. Strocov, *Polaronic metal state at the $\text{LaAlO}_3/\text{SrTiO}_3$ interface*, *Nature Communications* **7** (2016).
- [176] L. Berggren, A. Azens, and G. A. Niklasson, *Polaron absorption in amorphous tungsten oxide films*, *Journal of Applied Physics* **90**, 1860 (2001).
- [177] P. Zubko, S. Gariglio, M. Gabay, P. Ghosez, and J.-M. Triscone, *Interface physics in complex oxide heterostructures*, *Annual Review of Condensed Matter Physics* **2**, 141 (2011).
- [178] C. Ahn, J.-M. Triscone, and J. Mannhart, *Electric field effect in correlated oxide systems*, *Nature* **424**, 1015 (2003).
- [179] S. V. Kalinin and N. A. Spaldin, *Functional ion defects in transition metal oxides*, *Science* **341**, 858 (2013).
- [180] D. A. Muller, N. Nakagawa, A. Ohtomo, J. L. Grazul, and H. Y. Hwang, *Atomic-scale imaging of nanoengineered oxygen vacancy profiles in SrTiO_3* , *Nature* **430**, 657 (2004).
- [181] J. Jeong, N. Aetukuri, T. Graf, T. D. Schladt, M. G. Samant, and S. S. Parkin, *Suppression of metal–insulator transition in VO_2 by electric field-induced oxygen vacancy formation*, *Science* **339**, 1402 (2013).
- [182] A. B. Stambouli and E. Traversa, *Solid oxide fuel cells (SOFCs): A review of an environmentally clean and efficient source of energy*, *Renewable and Sustainable Energy Reviews* **6**, 433 (2002).
- [183] V. Kharton, F. Marques, and A. Atkinson, *Transport properties of solid oxide electrolyte ceramics: A brief review*, *Solid State Ionics* **174**, 135 (2004).
- [184] R. Waser and M. Aono, *Nanoionics-based resistive switching memories*, *Nature Materials* **6**, 833 (2007).
- [185] S. D. Ha and S. Ramanathan, *Adaptive oxide electronics: A review*, *Journal of Applied Physics* **110**, 14 (2011).
- [186] N. Manca, L. Pellegrino, and D. Marré, *Reversible oxygen vacancies doping in $(\text{La}_{0.7}\text{Sr}_{0.3})\text{MnO}_3$ microbridges by combined self-heating and electromigration*, *Applied Physics Letters* **106**, 203502 (2015).
- [187] M. Prezioso, F. Merrih-Bayat, B. Hoskins, G. Adam, K. K. Likharev, and D. B. Strukov, *Training and operation of an integrated neuromorphic network based on metal-oxide memristors*, *Nature* **521**, 61 (2015).
- [188] S. Kumar, J. P. Strachan, and R. S. Williams, *Chaotic dynamics in nanoscale NbO_2 Mott memristors for analogue computing*, *Nature* **548**, 318 (2017).
- [189] J. G. Swallow, J. J. Kim, J. M. Maloney, D. Chen, J. F. Smith, S. R. Bishop, H. L. Tuller, and K. J. Van Vliet, *Dynamic chemical expansion of thin-film non-stoichiometric oxides at extreme temperatures*, *Nature Materials* (2017).
- [190] J. Zhang, X. Liu, G. Neri, and N. Pinna, *Nanostructured materials for room-temperature gas sensors*, *Advanced Materials* **28**, 795 (2016).
- [191] T. Hübert, L. Boon-Brett, G. Black, and U. Banach, *Hydrogen sensors—a review*, *Sensors and Actuators B: Chemical* **157**, 329 (2011).
- [192] S. Phanichphant, *Semiconductor metal oxides as hydrogen gas sensors*, *Procedia Engineering* **87**, 795 (2014).
- [193] O. K. Varghese, D. Gong, M. Paulose, K. G. Ong, and C. A. Grimes, *Hydrogen sensing using titania nanotubes*, *Sensors and Actuators B: Chemical* **93**, 338 (2003).
- [194] B. Wang, L. Zhu, Y. Yang, N. Xu, and G. Yang, *Fabrication of a SnO_2 nanowire gas sensor and sensor performance for hydrogen*, *The Journal of Physical Chemistry C* **112**, 6643 (2008).
- [195] E. Strelcov, Y. Lilach, and A. Kolmakov, *Gas sensor based on metal–insulator transition in VO_2 nanowire*

- thermistor*, *Nano Letters* **9**, 2322 (2009).
- [196] M. Wang, S. Shen, J. Ni, N. Lu, Z. Li, H.-B. Li, S. Yang, T. Chen, J. Guo, Y. Wang, *et al.*, *Electric-field-controlled phase transformation in WO₃ thin films through hydrogen evolution*, *Advanced Materials* (2017).
- [197] S. Ippolito, S. Kandasamy, K. Kalantar-Zadeh, and W. Wlodarski, *Hydrogen sensing characteristics of WO₃ thin film conductometric sensors activated by Pt and Au catalysts*, *Sensors and Actuators B: Chemical* **108**, 154 (2005).
- [198] W.-C. Hsu, C.-C. Chan, C.-H. Peng, and C.-C. Chang, *Hydrogen sensing characteristics of an electrodeposited WO₃ thin film gasochromic sensor activated by Pt catalyst*, *Thin Solid Films* **516**, 407 (2007).
- [199] J. Kukkola, M. Mohl, A.-R. Leino, J. Mäklin, N. Halonen, A. Shchukarev, Z. Konya, H. Jantunen, and K. Kordas, *Room temperature hydrogen sensors based on metal decorated WO₃ nanowires*, *Sensors and Actuators B: Chemical* **186**, 90 (2013).
- [200] A. Boudiba, C. Zhang, P. Umek, C. Bittencourt, R. Snyders, M.-G. Olivier, and M. Debliquy, *Sensitive and rapid hydrogen sensors based on Pd-WO₃ thick films with different morphologies*, *International Journal of Hydrogen Energy* **38**, 2565 (2013).
- [201] R. S. Crandall and B. W. Faughnan, *Dynamics of coloration of amorphous electrochromic films of WO₃ at low voltages*, *Applied Physics Letters* **28**, 95 (1976).
- [202] H. Chen, N. Xu, S. Deng, D. Lu, Z. Li, J. Zhou, and J. Chen, *Gasochromic effect and relative mechanism of WO₃ nanowire films*, *Nanotechnology* **18**, 205701 (2007).
- [203] L. F. Zhu, J. C. She, J. Y. Luo, S. Z. Deng, J. Chen, and N. S. Xu, *Study of physical and chemical processes of H₂ sensing of Pt-coated WO₃ nanowire films*, *The Journal of Physical Chemistry C* **114**, 15504 (2010).
- [204] P. Shaver, *Activated tungsten oxide gas detectors*, *Applied Physics Letters* **11**, 255 (1967).
- [205] C. Kilic and A. Zunger, *n-type doping of oxides by hydrogen*, *Applied Physics Letters* **81**, 73 (2002).
- [206] C. T. Campbell, *Ultrathin metal films and particles on oxide surfaces: Structural, electronic and chemisorptive properties*, *Surface Science Reports* **27**, 1 (1997).
- [207] C. Zhou, J. Wu, A. Nie, R. C. Forrey, A. Tachibana, and H. Cheng, *On the sequential hydrogen dissociative chemisorption on small platinum clusters: A density functional theory study*, *The Journal of Physical Chemistry C* **111**, 12773 (2007).
- [208] K. K. Mackay, J. B. Freund, and H. T. Johnson, *Hydrogen recombination rates on silica from atomic-scale calculations*, *The Journal of Physical Chemistry C* **120**, 24137 (2016).
- [209] S. Triwahyono, T. Yamada, and H. Hattori, *Kinetic study of hydrogen adsorption on Pt/WO₃-ZrO₂ and WO₃-ZrO₂*, *Applied Catalysis A: General* **250**, 65 (2003).
- [210] Y. Xi, Q. Zhang, and H. Cheng, *Mechanism of hydrogen spillover on WO₃ (001) and formation of H_xWO₃ (x = 0.125, 0.25, 0.375, and 0.5)*, *The Journal of Physical Chemistry C* **118**, 494 (2013).
- [211] J. Y. Luo, S. Z. Deng, Y. T. Tao, F. L. Zhao, L. F. Zhu, L. Gong, J. Chen, and N. S. Xu, *Evidence of localized water molecules and their role in the gasochromic effect of WO₃ nanowire films*, *The Journal of Physical Chemistry C* **113**, 15877 (2009).

CURRICULUM VITÆ

Giordano MATTONI

27/04/1990 Born in Rome, Italy.

EDUCATION

- 2003–2008 High School
Liceo Scientifico *Louis Pasteur*
Rome, Italy
- 2008–2011 BSc. in Materials Science (*cum laude*)
University of Rome Tor Vergata
Rome, Italy
Thesis: *Strain-Induced Faceting Transition of Ge Islands on Vicinal Si(001)*
Supervisor: Dr. A. Sgarlata
- 2011–2013 MSc. in Materials Science and Technology (*magna cum laude*)
University of Rome Tor Vergata
Rome, Italy
Thesis: *Exploring the Controlled Doping and Nanostructuring of Germanium with P₂ Molecules*
Supervisor: Dr. G. Scappucci
- 2013 Internship
Centre for Quantum Computation and Communication Technology
Sydney, Australia
- 2013–2017 PhD in Applied Physics
Delft University of Technology
Delft, The Netherlands
Thesis: *Metal–Insulator Transitions in Heterostructures of Quantum Materials*
Supervisor: Dr. A. D. Caviglia

LIST OF PUBLICATIONS

16. **G. Mattoni**, *et al.*
Mechanical properties of free-standing WO₃ microbridges controlled by H₂ gas
(manuscript in preparation)
15. **G. Mattoni**, B. de Jong, N. Manca, M. Tomellini, and A. D. Caviglia
Hydrogen sensing with heteroepitaxial WO₃
(manuscript in peer review)
14. **G. Mattoni**, A. Filippetti, N. Manca, P. Zubko, and A. D. Caviglia
Charge doping and large lattice expansion in oxygen-deficient heteroepitaxial WO₃
(manuscript in peer review)
13. N. Manca, D. J. Groenendijk, I. Pallecchi, C. Autieri, L. Tang, F. Telesio, **G. Mattoni**, A. McCollam, S. Picozzi, and A. D. Caviglia
Balanced electron–hole transport in spin–orbit semimetal SrIrO₃ heterostructures
(manuscript in peer review)
12. **G. Mattoni**, N. Manca, M. Hadjimichael, P. Zubko, A. J. H. van der Torren, C. Yin, S. Catalano, M. Gibert, F. Maccherozzi, Y. Liu, S. S. Dhesi, and A. D. Caviglia
Light control of the nanoscale phase separation in heteroepitaxial nickelates
(manuscript in peer review)
11. D. J. Groenendijk, C. Autieri, J. Girovsky, M. C. Martinez-Velarte, N. Manca, **G. Mattoni**, A. M. R. V. L. Monteiro, N. Gauquelin, J. Verbeeck, A. F. Otte, M. Gabay, S. Picozzi, and A. D. Caviglia
Spin–orbit semimetal SrIrO₃ in the two-dimensional limit
Physical Review Letters (accepted for publication)
[preprint arXiv:1706.08901](https://arxiv.org/abs/1706.08901)
10. **G. Mattoni**, D. J. Baek, N. Manca, N. Verhagen, D. J. Groenendijk, L. F. Kourkoutis, A. Filippetti, and A. D. Caviglia
Insulator-to-metal transition at oxide interfaces induced by WO₃ overlayers
ACS Applied Materials & Interfaces (2017)
9. N. Manca, L. Pellegrino, T. Kanki, W. J. Venstra, **G. Mattoni**, Y. Higuchi, H. Tanaka, A. D. Caviglia, and D. Marré
Selective high-frequency mechanical actuation driven by the VO₂ electronic instability
Advanced Materials **29**, 35 (2017)

8. N. Manca, L. Pellegrino, T. Kanki, W. J. Venstra, **G. Mattoni**, Y. Higuchi, H. Tanaka, A. D. Caviglia, and D. Marré
VO₂: A phase change material for micromechanics
Proceedings **1**, 294 (2017)
7. M. Först, K. R. Beyerlein, R. Mankowsky, W. Hu, **G. Mattoni**, S. Catalano, M. Gibert, O. Yefanov, J. N. Clark, A. Frano, J. M. Glownia, M. Chollet, H. Lemke, B. Moser, S. P. Collins, S. S. Dhesi, A. D. Caviglia, J.-M. Triscone, and A. Cavalleri
Multiple supersonic phase fronts launched at a complex-oxide heterointerface
Physical Review Letters **118**, 027401 (2017)
6. **G. Mattoni**, P. Zubko, F. Maccherozzi, A. J. H. van der Torren, D. B. Boltje, M. Hadjimichael, N. Manca, S. Catalano, M. Gibert, Y. Liu, J. Aarts, J.-M. Triscone, S. S. Dhesi, and A. D. Caviglia
Striped nanoscale phase separation at the metal–insulator transition of heteroepitaxial nickelates
Nature Communications **7**, 13141 (2016)
5. D. J. Groenendijk, N. Manca, **G. Mattoni**, L. Kootstra, S. Gariglio, Y. Huang, E. van Heumen, and A. D. Caviglia
Epitaxial growth and thermodynamic stability of SrIrO₃/SrTiO₃ heterostructures
Applied Physics Letters **109**, 041906 (2016)
4. M. A. D. Diez, A. M. R. V. L. Monteiro, **G. Mattoni**, E. Cobanera, T. Hyart, E. Mulazimoglu, N. Bovenzi, C. W. J. Beenakker, and A. D. Caviglia
Giant negative magnetoresistance driven by spin-orbit coupling at the LaAlO₃/SrTiO₃ interface
Physical Review Letters **115**, 016803 (2015)
3. G. Capellini, W. M. Klesse, **G. Mattoni**, M. Y. Simmons, and G. Scappucci
Alternative high n-type doping techniques in germanium
ECS Transactions **64**, 163-171 (2014)
2. **G. Mattoni**, W. M. Klesse, G. Capellini, M. Y. Simmons, and G. Scappucci
Phosphorus molecules on Ge (001): A playground for controlled n-doping of germanium at high densities
ACS Nano **7**, 11310–11316 (2013)
1. L. Persichetti, A. Sgarlata, **G. Mattoni**, M. Fanfoni, and A. Balzarotti
Orientational phase diagram of the epitaxially strained Si (001): Evidence of a singular (105) face
Physical Review B **85**, 195314 (2012)

ACKNOWLEDGEMENTS

The four years of this PhD have been a very intense and challenging period of my life, rich of memories and meaningful events. Here, I want to make an attempt at taking a snapshot of all that has been, and acknowledge the ones who made it so special. I know that few lines will never be enough to give the right credits, I will thus limit myself to depict just a few colourful aspects.

THE TOPS

First and foremost, I would like to thank my copromotor, Dr. Andrea D. Caviglia, for giving me the opportunity to do my PhD in this fantastic place, leaving me plenty of freedom and allowing me to collaborate with many beautiful people. Thanks a lot!

I would never have considered Delft for a PhD if it was not for Dr. Gianluca Stefanucci from Tor Vergata, a scientist for whom I have a great esteem and that nurtured my passion for physics. Thanks for telling me, over a random coffee break, about *this funny and nice guy that does very good physics* that you met in Como, and for suggesting me to contact him for a possible PhD position.

An enormous thanks goes to Duca Robbe de la Sabia—vulgarly known as *Herre*—for being *this funny guy* and inviting me for a PhD interview. I really appreciated that he let complex oxides take over me (sorry Herre, molecular break junctions were really not my business) and "limited" himself to being my promotor. The MED atmosphere he created in the group was simply amazing, and it allowed me to quickly develop a pleasant social network, where I could ask and learn everything I needed. Thanks again for all this, and for being always available to provide very expert advice.

My profound gratitude goes to the members of my PhD committee: Nini Pryds, for coming all the way from Copenhagen; Manuel Bibes, for the neat summarising skills that surprisingly gave a very important contribution to this thesis; Alessio Filippetti, for the many valuable theory collaborations—it has been a real pleasure working with you; Guus Rijnders, for keeping high the Dutch research on complex oxides; Yaroslav Blanter, for his inspiring corridor walks and for being always accessible for theory discussions; Peter Steeneken, for his perspectives and the relaxed life chats.

A real asset to the scientific research detailed in this thesis have been the external collaborations with the group of Jean-Marc Triscone, above all thanks for the amazing weekend in Geneva; Michael Forst, I really enjoyed our nickelates business; and Pavlo Zubko, whose thorough investigation of details and joint scientific ventures have been both very profitable and plenty of fun.

A special tribute goes to Gary, for buying an amazing Italian coffee machine, for being always ready for random technical explanations and suggestions which have been an invaluable source of learning; to Teun, for the precious lunch–life chats, and for proving how much better science is when one takes it as his own hobby; to Sander, for being the coolest and most social Sinterklaas I have ever seen, and for taking the liberty to switch

off the degrading social attitude of our group; to Simon, for his fast-growing *G-lab*; to Sonia, for the Mediterranean taste; to Toeno, for his openness; to Anton, for his burning spirit; to Yuli, for being so unique; to Akira and Gao, for taking good care of the coffee room sink; to Diana, for the crazy parties, the spanking event and for her long investigation concerning the *crop circle* appeared at Rocco's setup—now I can confess: it was my creation!

THE DRESSED AND THE NAKED

A unique alignment of celestial bodies, the fire and, ultimately, divine intervention determined the appearance of four defensive figures to accompany me against the *masked battalion*. However, formality and rigid regulations didn't want all of them to be dressed. To value the effort they will make to come along my side, black fabric and a tail were allocated only to the geographically further guys. I will make use of this ordering criterion to thank them.

Among the dressed, I want to thank my other-side-of-the-border friend Simone, for being always so close, even if technically far. I'm glad that I started with him the quest for academic education, and that he will be standing on my side to defend its fulfilment.

"*Manus orante, magno silentio, honorem adducere magistri Gaudentius*". My gratitude towards this person cannot be expressed with words, nor with any ordinary expression. Against his will, he was cast in a world of technology and innovation, his attitude suddenly put him along *Las Promesas de la Física*, but his romance constantly made him strive for philosophy and the vintage. Many the discussions, many the deep personal reflections, almost as much as the many blackout interventions ".....eh!" [moves hands]. I really cannot go deeper, I just want to thank him for being *The Preacher*.

Next in line is a naked paronym—*and sit tight* because the *temperàture* is rising, and things might get quickly *e-spicy*. It is not clear whether he was meant to be naked so that he could show off his personal taste for fine clothing, or to ensure he would stay *comfortable* and prepare for his upcoming *effort*. I only recently realised he risked to become the Ronald of my PhD defence, but I lately turned things *the way around*, and got a remarkable five hours head start. As a good southern person, he finds soap operas so much *interesting*, that they became his constant and *challenging* life occupation. Admirable I find his ability to exploit things to the maximum, his determination, the political awareness and the unique Mediterranean tune, which gave rise to the Cartamil-Bueno family and years of intense *compenetration*. He is constantly *temptated* to live an *e-sweet* life style, I wish he could consume less of his favourite *padwer* white. Much more things should be said here, but the *conspiranoic* eyes are always open, and I prefer to greet him with few words from Vigenère—expressed in pure *MediterraneanEstile*—"qwek tvyl xv krriui Aytvt!".

And there he comes *Dottor Cche Ggey: come farei senza di lei?! The greatest hobby of this guy is to exploit the antenna on his Ā to spread radio frequencies into the world, as much that his phone provider worships him as if he were the Skopjan "Warrior on a Horse". He certainly is one of the most intelligent persons that I know, and I wish he could control his investments in basic commodities, for which he always seeks my strong advice. Because infinite are his kindness, humour and support, I want to greet him with a simple *Doberman!*: the rest he already knows.*

THE ONES WHO PUSH!

In this circle, used to be a guy that *it's not that he cannot be careful, it's just that he never tried*. Imported into the Netherlands with the main purpose of *washing the dirty laundry home*, he was honoured with the title of postdoc, and ever since *The Postdoc* he was called. I owe a debt of gratitude to Nicola's Mediterranean social attitude and mediation skills, which built a delicate and pleasant equilibrium out of tense and potentially explosive initial conditions. Science with him has been very prolific and fun, many the feedback loops with the magic *cagarella*-ink, unforgettable the times when, in a tremendous lack of sleep, we both started *seeing do'ains* everywhere, or when, high in the mountains, he inexplicably revealed me to be terribly afraid of AIDS. That said, I can state with no doubts, that he has been a great scientific advisor and a real friend in the many hangouts! A tender hug goes to his energetic Francesca and their little Silvia.

I want to sincerely thank Doctor Ğlu Ğlu—say hurrah for the Sultan!—for his infinitely *svit* heart and for sharing, since day one, residency on perdition island. Just before my arrival, a vehement yell came out of his mount "GELME, BU BIR TUZAK!", but it was too late for me to resist his charm, and after a *ratatouille* invitation and a few drinks at *Bebop*, he immediately made me feel home. He tried his best to embrace the Mediterranean attitude—proverbial his high-pitched "E! E! E!" corridor exclamations right after San Sebastian—, but I want to acknowledge him for being a man of honour, and for when he allowed the coin-flip that long bound him to his favourite TU Delft companion. He probably cannot imagine what was missed when the Turkish army April's fool was called off, but he certainly knows that he will miss his favourite *Spastrun* alcohol. I will miss him too.

"There's a guy who's sure // all the physics is untrue // but he's riding a stairway to Nature. // Right there, behind the wall // he gets annoyed more and more // with a word you can call him The German". On behalf of the Dutch–European funding agencies, I want to sincerely thank this guy for preserving their valuable money by attending exclusively conferences held in his office. Bastion of the fading third-floor sociality, his constant presence was a strong reference point during the long working days, weekends and nights. Never he tolerated being fed with *bla*-discussions, but he always strived for in-depth analysis, with which he enriched any *figure of science* being developed around. I wish for him a brilliant and adventurous career, and I cannot wait to receive his selfie with D. M. Eagles, his beloved brigadier.

Next in line is a guy of golden colours, not clear whether of human nature or of alien origins, which is strongly determined and successful in whatever he does. This thesis acknowledges his left hand for giving *rough suggestions* of more than perfect quality, and all his support in dealing with $\cos(1/t^3)$ and jumping on trains that are running. I wish him to get rid of all the boring physics from the 80s—you may try to involve the guy just above—, and get some well-deserved Tier A, that we are expecting more and more.

Maflafa (for friends also Fafalda)—in short Miss AMRVLMG—mostly deserves to be thanked for her contributions to the gender equality of our labs and conferences! It was a real pleasure betting with her, and I wish she would never have stopped believing me. Thanks for sharing my burden of dealing with $\sin(1/t^3)$, for the many funny gossips and for the detailed science discussions. To her and Dirk I owe many beautiful memories, going from the fake fainting episodes at the Navy Beach, to the real ones at Lille's cursed,

round table. That said, Dirk you MUST NOW close this thesis. Please do not open it ever again: *there are plenti-of miskates!!*

To Si-ri-jjit, the eminent postdoc, thanks for being my cleanroom mentor back in the days when fabrication of complex oxides was a pure fantasy, and for teaching me the basics that allowed me to grow fast. Even if it isn't always properly acknowledged, I think you gave a very important contribution to all our lab, and I wish you the best of success with you QT career.

An enormous thanks goes to all the bachelor and master students I had the pleasure to work with, among them Nils, the quiet and focused analyst; Lucinda, the magician which turned iridate films into carbon nanotubes, and convinced me that my time to start playing volleyball was finally arrived; Bas, from the squad that defeated Cthulhu, to the one that defeated my personal boardgaming limits—thanks for the cool times and for embracing the Mediterranean attitude since day one!

I want to thank Dima for sharing the domestic walls, for the post-midnight LAO/STO talks, and for finding the right Polish professionals to open Rocco's car. I wish him best of luck with his wall-burning lasers, and with his constant chairing activity in our Monday lab meetings.

To the rest of our lab, Yildiz, Thierry and Jorrit, I wish good luck with their PhD, and to enjoy the many *outjes* that there will finally be!

THE ONES THAT SAW MED

Does this circle of people know *Where is Max?* I personally remember a young Dr. Sfiga-Carbone disappearing down the ski slopes with very good company, I remember him developing the *piano-piano* culture, I remember him stating that *we are all grown-ups*, and I recently heard that he is building a family. My greatest congrats to him!

With a rope, from the Oude Kerk, I see coming down *Perrino Michelinò-Michelle*. I will never forget the talk this guy gave at the Winter Retreat in Courchevel, and the hours and hours of science discussion we spent in front of my poster, right afterwards. I occasionally met him on some ski slope, where he taught me the word E-P-I-C and *not that much more*. Certainly epic were our photo-bombings, the French-Swiss Alps and the many cheese Fondue.

I am very glad that the youngest disciple of the *Radical order*, menheer Joeri—de Vlaams—, is on a quest of conversion to *god Python*, the supreme. He still doesn't admit that $1 + 1 = 2$ *if and only if he is a random god*, but I see his patience coming to an end, and I know that soon he will come to confess.

"But now, to make a barbecue? Really? I grab my zacht and we go!" says our kind Greek companion, a man of pure soul that I will never forget. Thanks for the unexpected mezes and amazing home-made Rakia, the fantastic stories and the beautiful company.

Next, I want to acknowledge Ranko for the very nice concerts and for his legendary timing at parties. I know he values his importance according to the number of lines that are dedicated to him in a thesis, so I will try my best to thank him multiple times, Ranko, also in order to increase the amount of characters that have been pressed for him, oh Ranko, and in case he simply scans through this text to find his name, I want to highlight it by repeating, oh Ranko, that this is for Ranko, yes that Ranko-Ranko and, oh Ranko, thanks a lot Ranko!

An ex-office mate and amazing circus performer, I must thank señor Ignacio de Chile, among all also for his iconic "*how are you doing?*" and unexpected appearances in random conversations—Ranko, you almost spotted the right location, your acknowledgement was just a few lines above!

Among the sporadic members of my almost-private office, vivid memories go to *Florianissimo*—also known as *Floriano, con la liquirizia in mano*—, an excellent C6-high singer and FOM-nights dancer, whose precious ring of power and wedding bitterballen will always be remembered; to Nandini, as funny as stubborn, her presence was always a joy for the office humour; to *the hard-working* Anastasia, which kept high the *picirippi-piripippi* in the office—of which she probably never got to know; to the recently acquired Jacqueline, which calmly endured my stressed attitude and not-for-social determination; to Vera, for proving that quantum tunnelling of voice waves is enough to be allocated into my office, even if physically not being there.

Among the *women of science*, I want to acknowledge *Gabi-babi*, for saving my phone number under the letter *J*, being part of many adventures, and keeping me updated with the super-funny Bankastraal tales; Magda, one of the most—LENA (sorry, sorry Maddy!)—awesome co-host of parties, and...what I wanted to tell you...hm...ah! *Le-Le-Le-Le!*; Katya, for welcoming me and Siffredi in her touring ballet group; Andrea and Yasemin, for the many nice occasions spent in their company.

THE FLUENT

For obvious reasons this section has to begin by thanking *Riccardo-from-Ouxfourd*, gifted creator of many amazing MED songs, which revealed to the Dutch the power of Italian food, and made a stunning wedding celebration. Because he has always been fond of my coloured slides, I am sure he will appreciate the many oranges and blues sprinkled over this thesis, which are my tribute to him.

I want to thank Michele, for his inspiring engineering entrepreneurial skills; Anna, for growing high the *myths* of Rome & Ronald in MED; *Lacarissimacarlanna*, for the fun chit-chats in the cleanroom; Davide, for the skiing adventures; Diego, for the casual coffees; Ale Bruno, for his many wild parties, and for his later discovery of wisdom and knowledge.

Giordano—not me, but the other one—is a person I first met in the land down-under, with whom I formed an interestingly strong bond. He wanted so much to keep me in Australia, that he really couldn't cope with the idea of seeing me go away: I'm glad he somehow managed to chase me down to Delft—to him, Clelia and the little Gabry goes a very warm thanks!

STARS OF THE PAST, NEBULAS OF THE FUTURE

When talking about the stars, nothing comes to mind but Him, the famed captain of a sinking ship *Ronaldo di Leone*. I infinitely thank him for having *hid his pressure chamber, in the desiccator, crappy resonators*, definitely one of the best soundtracks to sing under the shower! His unstoppable attitude, his punch-lines, his lunch and coffee addictions probably annoyed many, but certainly reunited all.

My best regards go to Shun-san, for being representative of a crucial and otherwise very missing character in the group. I know he's almost done with his PhD, and I wish him to keep up with the last few moments, because I cannot wait to celebrate all his efforts!

Back in the days, there used to be Julien, which brought plenty *dirty scenarios* into the department; *sir Salvatore Tagliaboschi*, who transformed his crazy superconducting circuits into a quite interesting business; Big Ben, which preserved the purity of the British language; Joshua, which fostered everyone's hidden *yo-attitude*; Small Ben, first survivor of Gary's upbringing; Enrique, the one that was introduced to me as *Enrique-one*; Andres, the highly skilled science-politician; Nathan, whose amazing beer-brewing in the Navy Beach's pump room should have been passed on to new generations; Jan, whose spot-on science discussions were very enlightening; Chris, whose stop-over in Delft was definitely short, but enough to bring many moments of fun; Samer, who balanced—and at the same time fed—the many *conspiranoias*.

Among the new pupils, I want to thank Robin, for showing the importance of having his own model, his own sample, his own setup, his own PhD, etc., and for being my model of hairstyle!—this is actually not true, but I find it quite fun to invent random motivations at the very end, just like in science—; Joao, for partially taming Mafalda's desire to gossip; Mark, for his loud corridor laughs which reduced the general perception of Italians as loud individuals; Pascal, for finally bringing some fresh wind of MED style in Herre's group—may traditions be kept alive.

Among the many new guys, a wish of good luck goes to Richard, Clemens, Igor, Andreas and Moritz; Daniel, Mark, Martijn, Mario, Felix, Ines and Marios; Andrew, Pablo, Makars and Martin; Filippo, Thomas, Lorenzo and Irina; Mari Carmen, Jeremie, Willeke and Sabina.

After this quite long list, I want to briefly acknowledge some of our many adventures, going from the *I-don't-give-a* spring school, Sebastian, the *Otowedding*, Lille's lobsters, and the Macedonian-Albanian Schampions, to the many ski trips, the MED barbecues, the paintball, Terschelling's wadlopen, the shoes *got'em in New Orleans Louisiana*, the East Coast, and the crazy Antwerp, Brussels and Como road trips—and I here finally mention the never-happened *Prank Week*.

THE INDISPENSABLE

Among the pillars behind this whole organisation, I must thank Tino, the ever-green technician; Mark Ammerlaan, the hard working AJA's and helium's paladin; Allard, the *sciencician*; Mascha & Ron, icons of the good old MED; the whole DEMO staff among which the Navy Beach's surgeon Ruud, and Hi-Frosti's nurse Hans; the whole Kavli Nano-lab staff, among which the wanna-be Italian Charles, Mark & Marco, Eugene, Anja & Arnold.

Of fundamental importance has been our administrative staff: thanks to Marijke, for her kindness and efficiency; to Ety, for being very helpful and for dropping that seed of paranoia that made *The Prank* possible; to Heleen, Erika, Dorine, and, finally, to Maria, for spelling my name correctly most of the times—I really appreciated that!

I need to spend a very few lines to also acknowledge Sodexo, for motivating me to bring my own lunch, the Döner place, for feeding me in late weekends and nights, and of course Domino's pizza, for preserving my pizza-on-Sunday tradition and for giving Ronald so much to talk about.

THE ONES FROM A PARALLEL WORLD

The work leading to this thesis could never have been possible without the *company of the spinning ball*. If there was such a thing in volleyball, I'm sure it would be called *Il processo di Bulgarini*, which I want to thank for the continuous analysis, and for giving our passion a whole new drive! I want to thank Marius, the spearhead of the *Mangiatori di Sabbia*; Edgars, the wall and legendary *hi-fiver*; *Rónán, le ballon voilà*; Rob, the 80s idol; Jorn, Bart, Frank and Maarten: *A je to guys!* An acknowledgement to the Buurmannen 11, the H10 tribe, all the Kratos'08 and beachvolley in TU Delft guys.

I want to thank *Ale*, for sharing with me some of the most beautiful moments of these last few years, and the little *Vikulina*, for teaching me so many things that a whole lifetime would not be enough to pay back.

Un ringraziamento speciale agli amici di Roma: Luca, Giulia, il Benso e Dario, per essere venuti in mio supporto; a Lore e Dimi, per la *costante presenza*; alla mia famiglia allargata dei Rotti–Mattoni–Bertacche, per le Pasque felici e per esserci sempre; a Francy, per i weekend tra le nevi; a Silvia, per aver reso speciale la mia infanzia; a Paola, per averci lasciato mischiare il caffè con la tempera ed il sale, nostra rudimentale scienza; ad Antonio l'artista, per i suoi colorati lavori che hanno accompagnato le mie lunghe giornate in ufficio; ai miei geni, la nonna Renata e tutti gli altri parenti.

Un ringraziamento finale, va a mia madre, per la creatività, l'amore per l'insegnamento e per cercare di avvicinarsi sempre a quello che faccio, sia per lingua che per *pseudoscienza*; e a mio padre, per aver sempre esaurito le mie curiosità tecnologiche, ed essersi rifiutato di installare videogiochi sul mio PC da bambino: il VBasic mi ha fatto certamente molto più contento!

With all this being said, I can finally DECLARE, THIS THESIS, TO BE OVER.

Delft, November 2017

